UNIVERSITY OF CALIFORNIA,
IRVINE

Using Computational Chemistry to Study the Interactions of Indoor Relevant Organic Compounds on Indoor Surfaces

DISSERTATION

submitted in partial satisfaction of the requirements
for the degree of

DOCTOR OF PHILOSOPHY

in Chemistry

by

Elianna Sue Frank

Dissertation Committee:
Professor Douglas J. Tobias, Chair
Professor Craig Martens
Professor Ioan Andricioaei

2022

DEDICATION

For Angus and Bella 2

TABLE OF CONTENTS

Page

LIST OF FIGURES **vi**

LIST OF TABLES **xv**

ACKNOWLEDGMENTS **xvii**

VITA **xix**

ABSTRACT OF THE DISSERTATION **xxii**

1 Introduction **1**
- 1.1 The Indoor Environment . . . 1
- 1.2 Computational Methods . . . 2
- 1.3 Classical Molecular Dynamics . . . 5
  - 1.3.1 Umbrella Sampling . . . 7
- 1.4 *ab initio* Molecular Dynamics . . . 9
  - 1.4.1 Power Spectra Calculations . . . 12
- 1.5 Conclusions . . . 13

2 Impact of Adsorbed Water on the Interaction of Limonene with Hydroxylated SiO_2 Implications of $\pi-$Hydrogen Bonding for Surfaces in Humid Environments **14**
- 2.1 Background . . . 14
- 2.2 Simulation Protocols . . . 16
  - 2.2.1 Classical Molecular Dynamics Simulations . . . 16
  - 2.2.2 *ab initio* Molecular Dynamics Simulations . . . 17
  - 2.2.3 Surface Analysis Techniques . . . 17
- 2.3 Results . . . 18
  - 2.3.1 Experimental Results . . . 18
  - 2.3.2 *ab initio* Molecular Dynamics Results . . . 20
  - 2.3.3 Classical Molecular Dynamics Results . . . 23
- 2.4 Conclusions . . . 30

3 Adsorption of Constitutional Isomers of Cyclic Monoterpenes on Hydroxylated Silica Surfaces **31**
3.1 Background . . . 31
3.2 Simulation Protocols . . . 32
3.2.1 Classical Molecular Dynamics Simulations . . . 32
3.2.2 *ab initio* Molecular Dynamics Simulations . . . 33
3.2.3 Surface Analysis Techniques . . . 33
3.3 Results . . . 33
3.3.1 Experimental Results . . . 34
3.3.2 Classical Molecular Dynamics Results . . . 37
3.3.3 *ab initio* Molecular Dynamics Results . . . 41
3.4 Conclusions . . . 45

4 Heterogeneous Interactions of Prevalent Indoor Oxygenated Organic Compounds on Hydroxylated SiO_2 **47**
4.1 Background . . . 47
4.2 Simulation Protocols . . . 48
4.2.1 Surface Analysis Techniques . . . 49
4.3 Results . . . 49
4.3.1 Experimental Results . . . 50
4.3.2 Classical Molecular Dynamics Results . . . 56
4.3.3 *ab initio* Molecular Dynamics Results . . . 59
4.3.4 Electronic Structure Calculations Results . . . 63
4.4 Conclusions . . . 64

5 Heterogeneous Interactions between Carvone and SiO_2 **65**
5.1 Background . . . 65
5.2 Simulation Protocols . . . 66
5.2.1 Surface Analysis Techniques . . . 67
5.3 Results . . . 68
5.3.1 Experimental Results . . . 68
5.3.2 Kinetic Modeling Results . . . 72
5.3.3 Computational Results . . . 74
5.4 Conclusions . . . 83

6 Interactions of Limonene and Carvone on Titanium Dioxide (TiO_2) Surface **84**
6.1 Background . . . 84
6.2 Simulation Protocols . . . 87
6.2.1 Classical Molecular Dynamics Simulations . . . 87
6.2.2 *ab initio* Molecular Dynamics Simulations . . . 89
6.2.3 Surface Analysis Techniques . . . 90
6.3 Results . . . 91
6.3.1 Experimental Results . . . 91
6.3.2 Classical Molecular Dynamics Results . . . 100

6.3.3 *ab initio* Molecular Dynamics Results 115
6.3.4 Kinetic Model Parameters 124
6.4 Conclusions 130

7 Adsorption of 6-MHO on Two Indoor Relevant Surface Materials: SiO_2 and TiO_2 131
7.1 Background 131
7.2 Computational Methods 133
7.2.1 Surface Analysis Techniques 133
7.3 Results 134
7.3.1 Experimental Results 134
7.3.2 Classical Molecular Dynamics Results 141
7.3.3 *ab initio* Molecular Dynamics Results 147
7.3.4 Electronic Structure Calculation results 152
7.4 Conclusions 153

8 Conclusion 154
8.1 Using Computational Chemistry Study the Indoor Environment 154

Bibliography 156

LIST OF FIGURES

Page

2.1 FT-IR spectra of limonene adsorbed on SiO_2 surface at an equilibrium pressure of 50 mTorr under different RH condition (scale bar = 0.05 absorbance units). The RH is increased from < 1% to 78% RH in the following increments: < 1%, 29%, 38%, 58% and 78%. 19

2.2 Snapshots from the AIMD simulations of limonene with an increasing number of water molecules (0, 12, 24, 48) on the SiO_2 surface. 20

2.3 Power spectra calculated from the AIMD simulations for the hydrogen atoms near limonene in the low wavenumber region. 21

2.4 Power spectra calculated from the AIMD simulations for the hydrogen atoms near limonene in the high wavenumber region. 22

2.5 Power spectra of blue shifting region from the AIMD simulation for water hydrogen atoms on SiO_2 surfaces with no limonene present but an increasing number of water molecules. 23

2.6 Snapshots from MD simulations of 0.5, 1, 2, and 3 ML of water on the SiO_2 surface. Each snapshot shows a limonene-water π-hydrogen bond. 24

2.7 Density profiles of water molecules and limonene (enhanced at 5X magnification) for each monolayer system. A water number density of 0.033 $\mathring{A}^{-3}$ corresponds to bulk water. 25

2.8 Histogram of average number of bonds formed with a water oxygen on the x-axis of the simulation cell, where x is the direction normal to the surface of SiO_2. 26

2.9 Histograms of minimum distance between carbon atoms of two limonene molecules in 2 and 3 monolayers. 28

2.10 Histograms of minimum distance between carbon atoms of five limonene molecules in 2 and 3 monolayers. 28

2.11 Potential of mean force (PMF) for limonene desorption from the SiO_2 surface at various levels of hydration computed from classical MD simulations. . . . 29

3.1 Absorbance spectra of limonene, γ-terpinene, terpinolene, and α-pinene adsorbed on the SiO_2 surface as a function of pressure. ($\sim$ 26, 100, and 280 mTorr) in the 1200-4000 cm^{-1} spectral region. The clean SiO_2 surface is used as the background spectrum and gas-phase absorptions are subtracted from each of the spectra. 35

3.2 Normalized peak intensity of surface hydroxyl group (3745 cm^{-1}) loss as a function of γ-terpinene, terpinolene, and α-pinene, and limonene adsorption on SiO_2 surface. 36
3.3 (a) FT-IR spectra of limonene adsorption on the SiO_2 surface and subsequent displaced by α-pinene (using pre-adsorbed limonene SiO_2 surface as the background spectrum). (b) FT-IR spectra of limonene adsorption on the SiO_2 surface and subsequent displaced by terpinolene (using pre-adsorbed limonene SiO_2 surface as the background spectrum). 37
3.4 Potential of mean force (PMF) for the desorption of each isomer from the SiO_2 surface computed from the classical MD simulations 38
3.5 Desorption enthalpy profile computed from the MD simulation of α-pinene. The error bars are based on the standard deviation of the energy computed for the initial 100 structures. 39
3.6 The mass accommodation coefficient was calculated for the following five limonene isomers. Relevant C=C bonds listed for further discussion in Section 3.3.2. 40
3.7 Left to right, snapshots from AIMD simulations of γ-terpinene, terpinolene, limonene and α-pinene isomers on the SiO_2 surface. The $C_{sp}{}^2$ carbon atoms responsible for π-hydrogen bonding are highlighted in green and the snapshots depict the close proximity between $C_{sp}{}^2$ carbons for γ-terpinene and terpinolene compared to limonene. 41
3.8 (a) Experimental spectra and (b) power spectra calculated from AIMD simulations of limonene, γ-terpinene, terpinolene, α-pinene adsorbed on the SiO_2 surface. The concentration of limonene, γ-terpinene, and terpinolene is $\sim$ 26 mTorr and α-pinene concentration is 280 mTorr. 42
3.9 Radial distribution functions calculated among the hydroxyl hydrogen atoms and $C_{sp}{}^2$ carbon atoms of limonene isomers. 43

4.1 Three molecules of interest for this study. 48
4.2 FT-IR spectra of SiO_2 particles exposed to dihydromyrcenol (7mTorr), α-terpineol (6 mTorr), linalool (7 mTorr), and limonene (276 mTorr). The clean SiO_2 surface is used as the background spectrum. 51
4.3 The first order decay for the initial desorption of OOCs as well as limonene from the SiO_2 surface. A_t is the integrated absorbance of peak isolated Si-OH groups (3745 cm^{-1}) at specific time t. A_0 is the initial integrated absorbance peak of isolated Si-OH groups. 55
4.4 The dihedral angle (1-2-3-4) that can cause a change in linalool orientation during the simulations. The π bonds are labeled in red and discussed in Table 4.3. 56
4.5 Free energy profile as a function of the orientation of linalool on the hydroxylated SiO_2 surface computed from 0.30 μs force classical MD simulation. . . 57
4.6 Potential of mean force (PMF) for OOCs desorption from the SiO_2 surface computed from the classical MD simulation. 59

4.7 Snapshots from the AIMD simulations of (a) dihydromyrcenol, (b) α-terpineol and (c,d) linalool adsorbed on the SiO_2 surface in their most predominant positions. There exists two orientations for linalool, as discussed in the classical MD section. The oxygen, carbon, hydrogen, and silicon atoms are colored red, cyan, white, and yellow, respectively. 60
4.8 Radial distribution functions (RDFs) calculated for distances r between the SiO_2 hydroxyl hydrogen atoms and the oxygen atoms of dihydromyrcenol, α-terpineol, and linalool. The high RDF peak at ~ 1.6 $\mathring{A}$ is observed for all three OOCs suggests the formation of O-H hydrogen bonding with the surface hydroxyl groups. 61
4.9 (a) Experimental spectra and (b) power spectra calculated from AIMD simulations of dihydromyrcenol, α-terpineol, and linalool adsorbed on SiO_2 surface. The insert shows that the peak for the surface hydroxyl groups in systems in the presence of linalool and dihydromyrcenol, as shown by the black arrows, are blue shifted compared to the corresponding peak for the SiO_2 surface with no adsorbate present, as shown by the black dashed line. 62

5.1 (a) FT-IR spectra of 52 mTorr of gas-phase carvone (black line) at 296 K. (scale bar = 0.002 absorbance units). (b) FT-IR absorbance spectra of carvone on SiO_2 surface at an equilibrium pressure of 4 mTorr under dry conditions. (scale bar = 0.1 absorbance units). 69
5.2 Absorbance spectra of carvone on SiO_2 as a function of pressure in the spectral range of 1200 to 1800 cm^{-1}. (scale bar = 0.1 absorbance units) 70
5.3 Absorbance spectra of carvone on SiO_2 as a function of pressure in the spectral range of 2600 to 4000 cm^{-1}. The peaks at 3745 cm^{-1} are flat starting at 4 mTorr, meaning there is no peak corresponding to the stretch of free isolated OH functional groups 71
5.4 First order desorption kinetics for carvone (black solid circles) and limonene (yellow solid squares) at 4 mTorr from the SiO_2 surface under dry conditions. The desorption rates constants determine this way are $2.4\times10^{-4}\pm4.8\times10^{-7}s^{-1}$ for carvone and $7.2\times10^{-3}\pm1.4\times10^{-4}s^{-1}$ for limonene. This reveals that the desorption kinetics of carvone is 30 times slower than that of limonene. . . . 72
5.5 Temporal evolution of carvone adsorption on hydroxylated SiO_2 surface at an equilirbium pressure of 2 mTorr (black solid circle) and 4 mTorr (red solid circle) under dry conditions. Triplicate experiments were measured and the shadow represents one standard error. The SiO_2 surface was exposed to carvone at time t = 0 min. The adsorption process reached equilibrium at t = 3 mins for 2 mTorr and t = 10 mins for 4 mTorr. At time t = 25 mins, the desorption process was initiated by the evacuation of gas-phase carvone. The solid lines show the kinetic modeling results including the pore mechanism and the kinetic modeling results without the pore mechanism are shown in dashed lines. 73
5.6 Schematic of the K2-SURF model for reversible adsorption of carvone on SiO_2 with two different adsorption sites cooresponding to pore and non-pore sites. 73

5.7 (a) Carvone molecular orientation most likely leading to oxygen silicon association. (b) Carvone molecular orientation most likely leading to hydrogen bond. (c) Distribution of $cos(\theta)$, where θ is the angle between carbon atoms 2C, 6C, and the SiO_2 surface described in Figures 5.7a and 5.7b. A $cos(\theta)$ of 1 indicates the ring is parallel to the surface and a $cos(\theta)$ between 0.25 and 0.80 indicates the carvone right is upright on the surface. Molecular snapshots come from classical MD simulations. Oxygen atoms are in red, Si atoms are in blue, hydrogen atoms are white, carbon atoms are teal, and the carbon atoms used to calculate θ are shown in pink. 75
5.8 Enthalpy as a function of the distance of the carvone molecule from the SiO_2 surface from 154 initial configurations with 108 configurations showing a hydrogen bond interaction and 48 showing an oxygen-silicon association. Enthalpy for each interaction type are also shown in blue and purple based on starting configurations with hydrogen bonding and oxygen-silicon associations, respectively. 76
5.9 Oxygen power spectra showing the slight red shift in the ~ 1600 cm^{-1} wavenumber in the AIMD simulation of carvone in the gas phase compared to the AIMD simulations of both carvone on a partially dehydroxylated SiO_2 surface with two 3-coordinated silicon atoms and carvone on a fully hydroxylated surface where the carvone molecule can only form hydrogen bonds with the surface. 77
5.10 Full oxygen power spectra of carvone on the partially dehydroxylated surface and the fully hydroxylated surface. 78
5.11 (a) Optimized geometry for carvone adsorbed to a fully hydroxylated SiO_2 surface via a hydrogen bond. (b) Optimized geometry for carvone adsorbed to a partially dehydroxylated SiO_2 surface via an oxygen silicon association. 79
5.12 (a) Electrostatic potential for carvone adsorbed to the fully hydroxylated SiO_2 surface through the hydrogen bond mechanism. (b) Electrostatic potential for carvone adsorbed to the partially dehydroxylated SiO_2 surface through the oxygen silicon association mechanism. Both electrostatic potentials are plotted on an isosurface density of 0.07 e/a.u^3. 81
5.13 (a) Potential of mean force (PMF) for the desorption of carvone on SiO_2 surface. (b) Fraction of the 10 ns window where the carvone oxygen was in an oxygen silicon association as a function of the PMF. 82

6.1 (a) FT-IR spectra of limonene adsorbed on TiO_2 surface under dry conditions (<1% RH) as a function of limonene pressure in the spectral range extending from 1200 to 4000 cm^{-1} (scale bar = 0.1 absorbance units). The equilibrium pressures increase from the light red to black spectra: 3, 6, 11, 20, 31, 42, 75, and 148 mTorr. (b) The ordinate plots the normalized integrated peak area of limonene in the spectral region from 2800 to 3115 cm^{-1} as function of limonene pressure (mTorr), the right ordinate plots the normalized peak height of the loss of Ti-OH function groups at 3656 cm^{-1}. 92

6.2 (a) FT-IR spectra of 148 mTorr of gas-phase limonene at 296 K in the spectral ranges extending from ca. 1200 to 4000 cm^{-1} (scale bar = 0.02 absorbance units). The modes are assigned as follows: 3087, 3020 cm^{-1} for the C-H $C_{sp}{}^2$ stretching motion from alkene and ring, respectively; 2977, 2930, 2868, 2849 cm-1 for C-H $C_{sp}{}^2$ stretching motion; 1654 cm^{-1} for C=C bond stretching vibrations; 1458, 1382 cm^{-1} for CH_3 and CH_2 bending vibrations motion, respectively. 93

6.3 (a) Absorbance FT-IR spectra of carvone adsorbed on TiO_2 surface under dry conditions (< 1% RH) as a function of pressure in the spectral range extending from ca. 1200 to 4000 cm^{-1} (scale bar = 0.04 absorbance units). (b) The above (a) spectra range extends from 1500 to 1800 cm^{-1} (scale bar = 0.02 absorbance units) (c) The ordinate plots the normalized integrated peak area of carvone at 1648 cm^{-1} (ranging from 1560 to 1720 cm^{-1}) as function of carvone pressure (mTorr), the right ordinate plots the normalized peak height of the loss of Ti-OH functional groups at 3656 cm^{-1}. The equilibrium pressures are 2, 8, and 18 mTorr, respectively. 95

6.4 The FT-IR spectra of limonene adsorbed on TiO_2 (about 8 mg) surface at an equilibrium pressure of 55 ± 1 mTorr under different RH conditions. The RH is increased in the following increments:< 1%, (a) 3% (scale bar = 0.02 absorbance units), (b) 10% (scale bar = 0.02 absorbance units), (c) 18% (scale bar = 0.02 absorbance units), (d) 25% (scale bar = 0.05 absorbance units), (e) 30% (scale bar = 0.05 absorbance units), (f) 51% (scale bar = 0.05 absorbance units). In each subfigure, the red spectrum is the FT-IR spectra of limonene adsorbed on TiO_2 surface under <1% RH condition; the blue solid spectrum is the FT-IR spectra of limonene adsorbed on TiO_2 surface under high RH condition; and the dashed blue spectrum is obtained by blue solid spectrum minus the red spectrum with a ratio of the percentage of limonene left on TiO_2 surface as listed in Table 6.1 to remove the limonene remaining on the hydrated TiO_2 surface from the spectrum so the increase in the adsorbed water absorption bands on the TiO_2 surface under high RH condition can be determined. The broad absorption band centered at around 3400 cm^{-1} and the adsorption band at 1625 cm^{-1} in the blue dashed spectra are assigned to the O-H stretching and H_2O bending vibration modes, respectively, for adsorbed water on the TiO_2 surface. 97

6.5 FT-IR spectra of carvone adsorbed on TiO_2 (about 8 mg) surface at an equilibrium pressure of 16 mTorr at <1% RH (black solid line) and 67% RH condition (purple solid line), that the peak at 1648 cm^{-1} shifts to 1660 cm^{-1} is attributed to the bending mode vibration for adsorbed H_2O. The dashed purple spectrum is obtained by the purple solid spectrum minus the black solid spectrum to show the "water growth" on the TiO_2 surface. (scale bar = 0.1 absorbance units) 98

6.6 (a-c) shows limonene on non-hydroxylated TiO_2 surfaces with increasing levels of hydration, (d-f) shows limonene on hydroxylated surfaces with increasing levels of hydration, (g-i) shows carvonce on non-hydroxylated TiO_2 surfaces with increasing levels of hydration, (j-l) shows carvone on hydroxylated TiO_2 surfaces with increasing levels of hydration. Water molecules engaged in hydrogen bonds (π-hydrogen or OH-hydrogen) with the adsorbate are shown in fully color, all other water molecules are shown transparent. Red atoms correspond to O atoms, pink atoms correspond to Ti atoms, white atoms correspond to H atoms and cyan atoms correspond to C atoms. The surfaces have been oriented to showcase surface/adsorbate interactions. 101
6.7 Density profile for the classical MD simulations for limonene (where limonene has been magnified by 10) for the non-hydroxylated surface with 0.5 ML . . 102
6.8 Density profile for the classical MD simulations for limonene (where limonene has been magnified by 10) for the hydroxylated surface with 0.5 ML 102
6.9 Density profile for the classical MD simulations for limonene (where limonene has been magnified by 10) for the non-hydroxylated surface with 1 ML . . . 103
6.10 Density profile for the classical MD simulations for limonene (where limonene has been magnified by 10) for the hydroxylated surface with 1 ML 103
6.11 Snapshots of each kind of hydrogen bonding interaction from the classical molecular dynamics simulations. (a) Carvone oxygen atom in a hydrogen bond with hydroxylated TiO_2 surface. (b) Carvone $C_{sp}{}^2$ carbon atom in π-hydrogen bond with hydroxylated TiO_2 surface. (c) Carvone oxygen atom in a hydrogen bond with water, where the water molecule is also forming a hydrogen bond with the surrounding water molecules. (d) Carvone oxygen atom in a hydrogen bond with water, where the water molecule is not forming a hydrogen bond with the surrounding water molecules. 109
6.12 Potential of mean force (PMF) for the desorption of limonene and carvone from non-hydroxylated surfaces calculated from the classical MD simulations. 111
6.13 Potential of mean force (PMF) for the desorption of limonene and carvone from hydroxylated surfaces calculated from the classical MD simulations. . . 112
6.14 Fraction of water molecules in hydrogen bond interactions with carvone that are also in hydrogen bonds with either the TiO_2 surface, surrounding waters, or no other molecules (thus disrupting the hydrogen bonding network) as a function of distance from the surface during the PMF calculation. 113
6.15 PMF of carvone and limonene on the non-hydroxylated 0.5 ML surface. There is a noticeable kink in the PMF around ~ 4 Å, which attribute to the endocylic C=C bond in limonene and the carvone oxygen atom forming hydrogen and π-hydrogen bonds with water molecules on the top of the water layer. This can be seen in the molecular snapshots roughly along the PMF. Additional sampling was done at windows close to 4 Å to ensure all configurations along the PMF were properly sampled. This kink is not seen in the 1 ML and hydroxylated systems to the full hydration of the surface layer of TiO_2 that allows for water to form more consistent monolayers, allowing for a more uniform desorption from the surface. 114

6.16 (a-c) shows limonene on a non-hydroxylated surface with 0 water molecules, on a non-hydroxylated surface with 4 water molecules and hydroxylated surface, (d-f) shows carvone on a non-hydroxylated surface with 0 water molecules, on a non-hydroxylated surface with 4 water molecules and on a hydroxylated surface. Note, a slightly larger TiO_2 system was used for carvone on the non-hydroxylated surface with 4 water molecules to fully accommodate the carvone and water molecules. 116
6.17 Oxygen power spectra for the non-hydroxylated TiO_2 surface, the non-hydroxylated surface with 1 limonene molecule and the non-hydroxylated surface with 1 carvone molecule. All intensity values have been rescaled to run from 0 to 1. . . 117
6.18 Oxygen power spectra for the non-hydroxylated TiO_2 surface with 4 water molecules, the non-hydroxylated surface with 4 water molecules and 1 limonene molecule and the non-hydroxylated surface with 4 water molecules and 1 carvone molecule. All intensity values have been rescaled to run from 0 to 1. 118
6.19 Oxygen power spectra for the hydroxylated TiO_2 surface, the hydroxylated surface with 1 limonene molecule and the hydroxylated surface with 1 carvone molecule. All intensity values have been rescaled to run from 0 to 1. 119
6.20 Hydrogen power spectra for the non-hydroxylated TiO_2 surface with 4 water molecules, the non-hydroxylated surface with 4 water molecules and 1 limonene molecule and the non-hydroxylated surface with 4 water molecules and 1 carvone molecule. All intensity values have been rescaled to run from 0 to 1. 120
6.21 Hydrogen power spectra for the hydroxylated TiO_2 surface, the hydroxylated surface with 1 limonene molecule and the hydroxylated surface with 1 carvone molecule. All intensity values have been rescaled to run from 0 to 1. 121
6.22 Oxygen power spectra of the carvone carbonyl stretching region. We see red shifting when the carvone molecule is on the surface, and greater red shifting without water/hydroxyl groups. All intensity values have been rescaled to run from 0 to 1 and the spectra for carvone on the TiO_2 surfaces has been scaled by 5x for clarity. 123
6.23 Difference between distance (1) and distance (2), in Å, during the course of the 30 ps AIMD simulation. 124
6.24 Box plot of 15 interaction energies calculated from AIMD simulations for (a) limonene (b) carvone 126
6.25 Potential of mean force (PMF) for the desorption of one water molecule from the hydroxylated TiO_2 surface with 0 ML water calculated from the classical molecular dynamics simulations. The free energy profiles are placed vertically, such that their minima are at the zero of free energy. 127
6.26 Potential of mean force (PMF) or ΔG, the enthalpic contribution, ΔH, used as the desorption enthalpy in the kinetic model, and the entropic contribution $-T\Delta S$ for one water molecule on the hydroxylated TiO_2 surface with 0 ML water. 128

6.27 Potential of mean force (PMF) or ΔG, the enthalpic contribution, ΔH, used as the desorption enthalpy in the kinetic model, and the entropic contribution -TΔS for limonene on the non-hydroxylated surface with 0.5 ML water (b) the hydroxylated surface with 0.5 ML water, (c) the non-hydroxylated surface with 1 ML water (d) the hydroxylated surface with 1 ML water. 129
6.28 Potential of mean force (PMF) or ΔG, the enthalpic contribution, ΔH, used as the desorption enthalpy in the kinetic model, and the entropic contribution -TΔS for carvone on the non-hydroxylated surface with 0.5 ML water (b) the hydroxylated surface with 0.5 ML water, (c) the non-hydroxylated surface with 1 ML water (d) the hydroxylated surface with 1 ML water. 130

7.1 FT-IR gas-phase spectra of 550 mTorr 6-MHO at 296 K in the spectral ranges extending from ca. 1200 to 4000 cm^{-1}. (scale bar = 0.01 absorbance units) (b) FT-IR absorbance spectra of 6-MHO on the SiO_2 surface at an equilibrium pressure of 2, 5, 10, 21, 42, 76, 119, and 161 mTorr under dry conditions, respectively. (scale bar = 0.1 absorbance units) (c) The surface adsorption spectral range extending from ca. 1500 to 1800 cm^{-1} as function of pressures from (b). (scale bar = 0.05 absorbance units) 136
7.2 Temporal evolution of 6-MHO adsorption on the hydroxylated SiO_2 surface at an equilibrium pressure of 5, 12, 24, and 48 mTorr under dry conditions . 138
7.3 The apparent first order desorption kinetics $ln\frac{[VOC]_t}{[VOC]_{equ}}$ vs t(s)) for α-terpineol (blue solid pentagons), carvone (black solid circles), dihydromyrcenol (green solid diamonds), linalool (purple solid triangles), 6-MHO (red solid circles) and limonene (yellow solid squares) at 4 mTorr from the hydroxylated SiO_2 surface under dry conditions. The order of desorption kinetics are: $k_{des}^{\alpha-terpineol} < k_{des}^{carvone} < k_{des}^{dihydromyrcenol} < k_{des}^{linalool} < k_{des}^{6-MHO} < k_{des}^{limonene}$ 139
7.4 Absorbance FT-IR spectra of 6-MHO adsorbed on TiO_2 surface under dry conditions at an equilibrium pressure of 3 mTorr in the spectral range extending from ca. 1200 to 4000 cm^{-1}. (scale bar = 0.05 absorbance units) 140
7.5 Molecular snapshots of 6-MHO on the SiO_2 and TiO_2 surfaces from force field-based MD simulations. (a) 6-MHO on the non-hydroxylated TiO_2 surface. (b) 6-MHO on the hydroxylated TiO_2 surface. (c) 6-MHO on the SiO_2 surface where the 6-MHO oxygen atom is engaged in a hydrogen bond with the surface OH groups. (d) 6-MHO on the TiO_2 surface where the 6-MHO oxygen atom is engaged in an oxygen silicon association. O atoms are colored red, Ti atoms pink, Si atoms yellow, H atoms white, and C atoms, cyan. 142

7.6 (a) 6-MHO with a dihedral angle of 151°, with the atoms used to measure the dihedral angle colored pink. This is a common dihedral angle measured for all surfaces and surface interaction types. (b) 6-MHO with a dihedral angle of 21°, which is frequently observed for 6-MHO on the non-hydroxylated TiO_2 surface and less often observed for 6-MHO on the hydroxylated TiO_2 surface and the SiO_2 surface with 6-MHO is in an oxygen silicon association. (c) Distribution of the 6-MHO dihedral angle on SiO_2 when the 6-MHO oxygen is engaged in a hydrogen bond, for SiO_2 when the 6-MHO oxygen is engaged in an oxygen silicon association, for the non-hydroxylated TiO_2 surface, and for the hydroxylated TiO_2 surface 143
7.7 Potential of mean force (PMF) for the desorption of 6-MHO on the SiO_2 and TiO_2 surfaces calculated using classical MD simulations and umbrella sampling. 145
7.8 Power spectra for all hydrogen atoms for 6-MHO adsorbed on the fully hydroxylated SiO_2 surface and partially dehydroxylated SiO_2 surface. All intensity values have been rescaled to run from 0 to 1. 148
7.9 Power spectra for all oxygen atoms in the region of the 6-MHO C=O stretch for 6-MHO in the gas phase, on a fully hydroxylated SiO_2 surface, and on a partially dehydroxylated SiO_2 surface. There is a slight red shift in the 1670 cm^{-1} wavenumber peak for 6-MHO on either surface. Consistent with our study of carvone, the red shift is greater for the fully hydroxylated SiO_2 surface compared to the partially dehydroxylated SiO_2 surface. All intensity values have been rescaled to run from 0 to 1 and the spectra for 6-MHO on the fully hydroxylated and partially dehydroxylated surfaces has been scaled by 5x for clarity. 148
7.10 Power spectra for all hydrogen atoms for 6-MHO adsorbed on the non-hydroxylated TiO_2 surface with 4 water molecules and for 6-MHO adsorbed on the hydroxylated TiO_2 surface. All intensity values have been rescaled to run from 0 to 1. 150
7.11 Power spectra for all oxygen atoms for 6-MHO adsorbed on the non-hydroxylated TiO_2 surface with 0 water molecules, for 6-MHO adsorbed on the non-hydroxylated TiO_2 surface with 4 water molecules, and for 6-MHO adsorbed on the hydroxylated TiO_2 surface. All intensity values have been rescaled to run from 0 to 1. 150
7.12 Power spectra for all oxygen atoms in the region of the 6-MHO C=O stretch for 6-MHO in the gas phase, on a non-hydroxylated TiO_2 surface with 0 water molecules, on a non-hydroxylated TiO_2 surface with 4 water molecules, and on a hydroxylated TiO_2 surface. Note, compared to Figure 7.10, there are slight differences in the 6-MHO gas phase spectra due to the difference in AIMD functional used. There is a slight red shift in the 1710 cm^{-1} for 6-MHO in the gas phase compared to TiO_2 on any TiO_2 surface. All intensity values have been scaled by 5x for clarity. 151
7.13 Gas phase scan of 6-MHO dihedral angle. 152

LIST OF TABLES

Page

2.1 Changes in the amount of limonene adsorbed on SiO_2, as a function of relative humidity and coverage of coadsorbed water. 19
2.2 Limonene acceptor statistics for SiO_2 and water 27

3.1 π-hydrogen bonding criteria for each isomer 33
3.2 Surface mass accommodation coefficients from classical molecular dynamics simulations 40
3.3 Hydrogen bonding statistics for isomers 44

4.1 Experimental values for the desorption of OOCs from the SiO_2 surface. . . . 53
4.2 Desorption lifetime estimations. 56
4.3 Hydrogen bonding statistics for linalool in each surface conformation. 58
4.4 Average number and bond length of different hydrogen bonds for dihydromyrcenol, linalool, and α-terpineol. 63

5.1 Details on the two types of carvone-silica interactions observed in force field-based MD simulations. 75

6.1 Changes in adsorbed limonene and carvone on TiO_2 surface as a function of relative humidity and co-adsorbed water. 99
6.2 Average number of π-hydrogen bonds for carvone and limonene. π-hydrogen bonding criteria was determined if the $C_{sp}{}^2$ distance < 3.5 Å and the OH $C_{sp}{}^2$ angle was > 120 degrees. (n.a. - not applicable) 105
6.3 Carvone carbonyl oxygen hydrogen bonding statistic. Hydrogen bonding criteria was determined if the O-O distance < 3.5 Å and the OH..O angle was > 120 degrees. (n.a. - not applicable) 106
6.4 Proportion of trajectory where the nearest neighbor to the carvone carbonyl oxygen is either a water oxygen atom or a Ti atom and the average distance between interacting atoms. 108
6.5 Fraction of water-water hydrogen bonds, water-surface hydrogen bonds, and water-adsorbate hydrogen bonds. A hydrogen bond is defined as the O-O distance < 3.5 Å and OH..O angle is > 120 °. 110

6.6 Hydrogen bonding statistics for AIMD simulations. The non-hydroxylated surface with 0 water molecules cannot form any hydrogen bonds. Hydrogen bonding criteria was determined in the O-O or O-$C_{sp}{}^2$ distance was less than 3.5 Å and the OH...O angle of OH...$C_{sp}{}^2$ angle was greater than 120°. 122
6.7 Surface accomadation coefficient for limonene and carvone on various TiO_2 surfaces. 125
6.8 Mean and standard deviation for 15 interaction energies calculated from AIMD simulations for limonene and carvone on TiO_2 surfaces. 126

7.1 Hydrogen bonding statistics for 6-MHO for the full simulation on the SiO_2 surface, for the portions of the simulation where the 6-MHO oxygen atom was in a hydrogen bond, and for the hydroxylated TiO_2 surface. π-hydrogen bonding criteria was determined if the $C_{sp}{}^2$-O distance was less than 3.5 Å and the OH- $C_{sp}{}^2$ angle was $> 120\,^\circ$ and hydrogen bonding criteria was determined if the O-O distance was less than 3.5 Å and the OH-O angle was $> 120\,^\circ$. . 144

ACKNOWLEDGMENTS

I would like to thank the Alfred P. Sloan Foundation (Grants G-2017-9796, G-2019-12306, and G-2020-13912) for the funding during my PhD. I would like to thank my advisor, Professor Douglas J. Tobias for his mentorship. In addition, as chair of the chemistry department, Doug was dedicated to improving the chemistry department climate and culture, and I find this to be his most inspiring act of leadership. Furthermore, I would like to thank our collaborators, Professor Vicki Grassian, who instilled great confidence in my work, and her wonderful postdocs: Hanyu Fan and Liubin Huang, as well as Professor Manabu Shriawia and Project Scientist Pascale Lakely. I would like to thank my dissertation committee, Doug, Craig, and Ioan for teaching me about statistical mechanics.

I would also like to express my gratitude to all former and current group members, including (but not limited to): Vivek Tygai, Saleh Riahi, and Alfredo Friertes.

In addition, I would have never entered graduate school if not for my wonderful experience at Carleton College. I would like to thank the following professors from Carleton College: Buck Taylor, Dani Kohen, Marion Cass, Trish Ferrett, Deborah Gross, Tommy Occopiniti, Will Hollingsworth, and Jay Tasson.

I thank my "friends from the trenches": Alissa Matus, Dorothy Huang, Dave Knez, as well as some lifelong friends: Brynne, Nick, Kenneth, Anne, Katie, and Joe. Also, I would like to thank my family: Rachel (and Harrison!), Derek, Bella 1 and Bella 2, and my parents, Lisa and Dan.

The most important acknowledgement is for my ~~boyfriend~~ husband, Angus Zeng, for many years of support, laughter, and love. I could not have done this without you!

Chapter 2 of this dissertation is reprinted with permission from the American Chemical Society regarding the published work: Elianna S. Frank, Hanyu Fan, Mona Shrestha, Saleh

Riahi, Douglas J. Tobias, and Vicki H. Grassian. Impact of Adsorbed Water on the Interaction of Limonene with Hydroxylated SiO_2 Implications of $\pi-$Hydrogen Bonding for Surfaces in Humid Environments. Journal of Physical Chemistry A, 124(50):10592–10599, 2020.

Chapter 3 of this dissertation is reprinted with permission from the American Chemical Society regarding the published work: Liubin Huang, Elianna S. Frank, Saleh Riahi, Douglas J. Tobias, and Vicki H. Grassian. Adsorption of constitutional isomers of cyclic monoterpenes on hydroxylated silica surfaces. The Journal of Chemical Physics, 154(12):124703, 3 2021.

Chapter 4 of this dissertation is reprinted with permission from the American Chemical Society regarding the published work: Liubin Huang, Elianna S. Frank, Mona Shrestha, Saleh Riahi, Douglas J. Tobias, and Vicki H. Grassian. Heterogeneous Interactions of Prevalent Indoor Oxygenated Organic Compounds on Hydroxylated SiO_2 Surfaces. Environmental Science Technology, 55(10):6623–6630, 5 2021.

Chapter 5 of this dissertation is reprinted with permission from the American Chemical Society regarding the published work: Hanyu Fan, Elianna S. Frank, Pascale S. J. Lakey, Manabu Shiraiwa, Douglas J. Tobias, and Vicki H. Grassian. Heterogeneous Interactions between Carvone and Hydroxylated SiO_2. The Journal of Physical Chemistry C, 126(14):6267–6279, 4 2022.

Chapter 6 of this dissertation is reprinted with permission from the Royal Chemical Society regarding the published work: Hanyu Fan, Elianna S. Frank, Douglas J. Tobias, and Vicki H. Grassian. Interactions of Limonene and Carvone on Titanium Dioxide (TiO_2) Surface. Journal of Physical Chemistry Chemical Physics. Accepted. 2021.

VITA

Elianna Sue Frank

EDUCATION

Doctor of Philosophy in Chemistry **2022**

University of California, Irvine *Irvine, CA*

Bachelor of Arts in Chemistry **2018**

Carleton College *Northfield, MN*

RESEARCH EXPERIENCE

Graduate Research Assistant **2018–2022**

University of California, Irvine *Irvine, CA*

TEACHING EXPERIENCE

Teaching Assistant **2018–2021**

University of California, Irvine *Irvine, CA*

REFEREED JOURNAL PUBLICATIONS

Comparison of the Adsorption-Desorption Kinetics of Limonene and Carvone on Titanimum Dioxide (TiO_2) and Silica (SiO_2) Surfaces under Different Relative Humidity Conditions **2022**

In preparation

Interactions of 6-methyl-5-hepten-2-one on two indoor relevant surfaces: SiO_2 and TiO_2 **2022**

Submitted Chemical Science

Interactions of Limonene and Carvone on Titanium Dioxide Surface **2022**

Physical Chemistry Chemical Physics

Heterogeneous Interactions between Carvone and Hydroxylated SiO_2 **2022**

J. Chem. Phys. C

Heterogeneous Interactions of Prevalent Indoor Oxygenated Organic Compounds on Hydroxylated SiO_2 Surfaces **2021**

Enviorn. Sci. Technol

Adsorption of Constitutional Isomers of Cyclic Monoterpenes on Hydroxylated Silica Surfaces **2021**

J. Chem. Phys

Impact of Adsorbed Water on the Interaction of Limonene with Hydroxylated SiO_2: Implications of π-Hydrogen Bonding for Surfaces in Humid Environments **2020**

J. Chem. Phys A

REFEREED CONFERENCE PUBLICATIONS

Using Computational Chemistry to Study Indoor Relevant Organic Compounds on Indoor Surfaces **July 2022**

Indoor Air

ABSTRACT OF THE DISSERTATION

Using Computational Chemistry to Study the Interactions of Indoor Relevant Organic Compounds on Indoor Surfaces

By

Elianna Sue Frank

Doctor of Philosophy in Chemistry

University of California, Irvine, 2022

Professor Douglas J. Tobias, Chair

Organic compounds are one of the major classes of indoor air pollutants and are emitted from a variety of sources including building materials, cleaning products, and human occupants. The composition and concentrations of these organic compounds can be significantly affected by chemical transformations on indoor surfaces and given the large surface area-to-volume ratio in the built environment, understanding these chemical processes are critical to understanding indoor chemistry. However, the detailed molecular interactions between organic compounds and indoor surfaces are still poorly understood. By using force field-based and *ab initio* molecular dynamics simulations, we are able to gain an atomistic understanding of the interactions between many indoor relevant organic compounds including cyclic monoterpenes and oxygenated organic species on two indoor relevant surfaces, SiO_2 and TiO_2. Our results indicate a range of interaction strengths for the adsorption of organic compounds on these surfaces coming from factors including the orientation of the molecule on the surface and the location of $C_{sp}{}^2$ carbon centers or oxygen atoms in the adsorbate. Our results are supported by experimental validation via infrared spectroscopy, where we see similar trends between our calculated *ab initio* power spectra of these molecules on the surface and the experimentally determined IR spectra.

Chapter 1

Introduction

1.1 The Indoor Environment

People spend up to 90% of their time indoors, and their time indoors has increased significantly during the COVID-19 pandemic. [1, 2] The indoor environment is of great importance to study as it encompasses many spaces full of unique sources and sinks of chemistry. [3] Some sources of indoor pollutants occur from cooking, cleaning, human occupants and outdoor air exchange, and this indoor chemistry occurs at a variety of time and length scales. [3, 4, 5, 6] In addition to the large range of indoor pollutants present in the built environment, there is also a great variation in building surfaces, furnishings, and other dynamic features such as relative humidity and temperature. [7]

Increased efforts have been made to study the indoor environment by bringing instrumentation developed for the outdoors to the inside, such as aerosol mass spectrometry, proton transfer reaction mass spectrometry, and chemical ionization mass spectrometry. [8, 9, 10, 11, 12, 13] However, the extrapolation of these specific systems is difficult due to the vast number of buildings in the world, all constructed with different building ma-

terials, possessing different interiors, and host to different occupant activities. [1, 14] To fully describe the indoor environment, models well aligned to experimental measurements are required and must represent the varying time and length scales present in the indoor environment.

In 2017, the MOCCIE, (MOdelling Consortium for Chemistry of the Indoor Environments) was initiated within the Chemistry of the Indoor Environments (CIE) Program of the Alfred P. Sloan Foundation. Molecular dynamics simulations have been employed by our lab to study the indoor environment by estimating parameters needed by kinetic models and elucidating mechanistic insight into indoor air processes.

In my Ph.D. work, I have focused on using computational chemistry to study indoor surfaces, as they play a critical role in the chemistry of the indoor environment. First, the indoors are host to a large surface-to-volume ratio (via walls, tables, carpets, seating, and windows) [15], second, indoor surfaces have a dynamic composition and each surface is highly variable in terms of environmental fluxes such as relative humidity [7], and third, indoor surfaces undergo a variety of surface chemistry processes, including oxidation, acid-base reactions, as well as the adsorption/desorption of organic molecules. [16, 17, 18]

I have studied interactions between indoor relevant surfaces and indoor relevant organic compounds, focusing on molecules present in cleaning and personal care products. My work has been done in collaboration with experimental spectroscopy performed by the Grassian Lab at UC San Diego.

1.2 Computational Methods

Here, I will describe the methods I have used to study the indoor environment at the atomistic level, inspired by *Statistical Mechanics* by Donald A. McQuarrie. [19] Consider a classical

system with N (interacting) particles. Each particle can be described spatial coordinates q_i with a corresponding conjugate momentum p_i. q_i and p_i completely describe the classical mechanical state of the N-body system and can also be referred to as the phase space for the system. These coordinates, along with the equations of motion of the system determine the course of the system.

As the system evolves in time, the trajectory of the system is given by Hamilton's equations of motion:

$$\begin{aligned} \dot{q_i} &= \frac{\partial H}{\partial p_i} \\ \dot{p_i} &= -\frac{\partial H}{\partial q_i} \end{aligned} \tag{1.1}$$

Considering an ensemble of systems in phase space, we can define:

$$f(p, q, t) \tag{1.2}$$

As the probability density that any volume in phase space has phase points about p, q, at time t. Therefore, to integrate over the whole system gives us:

$$\int f(q, p; t) = \mathcal{A} \tag{1.3}$$

We can define the ensemble average of any function, such as $\phi(p, q)$ as:

$$\phi = \frac{1}{\mathcal{A}} \int \phi(p, q) f(q, p; t) \tag{1.4}$$

Here, the ensemble average is equal to the corresponding function, but integrating Hamilton's equations of motion for each q_i and p_i is not feasible. Molecular dynamics provides an approximation to the phase space average by sampling the phase spaces by evolving q_i and p_i through time. We are able to estimate thermodynamic properties from time averaged

properties obtained from molecular dynamics simulations due to the ergodic hypothesis that states a set of trajectories evolving in time due to Hamilton's equations of motion on a long enough time scale are representative of the probability distributions of phase space.

The equations of motion determine the trajectory at each phase point, thus they also must determine the density, Equation 1.2, at any time, resulting in a time dependence of f. This time dependence is given by the Liouville equation:

$$\frac{\partial f}{\partial t} = -\sum_{N}^{i=1} \left(\frac{\partial H}{\partial p_i} \frac{\partial f}{\partial q_i} - \frac{\partial H}{\partial q_i} \frac{\partial f}{\partial q_i} \right) \tag{1.5}$$

Because q and p commute and $f = f(q, p, t)$, the Liouville equation is equal to:

$$\frac{df}{dt} = 0 \tag{1.6}$$

This means the phase space density is constant:

$$f(q, p; t) = f(q_0, p_0; t_0) \tag{1.7}$$

This invariance of f during the evolution of time shows:

$$f(q, p; t) = f\left[H(q, p)\right] \tag{1.8}$$

Where H is the Hamiltonian of the system. For a system in thermal equilibrium with the surroundings, the probability distribution function becomes:

$$f\left[H(q, p)\right] = C \frac{e^{-\beta H(q,p))}}{\int e^{-\beta H(q,p)} \; dp \; dq} \tag{1.9}$$

Where $\beta = \frac{1}{k_B T}$

The denominator of this equation is referred to as the partition function, which is a func-

tion of thermodynamic state variables. In this case, this is the canonical partition function, meaning the partition function for an an ensemble with constant number of particles, volume and temperature (Q (N, V, T)). By interrogating the partition function we can obtain thermodynamic quantities. An example of this is the Helmholtz free energy:

$$F = -\frac{1}{\beta} ln(Q(N, T, V) \tag{1.10}$$

Now we must consider how this explicit time evolution of atoms is governed. In Section 1.3 and Section 1.4, two kinds of molecular dynamics simulations will be described, classical Molecular Dynamics (MD) and *ab initio* Molecular Dynamics (AIMD). In addition, two important techniques that have been utilized throughout this work will be discussed.

1.3 Classical Molecular Dynamics

In classical Molecular Dynamics (MD), atoms are propagated forward in time according to Newtonian mechanics and an empirically derived force field which accounts for all bonded and nonbonded interactions between atoms. These methods have been used for countless studies of physical systems. While there are many force fields that can be used, in this research, the CHARMM force field was used. In the CHARMM force field, to account for bonded interactions, bonds and angles between atoms are approximated by a harmonic potential, and the dihedral motion is assumed to have a trigonometric form. To account for nonbonded interactions, each particle is described by a partial charge, and electrostatic interactions between particles separated by at least three bonds are calculated using the Coulomb potential. Dispersion interactions are approximated by the Lennard-Jones potential. The overall form of the potential energy in the CHARMM force field is:

$$U = \sum_{bonds} K_b(r - r_0)^2 + \sum_{angles} K_\theta(\theta - \theta_0)^2 + \sum_{dihedral} K_\chi \left[1 + cos(n\chi - \sigma)\right] + \sum_{nonbonded\ pairs} \left(\epsilon_{ij} \left[\left(\frac{R_{min,ij}}{r_{ij}}^{12}\right) - 2\left(\frac{R_{min,ij}}{r_{ij}}^{6}\right)\right] + \frac{q_i q_j}{\epsilon r_{ij}}\right) \tag{1.11}$$

The first three terms of this force field correspond to the bonded interactions of bond and angle vibrations as well as the dihedral potential. As stated above, the bond and angle vibrations are modeled with a harmonic potential. The force constant for bonds is K_b and is centered at the equilibrium bond length, r_o. For the angles, the force constant is K_θ and equilibrium bond angle of θ_0. The torsion of every 4 sequentially bonded atoms is described by a periodic potential around the middle two atoms with periodicity n and a phase shift angle of σ.

The last two terms as indicated by the label, are the nonbonded parameters, which are Van der Waals (VDW) and electrostatic interactions. The Lennard-Jones potential (LJ) represents the VDW or non-electrostatic interactions. The LJ potential approximates the potential energy of non-electrostatic interactions as described by the parameters $R_{min,i,j}$, the distance where the intermolecular potential between atoms is 0, and $\epsilon_{i,j}$, the strength of the interaction. To describe the electrostatic interactions, Coulomb's law is used where $r_{i,j}$ is the distance between atoms and q_i and q_j are the partial charges of atoms i and j.

The LJ parameters are obtained for basic molecules, such as amino acids, and are transferable across atoms types. Partial charges, bonded interaction force constants, and equilibrium lengths can be determined via force field paramaterization. One method of parameterization is to use the CGenFF program that generates parameters with a given penalty to their accuracy. [20] Additional refinement may also be done using electronic structure calculations to determine partial charges by interactions with water and to determine satisfactory geometry

and conformation energies using the Force Field Toolkit as provided in the VMD program. [21]

For the indoor relevant organic molecules, a CHARMM compatible force field was required to perform MD simulations. For most molecules, using the CGenFF program leads to sufficient force field parameters (as indicated by a penalty of less than 10). For 6-MHO, carvone, α-pinene, and β-pinene, additional paramterization was required. 6-MHO was parameterized by Michael von Dommes, and I used the Force Field Toolkit to construct the force fields for the other molecules.

For indoor surfaces, a previous force field for SiO_2 has been described by Zhuravlev. [22] For TiO_2, for the non-hydroxylated surface, the force field produced by Brandt and Lyubartsev [23] was used, and for the hydroxylated surface, minor changes were made to ensure in a neutral surface. These details will be described in Chapters 6 and 7.

While the force field describes the position and momenta in time, external regulatory schemes are used to maintain thermodynamic conditions. These include thermostats and barostats. Finally, the structural and energetic properties are collected during the simulation, and as shown in Equation 1.4, the time average of these parameters are reasonable estimates of the thermodynamics of the system.

1.3.1 Umbrella Sampling

In order to understand the interactions of indoor relevant organic molecules on indoor surfaces, it is vital to calculate the free energy of desorption for adsorbates from the surface.

However, due to the stabilizing surface interactions and the subsequent lack of stabilization in the gas phase, there is a high barrier of free energy associated with the desorption of these molecules from the surface. To calculate the free energy profile, the entire phase space

must be adequately sampled along the reaction coordinate. However, due to the high barrier in free energy associated with the desorption of these molecules, there are regions of phase space that would be not visited during an unbiased simulation. This means that on the time scale of obtaining a PhD, the probability of measuring this rare event through unbiased MD simulations is 0.

Therefore, free energy methods must be used to improve sampling and allow for rare events to be calculated by molecules dynamics simulations. One method to sample rare events is called umbrella sampling, and this method has been used throughout my work to determine the free energy profile (also known as the potential of mean force of PMF) for the desorption of indoor relevant organic compounds from indoor surfaces. Umbrella sampling divides the reaction coordinate into evenly spaced overlapping windows and uses a harmonic restraint to sample within each window. [24]

Johannes Kastner [25] gives a detailed explanation on how umbrella sampling can be used to determine rare events, and I have often referred to this text to to cement my understanding of this method. In each window, w_i, the bias potential (which in this case is a harmonic potential) is an additional energy term, which depends only on the reaction coordinate, ξ. So the potential energy E can be described as:

$$E^b(r) = E^u + w_i(\xi) \tag{1.12}$$

Where b are biased quantities and u are unbiased quantities. To obtain the unbiased free energy, $F_i(\xi)$, the unbiased distribution along the reaction coordinate is required. Since the MD simulation run in each window is biased, this may seem like a difficult task. However, because the bias only depends on the reaction coordinate, we can relate the biased and unbiased distribution in each window by the following equations:

By first defining the unbiased distribution as

$$P_i^u(\xi) = \frac{\int e^{-\beta E(r))}\delta[\delta'(r) - \delta(r)]d^N r}{\int e^{-\beta E(r))}d^N r} \tag{1.13}$$

And then defining the biased distribution as:

$$P_i^b(\xi) = \frac{\int e^{-\beta E^u(r)+w_i(\xi'(r))}\delta[\delta'(r) - \delta(r)]d^N r}{\int e^{-\beta E^u(r)+w_i(\xi'(r))}d^N r} \tag{1.14}$$

And then integrating over all degrees of freedom but ξ, and defining $P_i^u(\xi)$ in terms of the biased distribution:

$$P_i^u(\xi) = P_i^b(\xi)e^{\beta w_i(\xi)}e^{-\beta w_i(\xi)} \tag{1.15}$$

Then, the free energy per window, $F_i(\xi)$, can be evaluated as:

$$F_i(\xi) = -\frac{1}{\beta}ln(P_i^b(\xi)) - w_i(\xi) - \frac{1}{\beta}ln(e^{-\beta w_i(\xi)}) \tag{1.16}$$

Which allows us to unbias the simulation. However, this is only suitable when one window spans the entire range of the reaction coordinate. Since multiple windows of $F_i(\xi)$ must be combined, $\frac{1}{\beta}ln(e^{-\beta w_i(\xi)})$, referred to as F_i, cannot be obtained directly from sampling. Instead the weighted histogram method (WHAM) combines the free energy of all windows by minimizing the error associated with binning the data from the biased simulation. [26]

1.4 *ab initio* Molecular Dynamics

While classical MD relies on a force field to describe the motion of atoms moving forward through time and can be used for huge numbers of atoms, sometimes it is required to describe

electronic interactions in a more accurate manner. These tend to be systems with dominating electronic interactions.

In *ab initio* molecular dynamics simulations, electronic interactions are obtained "on the fly," and nuclei are treated classically. This means that the forces applied to the nuclei are calculated using the Born-Oppenheimer approximation after every electronic structure calculation. In this case, a force field is no longer required as all nonbonded and bonded interactions come from the electronic structure interaction calculations. Any quantum mechanics method can be used to calculate the electronic interactions, but density functional theory (DFT) methods are used in AIMD simulations due to the efficiency and accuracy compared to traditional wave function based methods.

The foundation of DFT is the Hohenberg-Kohn theorem that states there is a one-to-one mapping between the electron density and the energy of the system. [27] The Kohn-Sham scheme allows us to map a system of interacting electrons onto a system of non-interacting particles under an external potential v_s. [28]

Here, the energy of the system is defined as:

$$E\left[n(r))\right] = T\left[n(r)\right] + E_H\left[n(r)\right] + E_{XC}\left[n(r)\right] + E_{ext}(r) \tag{1.17}$$

Where T is the kinetic energy, E_H is the Coulomb energy, E_{XC} is the exchange-correlation energy, and E_{ext} is the external energy and $n(r)$ is the electron density of the system.

The electron density can be described as:

$$n(r) = 2\sum_{N/2}^{\alpha} \left|\phi_\alpha(r)^2\right| \tag{1.18}$$

and $\{\phi_\alpha\}$ is the Slater determinant form of the ground state wavefunction for N-particles.

The kinetic energy, $T[n(r)]$ is:

$$T[n(r)] = -\sum_{i=1}^{N/2} \int d^3r \phi_i^*(r) \nabla^2 \phi_i(r) \tag{1.19}$$

And the Coulomb energy, E_H is:

$$E_H[n(r)] = \int d^3r \int d^3r \frac{n(r)n(r')}{|r - r'|} \tag{1.20}$$

Therefore, when considering the total energy equation in Equations 1.19 and 1.20, E_{XC} and E_{ext} are an implicit definition of the exchange-correlation energy and the difference in kinetic energy of the interacting and non-interacting systems.

Upon self consistently solving the equation below, the energy of the molecular system is obtained. [29]

$$\left[-\frac{1}{2}\nabla^2 + \int dr' \frac{n(r')}{|r - r'|} + V_{XC}(r) + V_{ext}(r) \right] \phi_i(r) = \varepsilon_i \phi(r) \tag{1.21}$$

Pure electronic structure calculations, like of binding energies and the calculation of electrostatic potential surfaces which will be described in later chapters, describe $n(r)$ as expanded Gaussian basis functions, in AIMD calculations, the hybrid and plane wave (GPW) formulation is used. The plane waves are used to represent electron density in reciprocal space, $\tilde{n}(G)$.

The transformation is shown below:

$$n(r) \approx \frac{1}{\Omega} \sum_G \tilde{n}(G) e^{iG.r} \tag{1.22}$$

By using this transformation, the Coulombic interactions are calculated in reciprocal space,

and it is convenient to apply this formalism to systems under periodic boundary conditions. Under periodic boundary conditions, Coulombic interactions are calculated by mapping the density on a 3D grid and using Ewald summation methods and the Fast Fourier Transform algorithm (FFT) to calculate E_H. Since this work is focused on studying surface interactions, PBCs are used in all simulations. Furthermore, plane wavefunctions are naturally delocalized, therefore, there is no superposition error. [30]

1.4.1 Power Spectra Calculations

Computational chemistry cannot exist without a connection to reality. High accuracy experimental measurements like unit cell dimensions can be used to evaluate the accuracy of empirically parameterized force field-based molecular dynamics simulations. In this work, we are able to form an additional and extremely strong connection between theory and experiment by comparing trends in power spectra calculated from AIMD simulations to trends in FT-IR spectroscopy measurements. This has led to great insight into the mechanistic interactions between indoor relevant organic compounds and indoor surfaces and formed a strong connection between theory and experiment. All power spectra have been constructed by using the Fourier transform of the mass-weighted velocity autocorrelation function:

$$p(\omega) = m \int \langle v(0)v(t)\rangle_\tau \, e^{i\omega t} dt \tag{1.23}$$

Where $v(t)$ is the velocity of the selected atoms with mass m, at time t, with frequency ω. For our work we have separately calculated the power spectra of the hydrogen atoms of the system and oxygen atoms of the system. The brackets represent an average over atoms and time throughout the trajectory. The power spectra was calculated using the TRAVIS code. [31, 32] Due to the nature of the velocity autocorrelation function, this measurement may only be made after sufficient sampling.

1.5 Conclusions

We now have obtained a clear understanding of why it is important to study the indoor environment, and how computational chemistry can be used to provide great insights into the indoor environment. The following chapters represent six interesting studies of investigating indoor relevant organic compounds on indoor surfaces. Each chapter will present a more detailed background on the system studied, as well as discuss the relevant simulation protocols. Chapters 2-5 discuss surface interactions with SiO_2, a proxy for a glass surface, therefore, relevant simulation information is mostly presented in Chapter 2, with slight details regarding simulation protocols on a chapter-by-chapter basis in the following chapters. Similarly, Chapters 6 and 7 discuss surface interactions with TiO_2, a component of paint and self-cleaning materials, therefore the relevant simulation information is detailed in Chapter 6.

Chapter 2

Impact of Adsorbed Water on the Interaction of Limonene with Hydroxylated SiO_2 Implications of $\pi-$Hydrogen Bonding for Surfaces in Humid Environments

2.1 Background

One important environmental physical factor in indoor spaces is relative humidity (RH). RH is defined as the partial pressure of water vapor divided by the saturation water pressure. Percent relative humidity is defined according to Equation 2.1:

$$\%RH = RH * 100 \tag{2.1}$$

% RH represents a key aspect of the dynamic indoor environment, as % RH values can range from 10% to 90% indoors, and % RH varies widely across indoor surfaces and spaces.[7] In addition, it has been shown that the concentration of gases in indoor spaces is dependent on % RH. [16, 33] Yet, despite the importance of % RH, there remains a lack of information on how % RH impacts the interactions of semivolatile indoor relevant organic compounds on indoor surfaces. While some studies have investigated the interaction of organic compounds on SiO_2 surfaces, few have probed the details of these interactions in the presence of coadsorbed water. [34, 35, 36]

One indoor relevant organic compound that will be discussed in this chapter, as well as Chapters 3 and 6, is limonene. This molecule produces a lemon scent and one study has shown limonene is in 84.2% of 121 cleaning products.[37, 38] Products containing limonene often include glass surface cleaners, thus limonene can interact with glass surfaces, and become oxidized and form secondary organic aerosols or secondary organic films. [39, 40]

In our lab's previous research, we have determined that the major mechanisms for limonene adsorption onto a hydroxylated SiO_2 surface (a proxy for a glass surface) without water are through dispersion forces and the formation of π-hydrogen bonds between the limonene $C_{sp}{}^2$ carbon centers and the surface hydroxyl groups. Hydrogen bond formation results in a weakening of the hydroxyl O-H bond, thus resulting in a red shift observable by FT-IR spectroscopy.

To study the effect of relative humidity on the hydroxylated silica surface in the presence of limonene, we have performed a joint classical and *ab initio* molecular dynamics study in conjunction with our collaborators in the Grassian lab at UC San Diego to determine the detailed interactions at play in the silica/air/water interface.

2.2 Simulation Protocols

The simulation protocols for this project are very similar to methods used in Chapters 3, 4, and 5. Any differences will be highlighted in each chapter.

2.2.1 Classical Molecular Dynamics Simulations

Classical MD simulations were used to calculate π-hydrogen bond populations and desorption binding energies on limonene on SiO_2 at varying hydration levels. A 24 Å x 52 Å x 50 Å SiO_2 structure was used with a silanol surface density of 4.7 OH^{-2}, which is the silanol surface density of a glass surface. [22] Each water monolayer corresponded to 636 TIP3P [41] water molecules and we constructed systems with one-half, one, two and three monolayers. In each system, the silica/water interface was equilibrated for 0.5 ns before the addition of limonene.

The LAMMPS [42]package was used to perform all of the classical MD simulations. The equations of motion were integrated using a velocity-Verlet algorithm [43] with a time step of 1 fs. Electrostatic interactions were evaluated directly up to a cutoff of 14 Å and with a particle-particle-particle-mesh solver [44] with a relative accuracy of 10^{-5}. Lennard-Jones interactions were cut off after 14 Å. The simulation temperature was maintained at 300 K, using a Nose-Hoover thermostat [45] with a relaxation time for 100 fs.

As discussed in the introduction, the CHARMM-compatible force field parameters was used for SiO_2, the TIP3P model [41] was used for water and the CHARMM CGenFF [20] parameters were used for limonene. Water molecules were constrained by the SHAKE algorithm. [46]

Umbrella sampling [25] was used to calculate the free energy of desorption of limonene from the surface of the SiO_2 systems as a function of % RH. As discussed in the introduction, the

reaction coordinate was described as the distance between the center-of-mass of limonene and the SiO_2 surface. The process was divided into at least 31 windows in 0.5 to 0.25 Å windows, based on the number of monolayers of water. A harmonic potential of 5 kcal mol $^{-1}$ Å^{-2} was applied in each window and each window was run for 10 to 20 ns long, and the free energy profile was generated using the WHAM scheme. [26]

2.2.2 *ab initio* Molecular Dynamics Simulations

AIMD simulations were used to compute the power spectra for water H atoms to compare with the experimental infared spectra, as a function of hydration level. AIMD simulations of limonene on a cluster of hydroxylated silica surface with 12, 24, and 48 water molecules were performed using the CP2K program. [30] The SiO_2 cluster size was $Si_{23}O_{66}H_{40}$ and selected to fully accommodate water and limonene molecules while allowing moieties to interact with each other. For all systems, a 20 ps AIMD simulation at 295 K with a 0.5 fs timestep was performed. The temperature was maintained at 295 K using a Nose-Hoover thermostat with a relaxation time of 100 fs. The BLYP-D3 exchange-correlation functional [47, 48] with the TZV2P-MOLPT-GTH basis set [49, 50] and the GTH pseudopotentials in the QUICKSTEP [30] module of the CP2K package were used. A SCF convergence criterion of 10^{-6} (a.u.) with the orbital transformation scheme [51] and conjugate gradient minimization were used in each simulation. All systems were places in orthorhombic boxes under periodic boundary conditions with a cell size of 30 Å x 25 Å x 25 Å.

2.2.3 Surface Analysis Techniques

A variety of data analysis techniques were used to study the effect of % RH on the adsorption of limonene on SiO_2 surfaces. Density profiles and hydrogen bond populations were calculated from 20 ns unbiased classical MD simulations. Distances between limonene sp^2 carbons

(C_{sp^2}) centers and surrounding oxygen donors as well as the angle between limonene C_{sp^2}, donor H, and donor O atoms were measured every 1000 fs. Hydrogen bonds were defined as present if the distance between a single C_{sp^2} center acceptor and oxygen donor was less than 4.0 Å and if the angle between the acceptor, donor H, and donor O was within 120 - 180 °. Hydrogen bonding probabilities were calculated for each C_{sp^2} center independently.

Details of the vibrational power spectra are discussed in section 1.4.1

2.3 Results

To study the role of % RH on the adsorption of limonene on a hydroxylated SiO_2 surface, a joint experimental and theoretical study was performed. First the results of the experimental IR measurements will briefly be described in Section 2.3.1, and secondly, results from AIMD simulations will be reported in Section 2.3.2. Finally, results of the classical MD simulations will be reported in Section 2.3.3. Both of these computational methods coupled with experimental results shed light on the complex water/silica/air interface.

2.3.1 Experimental Results

The FT-IR spectra for the adsorption of limonene on the SiO_2 surface at an equilibrium pressure of 50 +/- mTorr as a function of % RH is shown in Figure 2.1. As % RH varies from <1 % RH to 78, and absorption bands at 3400 cm^{-1} and 1635 cm^{-1} grow in intensity. The bands at 3400 cm^{-1} represent water adsorption bands, and as they grow in intensity, there is a decrease of intensity in the limonene adsorption bands, indicating that the amount of limonene adsorbed on the SiO_2 surface decreases with increased % RH.

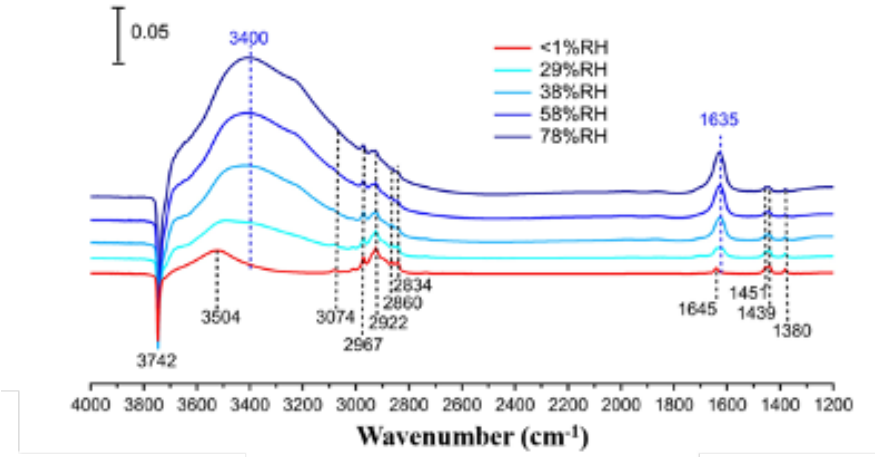

Figure 2.1: FT-IR spectra of limonene adsorbed on SiO_2 surface at an equilibrium pressure of 50 mTorr under different RH condition (scale bar = 0.05 absorbance units). The RH is increased from < 1% to 78% RH in the following increments: < 1%, 29%, 38%, 58% and 78%.

The relative decrease in the amount of limonene as a function of % RH, are shown in Table 2.1 along with the adsorbed water coverages determined in Goodman et al. [52] Most notable is that even at the highest % RH value, equal to more than 3 monolayers of water, limonene remains on the surface.

%RH (±3%)	water coverage in monolayers (±0.1)	% limonene remaining on the surface, relative to dry conditions (±0.4%)
1	0.1	100
29	1.2	90
38	1.5	82
58	2.1	65
78	3.3	53

Table 2.1: Changes in the amount of limonene adsorbed on SiO_2, as a function of relative humidity and coverage of coadsorbed water.

2.3.2 *ab initio* Molecular Dynamics Results

AIMD simulations were used to qualitatively reproduce the experimental FT-IR spectra. Note that the positions and not exact intensities are comparable to the experimental data. However, it is reasonable to compare trends in the AIMD power spectra to trends in the experimental results. To model the increase in % RH, we constructed a SiO_2 surface with one limonene molecules and 12-48 water molecules, as shown in Figure 2.2.

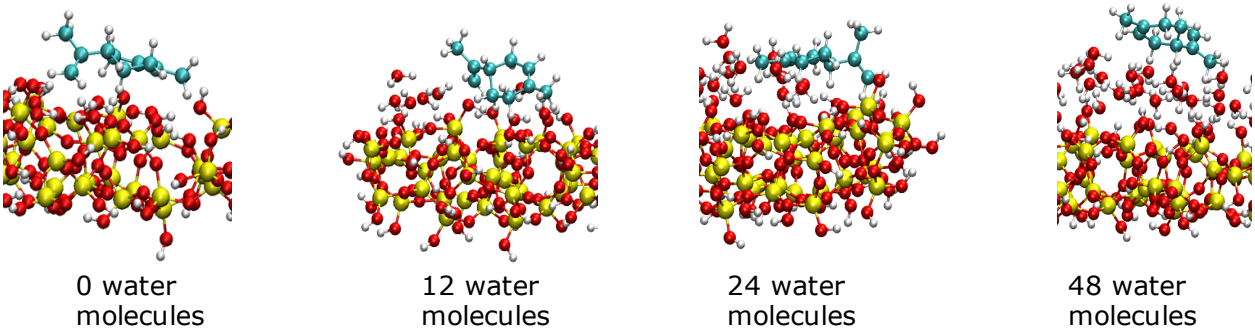

Figure 2.2: Snapshots from the AIMD simulations of limonene with an increasing number of water molecules (0, 12, 24, 48) on the SiO_2 surface.

We were able to reproduce two main trends present in the experimental FT-IR spectra as shown in Figures 2.3 and 2.4: first, in the low wavenumber region, we reproduce the increasing peak intensity due to the water bending mode at around $\sim$1640 cm^{-1} with increasing RH, and second we reproduce the decreasing peak intensity near 1450 cm^{-1} with increasing RH, as shown in Figure 2.3. This is not a monotonic decrease as shown by the experimental data, and the integrated peak area does not decrease.

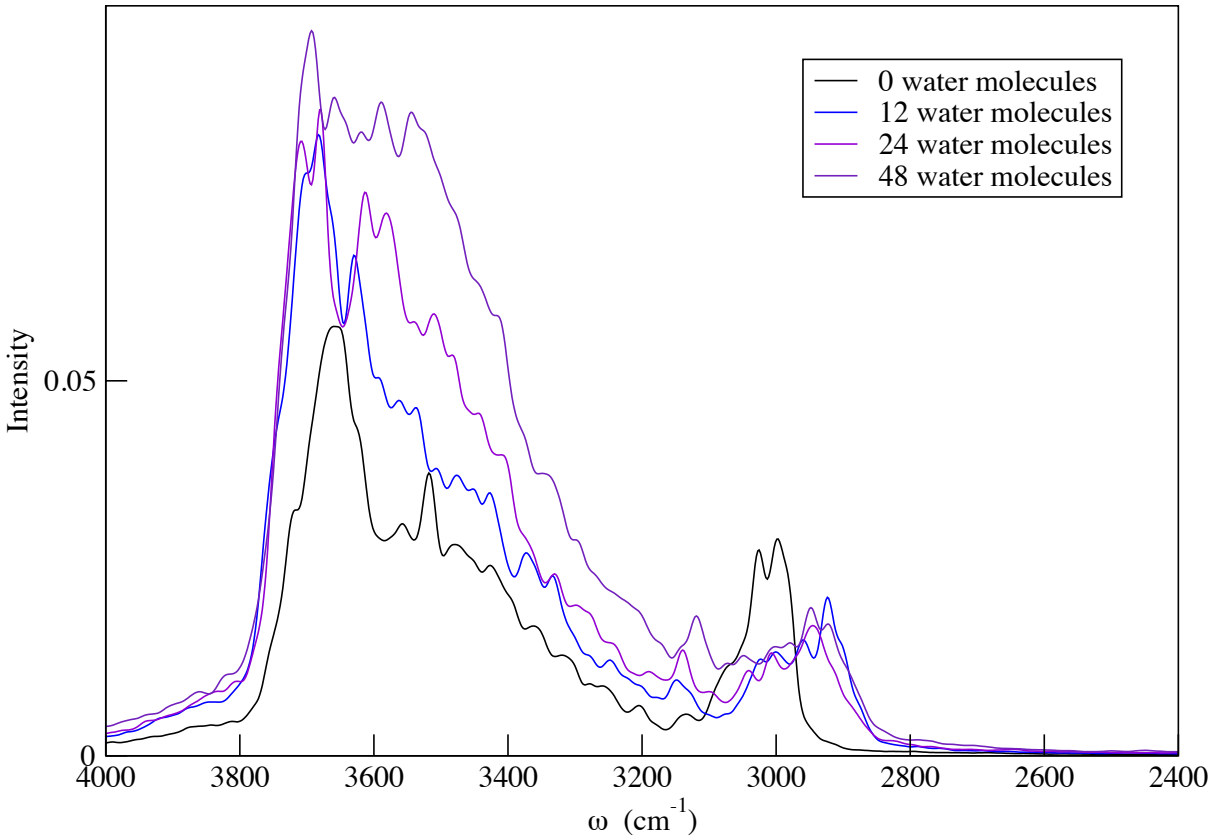

Figure 2.3: Power spectra calculated from the AIMD simulations for the hydrogen atoms near limonene in the low wavenumber region.

Figure 2.4 shows the high wavenumber region and the red shifting of the OH frequency in all simulations.

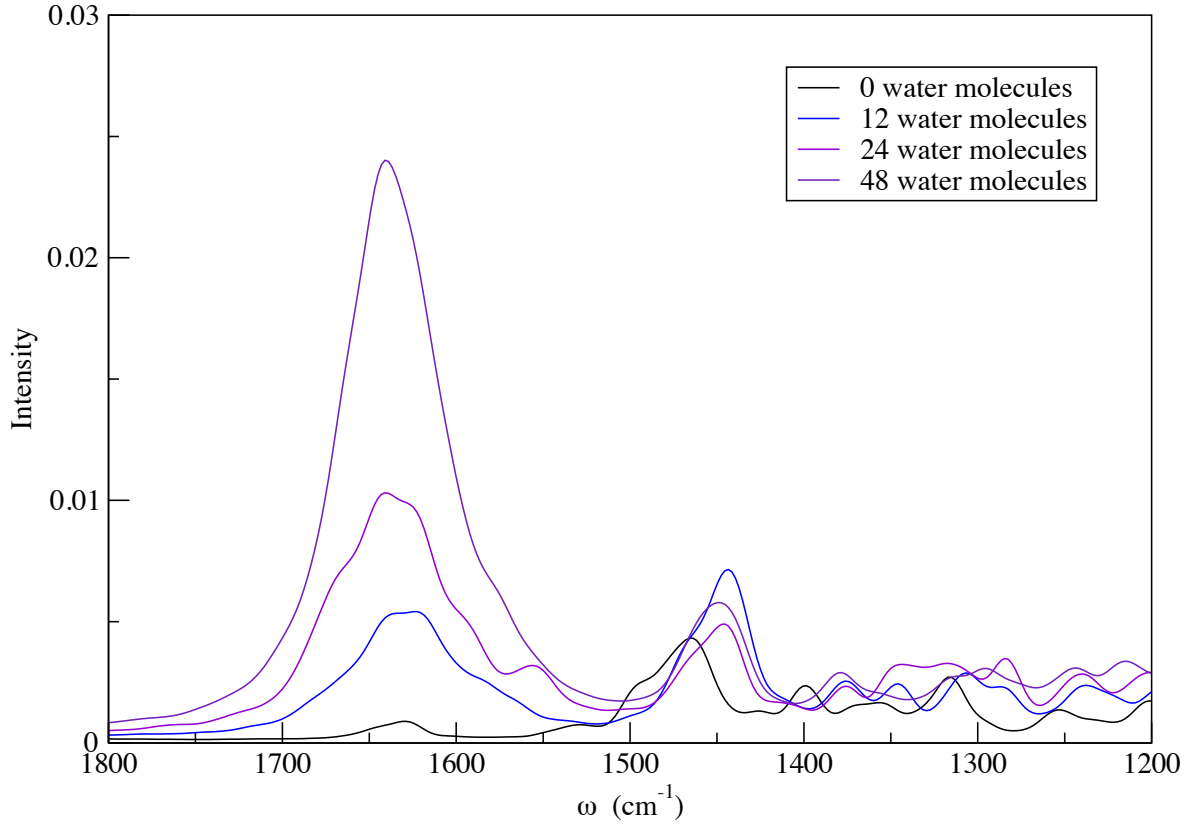

Figure 2.4: Power spectra calculated from the AIMD simulations for the hydrogen atoms near limonene in the high wavenumber region.

In addition, the power spectra also show a slight blue shift in the presence of water; however, we find this blue shift is present in all SiO_2 systems with water, as shown in Figure 2.5.

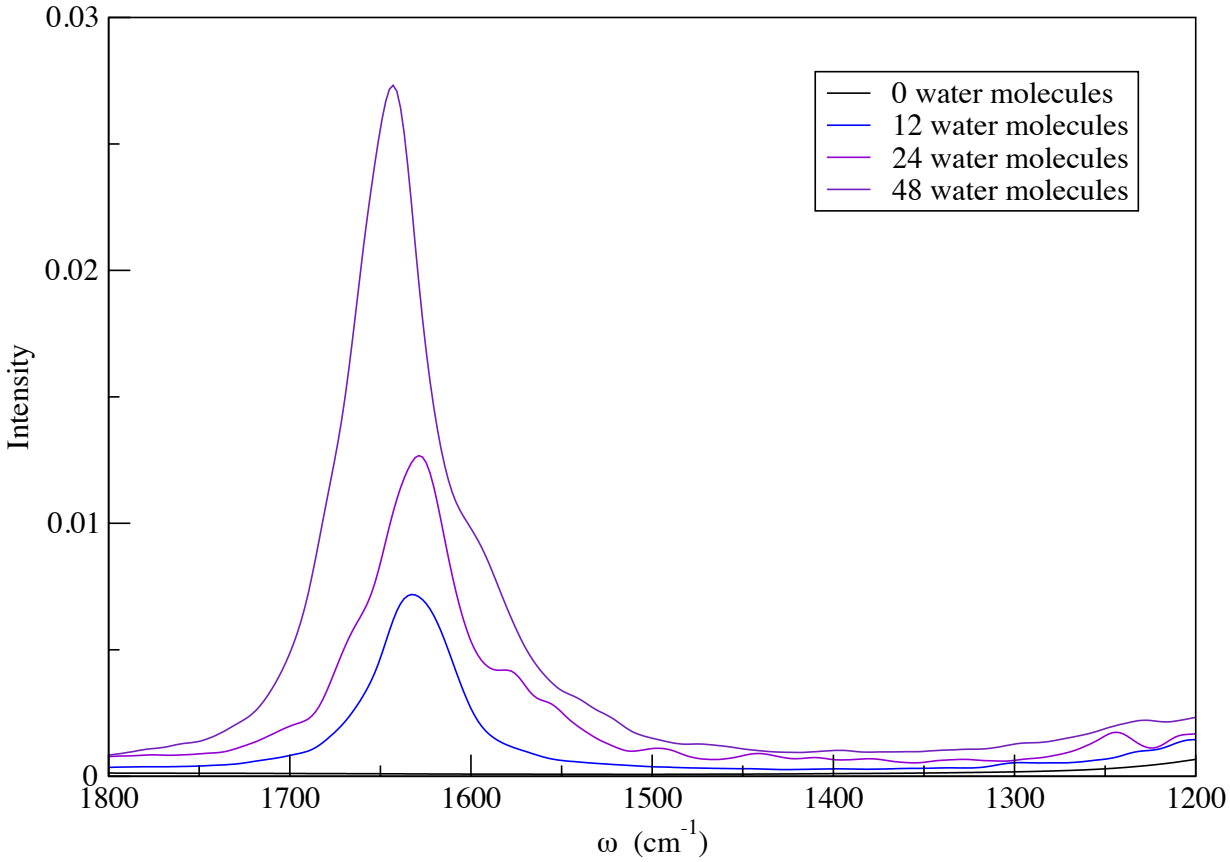

Figure 2.5: Power spectra of blue shifting region from the AIMD simulation for water hydrogen atoms on SiO_2 surfaces with no limonene present but an increasing number of water molecules.

During the AIMD simulations, water molecules interact with the limonene $C_{sp}{}^2$ centers and the cyclic part of the limonene molecules remain parallel to the SiO_2 cluster. This shows there are favorable interactions keeping limonene near the SiO_2 surface.

2.3.3 Classical Molecular Dynamics Results

Our previous studies showed the presence of π-hydrogen bonding between SiO_2 and unsaturated carbon bonds in limonene. [53] Additional research has shown that volatile organic compounds can engage in dispersion and π-hydrogen interactions with water. [54] Because

of this research and the close proximity of water to limonene $C_{sp}{}^2$ carbon centers, we suggest that there are also π-hydrogen interactions between adsorbed water and unsaturated carbon bonds within limonene. To quantify the extent of these interactions between limonene and either SiO_2 or water and to measure the free energy of desorption of limonene on the SiO_2 surface, we used force field based MD simulations to construct four model systems representing increasing RH values, as shown in Figure 2.6.

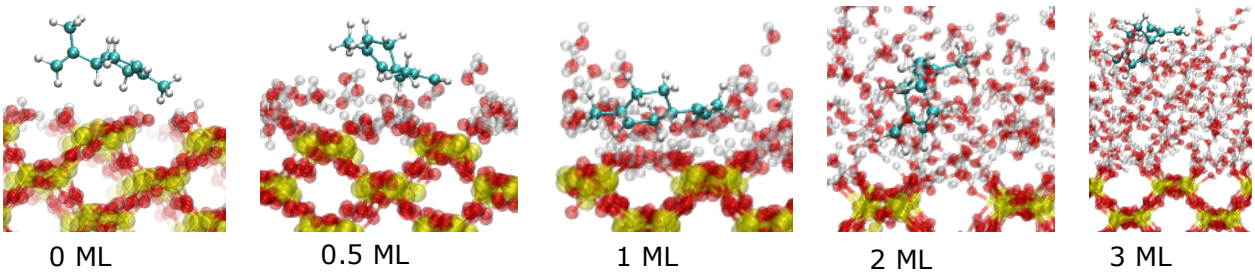

Figure 2.6: Snapshots from MD simulations of 0.5, 1, 2, and 3 ML of water on the SiO_2 surface. Each snapshot shows a limonene-water π-hydrogen bond.

In addition, density profiles of each system were constructed in Figure 2.7, showing the displacement of limonene by water with increasing levels of hydration. Histograms constructed to show the average number of bonds water forms with its surroundings as a function of location along the surface normal are shown in Figure 2.8. For 1 ML and greater, the density plots indicate bulk water is established, due to the shoulder of $\sim$0.033 $\mathring{A}^{-3}$ at 12 Å, which is just past the hydroxylated silica surface. This is also supported by the distribution of hydrogen bonds to water in the water hydrogen bonding histogram. These distributions show a maximum of 3.5 bonds for each water, which is the average number of hydrogen bonds per water molecule in the bulk.

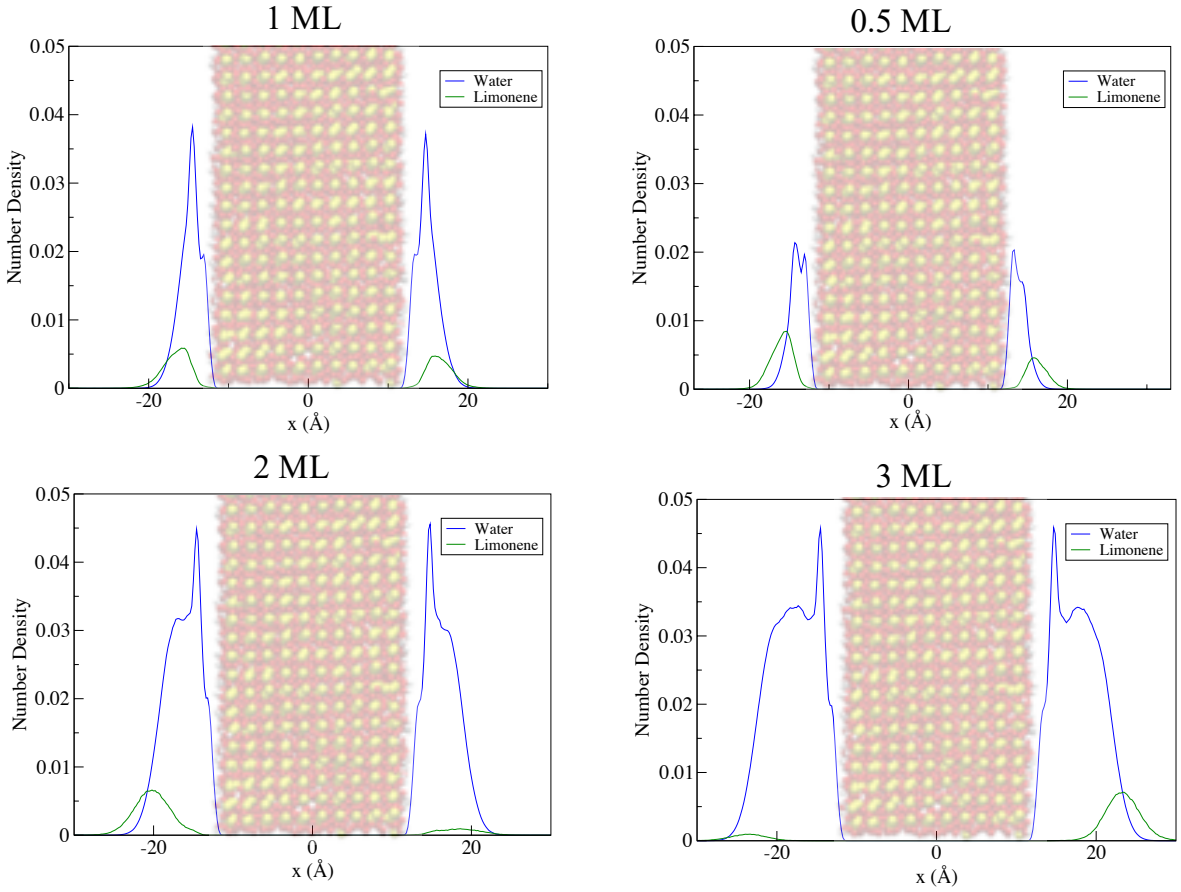

Figure 2.7: Density profiles of water molecules and limonene (enhanced at 5X magnification) for each monolayer system. A water number density of 0.033 $\mathring{A}^{-3}$ corresponds to bulk water.

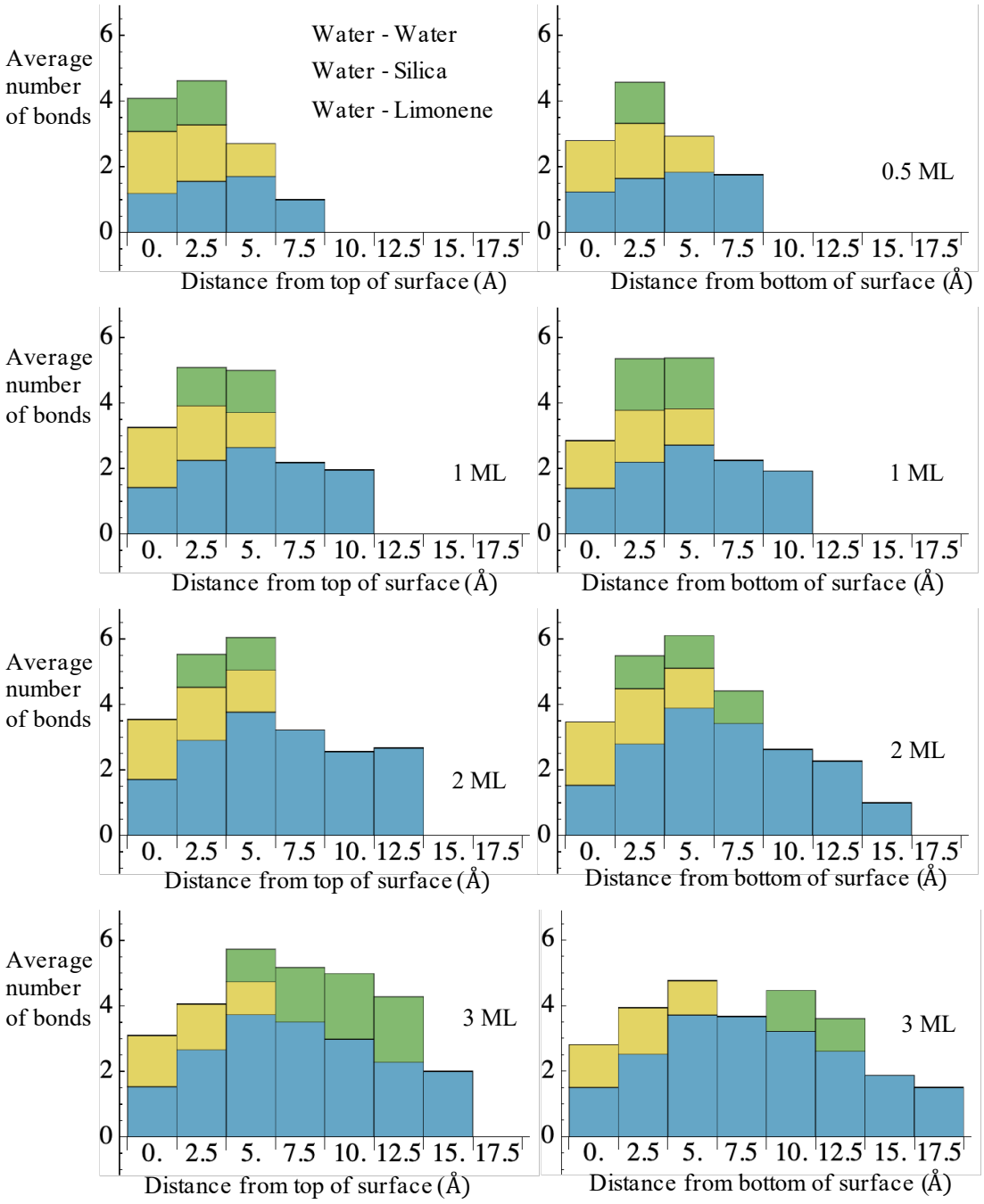

Figure 2.8: Histogram of average number of bonds formed with a water oxygen on the x-axis of the simulation cell, where x is the direction normal to the surface of SiO_2.

To understand differences in π-hydrogen bonding for each system, we measured the probability of π-hydrogen bond formation, as described in Section 2.2.3. Table 2.1 shows these results and indicates that while limonene does not always form a π-hydrogen bond with SiO_2 or water, the probabilities of each type of hydrogen bonding differ with the number of monolayers of water.

Number of monolayers	% probability of SiOH donor	% probability of water donor
0.5	7.96	13.3
1	3.96	30.5
2	0.08	38.1
3	0.00	35.5

Table 2.2: Limonene acceptor statistics for SiO_2 and water

As the number of monolayers increases, more water molecules move to form hydrogen bonds with the hydroxylated SiO_2 surface, thus displacing limonene. This severely reduces the probability of π-hydrogen bonds between limonene and SiO_2. Increasing the number of water monolayers results in more π-hydrogen bonding to limonene, but has a maximum of 2 ML. This is due to the fact that water hydrogen bonds are much stronger than π-hydrogen, or any other adsorbate interaction.

We have also investigated the role of limonene-rich and water-rich domains in our study, as shown in Figures 2.9 and 2.10. We have constructed simulations of two limonene molecules on the SiO_2 surface with 2 and 3 monolayers of water. Using the minimum of 6 Å as a cutoff for contact between limonene molecules, there is a 33% probability of contact between limonene molecules in 2 monolayer system and 20% probability of contact between limonene molecules in 3 monolayer systems. We have also constructed two similar simulations by increasing the number of limonene molecules from two to five. Figure 2.9 shows the minimum distance between carbon atoms of any of the five limonene molecules. In this case, we find that there

are high probabilities of limonene rich domains formed, as shown by the inserted molecular snapshots of five limonene molecules on 2 and 3 monolayers respectively.

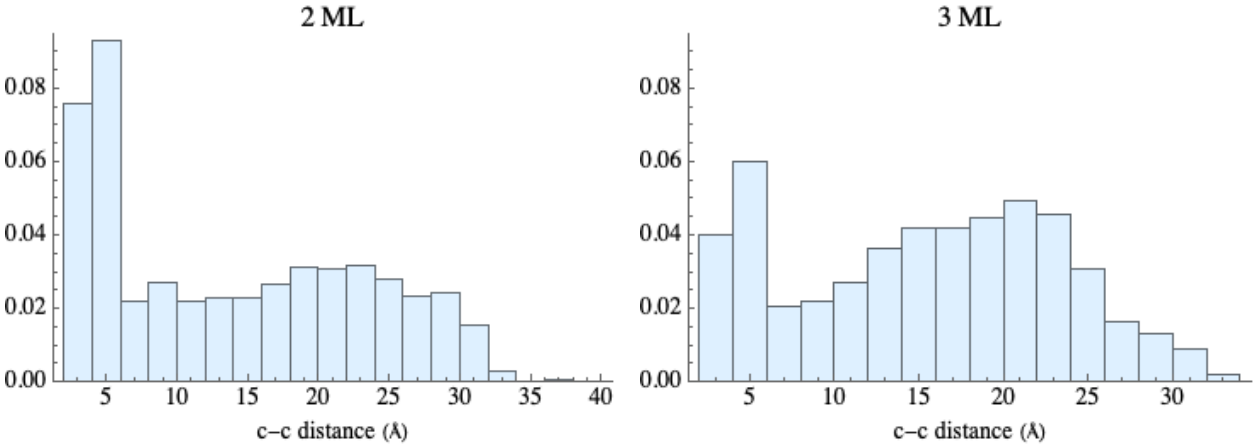

Figure 2.9: Histograms of minimum distance between carbon atoms of two limonene molecules in 2 and 3 monolayers.

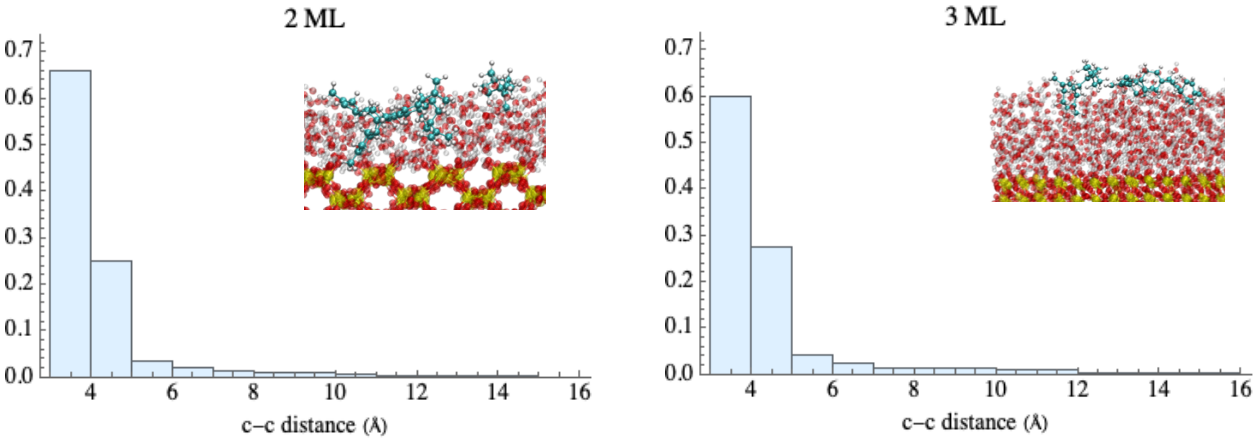

Figure 2.10: Histograms of minimum distance between carbon atoms of five limonene molecules in 2 and 3 monolayers.

Using the same minimum of 6 Å as a cutoff for contact between limonene molecules, there is a 94% probability of contact between limonene molecules in 2 monolayer system and 90% probability of contact between limonene molecules in 3 monolayer systems.

Ultimately, we conclude that our experimental evidence does not indicate the formation of any limonene rich domains, we do see evidence of limonene clusters forming during the course

of classical MD simulations.

Free energy profiles or potentials of mean force (PMFs) for limonene desorption are shown in Figure 2.11, they are placed vertically, such that their minima are at the zero free energy.

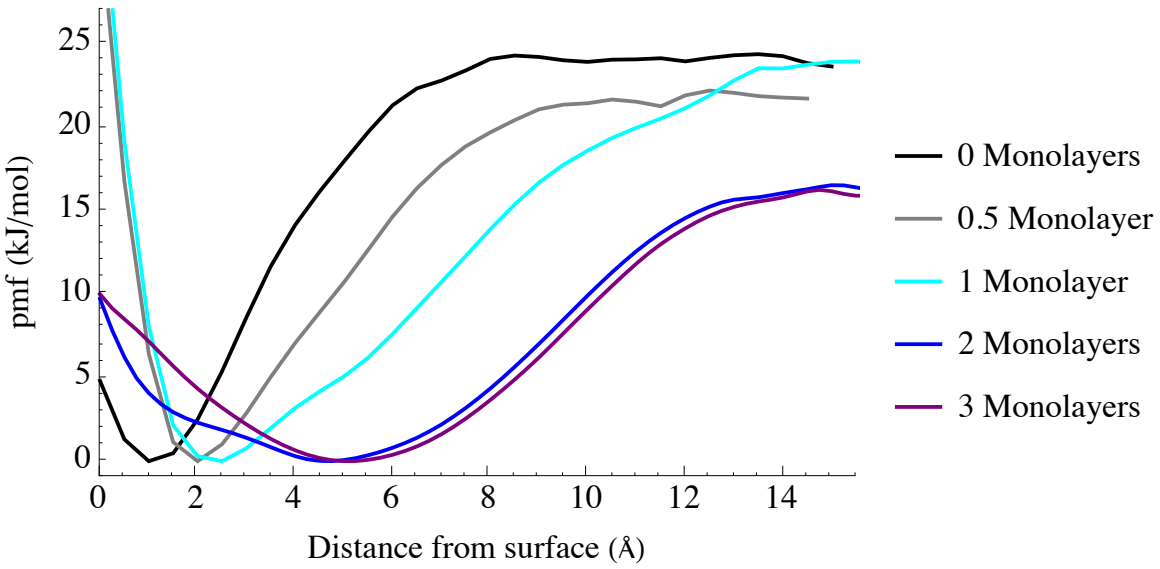

Figure 2.11: Potential of mean force (PMF) for limonene desorption from the SiO_2 surface at various levels of hydration computed from classical MD simulations.

The limonene desorption free energy is largest for a bare SiO_2 surface, followed by the 1 and 0.5 ML systems. The 2 and 3 ML systems have much lower desorption free energies due to the displacement of limonene from the surface by water and consequently the lack of hydrogen bonds between the surface hydroxyl groups and limonene. In addition, it is shown the desorption curve is not as steep for these larger monolayers as the water extends up to 10 Å from the SiO_2 surface. However, it is vital to note that even with this flattening, the binding energy to the SiO_2 surface is still nonzero, as there are still dispersion and hydrogen bonding interactions (the latter depicted in Figure 2.7) between limonene and water molecules as limonene is displaced from the SiO_2 surface but remains associated within the adsorbed water layers.

2.4 Conclusions

In summary, experimental results using FT-IR spectroscopy of adosrbed limonene at various % RH, AIMD and force field based MD simulations were integrated and combined to further our understanding of the roles of % RH and coadsorbed water on the adsorption of limonene, a hydrophobic organic compound on an SiO_2 surfaces. The story of limonene does not end in this chapter, and this molecule is studied in comparison to some of its isomers in Chapter 3, and on a TiO_2 surface in Chapter 7.

In this study we determined water molecules are able to displace limonene, thus breaking direct contact between limonene and the SiO_2 surface; however, the limonene molecule remains in the adsorbed state, because of π-hydrogen bond interactions with adsorbed water molecules. These hydrogen bond are a part of a much larger network that includes π-hydrogen bonds, water hydrogen bonds, and silica-water hydrogen bonds. This provides insight into the understanding of the role of adsorbed water in mediating the interactions of volatile organic compounds with a prevalent surface over a range of % RH in the indoor environment.

This study shows how organic compounds are partially displaced from the surface by adsorbed water as the RH increases, suggesting that changes in the partitioning of limonene to indoor surfaces will depend on RH.

Chapter 3

Adsorption of Constitutional Isomers of Cyclic Monoterpenes on Hydroxylated Silica Surfaces

3.1 Background

To further our understanding of the adsorption of limonene on a hydroxylated SiO_2 surface, we have extended our study to include a comparison of limonene and several constitutional isomers, (γ-terpinene, terpinolene, α-pinene, and β-pinene). These constitutional isomers can be observed in indoor environments, and due to their different structure and reactivities, the mechanism for the interactions of these compounds with the indoors may be different. [55, 56, 57] By including α-pinene in our study, we are able to compare our results and framework to a previous study of α-pinene done by Chase et al. [58, 59] Frequently throughout this chapter, connections to this previous work will be made. This chapter will explore differences in the adsorption of isomers of cyclic monoterpenes on SiO_2 surfaces and uncover the detailed

mechanisms that underlie these differences. We focused our work on γ-terpinene, terpinolene, and α-pinene, while β-pinene was included in a brief discussion on the role of $C_{sp}{}^2$ carbon atoms.

3.2 Simulation Protocols

In this study, molecular dynamics simulations and *ab initio* MD simulations were used to investigate the similarities and differences in the interactions of these constitutional isomers of limonene on the SiO_2 surface.

3.2.1 Classical Molecular Dynamics Simulations

The same MD protocol from Chapter 2 was used for the MD simulations, and the VMD forcefield toolkit was used construct CHARMM-compatible force field parameters for α-pinene and β-pinene. [20, 60]

In this work, the surface accommodation coefficient was calculated for each isomer on the SiO_2 surface. This was done by running 100 ps MD trajectories that were initiated with the isomer center-of-mass velocity vector directed towards the SiO_2 surface. This was done for 100 randomly positioned isomer molecules 2.5 nm above the SiO_2 surface. The fraction of these 100 trajectories where the isomer adsorbed to the surface was used to estimate the surface accommodation coefficient.

The α-pinene desorption enthalpy was estimated by energy minimization as a function of the separation of the α-pinene center of mass and the SiO_2 surface. This was repeated for 100 different initial structures extracted from the MD simulation.

3.2.2 *ab initio* Molecular Dynamics Simulations

The same AIMD protocol from Chapter 2 was used for the AIMD simulations, the only difference is that the DZVP-MOLOPT-SR-GTH basis set was used for all calculations, instead of the TZV2P-MOLPT-GTH basis set. [49, 50]

3.2.3 Surface Analysis Techniques

Hydrogen bonding statistics were measured in a similar way as in Chapter 2; however, different π-hydrogen bonding criteria were determined for each isomer, based on distributions of $C_{sp}{}^2$ atom to surface OH distance and angles during the course of the simulation. Table 3.1 shows the breakdown of π-hydrogen bonding criteria.

Adsorbate	Distance Criteria (Å) ($C_{sp}{}^2$ - O atom)	Angle Criteria (°) ($C_{sp}{}^2$ - H - O)
limonene	3.4	135 to 165
γ-terpinene	3.3	120 to 161
terpinolene	3.3	133 to 166
α-pinene	3.5	130 to 160

Table 3.1: π-hydrogen bonding criteria for each isomer

3.3 Results

To investigate the adsorption of constitutional isomers of cyclic monoterpenes on SiO_2, a joint experimental and theoretical study was performed. First the results of the experimental IR measurements and displacement studies will be described in Section 3.3.1, and secondly, classical MD simulations will be reported in Section 2.3.2, and then the results

of the AIMD simulations will be reported in Section 3.3.3. Together, this work indicates that when comparing very similar molecules, a detailed accounting of what types of surface interactions and when these interactions occur is required to fully understand differences in adsorption.

3.3.1 Experimental Results

The infrared spectra for the adsorption of limonene as well as three constitutional isomers (γ-terpinene, terpinolene, and α-pinene) on the SiO_2 surface as a function of pressure is shown in Figure 3.1 below. All isomers show an absorption around 3074 cm^{-1}, which can be assigned to C-H modes. The intensity of the characteristic C=C peak for all other isomers is lower than that of limonene. All spectra also show a decrease in the 3745 cm^{-1} peak which is assigned to the isolated silanol OH groups.

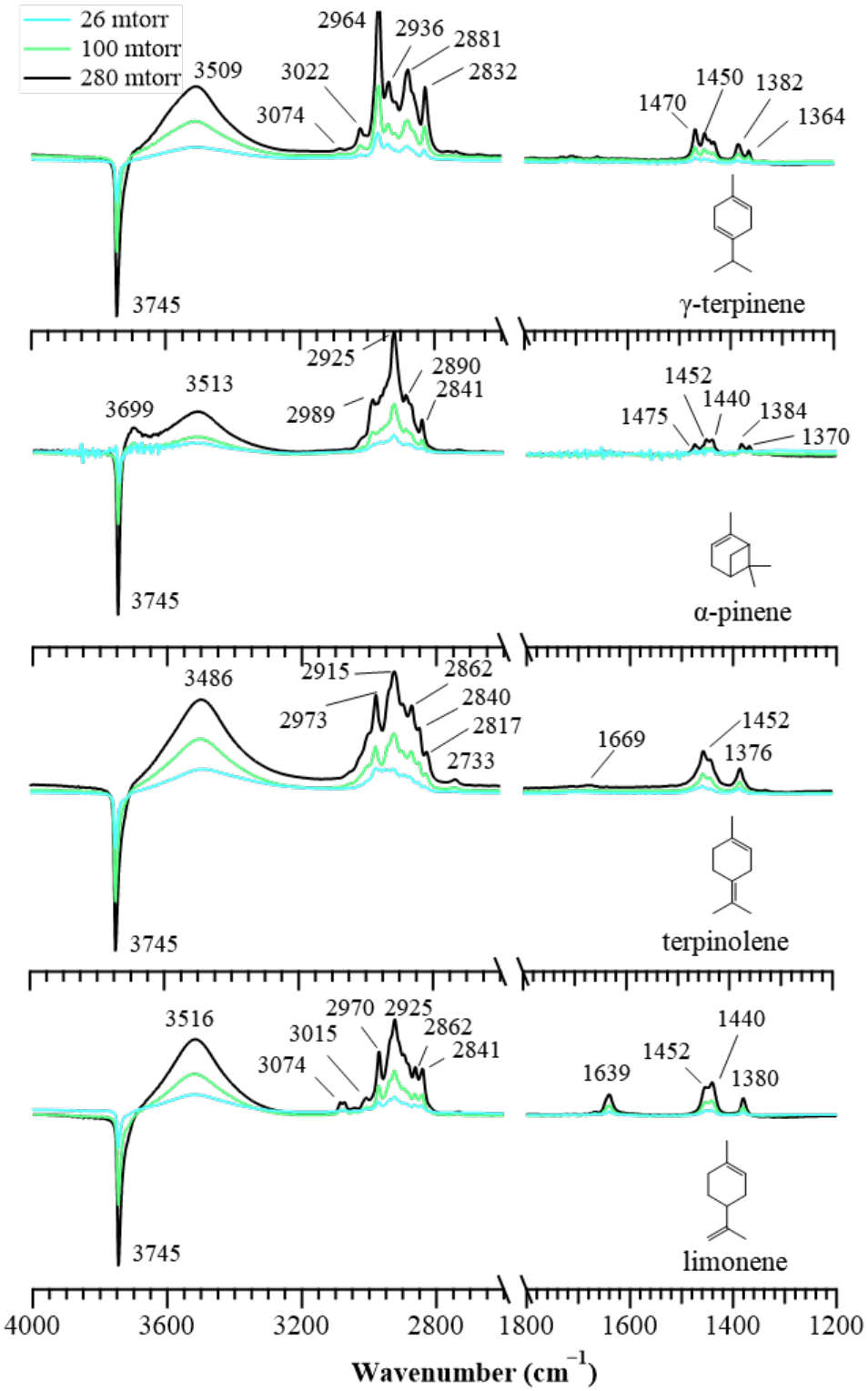

Figure 3.1: Absorbance spectra of limonene, γ-terpinene, terpinolene, and α-pinene adsorbed on the SiO_2 surface as a function of pressure. ($\sim$ 26, 100, and 280 mTorr) in the 1200-4000 cm^{-1} spectral region. The clean SiO_2 surface is used as the background spectrum and gas-phase absorptions are subtracted from each of the spectra.

Our results show a variation in the extent of Si-OH group loss for each isomer. Figure 3.2 shows the normalized loss of peak intensity of the OH groups at 3745 cm^{-1} as a function of pressure for each compound on SiO_2. All isomers with 2 C=C double bonds show a comparable fraction of OH group loss, while α-pinene, which only has 1 C=C double bond and a bridging methyl group in the middle of the ring, shows a much lower loss of surface OH groups, suggesting α-pinene has the weakest surface interactions in comparison to that of the other isomers.

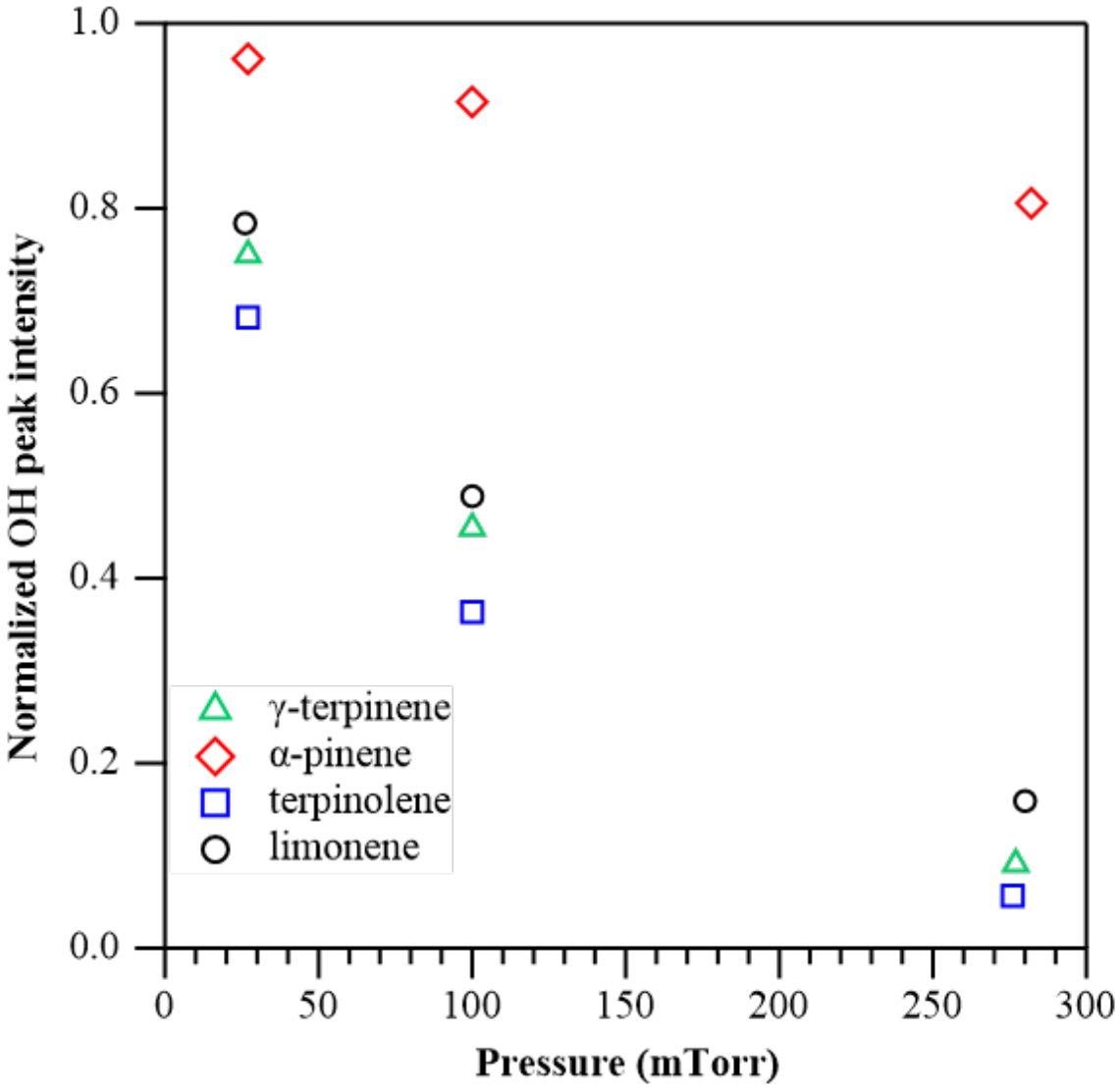

Figure 3.2: Normalized peak intensity of surface hydroxyl group (3745 cm^{-1}) loss as a function of γ-terpinene, terpinolene, and α-pinene, and limonene adsorption on SiO_2 surface.

Additional studies show that the addition of α-pinene cannot displace limonene from the SiO_2 surface, but terpinolene was able to partially displace limonene from the SiO_2 surface. This is shown in Figure 3.3.

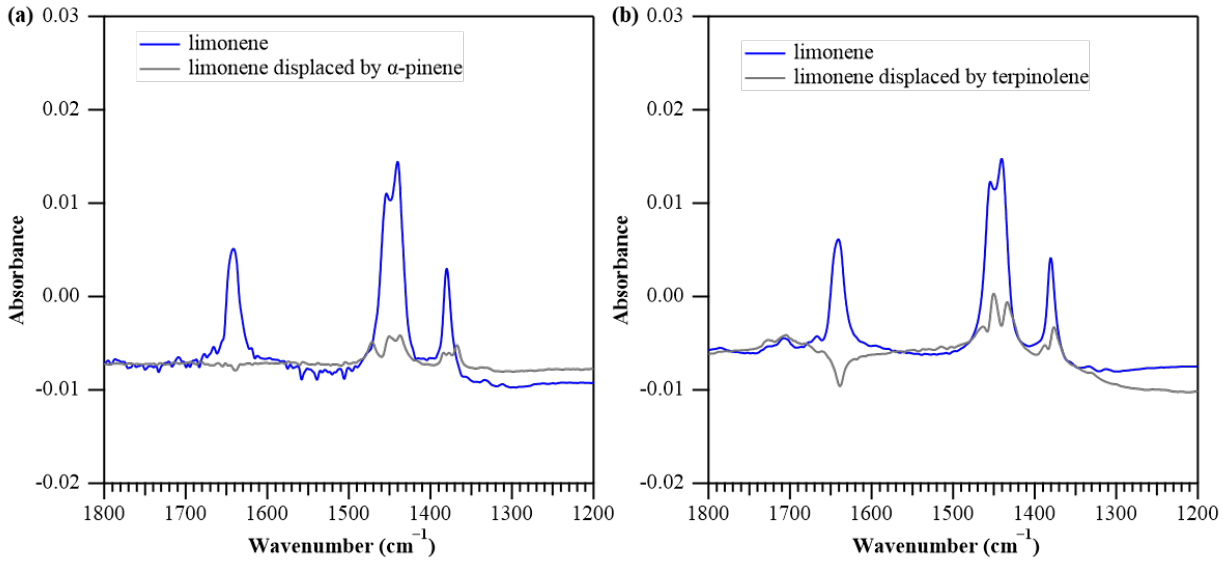

Figure 3.3: (a) FT-IR spectra of limonene adsorption on the SiO_2 surface and subsequent displaced by α-pinene (using pre-adsorbed limonene SiO_2 surface as the background spectrum). (b) FT-IR spectra of limonene adsorption on the SiO_2 surface and subsequent displaced by terpinolene (using pre-adsorbed limonene SiO_2 surface as the background spectrum).

Ultimately, the interactions that govern this unique surface chemistry can be further uncovered using molecular dynamics simulations.

3.3.2 Classical Molecular Dynamics Results

The free energy profiles (also referred to as potentials of mean force, or PMF) for the desorption of isomers have been constructed in the same method as Chapter 2 and are shown in Figure 3.4.

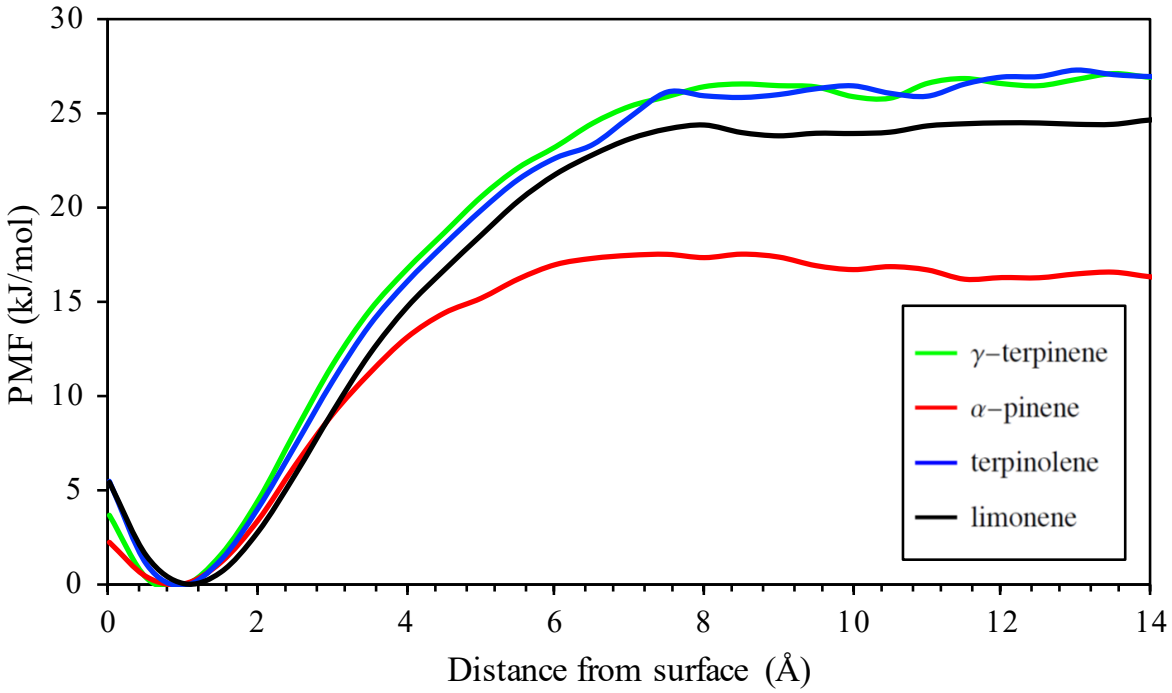

Figure 3.4: Potential of mean force (PMF) for the desorption of each isomer from the SiO_2 surface computed from the classical MD simulations

Figure 3.4 shows the desorption free energy of γ-terpinene, terpinolene, and limonene is about 10 kJ/mol higher than that of α-pinene. The trend in desorption free energy is consistent with our experimental results that the strength of the interaction of α-pinene on the SiO_2 surface is weaker compared to the interaction of limonene on the SiO_2 surface. We also find the α-pinene free energy of desorption is consistent with earlier calculations from kinetic adsorption models including Langmuir, Langmuir-Freundlich, and other models. [59] We have also calculated the desorption enthalpy, shown in Figure 3.5 of α-pinene from the SiO_2 surface of 37 $\pm$6 kJ/mol and this is in agreement with calculations reported by Chase et al. [59]

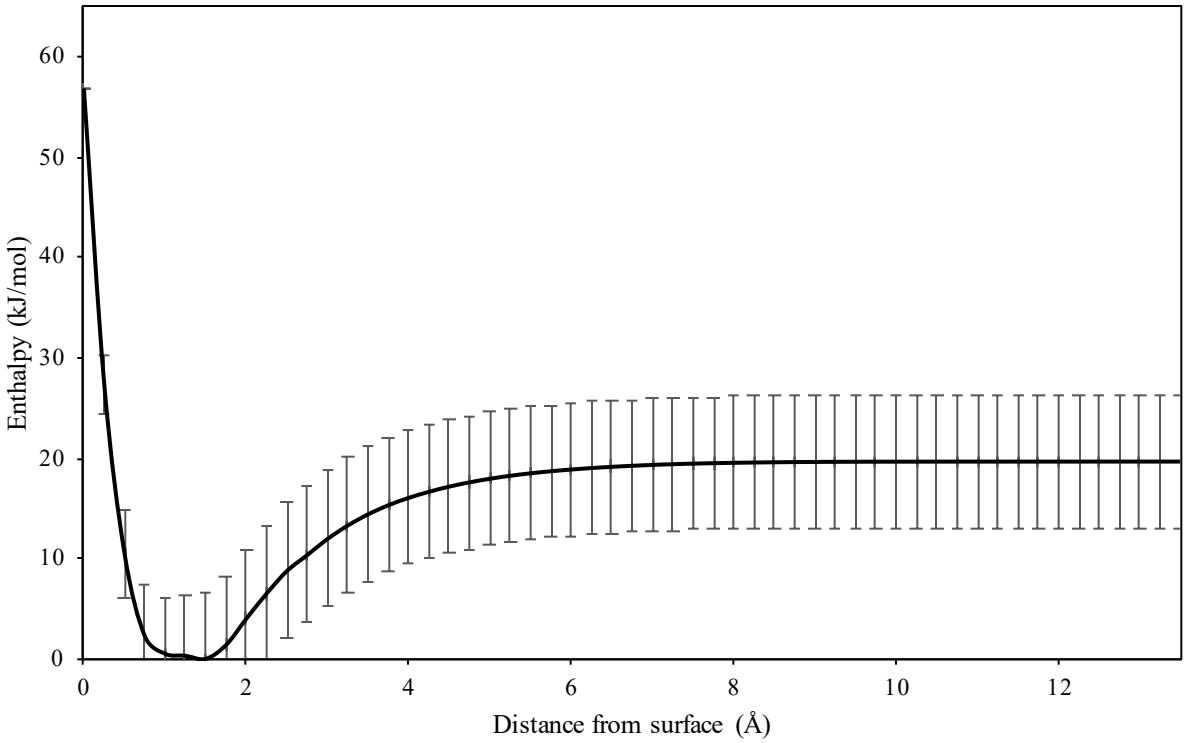

Figure 3.5: Desorption enthalpy profile computed from the MD simulation of α-pinene. The error bars are based on the standard deviation of the energy computed for the initial 100 structures.

The most obvious difference between α-pinene, the molecule with the lowest free energy of desorption, and the other studied molecules is the difference in number of C=C bonds. However, we have calculated the surface mass accommodation coefficients for these isomers, as well as the surface mass accommodation coefficient for β-pinene, another limonene isomer with only one C=C bond, as shown in Table 3.2. Figure 3.6 shows the structure of these molecules.

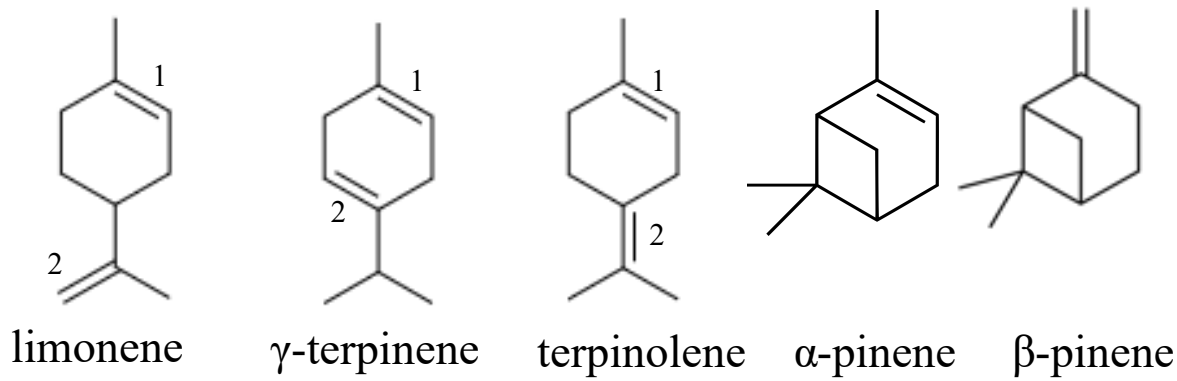

Figure 3.6: The mass accommodation coefficient was calculated for the following five limonene isomers. Relevant C=C bonds listed for further discussion in Section 3.3.2.

limonene	0.96
γ-terpinene	0.97
terpinolene	0.97
α-pinene	0.73
β-pinene	1.0

Table 3.2: Surface mass accommodation coefficients from classical molecular dynamics simulations

Our surface mass accommodation coefficients show that β-pinene does not have a lower value, implying that the number of C=C bonds is not a sufficient metric to fully determine the strength of the interaction between a limonene isomer and SiO_2. Therefore, to fully understand the role of each $C_{sp}{}^2$ carbon atom on the SiO_2 surface, we can use AIMD simulations to gain a more comprehensive understanding.

3.3.3 *ab initio* Molecular Dynamics Results

40 ps AIMD simulations were used to construct a power spectrum of γ-terpinene, terpinolene, and α-pinene, and limonene adsorbed on the SiO_2 surface, as well as to calculate the probabilities of π-hydrogen bond formation. Figure 3.7 show molecular snapshots of AIMD simulations of the constitutional isomers of limonene on the SiO_2 surface.

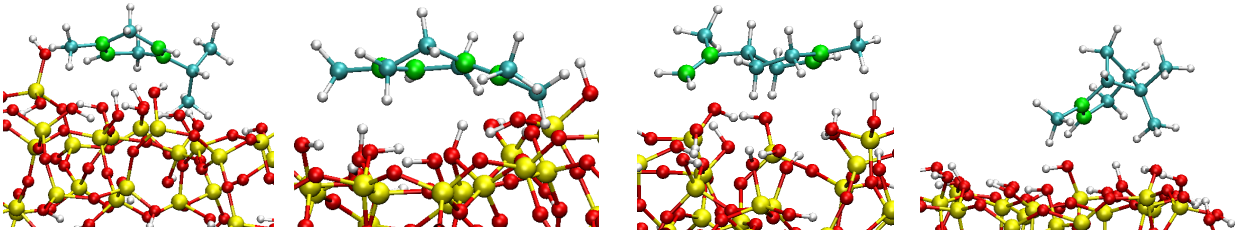

Figure 3.7: Left to right, snapshots from AIMD simulations of γ-terpinene, terpinolene, limonene and α-pinene isomers on the SiO_2 surface. The $C_{sp}{}^2$ carbon atoms responsible for π-hydrogen bonding are highlighted in green and the snapshots depict the close proximity between $C_{sp}{}^2$ carbons for γ-terpinene and terpinolene compared to limonene.

Figure 3.8 shows the power spectra of the limonene isomers adsorbed to the SiO_2 surface. Note that, in general, the frequencies of the power spectra but not the intensities are comparable to the experimental data; however, the AIMD simulations do qualitatively reproduce the FT-IR spectra.

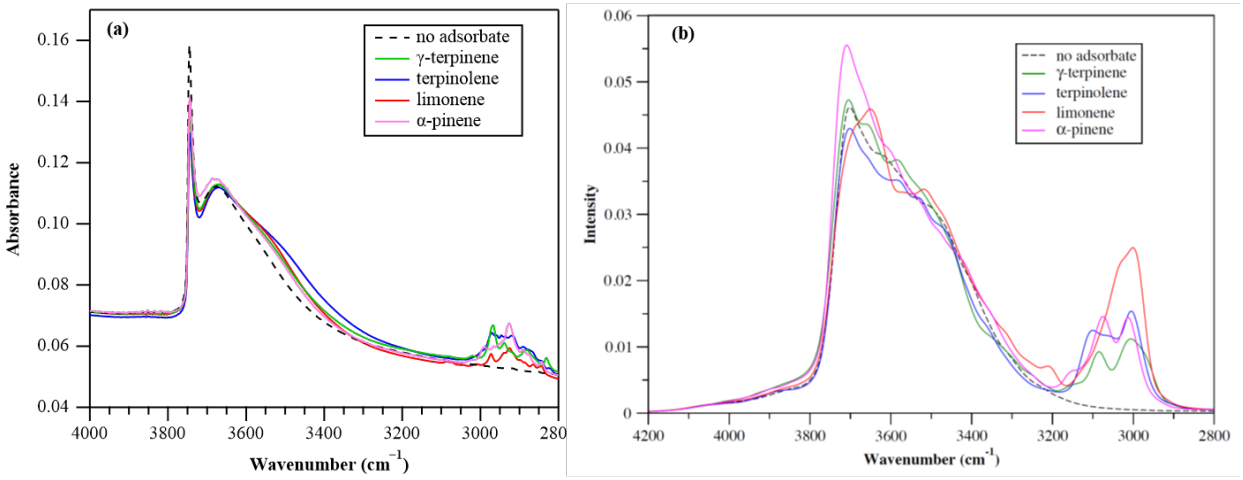

Figure 3.8: (a) Experimental spectra and (b) power spectra calculated from AIMD simulations of limonene, γ-terpinene, terpinolene, α-pinene adsorbed on the SiO_2 surface. The concentration of limonene, γ-terpinene, and terpinolene is $\sim$ 26 mTorr and α-pinene concentration is 280 mTorr.

During the 40 ps simulation, the cyclic part of limonene, γ-terpinene, and terpinolene was observed to stay parallel to the SiO_2 surface, with only small, insignificant variations in angles and distances between the surfaces. The conformation of α-pinene on fused silica has been extensively studied by Ho et al. [58] In their work, they showed that the bimodal distribution of the bridge methylene group on the four membered ring points either "towards" or "away from" the SiO_2 surface. Our trajectory showed the bridge methylene group was oriented away from the surface and the six-membered carbon ring was observed to stay at an 45° angle from the SiO_2 surface. This arises from the two methyl groups on the opposite side of the ring pointing down and forming a 90° angle with the SiO_2 surface, thus pushing the C=C bond away from the surface.

To assess the interaction of the isomer with the surface, the radial distribution function (RDF) has been calculated. The RDF is calculated between the SiO_2 hydroxyl hydrogen atoms and the $C_{sp}{}^2$ carbon atoms of each isomer. The position of the peaks in the RDF correspond to the preferred distances of hydrogen atoms of the hydroxyl groups near the selected carbon atoms. This is shown in Figure 3.6.

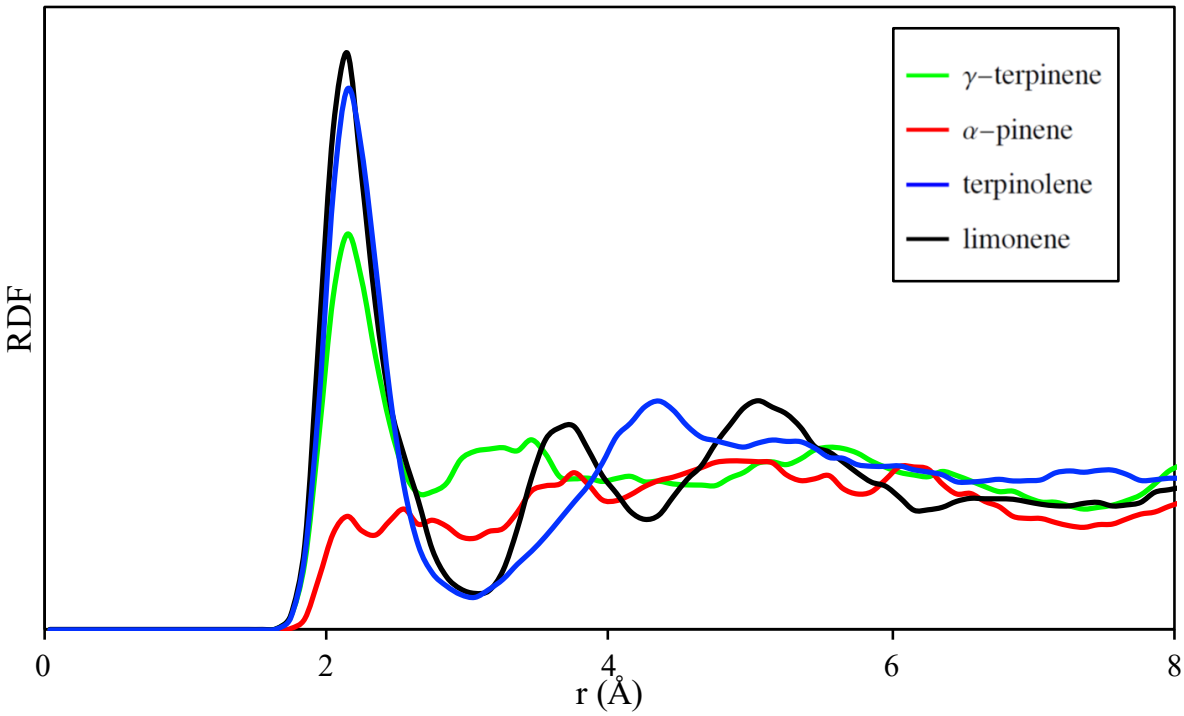

Figure 3.9: Radial distribution functions calculated among the hydroxyl hydrogen atoms and $C_{sp}{}^2$ carbon atoms of limonene isomers.

The RDF shows that only α-pinene lacks a peak around 2.5 Å, while the $C_{sp}{}^2$ carbon atoms for limonene, γ-terpinene, and terpinolene localize closer to the surface hydroxyl groups. This difference can be explained by the position of the bridge methylene group pointing away from the surface.

In addition, although the isomers with 2 C=C double bonds (limonene, γ-terpinene, and terpinolene) localize closer to the surface hydroxyl group, this does not result in all isomers having the same probability of π-hydrogen bonds.

For each isomer, we identified a π-hydrogen bond using a combined distance and angle criterion described in Section 3.2.3. The π-hydrogen bonding statistics are described in Table 3.3 and the relevant C=C bonds are highlighted in Figure 3.6.

Bond position	Average Number of π-hydrogen bonds	limonene	γ-terpinene	terpinolene	α-pinene
1	0	47.2	74.7	80.4	88.8
	1	24.7	13.9	12.9	7.2
	2	28.1	11.7	6.6	4
2	0	51.9	50.2	23.2	
	1	23.0	22.7	17.1	
	2	25.1	27.1	59.6	

Table 3.3: Hydrogen bonding statistics for isomers

As discussed previously, α-pinene has a low probability to form π-hydrogen bonds due to steric hinderance. More interestingly, both γ-terpinene and terpinolene show that one C=C bond has a much higher probability to form π-hydrogen bonds over the other, whereas limonene shows similar probabilities for both C=C bonds. These individual probabilities can be used to calculate the degree of correlation, g, which is defined as the degree at which forming a π-hydrogen bond for bond (1) influences bond (2). If $g < 1$, then we find the formation of a π-hydrogen bond for bond (1) is correlated with forming a similiar bond for C=C bond (2). The g values of limonene, terpinolene, and γ-terpinene were calculated as 1.10, 0.91, and 0.98. Both γ-terpinene and terpinolene have a minor negative correlation ($g < 1$) in the formation of hydrogen bonds involving their two double bonds. In the case of terpinolene, this negative correlation may arise from the steric hinderance of the ring and two methyl groups surrounding the exocyclic double bond, which rigidly locks the π-hydrogen bond parallel to the SiO_2 surface. While this allows for an 80% probability of forming a π-hydrogen bond, it also forces the endocyclic bond to be in a geometry that is unfavorable for interactions with surface hydoxyl groups.

We can attribute the negative degree of correlation between γ-terpinene due to the small

distance between γ-terpinene C=C bonds, where only one bond at a time is able to interact with the hydroxylated surface. Therefore, we suggest the proximity of the C=C bonds in both γ-terpinene and terpinolene limits their ability to have a positive degree of correlation ($g < 1$).

Limonene does have a positive degree of correlation, which is due to the larger separation between C=C bonds, allowing it to form more interactions with the SiO_2 surface, resulting in more π-hydrogen bond interactions and a larger extend of red shift, as described by the AIMD simulations. The hydrogen bonding statistics of α-pinene further support the conclusion that more C=C bonds result in a larger red shift, as long as those C=C bonds are in a conducive geometry for π-hydrogen bonding.

Even with the low probability of π-hydrogen bonding, there is still a red shift, comparable to γ-terpinene and terpinolene; however, this is much lower compared to the red shift due to limonene. This can lead to two conclusions from these AIMD simulations: first, that even an 11% probability of π-hydrogen bonding can result in a noticeable red shift; and second, that the ability to form more π-hydrogen bonds results in a larger red shift.

3.4 Conclusions

This study investigated the interactions of three limonene isomers, γ-terpinene, terpinolene, and α-pinene on a hydroxylated SiO_2 surface using infared spectroscopy and both force field-based and *ab initio* MD simulations. We found that the adsorption of limonene isomers on the SiO_2 surface proceeds via an analogous mechanism as discussed in our previous work. Moreover, we find there is a range of interaction strengths of these compounds with the SiO_2 surface that is a consequence of the orientation of the compound on the surface, where isomers that are positioned in geometries that are most likely to form as many π-hydrogen

bonds as possible show a stronger interaction. This implies that for these similar molecules, binding energies of these isomers cannot be explained by the extent of red shift in the SiO_2 O-H frequencies alone. This serves to improve our conceptual framework of the interactions of organic compounds with indoor relevant surfaces.

Chapter 4

Heterogeneous Interactions of Prevalent Indoor Oxygenated Organic Compounds on Hydroxylated SiO_2

4.1 Background

We now turn our study to oxygenated organic compounds (OOC) that are present in the indoor environment and on indoor surfaces. These compounds may be directly emitted by consumer products or are the produce of the oxidation of a non-oxygenated organic compound. [55, 61] Three prevalent OOCs that will be discussed in this chapter and are produced during cleaning activities are dihydromyrcenol, α-terpineol, and linalool, which are shown in Figure 4.1.

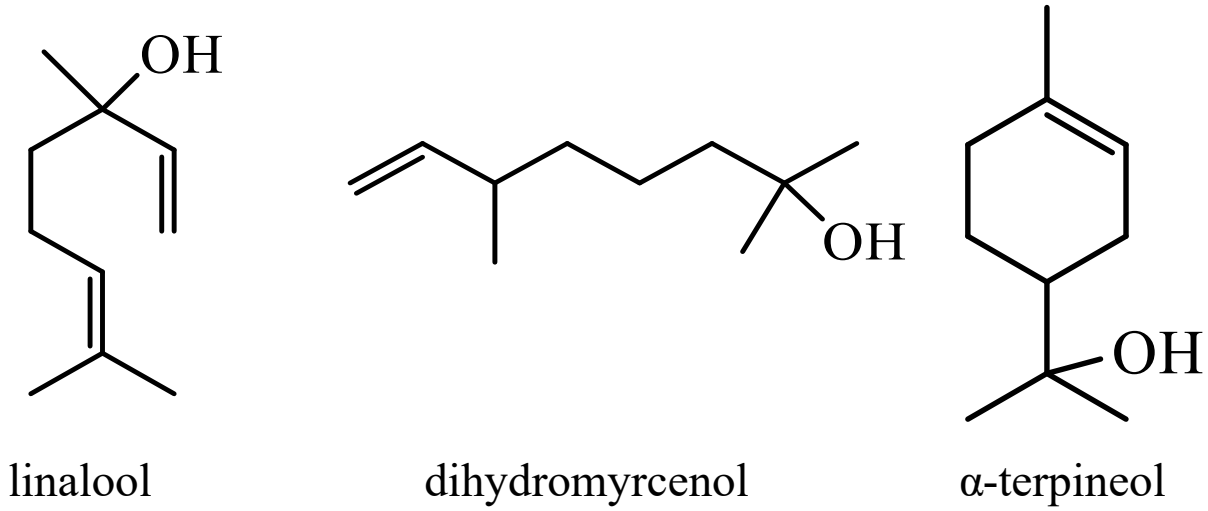

Figure 4.1: Three molecules of interest for this study.

Linalool is found in liquid floor detergents, room fragrance products, air fresheners, cleaning agents and pine oils. [40, 61, 62, 63, 64] α-terpineol is also found in liquid floor detergents, room fragrance products, air fresheners and bergamot oils, which is an essential oil. [40, 61, 62, 63]. Dihydromyrcenol is found in liquid floor detergents, room fragrance products, and lavender. [40, 61, 62].

Here, we study the adsorption of these molecules on a hydroxylated SiO_2 surface using a combination of classical MD simulations and *ab initio* MD simulations, as well as FT-IR spectroscopy. In addition, we prepared a comparison between the adsorption of these molecules and limonene on the hydroxylated SiO_2 surface.

4.2 Simulation Protocols

The same simulation protocols for classical MD simulations and *ab initio* simulations as described in Chapter 3 have been used in this study. [65] Additionally, to calculate the free energy profile for the reorientation of linalool on the SiO_2 surface, a 0.3 μs unbiased classical

MD simulation was performed.

Electronic structure calculations have been used to study the interactions of OOCs on the hydroxylated SiO_2 surface. The binding energy of OOCs to the SiO_2 surface was calculated using the Gaussian 16 package. [66] Optimized structures of dihydromyrcenol, α-terpineol, and linalool as well as the hydroxylated SiO_2 cluster in the isolated and complex forms were obtained with the M06-2X/6-311G(d) [67] level of theory. The counterpoise-corrected binding energies were calculated with the M06-2X/6-311G(d,p) level of theory. [68]

4.2.1 Surface Analysis Techniques

Hydrogen bonding statistics were calculated between adsorbate $C_{sp}{}^2$ carbon centers and surface OH groups as well as between adsorbate OH groups and surface OH groups. A hydrogen bond was defined using a combined distance (hydrogen bond accept or and donor distance < 3.2 Å) and angle criterion (angle between acceptor, donor H, and donor O was within 140 to 180°).

4.3 Results

To investigate the adsorption of oxygenated organic compounds on SiO_2, a joint experimental and theoretical study was performed. First the results of the experimental IR measurements and kinetic measurements will be described in Section 4.3.1, and secondly, classical MD simulations will be reported in Section 4.3.2, and the results of the AIMD simulations will be reported in Section 4.3.3. Finally, a discussion of electronic structure calculation results will be reported in Section 4.3.4. These results indicate the ability of these molecules to adsorb tightly on to the SiO_2 surface, much greater compared to molecules discussed in Chapter 3.

4.3.1 Experimental Results

The FT-IR spectra of the three OOCs is shown in Figure 4.2, with comparison to the spectrum of adsorbed limonene. The spectra show a decrease of the isolated Si-OH peak indicating hydrogen bonding interactions with surface hydroxyl groups are present.

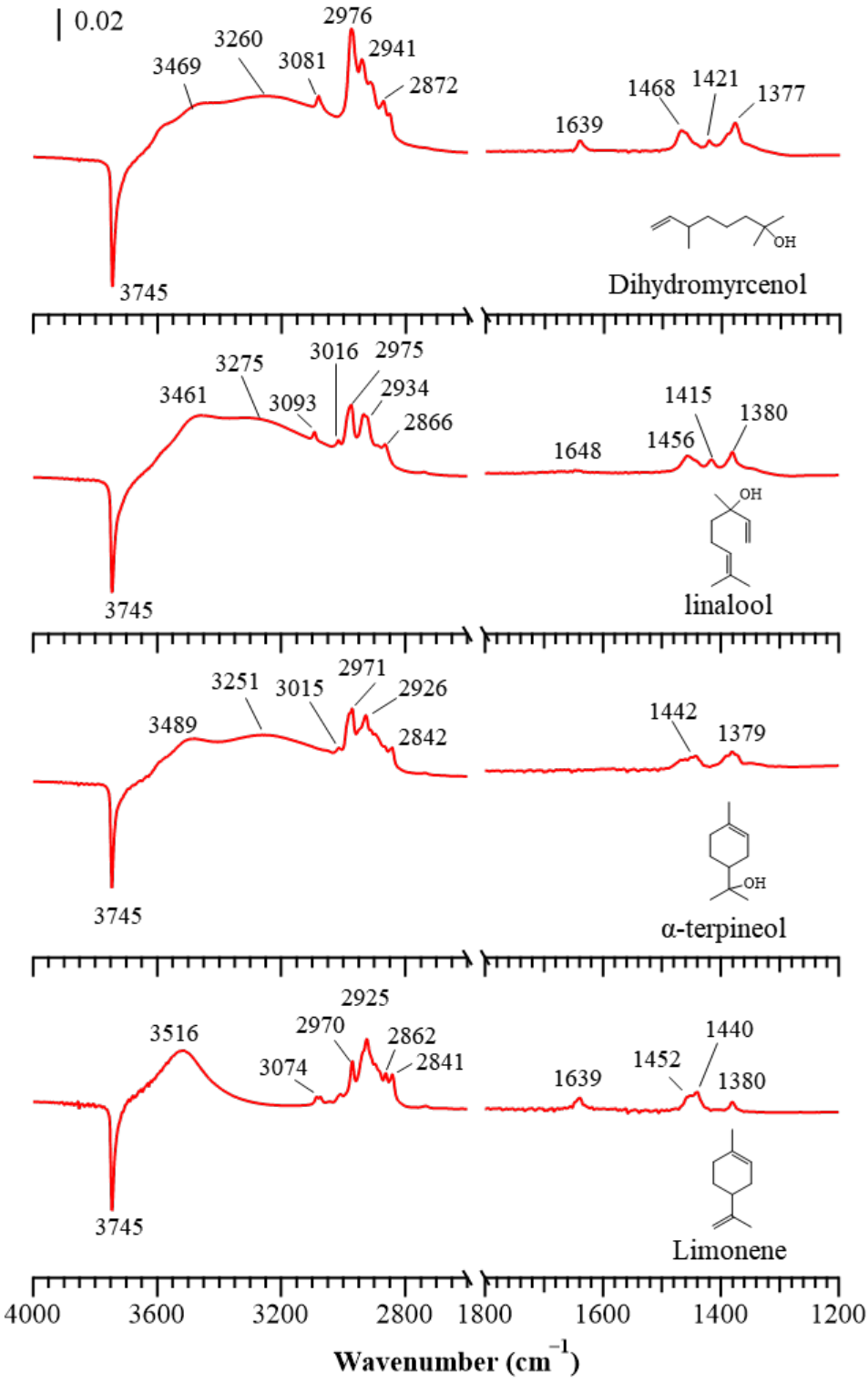

Figure 4.2: FT-IR spectra of SiO_2 particles exposed to dihydromyrcenol (7mTorr), α-terpineol (6 mTorr), linalool (7 mTorr), and limonene (276 mTorr). The clean SiO_2 surface is used as the background spectrum.

The kinetics of OOCs adsorption on the clean SiO_2 particles was characterized by an apparent heterogeneous uptake coefficient (γ). The value of γ was determined for the three OOCs at an initial pressure of 15 mTorr using equations 4.1 and 4.2.

$$\gamma = \frac{\frac{d\{C_{surf}\}}{dt}}{flux} \tag{4.1}$$

$$flux = \frac{PN}{\sqrt{2\pi MRT}} \tag{4.2}$$

$\frac{d\{C_{surf}\}}{dt}$ is the amount of OOC taken up by the particle BET surface area per second, P is the pressure of OOCs, N is Avaogadro's number, M is the molecular weight of the OOCs, R is the gas constant, and T is the temperature. The maximum surface coverage was determined by using volumetric measurements by the pressure difference for OOCs with and without SiO_2 particles on the tungsten grid. See [53] for more details. This value can be used to calibrate infared adsorptions for adsorbed OOCs, which were used to determine the number of molecules adsorbed on the surface. Additional details for this calculation can be found in the following sources. [52, 69]

The γ values for dihydromyrcenol, α-terpineol, and linalool are 7.0 +/- 1.5 x 10^{-8}, 1.7 +/- 0.4 x 10^{-7}, and 3.5 +/- 1.1 x 10^{-8}. These values are also listed in Table 4.1. While the γ values are comparable across OOCs, these values are an order higher than limonene, which is 5.1 x 10^{-9} under the same experimental conditions. The higher values for the OOCs suggest that these molecules have a stronger propensity for adsorption on the SiO_2 surface when compared to limonene, which is in agreement with our computational results.

In addition to surface adsorption, the OOCs can be oxidized by indoor oxidants, such as OH radicals and O_3 in the gas phase. [70, 71, 72] The rate constants of these compounds under-

going reactions with OH radicals and O_3 as determined by previous studies are summarized in Table 4.2. [70, 73, 74] The pathway for OOCs that are taken up by SiO_2 can be described by a lifetime τ_s, according to equation 4.3.

$$\tau_s = \frac{4}{\gamma \omega A_v} \tag{4.3}$$

Here, A_v is the surface to volume ratio, ω is the mean molecular velocity, and τ_s is the lifetime of each OOC with respect to heterogenous interactions with the surface. In this case, they are estaimted as 19.7, 8.1 and 40.4 hours for dihydromyrcenol, α-terpineol, and linalool. Assuming that the concentration of indoor OH radicals and O_3 is 1.7 x 10^5 molecules and 20 ppbv respectively, [75] the lifetimes of these compounds with respect to gaseous oxidiations were also calculated and are listed in Table 4.1.

	Dihydromyrcenol	α-terpineol	Linalool
γ	(7.0 ± 1.5) $\times 10^{-7}$	(1.7 ± 0.4) $\times 10^{-7}$	(3.4 ± 1.1) $\times 10^{-7}$
$k_{OH}(cm^3 molecule^{-1} s^{-1})$	(3.8 ± 0.9) $\times 10^{-11}$ [70]	(1.9 ± 0.5) $\times 10^{-10}$ [73]	(1.6 ± 0.4) $\times 10^{-10}$ [74]
$k_{O_3}(cm^3 molecule^{-1} s^{-1})$	(2.0 $\times$ 10^{-18}) [70]	(3.0 ± 0.2) $\times 10^{-16}$ [73]	(4.3 ± 1.6) $\times 10^{-16}$ [74]
τ_s (h)	19.7	8.1	40.4
τ_{OH} (h)	43.0	8.6	10.2
τ_{O_3} (h)	267.1	1.8	1.3

Table 4.1: Experimental values for the desorption of OOCs from the SiO_2 surface.

These results suggest that the removal of dihydromyrcenol and α-terpineol in indoor air by the heterogenous interactions on surfaces is comparable to that by gaseous reactions with OH radicals or O_3. Futhermore, Table 4.1 shows that the contributions of different pathways for the removal of OOCs are not related to the concentration of OOCs. Therefore, we can potentially extrapolate the results calculated at relatively high OOC concentration to that of the realistic concentration of OOCs in indoor air.

In addition to chemical transformations, it should be noted that the concentrations of OOCs in the indoor air are significantly affected by the air exchange rate. The average air exchange rate has been reported to be 0.71 h^{-1} (on the basis of 593 air exchange rate data measured in America). [76] Table 4.1 shows the removal of OOCs can be up to the rate equivalent of 0.12 h^{-1} air exchange. We believe, given the uptake coefficients calculated in this study using BET surface area represent the lower limit, which underestimate the rate equivalent to air exchange, this pathway may be able to compete with moderate and low air exchange. Therefore, the removal of these OOCs by heterogeneous interactions with indoor surfaces is a significant pathway with a fate of indoor air.

Additionally, the desorption kinetics have been measured on the SiO_2 surface as a function of time by the recovery of isolated Si-OH groups, as shown in Figure 4.3, as a first order decay.

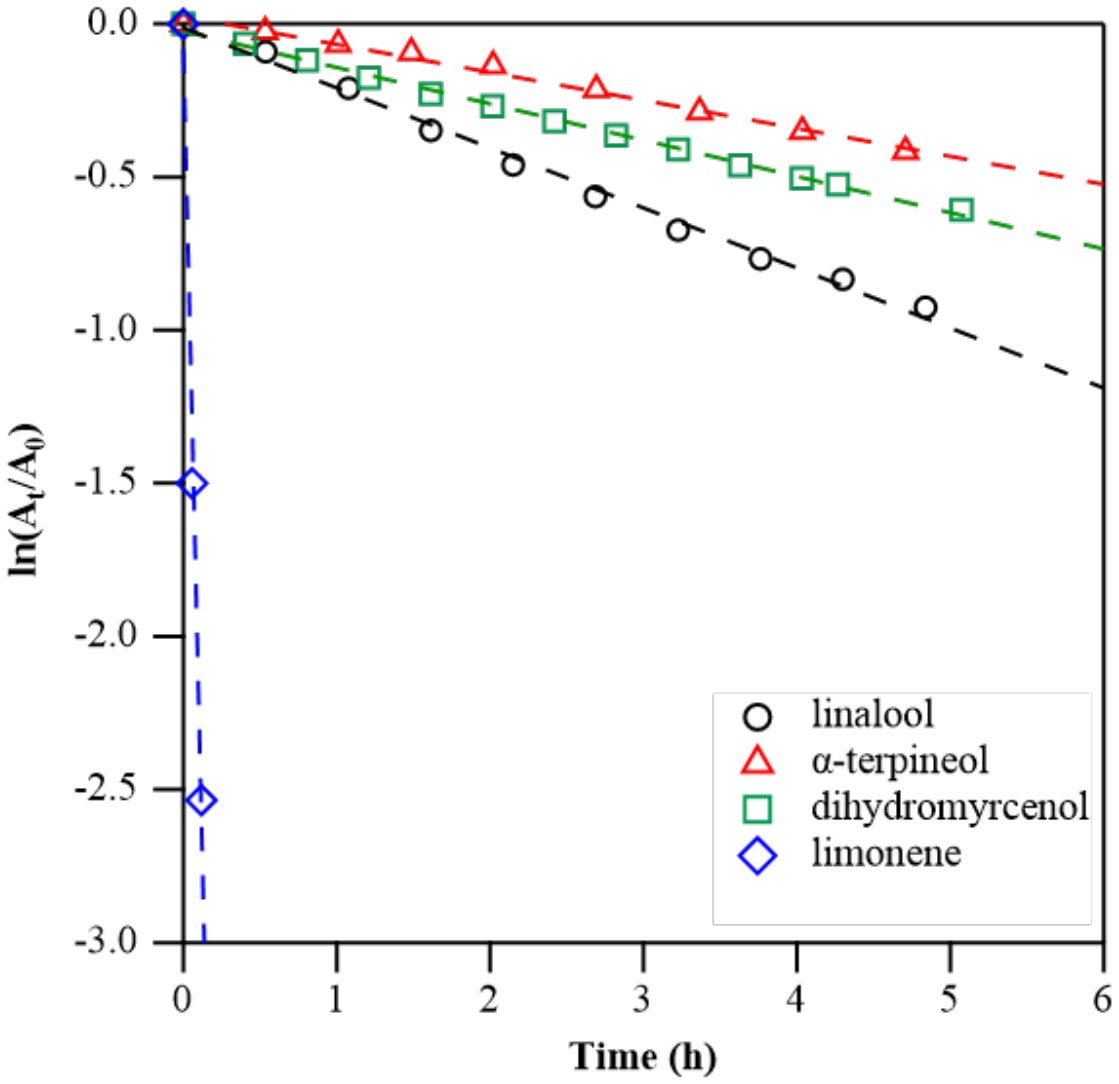

Figure 4.3: The first order decay for the initial desorption of OOCs as well as limonene from the SiO_2 surface. A_t is the integrated absorbance of peak isolated Si-OH groups (3745 cm^{-1}) at specific time t. A_0 is the initial integrated absorbance peak of isolated Si-OH groups.

Limonene desorption is readily completed within one hour, but the desorptions of OOCs can be continuous for ∼14 h and even longer pumping times. Thus, compared to limonene, these three OOCs on SiO_2 show a much slower desorption profile, in agreement with our MD simulations. The desorption rates have been estimated below in Table 4.2. The desorption rate of limonene is comparable to the literature result studying the desoprotion of limonene on SiO_2 dominated mineral dust. [77]

	Dihydromyrcenol	α-terpineol	Linalool	Limonene
Desorption lifetime (s^{-1})	3.3 $\times 10^{-5}$	2.5 $\times 10^{-5}$	5.4 $\times 10^{-5}$	6.1 $\times 10^{-2}$

Table 4.2: Desorption lifetime estimations.

Table 4.2 shows the desorption rate constants of the OOCs are over two orders of magnitude lower than the desorption rate constant of limonene. This is supported by the classical MD and AIMD simulation results below.

4.3.2 Classical Molecular Dynamics Results

In order to investigate the slow desorption and to analyze the heterogeneous interactions of OOCs on a hydroxylated SiO_2 surface, both classical MD and AIMD simulations were used. Over the course of both simulation trajectories, we determined that while dihydromyrcenol and α-terpineol were shown to have one singular predominant orientation on the surface, linalool has two orientations, due to a surface dihedral rotation, ϕ, as shown in Figure 4.3.

To investigate these two conformation of linalool on the surface, the free energy profile for the dihedral rotation of linalool on the SiO_2 surface was calculated from the probability distribution of the dihedral ϕ, shown in Figure 4.4.

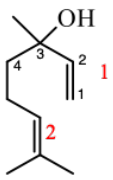

Figure 4.4: The dihedral angle (1-2-3-4) that can cause a change in linalool orientation during the simulations. The π bonds are labeled in red and discussed in Table 4.3.

The equation to determine the probability distribution of ϕ is:

$$F_\phi = -k_B T \, ln(p(\phi)) \tag{4.4}$$

Here, $p(\phi)$ is the probability distribution of ϕ acquired from the 0.30 μs classical MD simulation, k_B is Boltzmann's constant, and T is the temperature (300 K).

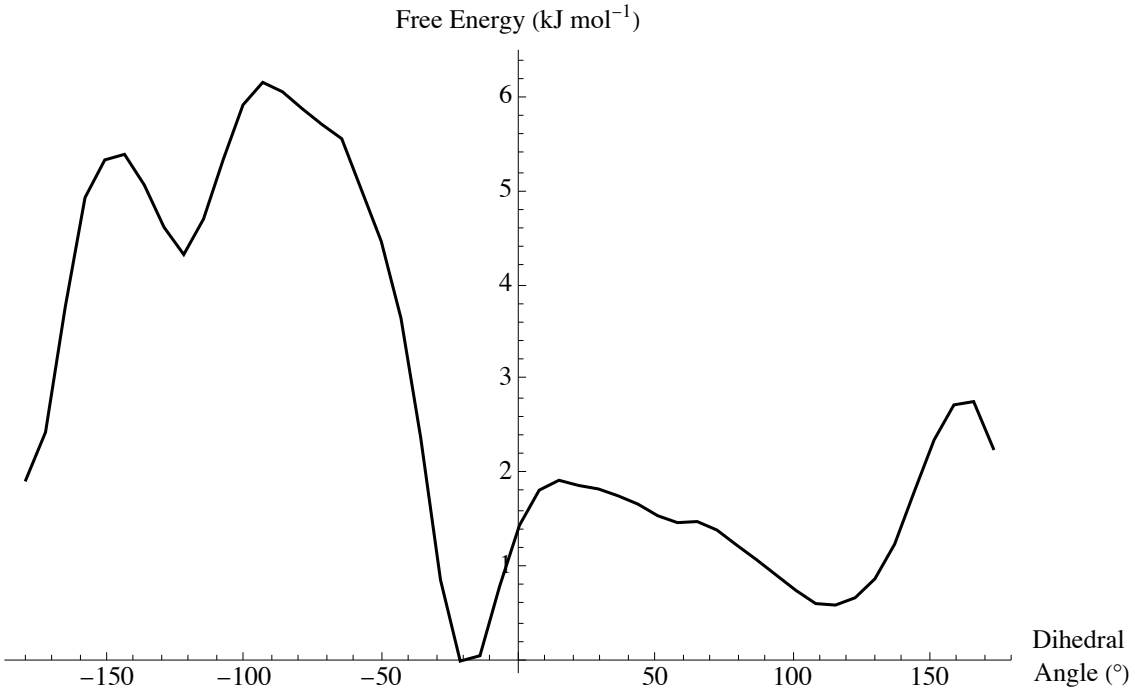

Figure 4.5: Free energy profile as a function of the orientation of linalool on the hydroxylated SiO_2 surface computed from 0.30 μs force classical MD simulation.

The zero of the free energy profile was taken to be the most probable dihedral angle, ϕ ∼-20°. There is an additional low energy orientation at ϕ ∼110°. The populations of ϕ ∼-20° and ϕ ∼110° are 78% and 22% respectively. According to this free energy profile, the free energy barrier between the stable conformers is 2.0 kJ mol^{-1}. The stabilizing factor in the lower energy conformation arises from the ability for the linalool to form more π-hydrogen bonds with the SiO_2 surface hydroxyl groups.

We find there is a difference in the average number of π-hydrogen bond formation depending on the conformation of ϕ, this is shown in Table 4.3.

Dihedral Angle (°)	π-hydrogen bond	probability of forming π-hydrogen bond
$\sim$ 120	1	0.00007
	2	34.2
$\sim$ -20	1	0
	3	52.0

Table 4.3: Hydrogen bonding statistics for linalool in each surface conformation.

In addition to this study of the two linalool conformations, we also calculated the potential of mean force (PMF) for the desorption of the OOCs from the SiO_2 surface, as shown in Figure 4.6.

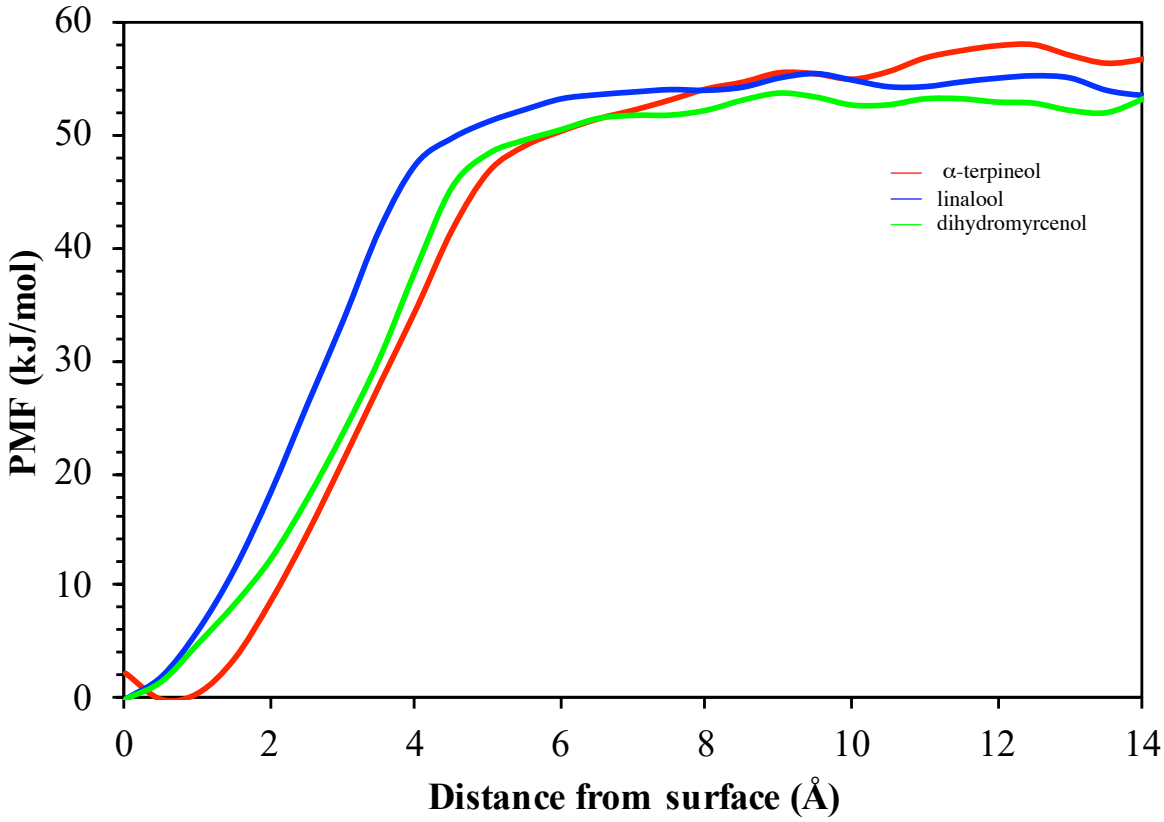

Figure 4.6: Potential of mean force (PMF) for OOCs desorption from the SiO_2 surface computed from the classical MD simulation.

The free energy desorption is found to be much higher than limonene and all of the studied limonene isomers as described in Chapter 3. This is consistent with the slower desorption lifetimes measured by the experimental measurements. To fully understand what interactions are govern these long desorption lifetimes, we can use our AIMD simulations to investigate the heterogeneous interactions at the surface.

4.3.3 *ab initio* Molecular Dynamics Results

To detail the mechanism for the interaction of dihydromyrcenol, α-terpineol, and linalool with the SiO_2 surface, a 40 ps AIMD simulations of each OOC on a fully hydroxylated SiO_2

surface was performed. Molecular snapshots of each adsorbate in it's predominant surface orientation is shown in Figure 4.6.

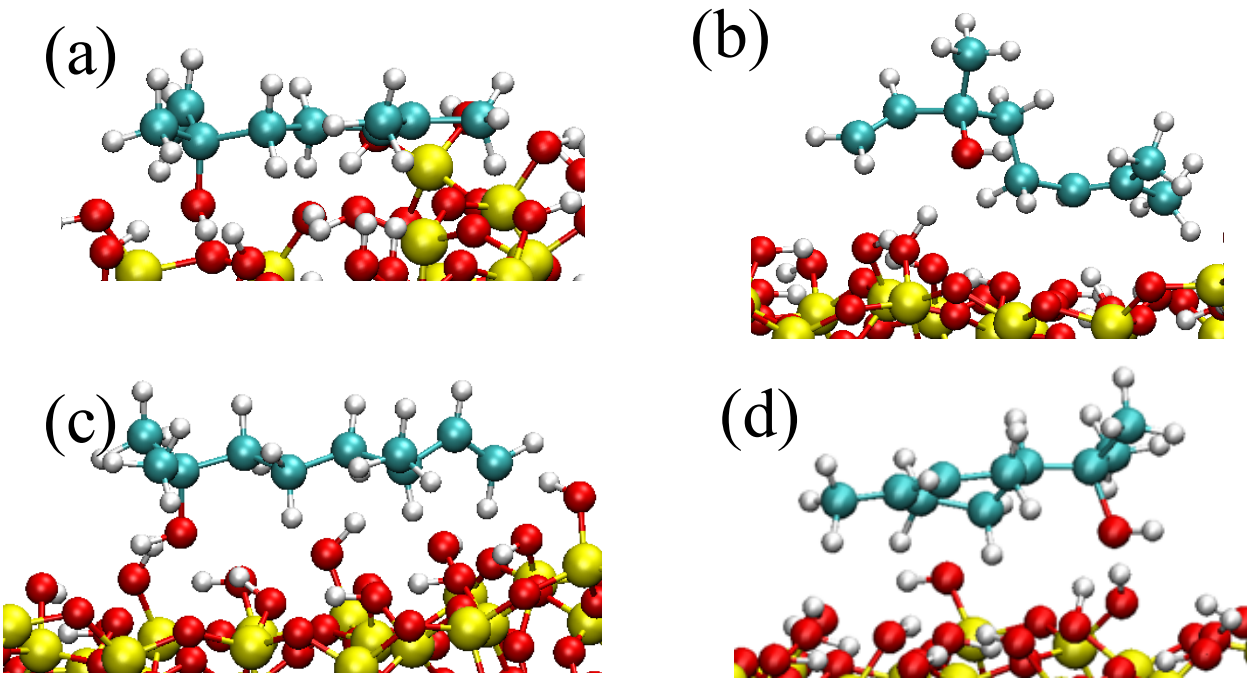

Figure 4.7: Snapshots from the AIMD simulations of (a) dihydromyrcenol, (b) α-terpineol and (c,d) linalool adsorbed on the SiO_2 surface in their most predominant positions. There exists two orientations for linalool, as discussed in the classical MD section. The oxygen, carbon, hydrogen, and silicon atoms are colored red, cyan, white, and yellow, respectively.

During the course of the AIMD trajectory, the OH group of the adsorbate stays within 2.0 to 3.0 Å of the SiO_2 surface, suggesting, that there may exist and interaction between the OH group and surface hydroxyl groups. To quantify this interaction, the radial distribution function (RDF) as calculated as a function of the distance between the oxygen atoms of the adsorbates and the SiO_2 hydroxyl hydrogen atoms. The RDF is shown in Figure 4.8.

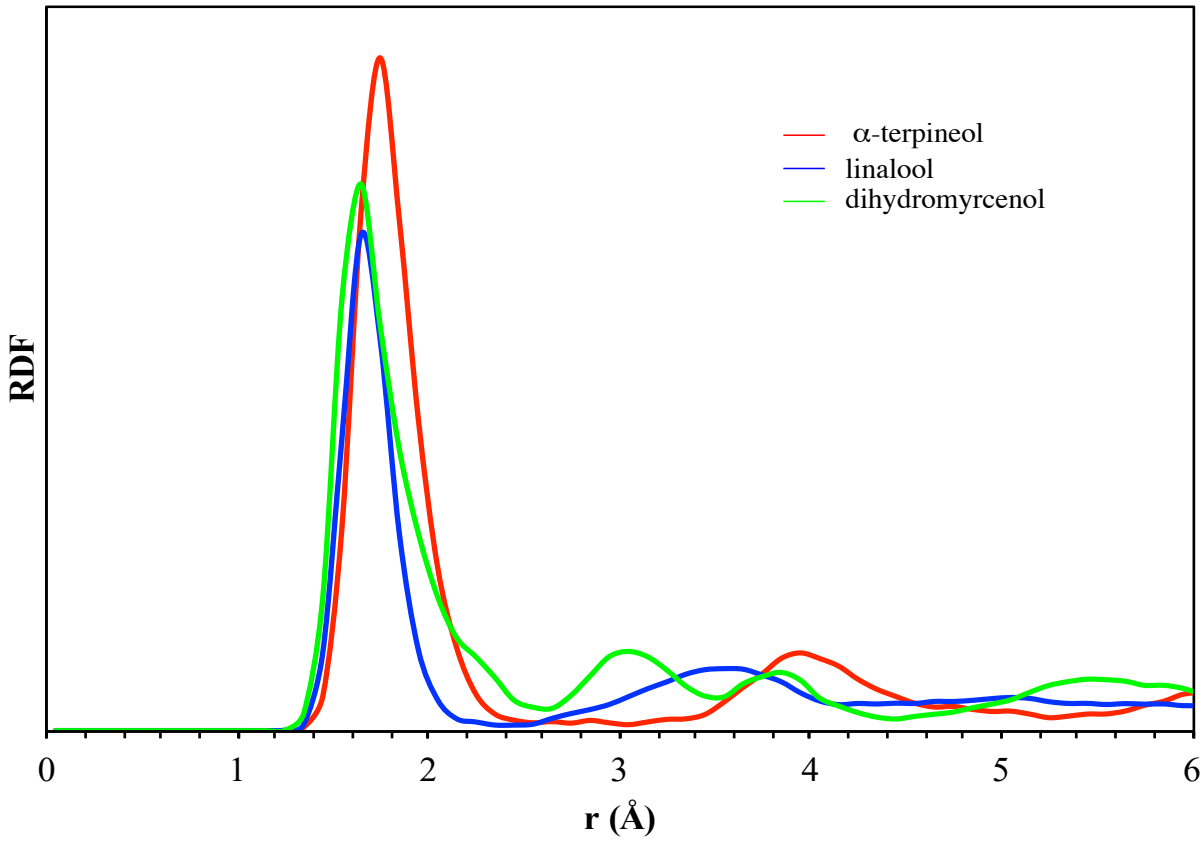

Figure 4.8: Radial distribution functions (RDFs) calculated for distances r between the SiO_2 hydroxyl hydrogen atoms and the oxygen atoms of dihydromyrcenol, α-terpineol, and linalool. The high RDF peak at ~ 1.6 $\AA$ is observed for all three OOCs suggests the formation of O-H hydrogen bonding with the surface hydroxyl groups.

Furthermore, the probability of hydrogen bond formation for the OH groups on each OOC to the surface hydroxyl groups was calculated using a combined distance and angle criterion (discussed in section 4.2.1). The average number of hydrogen bonds from the OH group on dihydromyrcenol, α-terpineol, and linalool was calculated as 1.5, 1.8, and 1.0 respectively. This indicates that these substrates can tightly adhere to the surface. Therefore, the adsoprtion of these compounds on SiO_2 is also driven by O-H hydrogen bonding in addition to the π-hydrogen bonding as observed previously with limonene. [53]

In addition, we have calculated the power spectra of dihydromyrcenol, α-terpineol, and linalool adsorbed on SiO_2 surface, as shown in Figure 4.8.

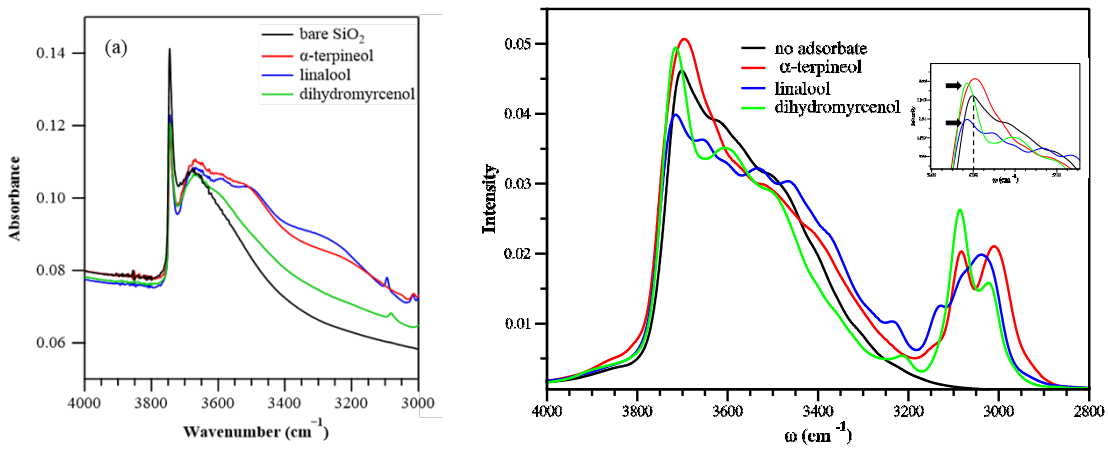

Figure 4.9: (a) Experimental spectra and (b) power spectra calculated from AIMD simulations of dihydromyrcenol, α-terpineol, and linalool adsorbed on SiO_2 surface. The insert shows that the peak for the surface hydroxyl groups in systems in the presence of linalool and dihydromyrcenol, as shown by the black arrows, are blue shifted compared to the corresponding peak for the SiO_2 surface with no adsorbate present, as shown by the black dashed line.

The calculated power spectra show that the adsorption of these compounds results in a shift of the stretching frequency of the hydroxyl groups of SiO_2. We noticed that the adsorption of dihydromyrcenol and linalool results in a blue shift, as shown in the insert of Figure 4.9b. A previous study revealed that the blue shift of hydrogen bonds implies shortening between X (the more electronegative atom) and H. [78] We have analyzed the bond lengths of all the surface OH groups participating in π-hydrogen and O-H hydrogen bonds in order to understand the nature of this blue shift, as shown in Table 4.4.

Compounds	Form of Hydrogen Bond	Average number of hydrogen bonds	Average O....H bond length
dihydromyrcenol	OH -hydrogen	1.5	1.011
	π-hydrogen	0.16	0.987
linalool	OH-hydrogen	1.0	1.008
	π-hydrogen	0.30	0.996
α-terpineol	OH-hydrogen	1.8	1.004
	π-hydrogen	< 0.01	-

Table 4.4: Average number and bond length of different hydrogen bonds for dihydromyrcenol, linalool, and α-terpineol.

This analysis reveals that the surface hydroxyl groups engaging in π-hydrogen bonds have shorter hydroxyl (O...H) bond lengths compared to those engaging in O-H group hydrogen bonding. Therefore, the blue shift is interpreted to be a consequence of the π-hydrogen bonding interaction of dihydromyrcenol and linlaool with the SiO_2 surface. This is supported by the fact that in our AIMD simulations of α-terpineol, that do not produce a blue shift in the calculated power spectra, has an extremely low probability of forming π-hydrogen bonds.

4.3.4 Electronic Structure Calculations Results

The binding energy of limonene and dihydromyrcenol adsorbed to the SiO_2 surface were calculated using electronic structure calculations. The binding energy of for limonene and the SiO_2 surface was -41.57 kJ/mol and for dihydromyrcenol was -35.26 kJ/mol. However, this interaction energy does not fully account for the associated increase in entropy resulting from the desorption of the adsorbate from the Si-OH surface. In addition, in our studies of carvone (detailed in Chapter 5), it was determined that electronic structure calculations that measure a single geometric minimum of a molecule on a surface may not be the best

description of a molecule adsorbed on a surface undergoing various surface interactions.

4.4 Conclusions

From our experimental results, it was determined the desorption rate of oxygenated organic compounds on a hydroxylated SiO_2 surface is two orders of magnitude lower than the desorption rate constant of limonene. From our computational results, we can explain this difference in desorption rate constants as due to the high average number of hydrogen bonds between the OOCs and the hydroxylated surface compared to the weaker π-hydrogen bonds.

As substantially high concentrations of OOCs can be observed during cleaning and room deodorizing we propose that before OOCs concentrations can achieve steady-state in indoor air, OOCs can be taked up by indoor surfaces, allowing these surfaces to serve as reserviors of OOCs that continuously affect air quality on longer time scales due to their slower desorption processes.

Chapter 5

Heterogeneous Interactions between Carvone and SiO_2

5.1 Background

Carvone is an oxidation product of limonene and can be emitted from wood resins surfaces. [63, 79, 80] Carvone can also produce contact allergens from indoor surfaces. [81, 82] While there are many interesting motivations to study carvone from the indoor air perspective, from a computational chemistry standpoint, our study of carvone was intriguing molecule because in our classical MD simulations, I saw what initially felt like an under representation of hydrogen bonds between the carvonce oxygen atom and surface OH groups, following the logic of the high number of average hydrogen bonds between adsorbates and the surface as discussed in Chapter 4, but I soon realized that this under representation was due to a novel surface interaction between carvone and the SiO_2 surface. As will be discussed in this chapter as well as Chapter 7, carvone and other carbonyl containing molecules can form a weak interaction (described by me as an association) between the carbonyl oxygen and

silicon atoms, and this result is supported by our experimental measurements.

In this chapter I will detail our 3-part integrated approach to study how carvone interacts with a SiO_2 surface by using experimental measurements, kinetic modeling, computational chemistry.

5.2 Simulation Protocols

The same protocol for the classical MD simulations as in Chapter 3 were done for this work, but the simulation temperature was maintained at 300 K. The CHARMM compatible force field parameters for S-carvone were constructed using the Force Field Toolkit [20]. The desorption enthalpy was calculated the same way as in Chapter 3, but instead of 100 initial structures, 156 initial structures were created, and the initial structure was classified as either a hydrogen bond or an oxygen silicon association. To classify this, the minimum distance between the carvone oxygen atom and the surface was measured. The surface accommodation coefficient was calculated in the same way as in Chapter 3. Umbrella sampling was used to calculate the free energy profile for desorption of carvone from the SiO_2 surface in the same manner as described in earlier chapters.

For the *ab initio* simulations, the same protocol as Chapter 2, (TZV2P-MOLOPT-GTH basis set) was used for all simulations. [49, 50] Two simulations were performed, a 40 ps AIMD simulation on a fully hydroxylated SiO_2 cluster and a 16 ps AIMD simulation of a carvone molecule on a partially dehydroxylated neutral SiO_2 cluster with two 3-coordinated Si atoms. Each 3-coordinated Si atom was given an unpaired electron spin, as described by Anderson et al. [83]

To corroborate the oxygen silicon association, electron structure calculations were performed with the Gaussian 16 package. [66] First stationary points were determined for the molecule

engaging in both potential interaction mechanisms, the hydrogen bond and the oxygen silicon association using the M06-2X/6-311G(d) level of theory. [67] Frequency calculations were performed to ensure a true stationary point. To ensure a stationary point of carvone in an oxygen silicon association, a partially dehydroxylated surface contained two 3-coordinated Si atoms, each with an unpaired electron spin. The molecular electrostatic potential was evaluated using electronic densities computed at the M06-2X/6-311G(d) level of theory using the ChelpG method. [84] Graphical representations were generated by mapping the ESP onto a molecular surface corresponding to an isodensity contour of 0.07 e/a.u^3 using UCSF Chimera. [85]

5.2.1 Surface Analysis Techniques

All surface interaction probabilities were calculated from the last 10 ns of the unbiased classical MD simulation, and measurements were made every 1 ps. Hydrogen bonding statistics were calculated between carvone $C_{sp}{}^2$ carbon centers and surface OH groups as well as between the carvone oxygen atom and surface OH groups. A hydrogen bond was defined using a combined distance (hydrogen bond acceptor and donor distance < 3.0 Å for carvone oxygen to surface and < 3.5 Å for $C_{sp}{}^2$ carbon to surface) and angle criterion (angle between acceptor, donor H, and donor O was within 120 to 180°). To determine the presence of a carvone oxygen silicon association, all distances between the carvone oxygen atom and surface were measured every 1 ps. The minimum distance between the carvone oxygen and the surroundings was determined per frame and the fraction of these distances that were to a 3-coordinated Si atom was used to determine the probability of oxygen silicon associations. This same method was also used for AIMD simulations, measuring every configuration from the simulation for 16 ps.

5.3 Results

To investigate the adsorption of carvone on a hydroxylated SiO_2 surface, a joint experimental, kinetic modeling, and theoretical study was performed. First, the results of the experimental IR measurements and kinetic measurements will be described in Section 5.3.1, and next, the results of the kinetic modeling calculations will be described in Section 5.3.2. Due to the complexity of the results from the classical MD, AIMD, and electronic structure calculation results, they will all be presented together in Section 5.3.3.

5.3.1 Experimental Results

The FT-IR spectrum of gas phase carvone is shown in Figure 5.1a at 52 mTorr and 296 K, and the FT-IR absorbance spectrum of carvone on the hydroxylated SiO_2 at 4 mTorr equilibrium under dry conditions (<1 % RH), using the clean hydroxylated SiO_2 surface as the background and with gas-phase contributions subtracted from the spectrum is shown in Figure 5.2b.

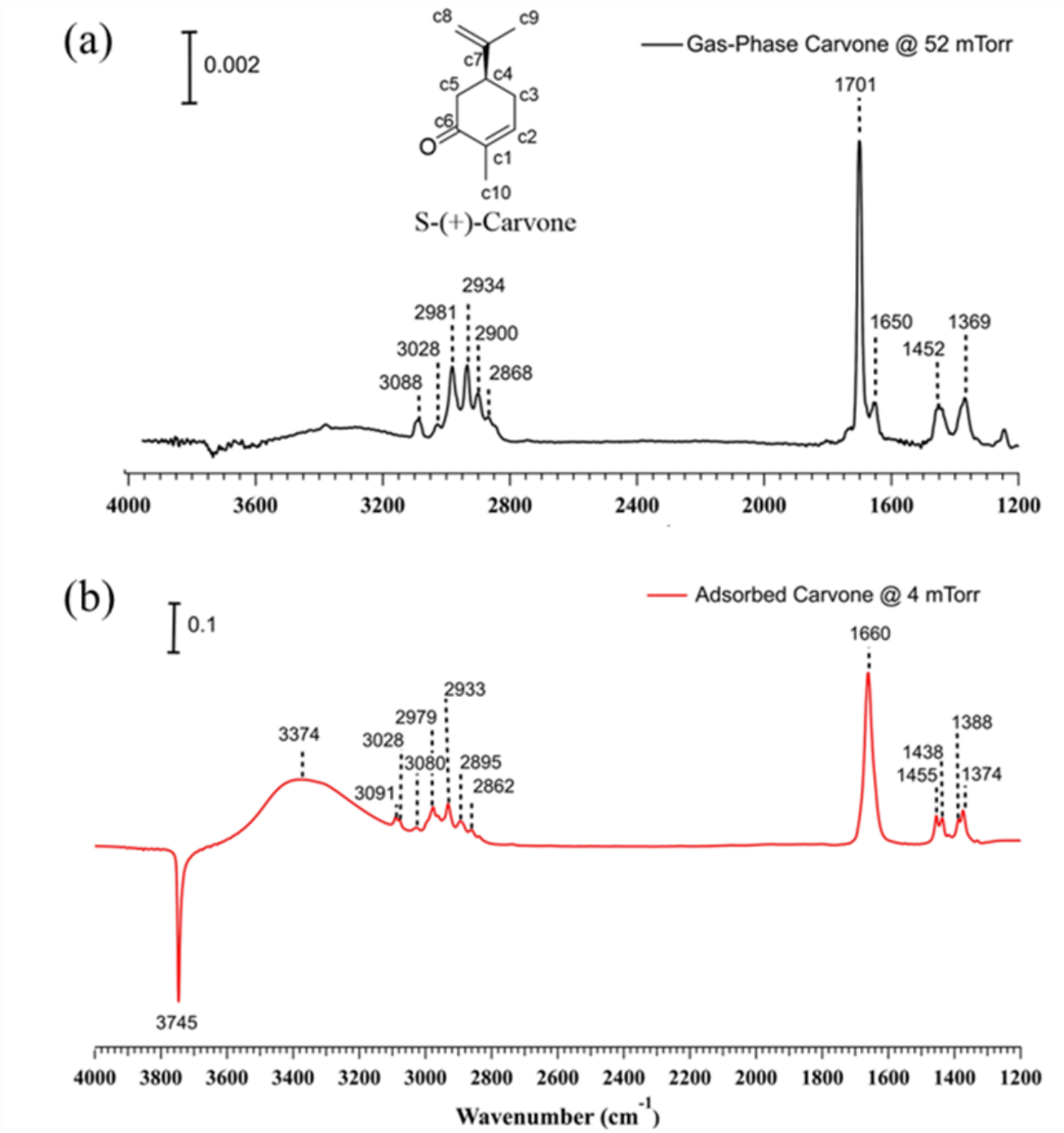

Figure 5.1: (a) FT-IR spectra of 52 mTorr of gas-phase carvone (black line) at 296 K. (scale bar = 0.002 absorbance units). (b) FT-IR absorbance spectra of carvone on SiO_2 surface at an equilibrium pressure of 4 mTorr under dry conditions. (scale bar = 0.1 absorbance units).

Figure 5.1b shows a negative peak at 3745 cm^{-1} and it is attributed to the loss of isolated Si-OH groups due to hydrogen bonding interactions. This results in a red shifted peak at 3374 cm^{-1}. A large band at 1660 cm^{-1} is observed for the coupling of C=O (ketone) and C=C

(alkene) stretching vibrations. Figure 5.2 shows the role of varying equilibirum pressure on the adsorption of carvone on the SiO_2 surface. A shoulder near 1683 cm^{-1} starts to form at 19 mTorr in the spectra. This shift towards higher wavenumbers will be discussed in detail in Section 5.3. Finally, figure 5.3 shows all the free isolated Si-OH surface sites can be bonded by the carvone at a low equilibrium pressure (4 mTorr).

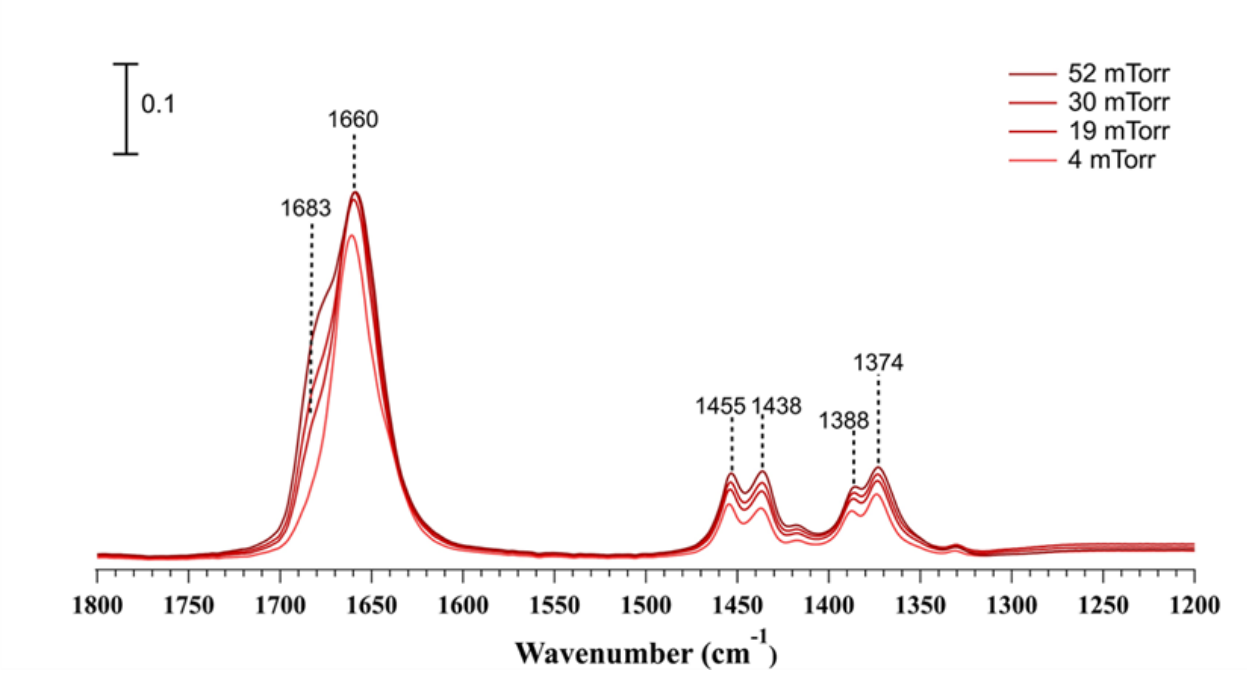

Figure 5.2: Absorbance spectra of carvone on SiO_2 as a function of pressure in the spectral range of 1200 to 1800 cm^{-1}. (scale bar = 0.1 absorbance units)

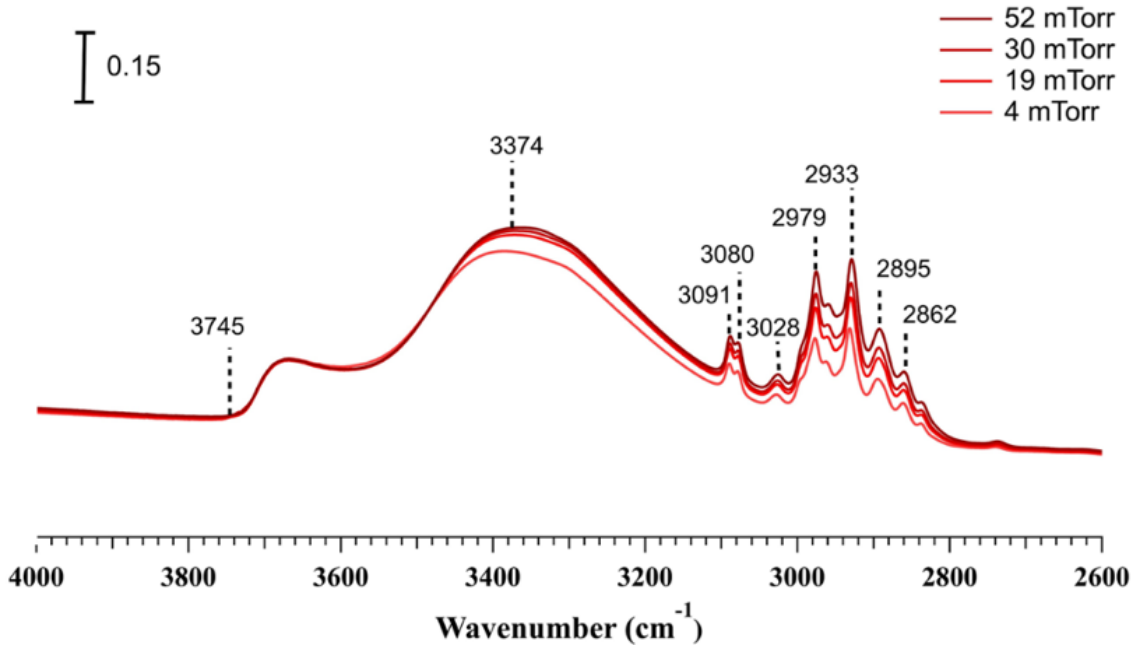

Figure 5.3: Absorbance spectra of carvone on SiO_2 as a function of pressure in the spectral range of 2600 to 4000 cm^{-1}. The peaks at 3745 cm^{-1} are flat starting at 4 mTorr, meaning there is no peak corresponding to the stretch of free isolated OH functional groups

In addition, the adsorption/desorption kinetics of carvone onto the hydroxylated SiO_2 surface at 2 mTorr and 4mTorr was measured. Previous literature suggests that carvone molecules may become blocked within small pores in porous silica leading to slow removal. [86] The pore volume of SiO_2 used in this study is 0.0061 $\frac{cm^3}{g}$ and the pore diameter is 17.1 Å. The kinetic modeling results can account for the presence of pores and is discussed in Section 5.3.

In addition, we can compare the relative desorption kinetics between limonene and carvone though a simplified first order analysis:

$$ln\frac{[VOC]_t}{[VOC]_{equ}} = -kt \tag{5.1}$$

As shown in Figure 5.4:

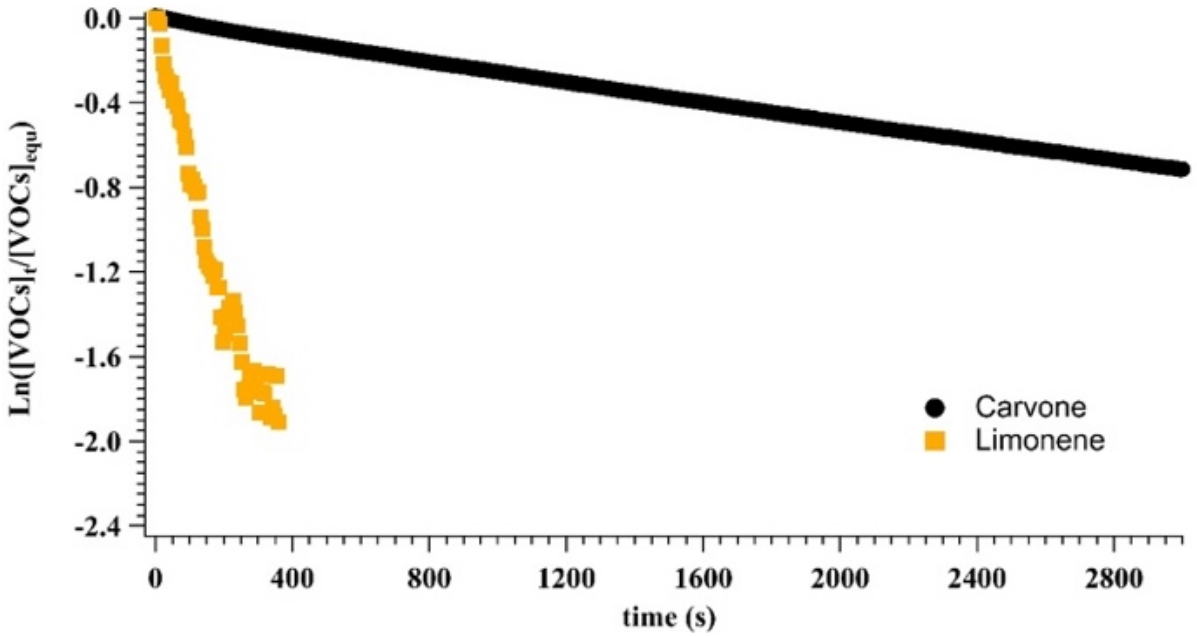

Figure 5.4: First order desorption kinetics for carvone (black solid circles) and limonene (yellow solid squares) at 4 mTorr from the SiO_2 surface under dry conditions. The desorption rates constants determine this way are $2.4 \times 10^{-4} \pm 4.8 \times 10^{-7} s^{-1}$ for carvone and $7.2 \times 10^{-3} \pm 1.4 \times 10^{-4} s^{-1}$ for limonene. This reveals that the desorption kinetics of carvone is 30 times slower than that of limonene.

The psuedo first order analysis of the desorption of both carvone and limonene reveals that the desorption kinetics of carvone is 30 times slower than that of limonene.

5.3.2 Kinetic Modeling Results

The K2-SURF model was used to model the temporal evolution of carvone on the SiO_2 surface at 2 mTorr and 4 mTorr, as shown in Figure 5.5. This modeling was done by our collaborators in the Shiraiwa lab. As shown in Figure 5.5, the SiO_2 surface model without pores does not accurately reproduce the experimental results.

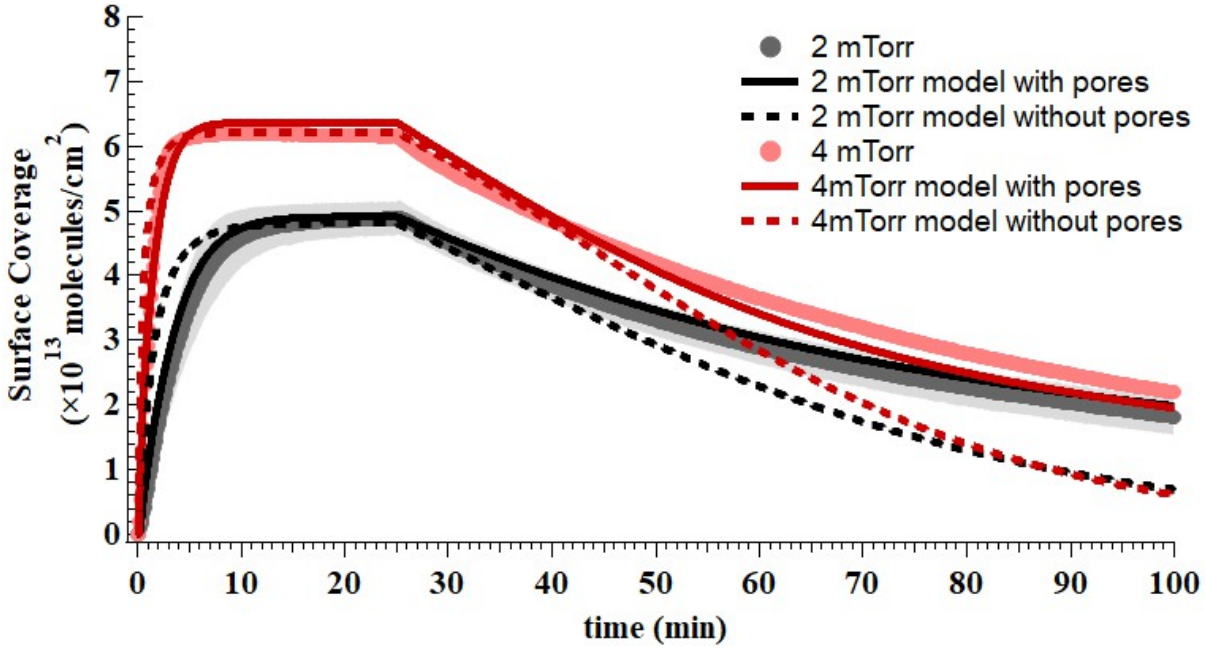

Figure 5.5: Temporal evolution of carvone adsorption on hydroxylated SiO_2 surface at an equilirbium pressure of 2 mTorr (black solid circle) and 4 mTorr (red solid circle) under dry conditions. Triplicate experiments were measured and the shadow represents one standard error. The SiO_2 surface was exposed to carvone at time t = 0 min. The adsorption process reached equilibrium at t = 3 mins for 2 mTorr and t = 10 mins for 4 mTorr. At time t = 25 mins, the desorption process was initiated by the evacuation of gas-phase carvone. The solid lines show the kinetic modeling results including the pore mechanism and the kinetic modeling results without the pore mechanism are shown in dashed lines.

To accurately reproduce the measurements, a mechanism with two different desorption sites is required with desorption occurring at a much slower rate from one site. This model is shown in the schematic in Figure 5.6 and these two sites represent non-pores and pores.

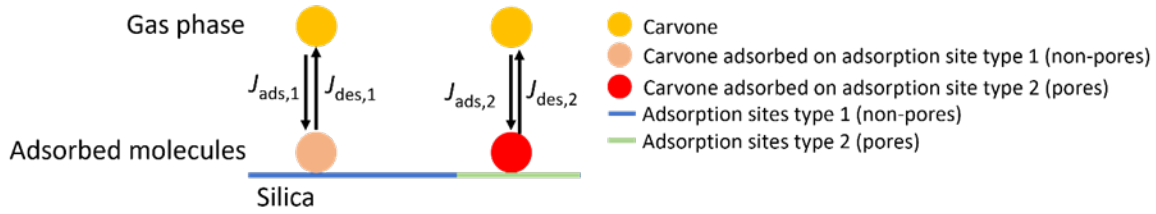

Figure 5.6: Schematic of the K2-SURF model for reversible adsorption of carvone on SiO_2 with two different adsorption sites cooresponding to pore and non-pore sites.

Carvone adsorbs and desobs rapidly from non-pore sites leading to the observed surface concentration pressure dependence at equilibrium, and slow desorption occurs when carvone becomes trapped within the pores. This is a departure from our study of limonene, but consistent with our study of 6-MHO, detailed in Chapter 7.

5.3.3 Computational Results

As stated previously, the silanol surface density of the SiO_2 surface used in our force field-based MD simulations was 4.7 OH nm^{-2}, which is the OH density of a glass surface. [22] Therefore, this resulted in surface 3-coordinated Si atoms. Our computational results show an unexpected interaction between the carvone molecule and SiO_2 surface, in the form of an association between the carvone oxygen atom and the 3-coordinated Si atoms. Note that while this association is not the predominant interaction between carvone and the surface, this oxygen silicon interaction, to our knowledge this has not been reported between indoor relevant organic molecules and SiO_2 surfaces. The MD simulations show the carvone molecule exists in two unique configurations, that can be described by the angle, θ, formed by carbon atoms 2C, 6C and the SiO_2 surface, as shown in Figure 5.7a and Figure 5.7b, respectively. The distribution of the $cos(\theta)$ from the last 10 ns of unbiased simulation is shown in Figure 5.7c.

While there is not a $cos(\theta)$ value directly corresponding to one interaction type, our simulation shows that at higher values of $cos(\theta)$, carvone often forms a hydrogen bond with the surface, as seen in Figure 5.7b. This is due to the fact that when $cos(\theta)$ is roughly equal to 1, the carvone ring is parallel to the surface, which is better suited for the carvone oxygen to form an approximate 180-degree angle with the OH group H atom and O atom on the SiO_2 surface. In addition, there is a second feature of the distribution of a softer degree of freedom where the carvone ring is upright with respect to the surface with a broad distribution of

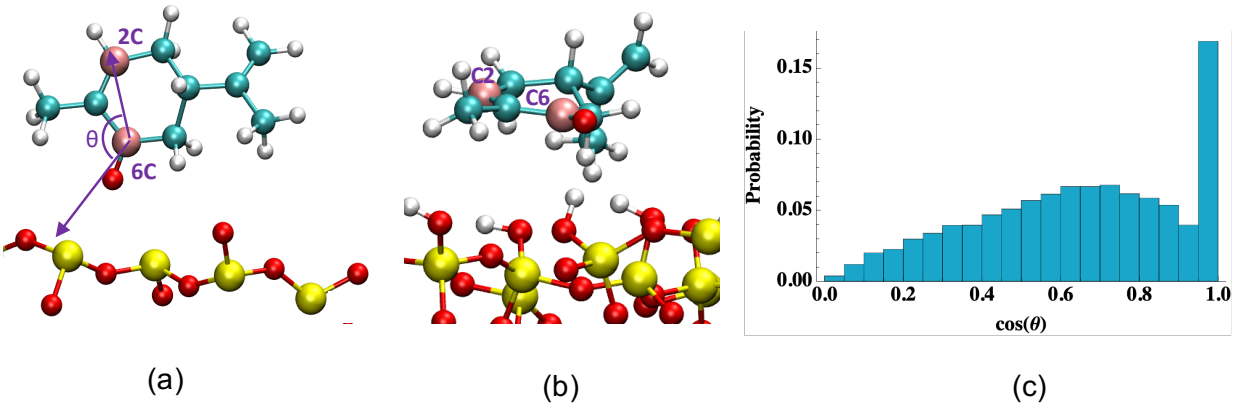

Figure 5.7: (a) Carvone molecular orientation most likely leading to oxygen silicon association. (b) Carvone molecular orientation most likely leading to hydrogen bond. (c) Distribution of $cos(\theta)$, where θ is the angle between carbon atoms 2C, 6C, and the SiO_2 surface described in Figures 5.7a and 5.7b. A $cos(\theta)$ of 1 indicates the ring is parallel to the surface and a $cos(\theta)$ between 0.25 and 0.80 indicates the carvone right is upright on the surface. Molecular snapshots come from classical MD simulations. Oxygen atoms are in red, Si atoms are in blue, hydrogen atoms are white, carbon atoms are teal, and the carbon atoms used to calculate θ are shown in pink.

$cos(\theta)$ that has a maximum at $cos(\theta) \sim 0.6$. The details of these two interactions observed in the force field-based MD simulations are described in Table 5.1.

Type of Interaction	Atom partial charge (e)	Fraction of trajectory	Average interaction length (Å)	Δ H (kJ/mol)
Hydrogen Bond	H atom: + 0.417	23%	2.74 ± 0.14	61.4 ± 1.1
Oxygen-silicon association	Si atom: +1.100	76%	2.89 ± 0.16	66.0 ± 1.9

Table 5.1: Details on the two types of carvone-silica interactions observed in force field-based MD simulations.

As a note, the hydrogen bond interaction length is the carvone O atom to surface O atom distance, and the oxygen silicon association interaction length is the carvone O atom to Si atom distance. One reason we detect such a high fraction of the trajectory corresponding to the oxygen silicon association is due to the more positive partial charge of the Si atom. In

addition, the carvone ring creates steric hindrance when forming hydrogen bonds with the SiO_2 surface. We suggest the slightly higher ΔH value for carvone when in an oxygen silicon association may be due to the stronger electrostatic interactions between surface and carvone molecule, as shown by the more positive partial charge of the Si atom. The calculated ΔH values are shown in Figure 5.8.

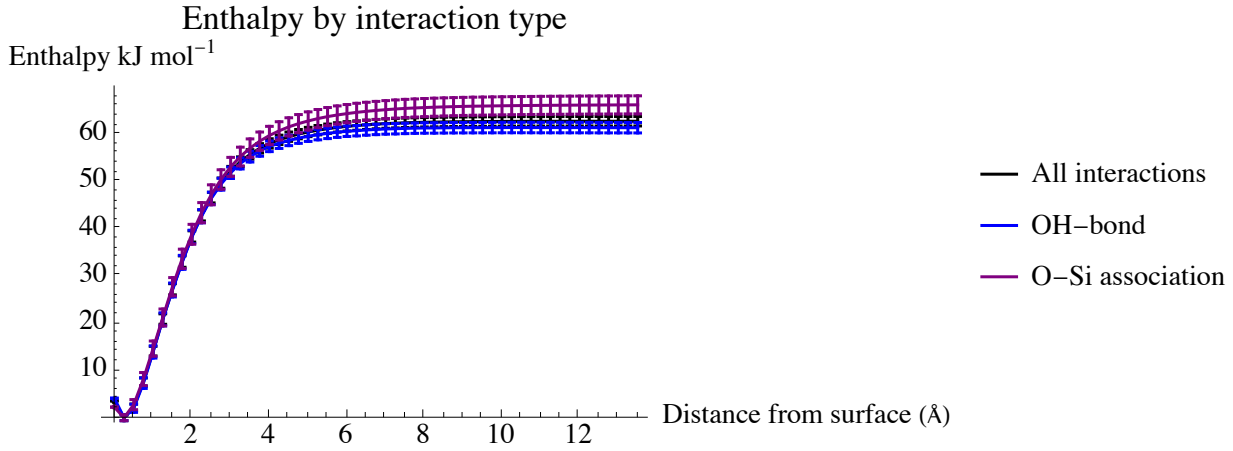

Figure 5.8: Enthalpy as a function of the distance of the carvone molecule from the SiO_2 surface from 154 initial configurations with 108 configurations showing a hydrogen bond interaction and 48 showing an oxygen-silicon association. Enthalpy for each interaction type are also shown in blue and purple based on starting configurations with hydrogen bonding and oxygen-silicon associations, respectively.

For the kinetics model discussed in Section 5.4, the average of all 154 ΔH calculations was used. In addition to the hydrogen bonding and oxygen silicon associations discussed, π-hydrogen bonds were detected in 10% of the classical MD trajectory. These occurred slightly more often when the carvone molecule was in an oxygen-silicon association. Our π-hydrogen bond calculations revealed that the endocyclic π bond was unable to form a π-hydrogen bond with the surface due to the close proximity to the carvone oxygen atom.

Interestingly, we find the oxygen silicon association is not an artefact of the force field, but rather a plausible mechanism for the adsorption of carvone on the SiO_2 surface. As shown in Figure 5.2, as the pressure of carvone is increased, there is a resulting left shifted shoulder

appearing at 1683 cm^{-1}. To validate that carvone oxygen silicon interaction observed in the force field-based MD simulation, we performed a 16 ps AIMD simulation of carvone on a partially dehydroxylated surface, with two 3-coordinated Si atoms. During this simulation, we determined that 16% of the time, the carvone oxygen is in an oxygen silicon association.

Figure 5.9 shows the calculated oxygen power spectra of carvone on a fully hydroxylated surface and on a partially dehydroxylated surface between 1700 cm^{-1} and 1500 cm^{-1}. The complete oxygen power spectra are reported in Figure 5.10. Although the peak position but not the intensities are comparable to experimental data, it is reasonable to compare trends in the AIMD power spectra to trends in the experimental FT-IR spectra.

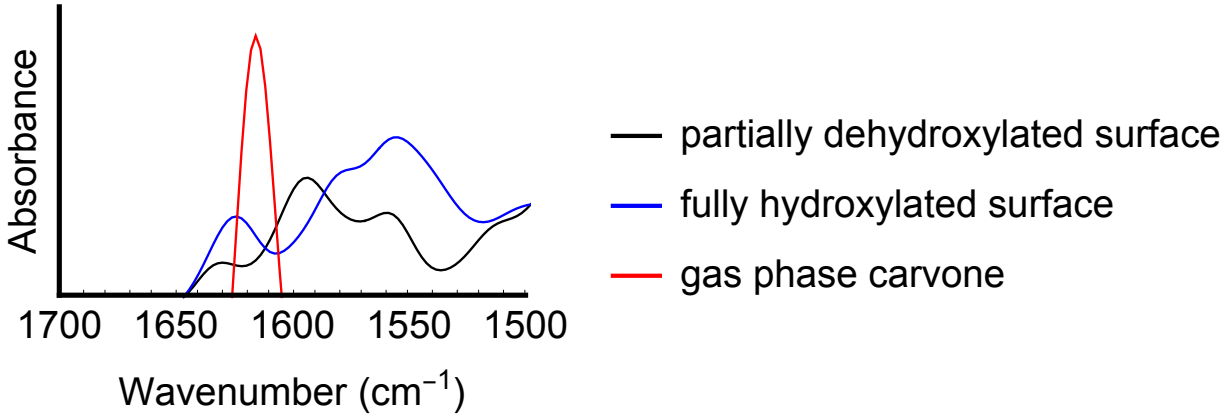

Figure 5.9: Oxygen power spectra showing the slight red shift in the $\sim$ 1600 cm^{-1} wavenumber in the AIMD simulation of carvone in the gas phase compared to the AIMD simulations of both carvone on a partially dehydroxylated SiO_2 surface with two 3-coordinated silicon atoms and carvone on a fully hydroxylated surface where the carvone molecule can only form hydrogen bonds with the surface.

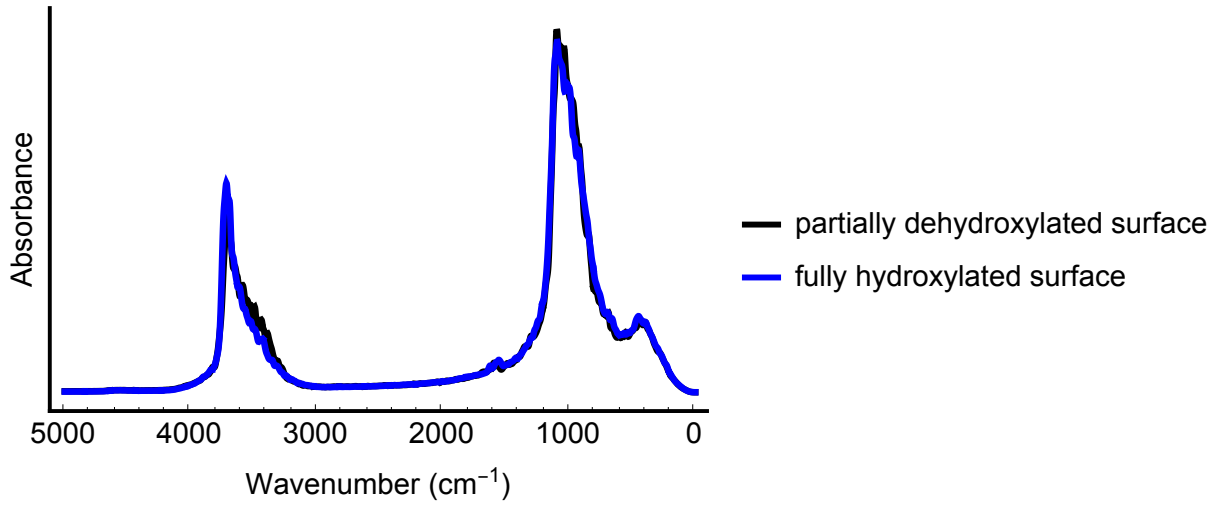

Figure 5.10: Full oxygen power spectra of carvone on the partially dehydroxylated surface and the fully hydroxylated surface.

Our experimental spectra in Figure 5.2 indicates that the isolated Si-OH stretch is not apparent when 4 mTorr of carvone is present. This suggests that all of the OH groups on the surface are engaged in hydrogen bonds with carvone molecules. Therefore, we propose the mechanism of carvone adsorption on the SiO_2 surface is as follows: first carvone adsorbs to the surface via dispersion forces and hydrogen bonding to the OH groups on the SiO_2 surface; second, once all the available OH groups are occupied in hydrogen bonds, oxygen silicon associations form, as indicated by the increasing shoulder at 1683 cm^{-1} in the experimental measurements.

While the AIMD simulations validate that the red shifted shoulder in the ∼1600 cm^{-1} range is the result of an oxygen silicon association between the carvone molecule and SiO_2 surface, it is also relevant to investigate this interaction at a higher level of electronic structure theory. To this end, the characterization of two unique configurations of carvone on the SiO_2 surface has been performed using electronic structure calculations at the M06-2X/6-311G(d) level of theory. First, geometry optimizations to determine stationary points for carvone engaging in both surface interaction types were performed. The resulting configurations are depicted

in Figure 5.11, with interaction distances (carvone O - silica O for the hydrogen bond and carvone O - silica Si for the oxygen silicon association) indicated on the images. Second, counterpoise corrected binding energies are reported below the optimized structures.

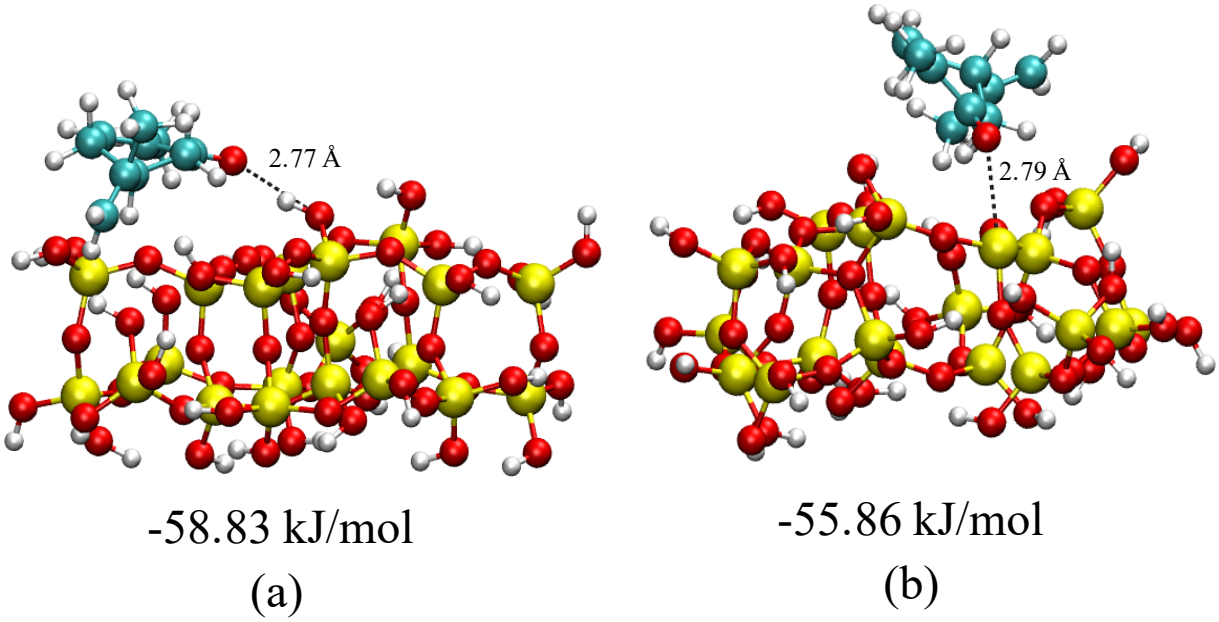

Figure 5.11: (a) Optimized geometry for carvone adsorbed to a fully hydroxylated SiO_2 surface via a hydrogen bond. (b) Optimized geometry for carvone adsorbed to a partially dehydroxylated SiO_2 surface via an oxygen silicon association.

The optimized geometry of carvone adsorbed to the surface via a hydrogen bond results in an oxygen - oxygen distance of 2.77 Å. For the oxygen silicon association, the optimized geometry results in an oxygen silicon distance of 2.79 Å. This close interaction distances corroborates the strong association between the carvone oxygen and Si surface atom we observed in both our force field-based MD and AIMD simulations. In addition, the ring angle defined in Figure 5.6 derived from the optimized geometries is consistent with the conclusions of our MD simulations, as the measured $cos(\theta)$ of carvone in the hydrogen bond interaction is 0.99, whereas the measured $cos(\theta)$ of carvone in the oxygen silicon association is 0.69. The binding energy for the oxygen silicon association is only slightly lower than the hydrogen bond interaction, which is consistent with our proposed mechanism of adsorption,

and also confirms that an oxygen silicon association is a pathway for a small organic ketone containing molecule to stick on the SiO_2 surface.

To investigate the chemistry responsible for an oxygen silicon association, the electrostatic potential (ESP) of the two stationary points are depicted on an 0.07 e/a.u^3 isodensity surface in Figure 5.12. Figure 5.12a shows the ESP map of the hydrogen bond interaction, where the electrostatic potential is shared between the surface and the carvone molecule, highlighting the strong non-covalent interactions associated with hydrogen bond formation. In the oxygen silicon association, as shown in Figure 5.12b, there is a small gap in the electrostatic potential between the surface and the carvone molecule at the 0.07 e/a.u^3 isodensity level, suggesting a much weaker role of non-covalent interactions in this association. Due to the fact that the ESP plots do not describe the stability of the oxygen silicon association, we can surmise that non-covalent interactions are not fully responsible for the high binding energy calculated for this association. We suggest that the lone pairs in the oxygen atoms may be able to interact with the electropositive Si atom; however, ongoing investigations are underway to fully characterize this interaction.

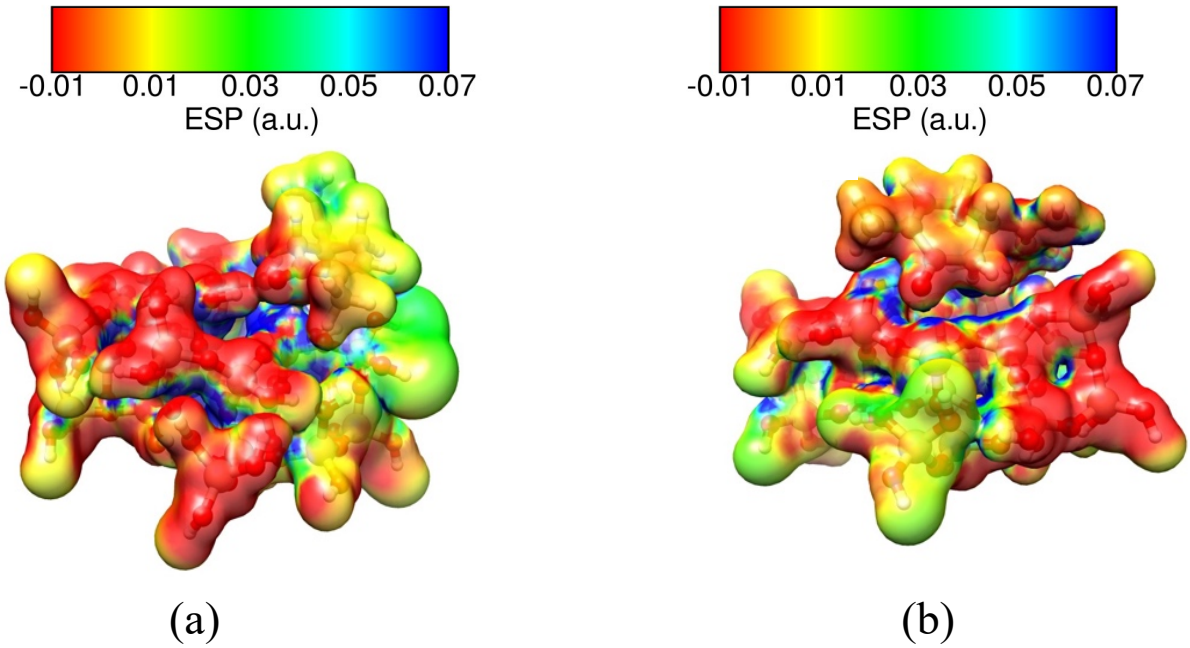

Figure 5.12: (a) Electrostatic potential for carvone adsorbed to the fully hydroxylated SiO_2 surface through the hydrogen bond mechanism. (b) Electrostatic potential for carvone adsorbed to the partially dehydroxylated SiO_2 surface through the oxygen silicon association mechanism. Both electrostatic potentials are plotted on an isosurface density of 0.07 e/a.u^3.

We have also used force field based MD simulations to calculate the potential of mean force (PMF) or free energy profile for the desorption of carvone from the SiO_2 surface, as shown in Figure 5.13. We have placed the PMF vertically so that the minimum is at zero free energy. We estimate the desorption free energy is 41 kJ/mol. In order to determine the type of interactions present (oxygen silicon association vs hydrogen bond) during the desorption of carvone from the surface, we have applied a color function to visualize the fraction of each PMF window where the carvone oxygen forms and oxygen silicon association, as shown in Figure 5.13b.

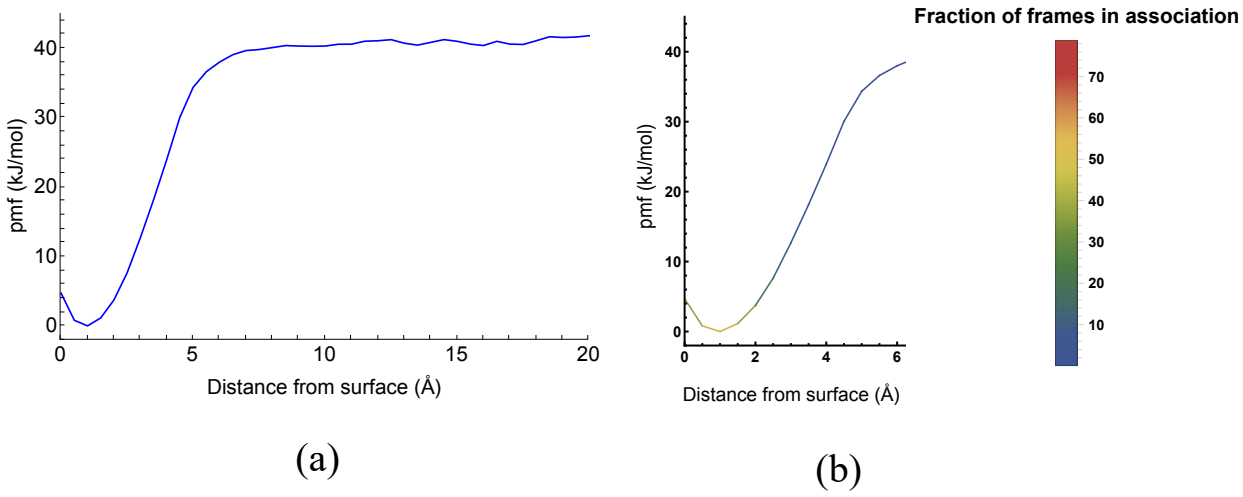

Figure 5.13: (a) Potential of mean force (PMF) for the desorption of carvone on SiO_2 surface. (b) Fraction of the 10 ns window where the carvone oxygen was in an oxygen silicon association as a function of the PMF.

The color function reveals an intriguing trend; at the most stable point of the desorption free energy, only 30% of the 10 ns simulation window showed that carvone was adsorbed to the surface via an oxygen silicon association, but at points near the minimum, 70% of the 10 ns simulation showed that carvone was adsorbed to the surface via an oxygen silicon association. The fact that at the most stable point there are mostly hydrogen bonds is consistent with our proposed mechanism of adsorption where the dominant interaction is hydrogen bonding.

Once the carvone molecule has passed the minimum, and the carvone molecule is at least 4 Å from the surface, extending the color function is not relevant. In order to make contact with the K2-SURF kinetic model, we have calculated the desorption enthalpy for carvone on the SiO_2 surface, as reported in Table 1 and shown in Figure 5.8. We have also used a calculated surface accommodation coefficient of 0.99. Although these calculated desorption enthalpies cannot alone be used to replicate the experimentally determined desorption lifetime, the ΔH value is used to model the non-pore desorption of carvone. In addition, we find the trend in ΔH values is consistent with our previous and current studies of indoor relevant organic

molecules on the SiO_2 surface. [53, 87]

5.4 Conclusions

This study investigated the complex interactions of carvone, an indoor relevant organic molecule, on a hydroxylated SiO_2 surface using infared spectroscopy, force field-based and *ab initio* MD simulations, electronic structure calculations, and the K2-SURF kinetic model. The experimental desorption kinetics indicate a long desorption lifetime for carvone on the SiO_2 surface, approximately 30 times longer than that of limonene. This finding agrees with our previous work studying oxygenated organic compounds (Chapter 4) which form stronger interactions with the SiO_2 surface compared to limonene and other limonene isomers (Chapter 3). MD simulations show that the adsorption of carvone on the SiO_2 surface is not only driven by the formation of hydrogen bonds between the carvone oxygen and Si-OH sites, but also interactions between the carvone oxygen and 3-coordinated Si atoms. Our kinetic model suggests that pore sizes need to be considered in controlling the desorption rate of carvone from the porous particle surface. In conclusion, our integrated approach for studying carvone provides a deep understanding of these surface interactions. The results reported herein showcase the potential of a multifaceted approach to indoor chemistry to provide unique insights into the partitioning of gases in indoor environments.

Chapter 6

Interactions of Limonene and Carvone on Titanium Dioxide (TiO_2) Surface

6.1 Background

While this dissertation has primarily discussed the interactions of indoor relevant organic compounds on SiO_2 surfaces, we have also investigated TiO_2 in the rutile (110) crystal structure, which is another indoor relevant surface. TiO_2 poses a unique challenge for computational chemistry, as our understanding of TiO_2 surfaces is much less refined when compared to that of SiO_2. For instance, even in vacuum, we are unable to determine the true state of surface hydroxylation of TiO_2. In addition, as of writing, there is still an outstanding debate over how to model the interactions of water on the TiO_2 surface in a simulation, to either represent the water via a molecular or dissociative association on the surface. [88, 89, 90, 91, 92] As described in detail in this chapter, we have constructed two TiO_2 crystal surfaces for classical MD simulations, to represent the extrema of a real world TiO_2 surface. We have constructed a non-hydroxylated TiO_2 surface with surface Ti atoms and

free water molecules, and a fully hydroxylated TiO_2 surface with all surface Ti atoms capped with OH groups. This has lead to some discrepancies between the heterogeneous surface as described by our experimental collaborators, but this also has lead to the chance to create an intriguing study in how to reconcile theory and experiment. Our studies on TiO_2 are described in this and the following chapter.

Titanium dioxide (TiO_2) is relevant for the indoors for two considerations. First, latex paint surfaces contain 38% by volume TiO_2 [93], making TiO_2 an abundant part of the indoor environment, and second TiO_2 can be used to clean the air. [94]

TiO_2 can be used to clean the air as the semiconductor material used in photocatalytic oxidation, which is a popular cost-effective method that mineralizes indoor pollutants at the ppb level using solar light irradiation without any chemical additives. TiO_2-based self cleaning materials such as coated glasses and tiles, are used both in indoors and outdoors on walls, floors, rooftops, and facades, and in public places like hospitals and public restrooms. [94] However, there may be unexpected consequences of using these indoor air cleaning processes. [95] The adsorption and desorption of air pollutants on the surface of TiO_2 are key steps in these heterogeneous photocatalytic oxidation techniques, and desorption is a critical step to restore the active surface catalytic sites of air cleaning products. [96, 97]

To study the interaction mechanisms of indoor relevant organic compounds with TiO_2 surfaces is essential to not only potentially enhance photocatalyst performance but also to develop a deeper understanding of the indoor environment. In this case, it is vital to understand the role of % RH on the adsorption of these compounds, given the complexity of the TiO_2 surface. In this study, we will discuss how two previously studied indoor relevant organic compounds, limonene and carvone, interact on TiO_2 surfaces. However, as TiO_2 is a new surface, it is relevant to briefly survey previous research of the adsorption of volatile organic compounds on TiO_2, which will be detailed below.

There are two general modes for the adsorption of volatile organic compounds on TiO_2: a weak physisorption bonding mode with surface Ti-OH groups and a stronger chemisorption bonding mode on Ti^{4+} atoms or reduced Ti^{3+} sites near oxygen vacancies. [98, 99] As mentioned at the start of this chapter, accounting for these two different surface interaction requires two TiO_2 surfaces, as in order to have Ti-OH groups, a fully hydroxylated surface is required and to have surface Ti atoms, a non-hydroxylated surface is required. It has also been shown that benzene and toluene can be adsorbed on a hydroxylated TiO_2 via Ti-OH...π electron interaction and chlorobenzene can be adsorbed via both a Ti-OH...π electron interaction and an additional Ti-OH...Cl hydrogen bond. In the same work, it was shown benzene, toluene, and chlorobenzene, can adsorb to a non-hydroxylated surface via Ti^{4+}...π interaction. [100] In addition, it has been shown pyruvic acid adsorbs on the TiO_2 surface via interactions between the carboxylic acid group and surface hydroxyl groups. [101] The degree of surface interaction strengths between VOCs and TiO_2 depends on the relative bonding energies of the hydrogen bond and it is expected hydrogen bonds will be stronger than π-hydrogen bonds. This implies that polar VOCs will be more strongly adsorbed to the TiO_2 surface. [102, 103, 104]

As discussed in Chapter 2, to best model the indoor environment, careful detail to variations in % RH should be considered. On the TiO_2 surface, water can form competitive adsorption against VOCs. [105] One example, using a different crystal TiO_2 surface, anatase, shows there is a decrease of 50% and 30% for the adsorption of toluene and 2-propanol at 60% RH compared to dry conditions, and this was found to be a result of direct replacement of water. [106]

Therefore, I have hopefully set the stage to study TiO_2, a rather complicated yet extremely relevant indoor surface.

6.2 Simulation Protocols

As this is a novel surface for our lab to study, and quite a complicated one, the simulation protocols have been split up into two sections, one detailing the classical MD simulations and one detailing the *ab initio* MD (AIMD) simulations. For both simulation methods, a 110 rutile TiO_2 unit cell was replicated in the x, y, and z directions to create the initial structure. [107]

6.2.1 Classical Molecular Dynamics Simulations

Force field-based MD simulations were used to investigate the adsorption of limonene and carvone on TiO_2 surfaces. Due to the outstanding debate over the nature of interactions of water on the TiO_2 surface, force field-based MD simulations for both a non-hydroxylated TiO_2 surface with surface Ti atoms and free TIP3P water molecules and a fully hydroxylated TiO_2 surface with no surface Ti atoms have been prepared. A 35 x 40 x 21 $Å^3$ TiO_2 slab was created and 77 Å of vacuum was placed separating the upper and lower surfaces in the z direction. From this initial surface with 720 Ti atoms and 1440 O atoms, the non-hydroxylated and hydroxylated TiO_2 surfaces were produced. For clarity, we can consider all TiO_2 surfaces consisting of two parts, the froze core Ti and O atoms and the surface atoms. In the case of the non-hydroxylated surface, the surface atoms are the bridging oxygen atoms and 5-coordinated Ti atoms. In the case of the hydroxylated surface, all atoms on the top and bottom of the surface were hydroxylated, thus the surface atoms are the surface OH groups. To investigate the role of % RH, TIP3P [41] water molecules were added to both sides of the TiO_2 surface, which in the text we will refer to as the 0.5 monolayer and 1 monolayer systems. The 0.5 monolayer system was represented by a total of 204 water molecules, corresponding to the number of bridging oxygen atoms in the non-hydroxylated surface. The 1 monolayer system was represented by 408 water molecules. The force field

produced by Brandt et al. was used for the non-hydroxylated surface. [108]

For the hydroxylated surface, the nonbonded parameters were set to 0 for hydrogen and the partial charge of all hydrogen atoms was set to $+0.44175e$. The O-H group oxygen partial charge was set to -0.80e to ensure a neutral surface. During the course of the simulation, all bulk atoms were frozen, and all surface atoms were allowed to move freely. There were small distortions of the TiO_2 surface; however, the general structure of the TiO_2 crystal was retained. For water, TIP3P water was used [41] and the limonene and carvone force-field details can be found in Chapters 2 and 5. As in the previous chapters, all classical molecular dynamics simulations were done with the LAMMPS [42] software package. The equations of motion were integrated using the velocity Verlet algorithm with a 1 fs time step [43]. Electrostatic interactions were evaluated directly up to a cutoff of 12 Å and with a particle-particle-particle mesh solver with a relative accuracy of 10^{-6}. [44] The simulation temperature was maintained at 300 K using a Nose-Hoover thermostat with a relaxation time of 100 fs. [45] As in previous chapters, umbrella sampling was used to calculate the free energy profile for the desorption of limonene and carvone from the TiO_2 surface. The initial coordinates of each adsorbate on TiO_2 were taken after 25 ns of simulation time, and the center-of-mass of the adsorbate to the TiO_2 surface was used as the reaction coordinate. The process was divided into a variable number of windows depending on the adsorbate. For limonene, 22 windows in 0.50 Å increments was sufficient, but for carvone, 0.25 Å increment windows were used. A harmonic restraining potential of 10 kcal mol^{-1} Å^{-2} was applied in each window. Each free energy profile was generated from 30 ns or longer biased trajectories for each PMF window using the WHAM scheme. [26]

In order to connect our study of TiO_2 to a kinetic process model, the surface accommodation coefficient of limonene and carvone on the TiO_2 surface was estimated by running MD trajectories of 100 ps that were initiated with the limonene and carvone molecules 5 Å above the TiO_2 surface, with the center-of-mass velocity vector directed towards the surface. This

procedure was repeated for 50 randomly positioned molecules. The surface accommodation coefficient was estimated to be the fraction of trajectories that resulted in the molecule adsorbed to the surface.

In addition, the desorption enthalpies for carvone and limonene were calculated from the various TiO_2 surfaces using the finite-difference temperature derivative of the potential of mean force (PMF) at 280, 300, and 320 K to calculate the enthalpy of desorption, as described by Wang et al. [109] The PMF was calculated for the desorption from each TiO_2 surface at three temperatures, 280, 300, and 320 K. This was done for both non-hydroxylated and hydroxylated surfaces at 0 ML, 0.5 ML and 1 ML of H_2O. These results provided agreement with experimental desorption enthalpy of water, of 92.66 kJ/mol, compared to the experimental literature value of ∼100 kJ/mol for the desorption enthalpy of water on a hydroxylated TiO_2 surface, but due to the complexity of the real world surface, failed to provide an adequate estimation for limonene and carvone required by the kinetic model.

Instead, to obtain accurate desorption enthalpy values, the interaction energy of 15 "snapshots" from the AIMD simulations were used. These values allowed for a realistic implementation of the kinetic model, while still retaining consistent with the force field calculations, as shown in the following results section, that the force field calculation and AIMD calculations show the same trends in interaction energy and the same types of surface interactions. These results are discussed separately, in section 6.3.4.

6.2.2 *ab initio* Molecular Dynamics Simulations

For the AIMD simulations, three surfaces have been prepared, a non-hydroxylated TiO_2 surface, a non-hydroxylated TiO_2 surface with 4 water molecules between the adsorbate and the surface, and a fully hydroxylated TiO_2 surface (with no surface Ti atoms). For all systems, a 10 ps AIMD simulation at 300 K with a time step of 0.5 fs was performed. At

300 K, some of the O-H groups of the fully hydroxylated surface underwent dissociations during the course of the AIMD simulation. The PBE [110] exchange-correlation functional with the DZVP-MOLOPT-SR-GTH[49, 50] basis sets and the GTH pseudopotentials in the QUICKSTEP [30] module of the CP2K package were used. A SCF convergence criterion of 10^{-6} (a.u.) with the orbital transformation scheme [51] and DIIS minimization [111] were used in each simulation. All systems were placed in orthorhombic boxes under periodic boundary conditions in the x and y directions with the z direction normal to the TiO_2 surface. The AIMD simulation cells had sizes of 15.960 x 12.638 x 36.821 $Å^3$ and for the slightly larger system for carvone on the non-hydroxylated surface with 4 water molecules, the cell size was 15.091 x 16.437 x 36.821 $Å^3$. In the case of the hydroxylated surface and non-hydroxylated surface with water molecules, only the top of the surface was either hydroxylated or added with water molecules, to save computational time. In addition, during the course of the simulation, the bottom half of the TiO_2 system was frozen. The power spectra were calculated the same way as described in Chapter 2.

6.2.3 Surface Analysis Techniques

In the hydroxylated surface, two forms of hydrogen bonding were considered, π-hydrogen bonds formed between carbon $C_{sp}{}^2$ atoms and the TiO_2-OH surface for both limonene and carvone, and hydrogen bonds formed between the carvone oxygen atoms and TiO_2-OH surface. To calculate these hydrogen bonding probabilities a similar methodology as described in earlier chapters has been used. Hydrogen bonds were defined to be present if the distance between donor and acceptor was < 3.5 Å and the angle between acceptor, donor H, and donor O was within 120 to 180° for both types in hydrogen bonds. Additionally, in systems with free water molecules, π-hydrogen bonds between $C_{sp}{}^2$ centers and water molecules, as well as hydrogen bonds between the carvone oxygen atom and water were measured in the same way as described above.

6.3 Results

Herein, I will detail the experimental results as measured by Hanyu Fan, with her permission. As this is a novel system, we have paid great attention to the strong connections between theory and experiment. Because of this, a large portion of this chapter will include her detailed work.

6.3.1 Experimental Results

Figure 6.1(a) shows FT-IR absorbance spectra of limonene adsorbed on TiO_2 as a function of varying pressure at 297 ± 1 K under dry conditions (<1% RH). The observed IR absorption band frequencies are close to gas-phase limonene, as shown in Figure 6.2. The absorption bands at 3085, 3074, 3010 cm^{-1} are for the C-H $C_{sp}{}^2$ stretching motion from the alkene and ring; the bands at 2968, 2922, 2860, and 2838 cm^{-1} are for the C-H $C_{sp}{}^3$ stretching motion The 1644 cm^{-1} band is assigned to the C=C stretching vibration of the vinyl group and in the ring. The absorptions observed at 1454, 1439, and 1378 cm^{-1} for CH_3 and CH_3 bending vibrations motion, respectively.

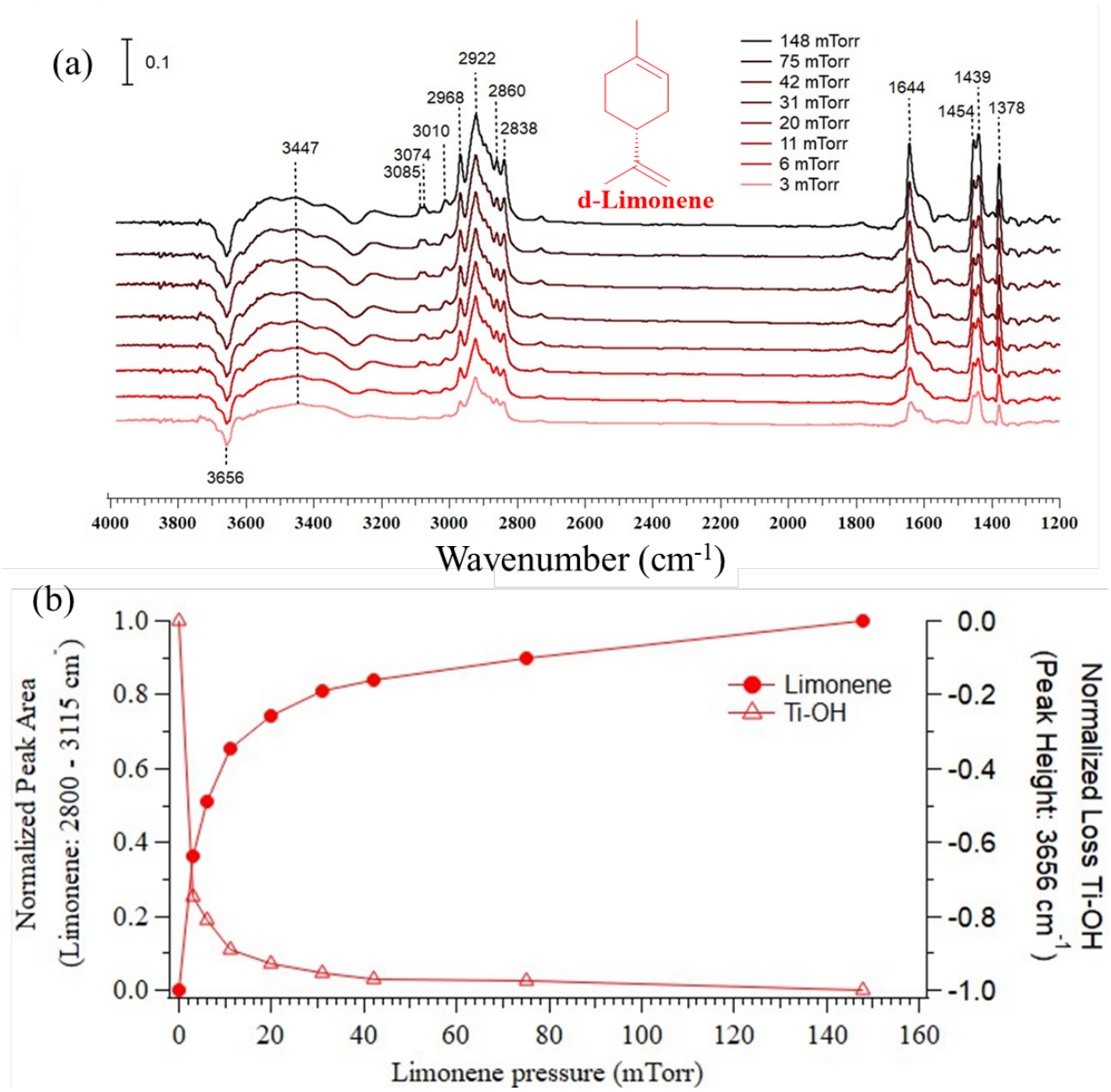

Figure 6.1: (a) FT-IR spectra of limonene adsorbed on TiO_2 surface under dry conditions (<1% RH) as a function of limonene pressure in the spectral range extending from 1200 to 4000 cm^{-1} (scale bar = 0.1 absorbance units). The equilibrium pressures increase from the light red to black spectra: 3, 6, 11, 20, 31, 42, 75, and 148 mTorr. (b) The ordinate plots the normalized integrated peak area of limonene in the spectral region from 2800 to 3115 cm^{-1} as function of limonene pressure (mTorr), the right ordinate plots the normalized peak height of the loss of Ti-OH function groups at 3656 cm^{-1}.

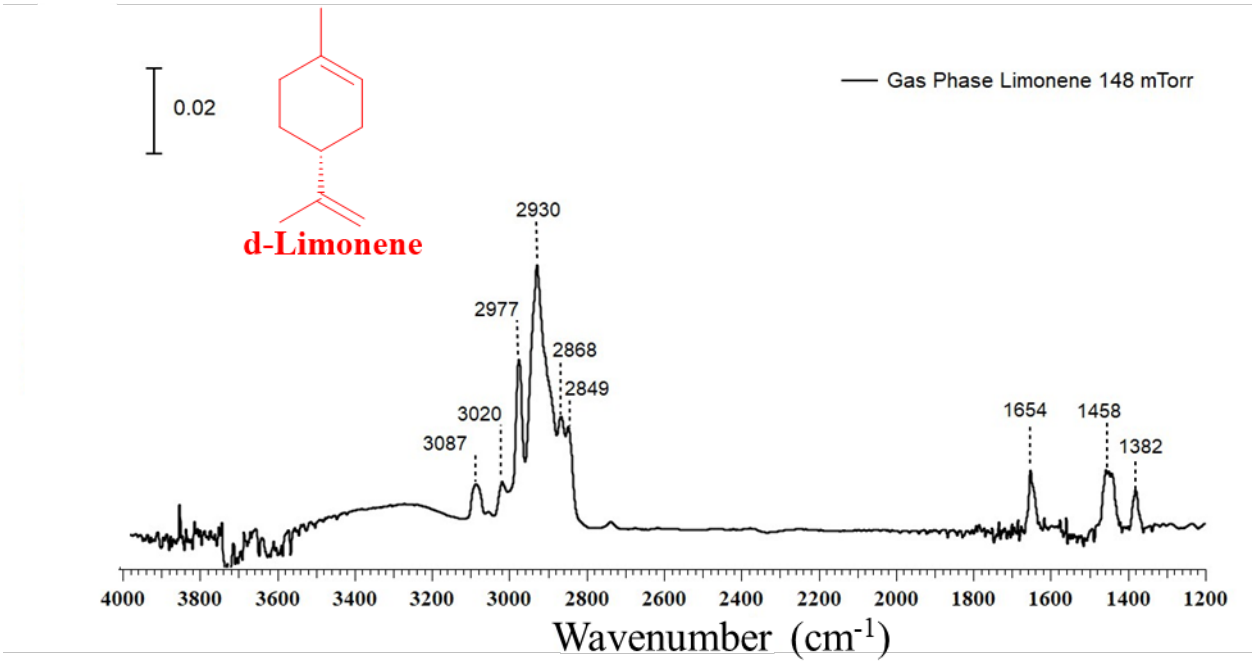

Figure 6.2: (a) FT-IR spectra of 148 mTorr of gas-phase limonene at 296 K in the spectral ranges extending from ca. 1200 to 4000 cm^{-1} (scale bar = 0.02 absorbance units). The modes are assigned as follows: 3087, 3020 cm^{-1} for the C-H $C_{sp}{}^2$ stretching motion from alkene and ring, respectively; 2977, 2930, 2868, 2849 cm-1 for C-H $C_{sp}{}^2$ stretching motion; 1654 cm^{-1} for C=C bond stretching vibrations; 1458, 1382 cm^{-1} for CH_3 and CH_2 bending vibrations motion, respectively.

The negative peak at 3656 cm^{-1} is attributed to the loss of Ti-OH groups due to the hydrogen-bonding interactions with limonene, as broad peak centered at $\sim$ 3447 cm^{-1} grows in with increasing limonene pressure. Figure 6.1(b) displays the integrated absorbance of the C-H stretching region (ranging from 2800 to 3115 cm^{-1}) and the loss of Ti-OH functional groups peak height (3656 cm^{-1}, right ordinate) as function of limonene pressure. There are no increases in the amount of the adsorbed limonene after 60 mTorr due to the lack of free Ti-OH functional groups present on TiO_2 surface. The desorption kinetics of limonene from the TiO_2 surface is about 2 times slower than that from the SiO_2 surface.

Figure 6.3(a) shows the IR absorbance spectra of carvone on the TiO_2 surface at equilibrium pressures of 2, 8 and 18 mTorr under dry conditions. The IR spectra shows that carvone

adsorbs to the TiO_2 surface via hydrogen bonding as shown by the loss of Ti-OH groups at 3656 cm^{-1} and the red-shifted broad peak at 3362 cm^{-1}. The observed IR surface absorption band frequencies are in agreement with the gas-phase carvone vibrational frequencies, as shown in Figure 5.1, except for the shifts in the spectral range extending from ca. 1560 to 1720 cm^{-1}.

The absorption bands at 3086, 3074 cm^{-1} and 3021 cm^{-1} are for the C-H $C_{sp}{}^2$ stretching motion from alkene and ring; the bands at 2968, 2927, 2893, and 2857 cm^{-1} are for the C-H $C_{sp}{}^3$ stretching motion; the bands at 1453, 1435 and 1378, 1373 cm^{-1} are for CH_3 and CH_2 bending vibrations motion, respectively; and the big broad band at 1648 cm^{-1} is attribute to the coupling of C=O (ketone) and C=C (alkene) stretching vibrations. As shown in Figure 6.3(b), there is a growth of new band at 1683 cm^{-1} starting at 8 mTorr.

Figure 6.3(c) displays the integrated peak area of adsorbed carvone at 1648 cm^{-1} (ranging from 1560 to 1720 cm^{-1}) and the loss of Ti-OH functional groups peak height at 3656 cm^{-1} (right ordinate) as function of different equilibrium carvone pressures. It is observed that almost all the free Ti-OH functional groups are occupied by carvone molecules at a low equilibrium pressure of 2 mTorr.

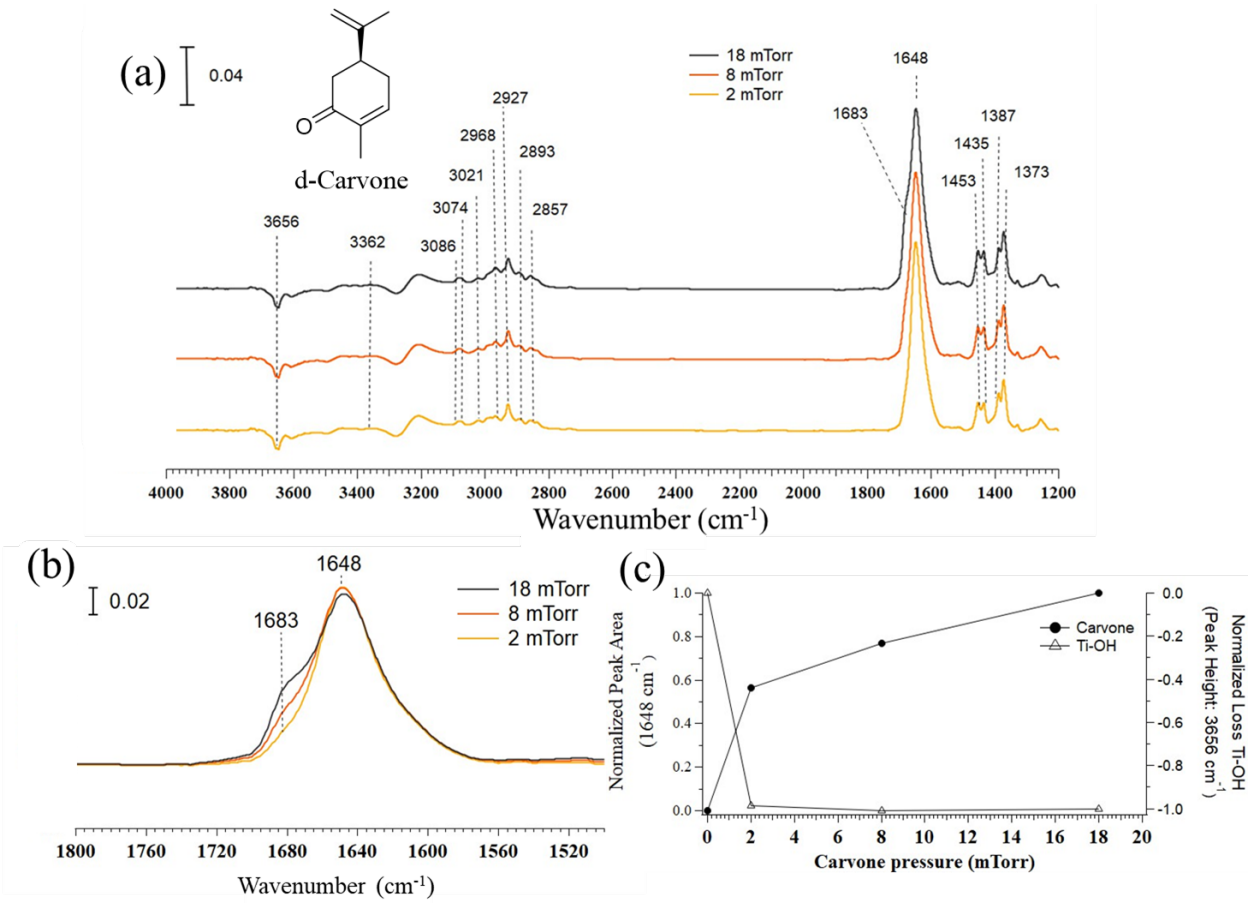

Figure 6.3: (a) Absorbance FT-IR spectra of carvone adsorbed on TiO_2 surface under dry conditions (< 1% RH) as a function of pressure in the spectral range extending from ca. 1200 to 4000 cm^{-1} (scale bar = 0.04 absorbance units). (b) The above (a) spectra range extends from 1500 to 1800 cm^{-1} (scale bar = 0.02 absorbance units) (c) The ordinate plots the normalized integrated peak area of carvone at 1648 cm^{-1} (ranging from 1560 to 1720 cm^{-1}) as function of carvone pressure (mTorr), the right ordinate plots the normalized peak height of the loss of Ti-OH functional groups at 3656 cm^{-1}. The equilibrium pressures are 2, 8, and 18 mTorr, respectively.

As the carvone pressure is changing from 8 mTorr to 18 mTorr, there is about 30% of amount carvone increased on TiO_2 surface. In Figure 6.1(b), when the limonene pressure is changing from 75 mTorr to 148 mTorr, there is only 10% of amount limonene is increased on TiO_2 surface. Once monolayer coverage on the TiO_2 surface is reached, ratio according to Equation 6.1 is:

$$\frac{\Delta increase\ amount\ of\ adsorbate}{\Delta increase\ pressure} \tag{6.1}$$

3 and 0.14 for carvone and limonene. This observation suggests there are multiple ways carvone may adsorb to the TiO_2 surface. The desorption of carvone from both SiO_2 and TiO_2 surfaces are irreversible, and the desorption kinetics of carvone from the TiO_2 surface is about 4 times slower than that from the SiO_2 surface.

The role of % RH was also probed. In these experiments, the TiO_2 surface was first exposed to either limonene or carvone and then following this water vapor was introduced into the infrared cell at different relative humidity, as shown in Figures 6.4 and 6.5. In the case where water displaces organic compounds from the surface, there is the growth of adsorbed water absorption bands on the surface concomitant with a loss of adsorbed organic compound from the surface. In the situation, where water co-adsorbs, there is the growth of adsorbed water absorption bands on the surface with little or no change in the amount of adsorbed organic compound. Finally, if the organic compound blocks water adsorption there will be little change in the spectrum. To quantify which of these different is occurring, we determined the change in coverage of the organic compound – either limonene or carvone – on the surface at different relative humidity compared to under dry conditions.

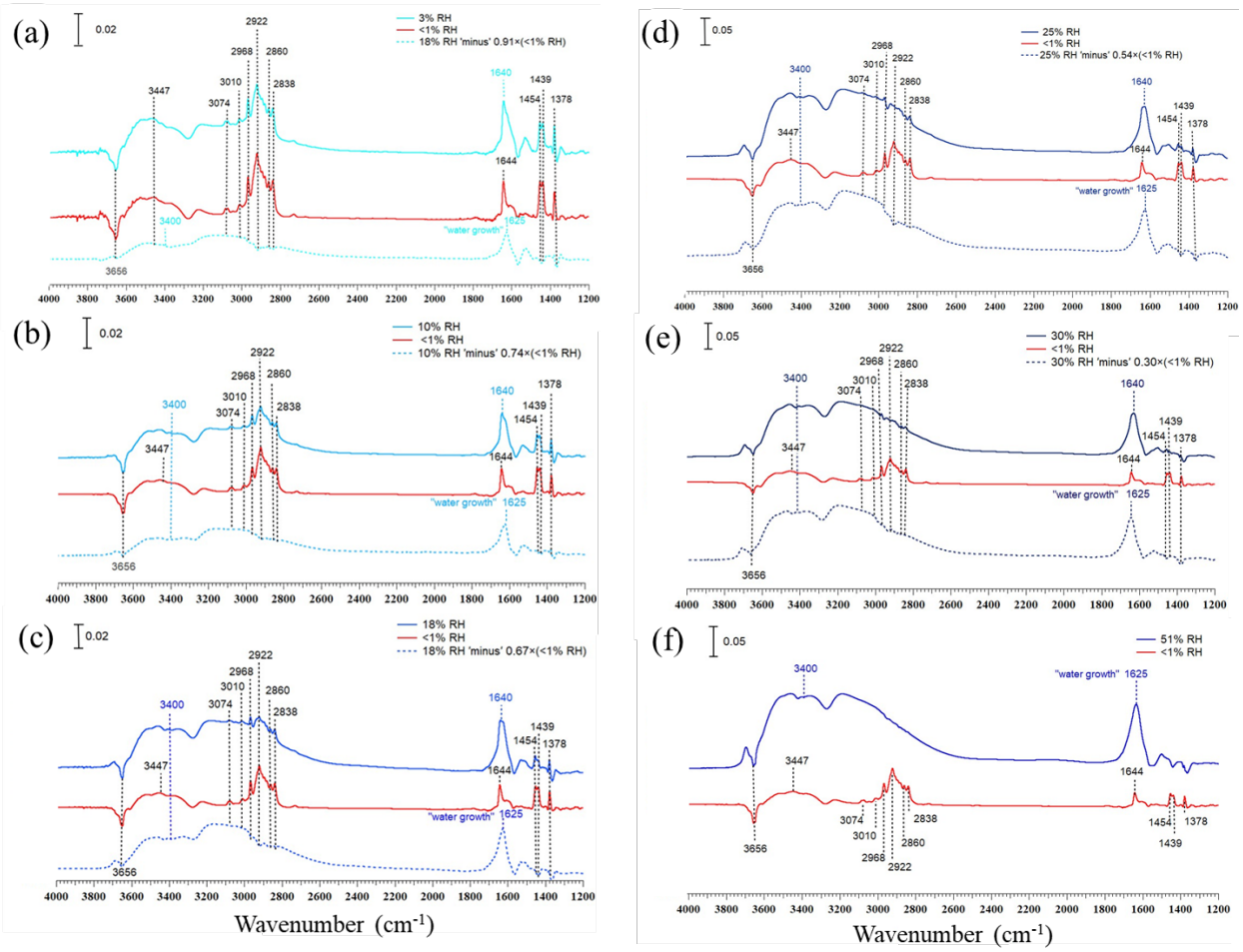

Figure 6.4: The FT-IR spectra of limonene adsorbed on TiO_2 (about 8 mg) surface at an equilibrium pressure of 55 ± 1 mTorr under different RH conditions. The RH is increased in the following increments:< 1%, (a) 3% (scale bar = 0.02 absorbance units), (b) 10% (scale bar = 0.02 absorbance units), (c) 18% (scale bar = 0.02 absorbance units), (d) 25% (scale bar = 0.05 absorbance units), (e) 30% (scale bar = 0.05 absorbance units), (f) 51% (scale bar = 0.05 absorbance units). In each subfigure, the red spectrum is the FT-IR spectra of limonene adsorbed on TiO_2 surface under <1% RH condition; the blue solid spectrum is the FT-IR spectra of limonene adsorbed on TiO_2 surface under high RH condition; and the dashed blue spectrum is obtained by blue solid spectrum minus the red spectrum with a ratio of the percentage of limonene left on TiO_2 surface as listed in Table 6.1 to remove the limonene remaining on the hydrated TiO_2 surface from the spectrum so the increase in the adsorbed water absorption bands on the TiO_2 surface under high RH condition can be determined. The broad absorption band centered at around 3400 cm^{-1} and the adsorption band at 1625 cm^{-1} in the blue dashed spectra are assigned to the O-H stretching and H_2O bending vibration modes, respectively, for adsorbed water on the TiO_2 surface.

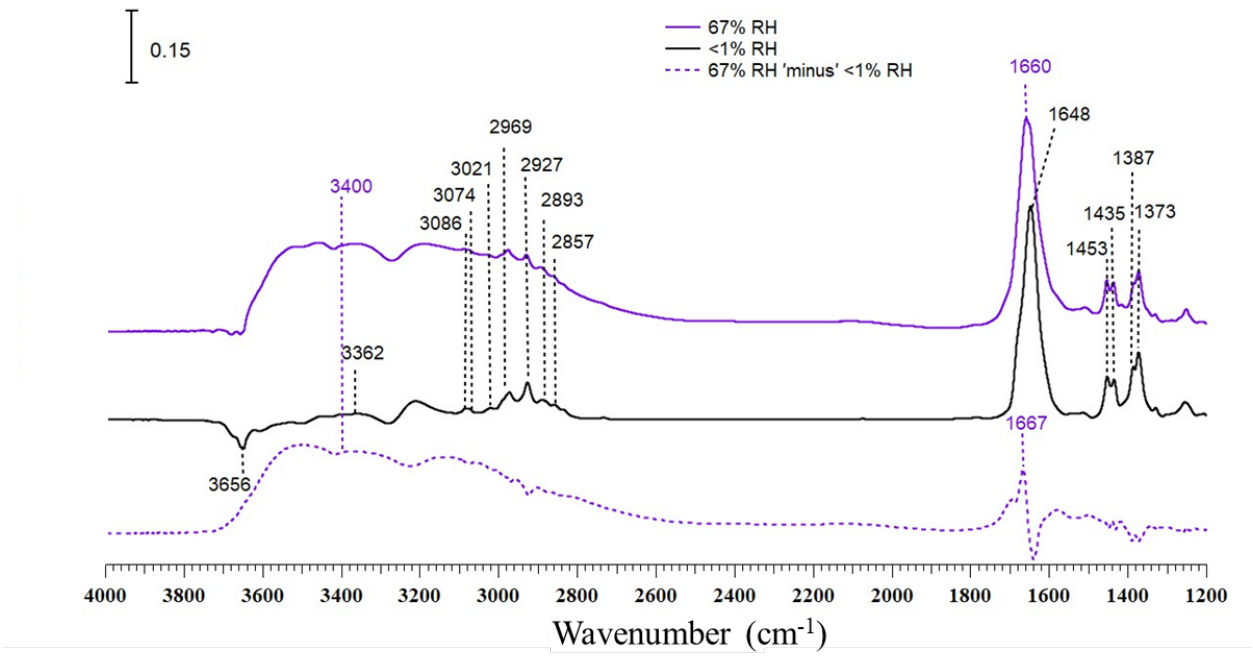

Figure 6.5: FT-IR spectra of carvone adsorbed on TiO_2 (about 8 mg) surface at an equilibrium pressure of 16 mTorr at <1% RH (black solid line) and 67% RH condition (purple solid line), that the peak at 1648 cm^{-1} shifts to 1660 cm^{-1} is attributed to the bending mode vibration for adsorbed H_2O. The dashed purple spectrum is obtained by the purple solid spectrum minus the black solid spectrum to show the "water growth" on the TiO_2 surface. (scale bar = 0.1 absorbance units)

Table 6.1 summarizes the FT-IR spectra by showing changes in adsorbed limonene and carvone on TiO_2.

% Relative Humidity (± 1 %)	Water Coverage (ML) (Bare TiO_2 Surface)	% of Organic Compound Remaining on Surface Relative to Dry Conditions	Water Coverage in ML (With Organic Compound Adsorbed on Surface)
Limonene			
< 1	< 0.1	100	<1
3	0.5	91	0.3
10	1.0	74	0.5
18	1.4	67	0.8
25	1.6	54	1.6
30	1.7	30	1.7
51	2.0	0	2.0
Carvone			
< 1	< 0.1	100	< 0.1
67	2.3	75	0.6

Table 6.1: Changes in adsorbed limonene and carvone on TiO_2 surface as a function of relative humidity and co-adsorbed water.

For limonene, it is seen that the coverage decreases significantly with increasing percent relative humidity while the amount of water adsorbed on the surface decreases. These data show that water displaces limonene from the surface into the gas phase. For carvone, there is little change in the surface coverage of carvone as a function of relative humidity and, additionally, little water is taken up by the surface. Overall, these data show that carvone, the oxidation product of limonene, is not easily displaced and also more strongly interacts with the surface compared to limonene.

6.3.2 Classical Molecular Dynamics Results

For each classical MD surface, a 50 ns unbiased MD simulation was constructed, and molecular snapshots shown in Figure 6.6 showcase limonene and carvone on the TiO_2 surface with differing monolayers of water.

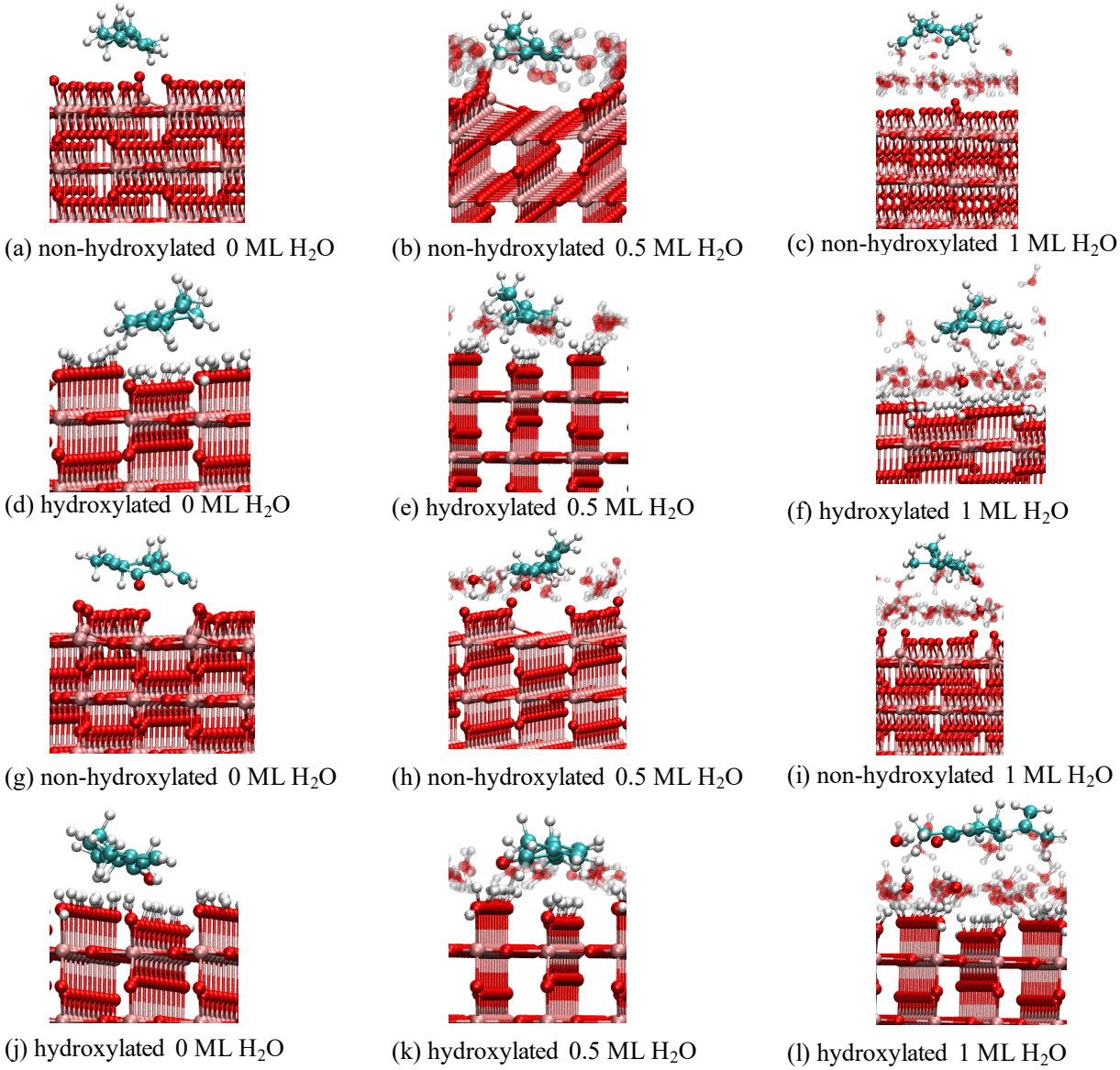

Figure 6.6: (a-c) shows limonene on non-hydroxylated TiO_2 surfaces with increasing levels of hydration, (d-f) shows limonene on hydroxylated surfaces with increasing levels of hydration, (g-i) shows carvonce on non-hydroxylated TiO_2 surfaces with increasing levels of hydration, (j-l) shows carvone on hydroxylated TiO_2 surfaces with increasing levels of hydration. Water molecules engaged in hydrogen bonds (π-hydrogen or OH-hydrogen) with the adsorbate are shown in fully color, all other water molecules are shown transparent. Red atoms correspond to O atoms, pink atoms correspond to Ti atoms, white atoms correspond to H atoms and cyan atoms correspond to C atoms. The surfaces have been oriented to showcase surface/adsorbate interactions.

In addition, the density profiles of the systems with limonene show that even at 1 ML, bulk

water is not achieved. This is because the water molecules form many hydrogen bonding interactions with the TiO_2 surface.

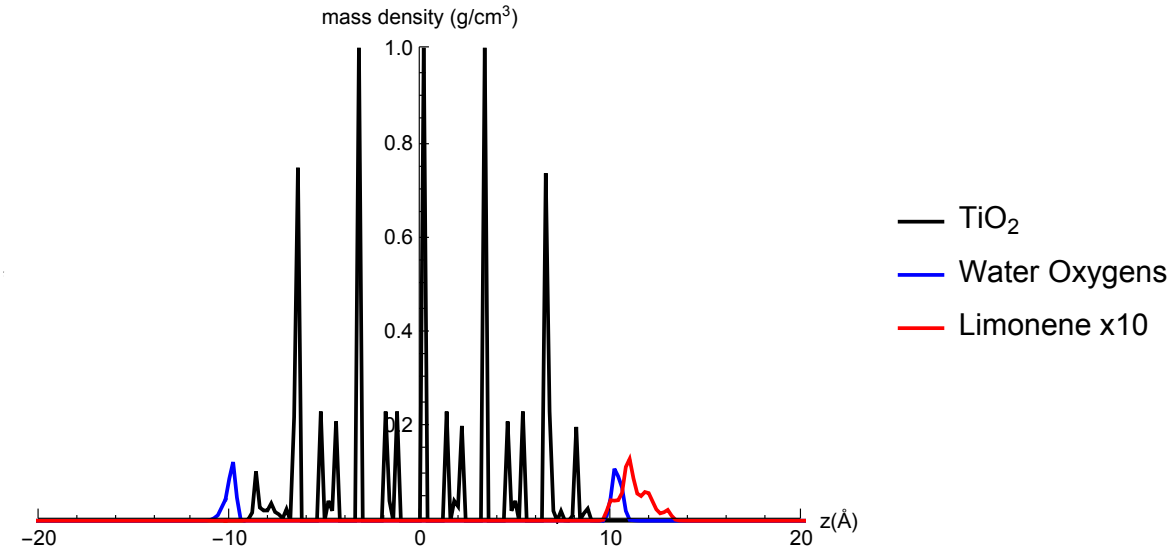

Figure 6.7: Density profile for the classical MD simulations for limonene (where limonene has been magnified by 10) for the non-hydroxylated surface with 0.5 ML

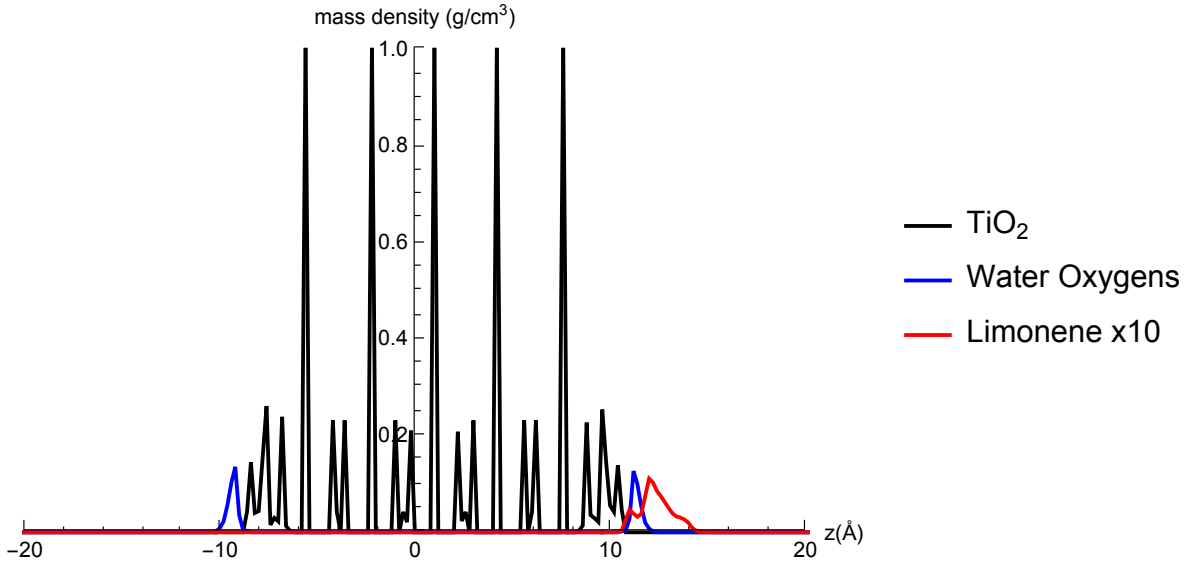

Figure 6.8: Density profile for the classical MD simulations for limonene (where limonene has been magnified by 10) for the hydroxylated surface with 0.5 ML

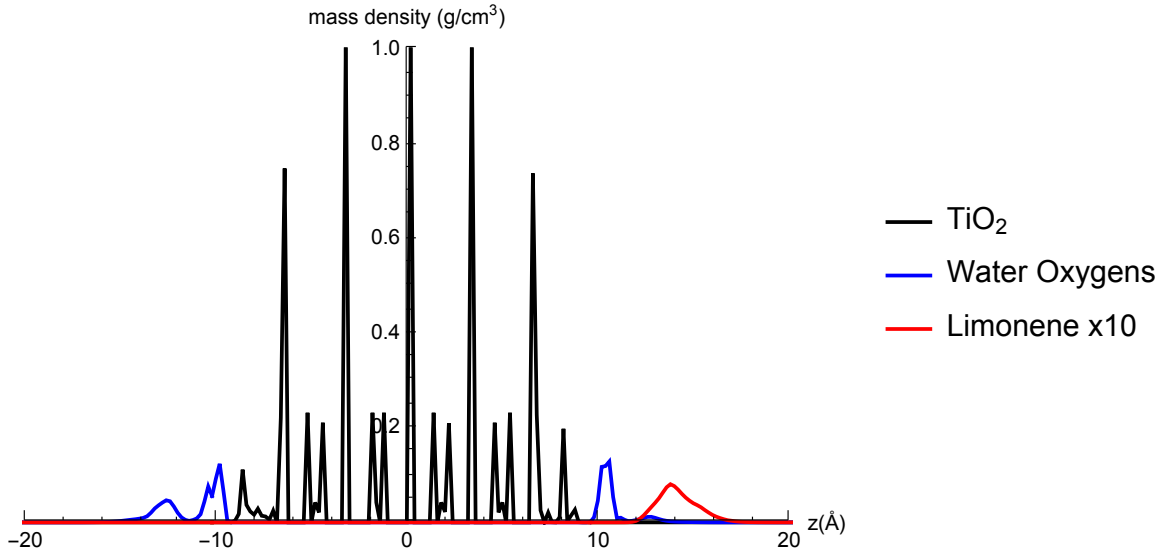

Figure 6.9: Density profile for the classical MD simulations for limonene (where limonene has been magnified by 10) for the non-hydroxylated surface with 1 ML

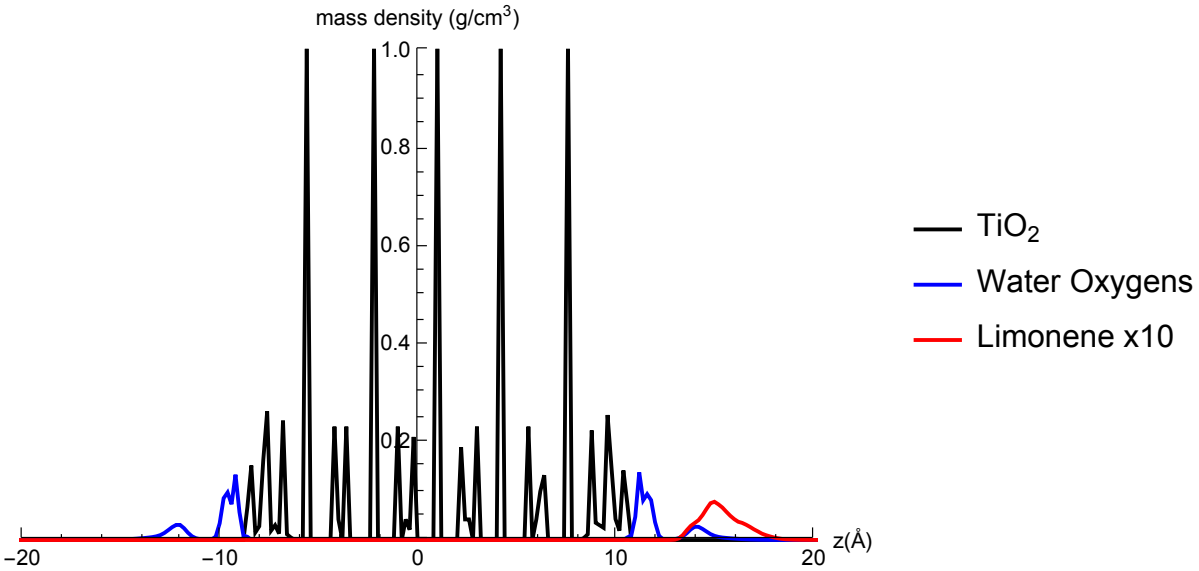

Figure 6.10: Density profile for the classical MD simulations for limonene (where limonene has been magnified by 10) for the hydroxylated surface with 1 ML

During the course of the 50 ns simulation, we observed the cyclic ring of carvone and limonene

predominantly stays parallel to the surface for the non-hydroxylated 0 ML H_2O and 0.5 ML H_2O systems and the hydroxylated 0 ML H_2O system. In the hydroxylated 0.5 ML H_2O system, the limonene ring was able to freely rotate on the surface. In both the non-hydroxylated and hydroxylated 1 ML H_2O surfaces, the limonene ring and carvone ring were able to freely rotate above the surface. On the non-hydroxylated 0 ML H_2O surface, we observed that both limonene and carvone stayed between two rows of bridging oxygen atoms for the course of the 50 ns simulation.

A second relevant measure of surface interactions are the formation of hydrogen bonds. To investigate the adsorption of limonene and carvone on the TiO_2 surface, we have studied the role of π-hydrogen bonds formed between $C_{sp}{}^2$ carbon centers and surface OH groups and hydrogen bonds formed between the carvone oxygen atom and surface OH groups. We have calculated the average number of π-hydrogen bonds during the course of the last 25 ns of the unbiased simulations. π-hydrogen bonds require hydrogen atoms as hydrogen bond donors, so no measurements were made for the non-hydroxylated surface with 0 ML H_2O, but the results for the rest of the surfaces are displayed in Table 6.2.

Surface	Water	Hydrogen Bond Donor	Average number of π-hydrogen bonds	
			Limonene	Carvone
Non-hydroxylated	0.5 ML	surface	n.a.	n.a.
		water	0.0049	0.0085
Non-hydroxylated	1 ML	surface	n.a.	n.a.
		water	0.13	0.05
Hydroxylated	0 ML	surface	0.28	0.15
		water	n.a.	n.a.
Hydroxylated	0.5 ML	surface	0.66	0.43
		water	0.017	0.005
Hydroxylated	1 ML	surface	0	0
		water	0.17	0.07

Table 6.2: Average number of π-hydrogen bonds for carvone and limonene. π-hydrogen bonding criteria was determined if the $C_{sp}{}^2$ distance < 3.5 Å and the OH $C_{sp}{}^2$ angle was $>$ 120 degrees. (n.a. - not applicable)

Overall, we see the formation of fewer π-hydrogen bonds with water molecules compared to hydrogen bonding statistics in Chapter 2. This is due to the fact that not only are water-water hydrogen bonds more favorable compared to π-hydrogen bonds, but also water hydrogen bonds to TiO_2 for either the non-hydroxylated or hydroxylated surface are quite strong, resulting in fewer water donor π-hydrogen bonds to limonene and carvone $C_{sp}{}^2$ carbon atoms. We see that that there are more surface to adsorbate π-hydrogen bonds on the hydroxylated surfaces, and these interactions occur frequently for the 0 ML H_2O and 0.5 ML H_2O surface. For the 1 ML H_2O surface, $C_{sp}{}^2$ carbon atoms on the adsorbate are too far away within the water layer to interact with the OH groups on the surface. Limonene and carvone both have two double bond sites and we found that the endocyclic C=C bond always has

a higher probability of π-hydrogen bond formation, and this is because the exocyclic C=C bond sometimes rotates above the water layer. Finally, there is a clear difference in π-hydrogen bonding probabilities between these two molecules, as the limonene molecules is much more likely to form π-hydrogen bonds compared to the carvone molecule. This does not indicate that limonene has a stronger interaction with the surface, but rather that carvone shows a much lower propensity for π-hydrogen bond formation. This can be attributed to interactions between the carvone carbonyl oxygen atom and TiO_2 surface. Tables 6.3 and 6.4 show the relevant carvone carbonyl oxygen interactions.

Surface	Water	Hydrogen Bond Donor	Average number of hydrogen bonds
Non-hydroxylated	0.5 ML	Surface	n.a.
		Water	0.08
Non-hydroxylated	1 ML	Surface	n.a.
		Water	0.80
Hydroxylated	0 ML	Surface	1.57
		Water	n.a.
Hydroxylated	0.5 ML	Surface	2.2
		Water	0.18
Hydroxylated	1 ML	Surface	0.0018
		Water	0.76

Table 6.3: Carvone carbonyl oxygen hydrogen bonding statistic. Hydrogen bonding criteria was determined if the O-O distance < 3.5 Å and the OH..O angle was > 120 degrees. (n.a. - not applicable)

In Table 6.3, we see few water carvone hydrogen bonds are formed for the non-hydroxylated 0.5 ML H_2O surface, which we attribute to the increase in stabilization from water-water and water-surface hydrogen bonds as discussed above. However, we see with 1 ML of water this is

an average of ∼0.80 hydrogen bonds between carvone and the surrounding water, regardless of the surface hydroxylation. As shown in Table 6.3, accounting for both π-hydrogen and hydrogen bonds, there are more surface interactions for the carvone molecule compared to those of limonene. This is consistent with our experimental results that indicate carvone has stronger interactions with the TiO_2 surface and suggests when carvone is not easily displaced by the addition of water.

As we will discuss in detail in the AIMD results in Subsection 6.3.3, there is an additional surface interaction between the carvone carbonyl oxygen atom and the surface Ti atoms in the non-hydroxylated surface. This is similar to the interaction discussed in Chapter 5, and in this case we have detected during the course of the 50 ns non-hydroxylated 0 ML H_2O simulation, the carvone carbonyl oxygen is found closest to the surface Ti atom with an average distance of 3.92 Å. More importantly, our AIMD power spectra support the validity of this interaction as there is a red shift in the C=O frequency compared to the gas phase carvone spectra. Table 6.4 showcases the proportion of the last 25 ns of each trajectory of carvone on a non-hydroxylated surface where the nearest neighbor to the carvone carbonyl oxygen is a Ti atom or surrounding water molecule. It is clear that with the presence of water, this carvone carbonyl oxygen - Ti surface interaction rapidly decreases.

Surface	Water	Interaction Type	Proportion of Trajectory	Average Bond Length (Å)
Non-hydroxylated	0 ML	O - Ti	100%	3.9 ± 0.26
		O - Water	n.a.	n.a.
Non-hydroxylated	0.5 ML	O - Ti	8%	4.18 ± 0.45
		O - Water	92%	3.45 ± 0.45
Non-hydroxylated	1 ML	O - Ti	0	0
		O - Water	100%	2.72 ± 0.18

Table 6.4: Proportion of trajectory where the nearest neighbor to the carvone carbonyl oxygen is either a water oxygen atom or a Ti atom and the average distance between interacting atoms.

A key benefit of atomistic MD simulations is the ability to study the arrangement of large numbers of molecules. In this case, we can investigate the hydrogen bonding network between water molecules and the TiO_2 surface, and how this is disrupted by the adsorption of limonene and carvone molecules. As our molecular snapshots show, water is adsorbed to the surface via hydrogen bonds to surface O atoms and surface OH groups, and other water molecules are also stabilized by water-water hydrogen bonds. Table 6.5 shows the extent that limonene and carvone disrupt the hydrogen bonding network by measuring the interactions of water molecules engaged in hydrogen bonding with the adsorbate. In some instances, the water molecule is able to form a hydrogen bond with the adsorbate and also a hydrogen bond with the surrounding water molecule or surface. In other cases, the hydrogen bonding network is "disrupted" as the water molecule is only engaged in a hydrogen bond with the adsorbate. These networks are also seen in our AIMD simulations.

Figure 6.11 shows the four kinds of hydrogen bonding interactions.

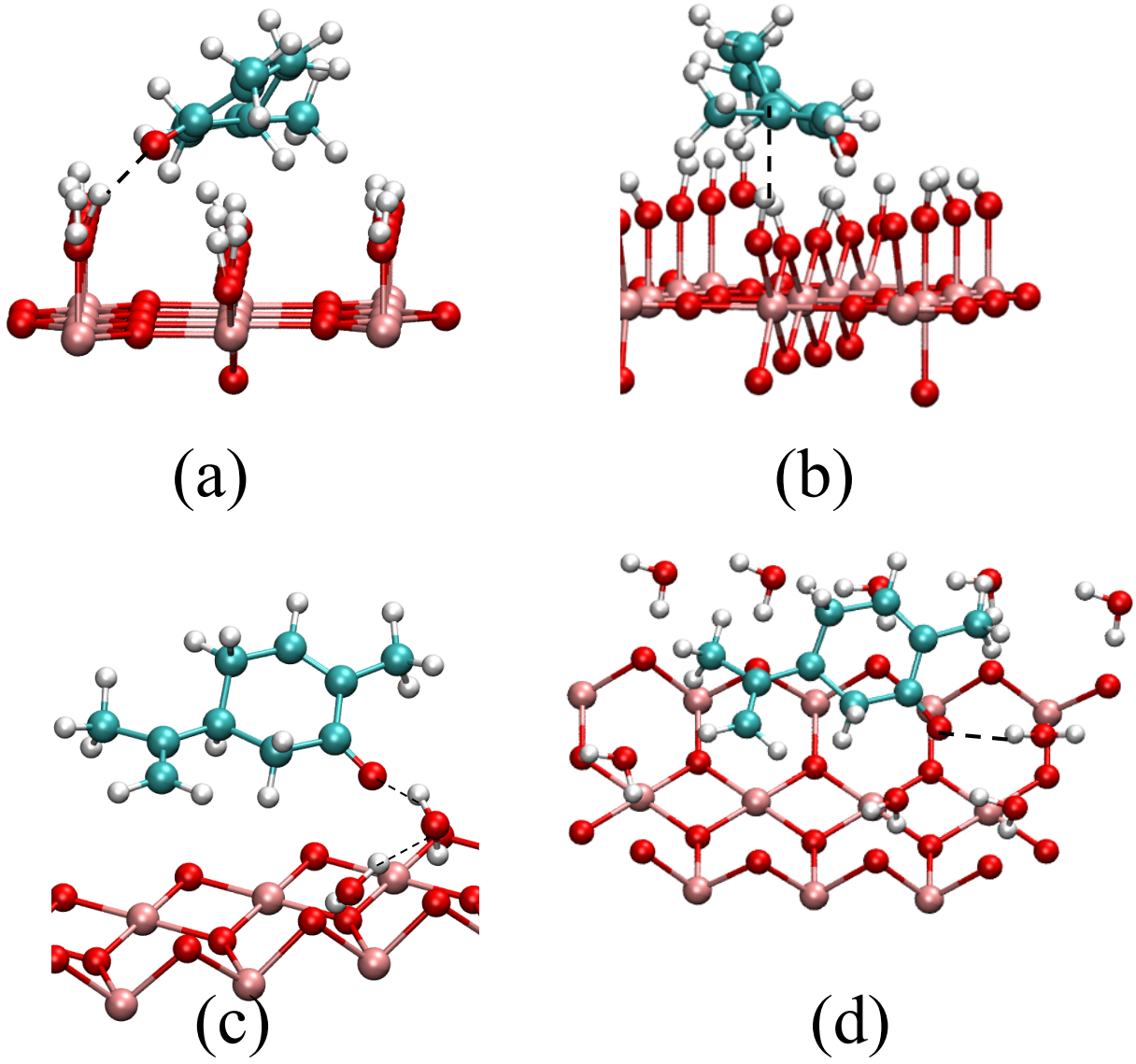

Figure 6.11: Snapshots of each kind of hydrogen bonding interaction from the classical molecular dynamics simulations. (a) Carvone oxygen atom in a hydrogen bond with hydroxylated TiO_2 surface. (b) Carvone $C_{sp}{}^2$ carbon atom in π-hydrogen bond with hydroxylated TiO_2 surface. (c) Carvone oxygen atom in a hydrogen bond with water, where the water molecule is also forming a hydrogen bond with the surrounding water molecules. (d) Carvone oxygen atom in a hydrogen bond with water, where the water molecule is not forming a hydrogen bond with the surrounding water molecules.

Surface	Water	Adsorbate	Fraction of bonding waters in water-water bonds	Fraction of bonding waters in water-surface bonds	Fraction of bonding waters only in adsorbate bonds
Non-hydroxylated	0.5 ML	Limonene	0.50	0.47	0.03
		Carvone	0.58	0.39	0.02
Non-hydroxylated	1 ML	Limonene	0.80	0.17	0.03
		Carvone	0.95	0.046	0.003
Hydroxylated	0.5 ML	Limonene	0.32	0.678	0.002
		Carvone	0.511	0.486	0.003
Hydroxylated	1 ML	Limonene	0.66	0.34	-
		Carvone	0.758	0.24	0.002

Table 6.5: Fraction of water-water hydrogen bonds, water-surface hydrogen bonds, and water-adsorbate hydrogen bonds. A hydrogen bond is defined as the O-O distance < 3.5 Å and OH..O angle is > 120 °.

Table 6.5 shows the difference in hydrogen bonding networks for the limonene and carvone molecules. Overall, this table shows that limonene forms more π-hydrogen bonds with water-molecules engaged in hydrogen bonding with the TiO_2 surface. Given the competitive adsorption of water on the TiO_2 surface, this suggests why limonene is displaced at high % RH. Contrary, carvone is shown to more often form hydrogen and π-hydrogen bonds with water molecules also in hydrogen bonding with other water molecules. In addition, in the case of the non-hydroxylated surface, limonene is shown to disrupt the hydrogen bond network more compared to that of carvone.

Overall, the hydrogen bonding statistics and initial insight gained by the water network analysis suggests why there is little change in the surface coverage of carvone as a function

of % RH.

To further quantify the difference in interaction strength to the surface, we have calculated the free energy profile for the desorption of the adsorbate from the surface, as shown in Figures 6.12 and 6.13. The free energy profiles are placed vertically, such that their minima are at the zero of free energy.

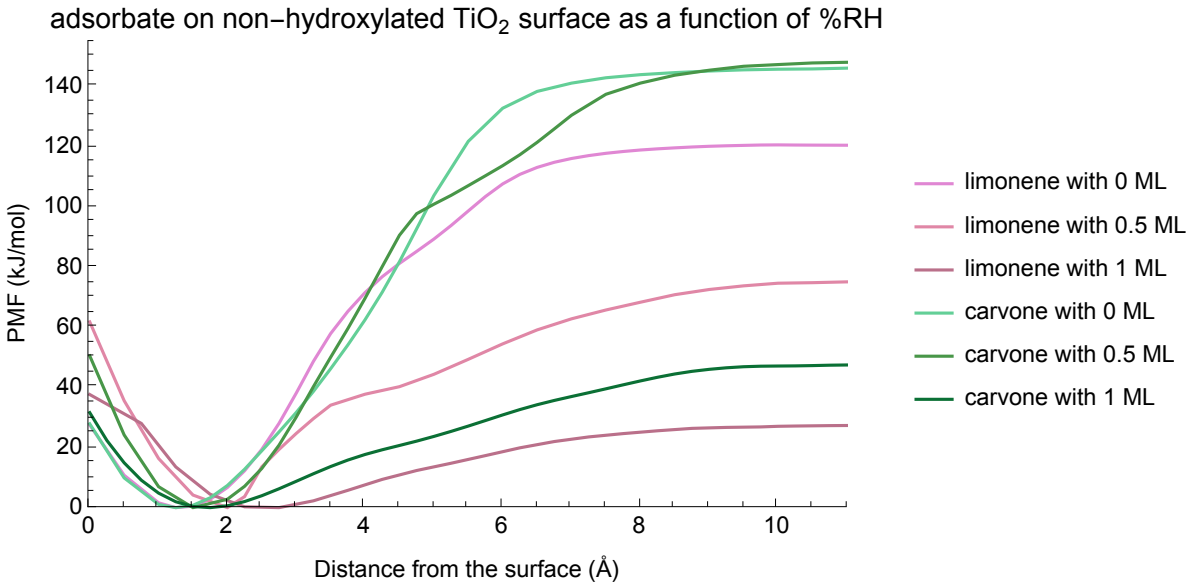

Figure 6.12: Potential of mean force (PMF) for the desorption of limonene and carvone from non-hydroxylated surfaces calculated from the classical MD simulations.

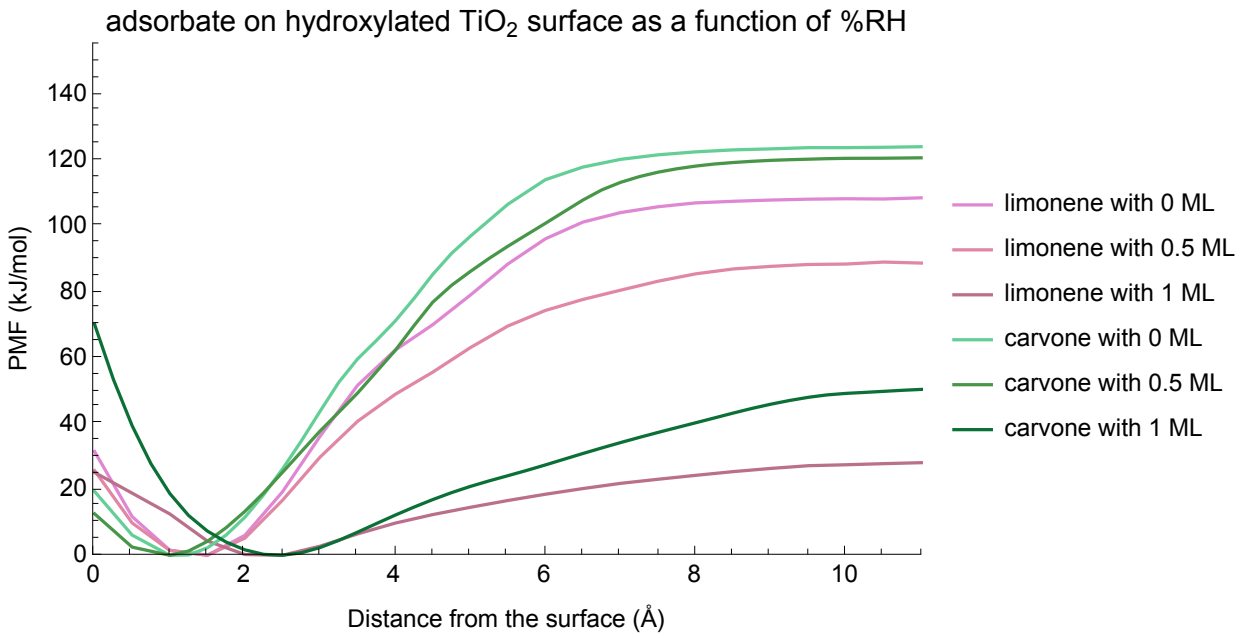

Figure 6.13: Potential of mean force (PMF) for the desorption of limonene and carvone from hydroxylated surfaces calculated from the classical MD simulations.

We first note that these desorption free energies are substantially higher than our results in previous chapters. This is to be expected as the partial charge of surface Ti and O atoms are much higher compared to those of SiO_2.

As seen in Figure 6.11, the desorption free energy for carvone on the non-hydroxylated with 0 ML H_2O is $\sim$ 30 kJ/mol higher than limonene. This is consistent with our experimental measurements, and our calculations suggest this is due to the close interaction between the carvone oxygen and surface Ti atoms, allowing for the carvone molecule to be in a closer proximity to the TiO_2 surface.

Interestingly, we the addition of 0.5 ML of water for the non-hydroxylated surface, the free energy of desorption is lower greatly by $\sim$40 kJ/mol for limonene but the free energy of desorption is slightly higher for carvone. As discussed in Chapter 2, water molecules can displace limonene from the SiO_2 surface, thus lowering the desorption energy. While this

was the case for limonene in both surfaces, the free energy desorption of carvone does not seem to follow the trend in the case of the non-hydroxylated 0.5 ML surface. However, as Table 6.5 indicates, the carvone molecule does not disrupt the hydrogen bonding network, so the addition of water would not displace carvone from the surface in the same way as limonene. In addition, we can see this trend by investigating the same disruption of the hydrogen bonding network as a function of distance from the surface in Figure 6.14. These results are in agreement with our experimental results that show low amounts of carvone are displaced initially with the addition of water.

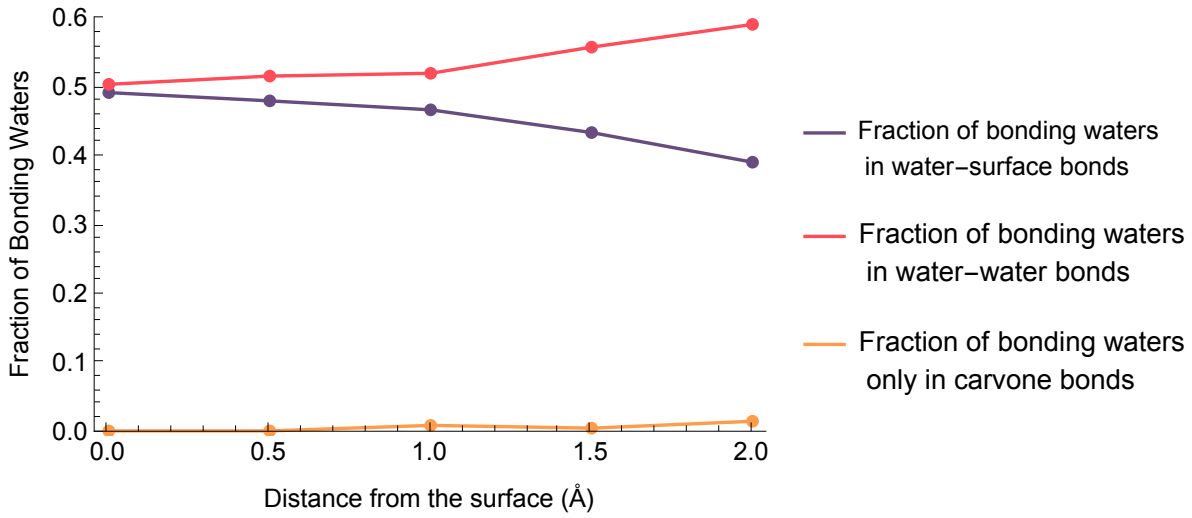

Figure 6.14: Fraction of water molecules in hydrogen bond interactions with carvone that are also in hydrogen bonds with either the TiO_2 surface, surrounding waters, or no other molecules (thus disrupting the hydrogen bonding network) as a function of distance from the surface during the PMF calculation.

An additional component of our study of the non-hydroxylated 0.5 ML H_2O surface is that for both limonene and carvone, the potential of mean force shows a kink when the adsorbate is 4 Å from the surface. This occurs when the molecule is removed from the water layer, resulting in a shift in free energy. We do not see this happen in the 1 ML H_2O surface system as there are more water molecules so the transition from water layer to gas phase is less abrupt. In addition, the geometries of the adsorbate are very different as they move out

of the water layer, as described in Figure 6.15.

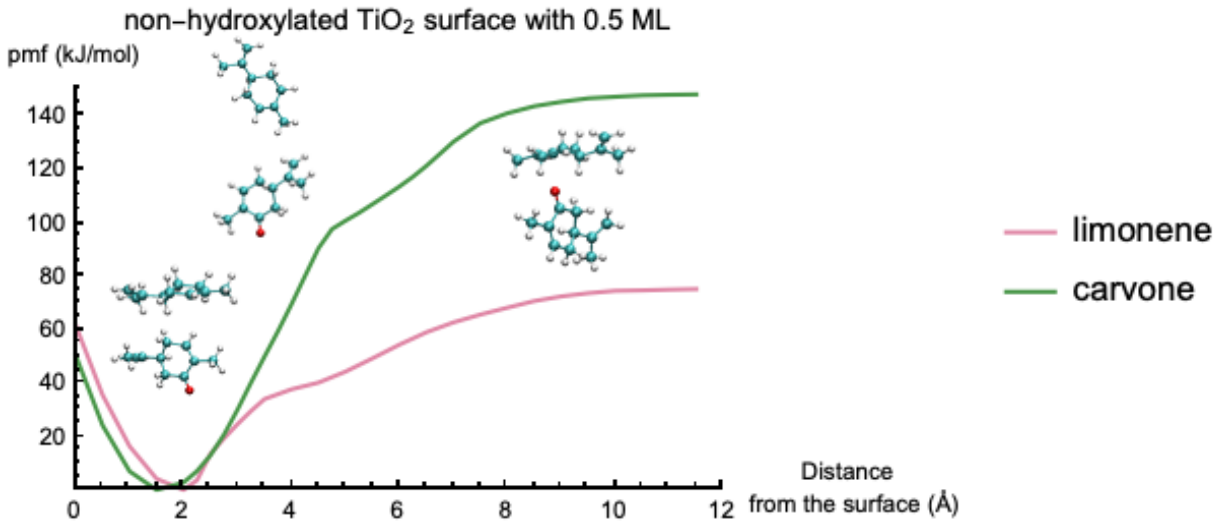

Figure 6.15: PMF of carvone and limonene on the non-hydroxylated 0.5 ML surface. There is a noticeable kink in the PMF around $\sim$ 4 Å, which attribute to the endocylic C=C bond in limonene and the carvone oxygen atom forming hydrogen and π-hydrogen bonds with water molecules on the top of the water layer. This can be seen in the molecular snapshots roughly along the PMF. Additional sampling was done at windows close to 4 Å to ensure all configurations along the PMF were properly sampled. This kink is not seen in the 1 ML and hydroxylated systems to the full hydration of the surface layer of TiO_2 that allows for water to form more consistent monolayers, allowing for a more uniform desorption from the surface.

Figure 6.13 shows the desorption free energy for the hydroxylated surfaces which are much lower compared to the free energy of desorption for the non-hydroxylated surface, and this is due to the hydroxylation of surface Ti atoms. We can also see a clear connection to our experimental results in the differences in decreasing desorption free energy with higher levels of hydration. Limonene, which is easily replaced by water at the surface, shows a 20 kJ/mol decrease in free energy with the addition of water compared to that of carvone which is only 4 kJ/mol. We attribute this to the hydrogen bonds formed between the carvone and the surrounding water molecules. Finally, both surfaces show with 1 ML of water, the free energy of desorption is similar for each adsorbate, converging around 28 kJ/mol for limonene and 50 kJ/mol for carvone.

6.3.3 *ab initio* Molecular Dynamics Results

As discussed in Section 6.1.1, we have constructed three surfaces to model the TiO_2 surface. First, we have constructed a non-hydroxylated TiO_2 surface with surface Ti atoms, secondly, we have constructed a non-hydroxylated TiO_2 surface with 4 water molecules, and thirdly we have constructed a fully hydroxylated surface. Figure 6.16 shows each surface with limonene or carvone.

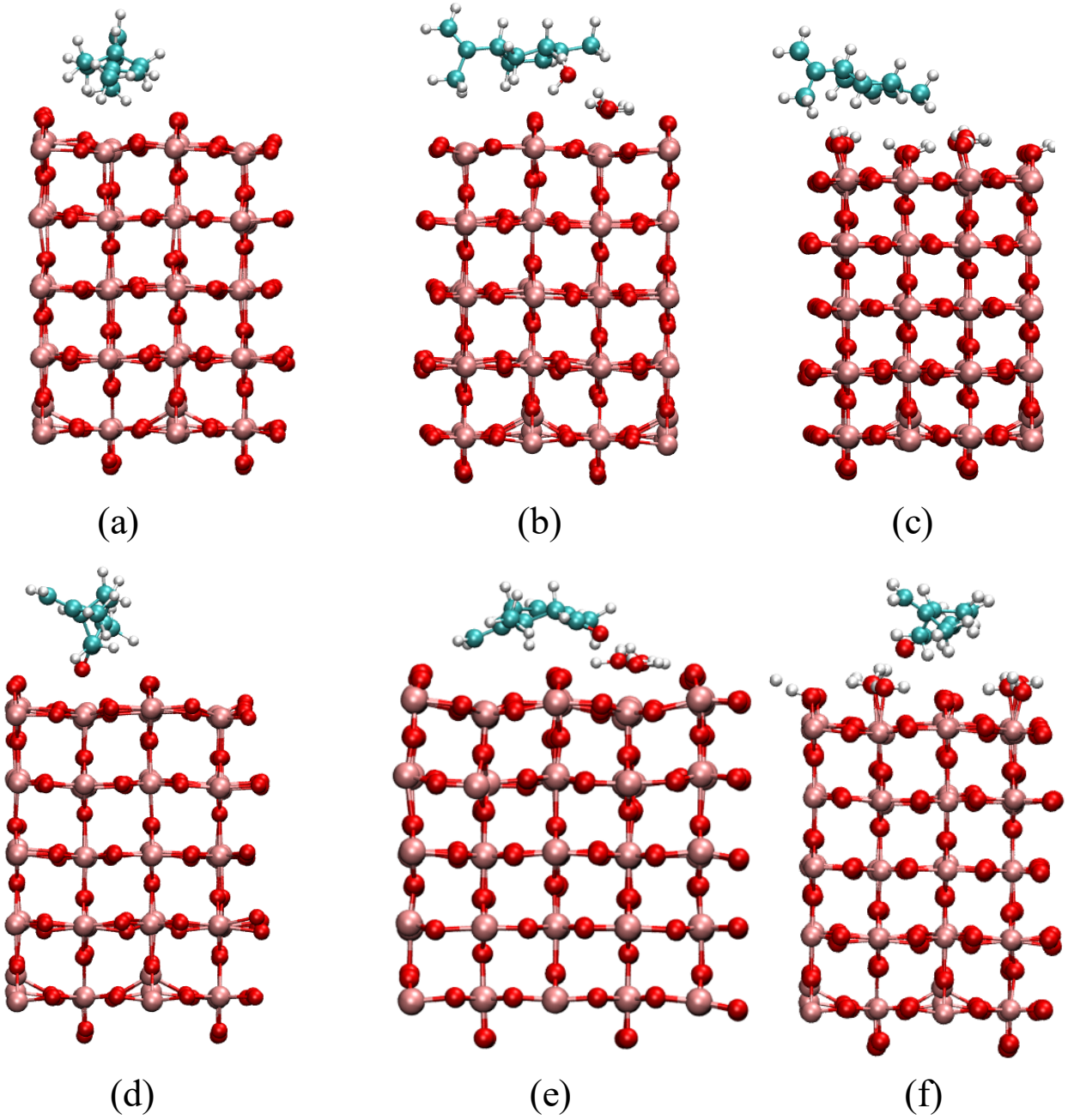

Figure 6.16: (a-c) shows limonene on a non-hydroxylated surface with 0 water molecules, on a non-hydroxylated surface with 4 water molecules and hydroxylated surface, (d-f) shows carvone on a non-hydroxylated surface with 0 water molecules, on a non-hydroxylated surface with 4 water molecules and on a hydroxylated surface. Note, a slightly larger TiO_2 system was used for carvone on the non-hydroxylated surface with 4 water molecules to fully accommodate the carvone and water molecules.

From our simulations, we have constructed the power spectra for the oxygen atoms of each

system, as shown in Figures 6.17, 6.18, and 6.19, and the hydrogen atoms of the system, as shown in Figures 6.20 and 6.21. Note that the positions and not exact intensities are comparable to the experimental data. However, it is reasonable to compare the trends in the AIMD power spectra to trends in the experimental FT-IR spectra.

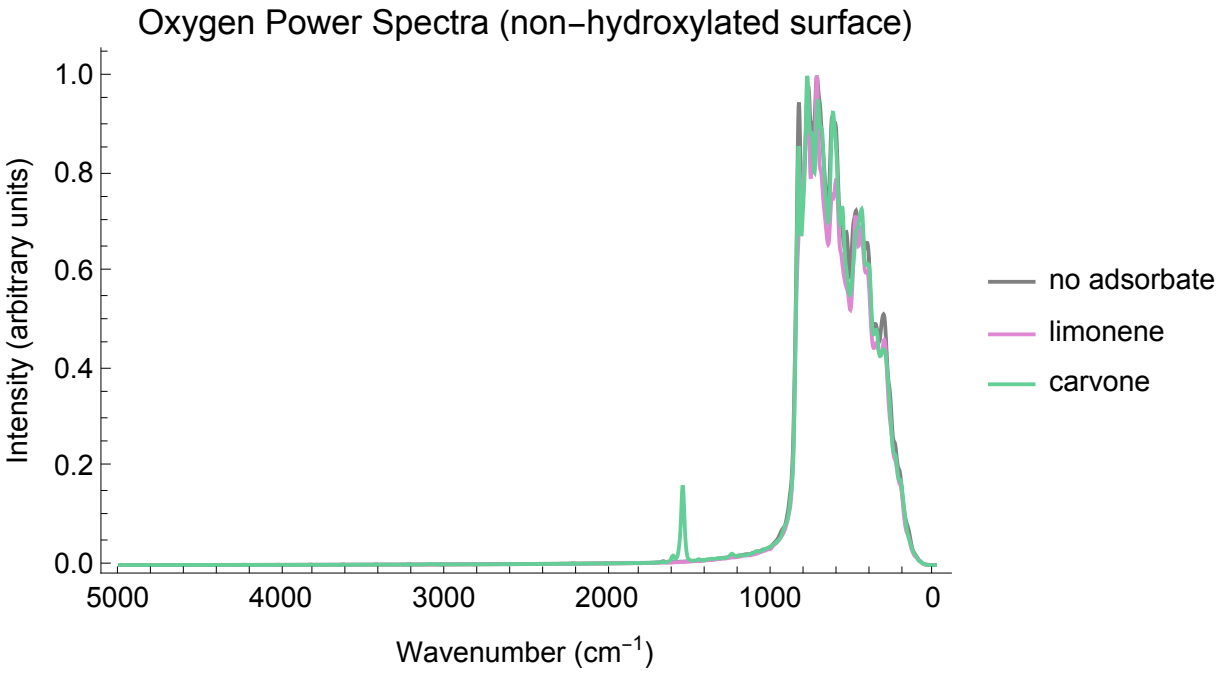

Figure 6.17: Oxygen power spectra for the non-hydroxylated TiO_2 surface, the non-hydroxylated surface with 1 limonene molecule and the non-hydroxylated surface with 1 carvone molecule. All intensity values have been rescaled to run from 0 to 1.

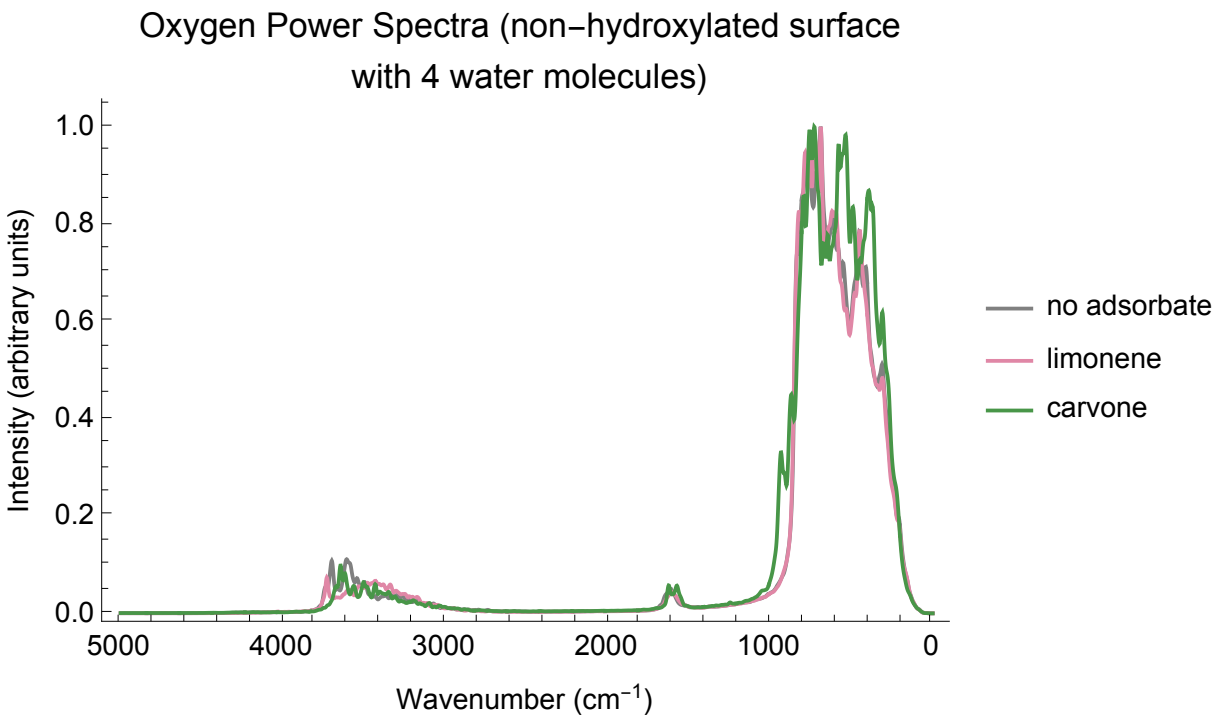

Figure 6.18: Oxygen power spectra for the non-hydroxylated TiO_2 surface with 4 water molecules, the non-hydroxylated surface with 4 water molecules and 1 limonene molecule and the non-hydroxylated surface with 4 water molecules and 1 carvone molecule. All intensity values have been rescaled to run from 0 to 1.

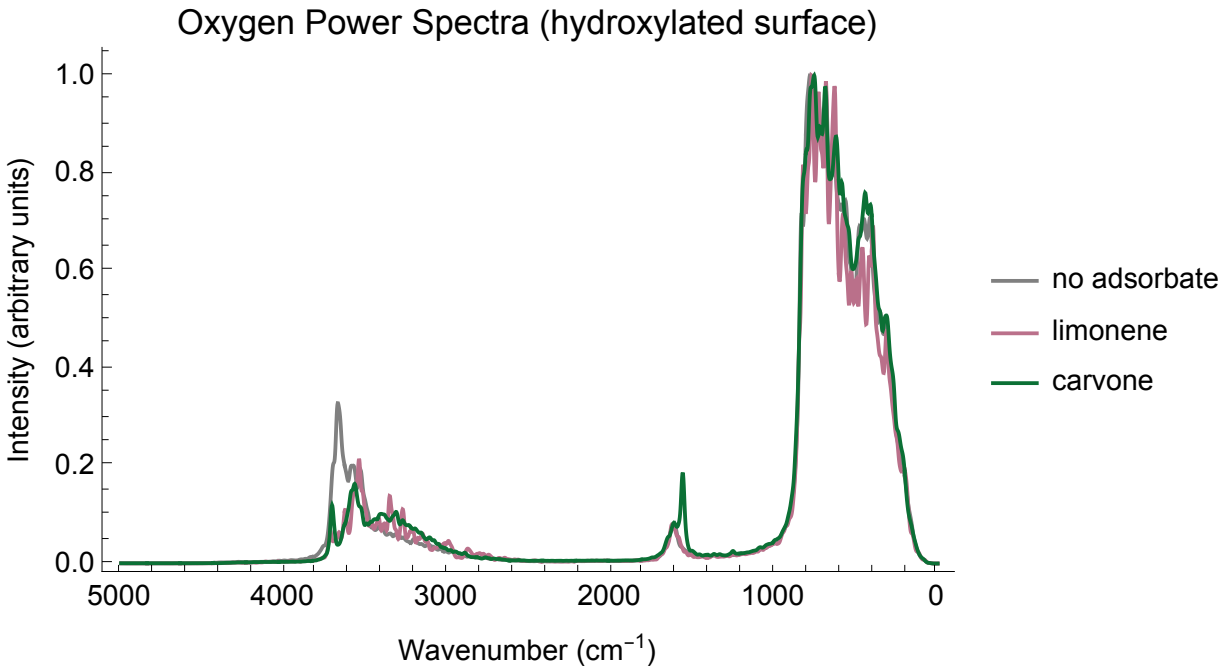

Figure 6.19: Oxygen power spectra for the hydroxylated TiO_2 surface, the hydroxylated surface with 1 limonene molecule and the hydroxylated surface with 1 carvone molecule. All intensity values have been rescaled to run from 0 to 1.

Figures 6.17 to 6.19 show consistency between the oxygen power spectra of all three simulated surfaces. For the carvone carbonyl stretch, we see agreement with our experimental results in Figures 6.17 and 6.18, where the carbonyl stretch is at a higher wavenumber with the addition of water. In addition, in the hydroxylated surface, Figure 6.18, we see the presence of both the water stretch at 1620 cm^{-1} and the carvone carbonyl stretch at 1575 cm^{-1}. This is more clearly seen in Figure 6.22.

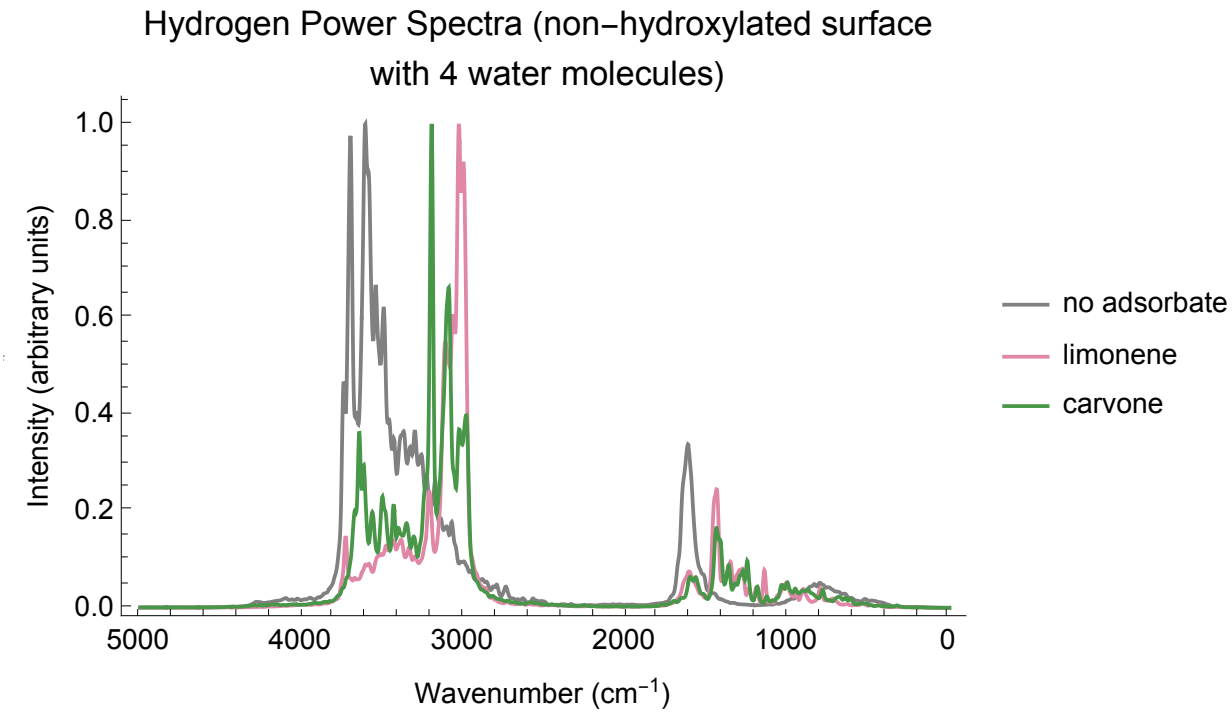

Figure 6.20: Hydrogen power spectra for the non-hydroxylated TiO_2 surface with 4 water molecules, the non-hydroxylated surface with 4 water molecules and 1 limonene molecule and the non-hydroxylated surface with 4 water molecules and 1 carvone molecule. All intensity values have been rescaled to run from 0 to 1.

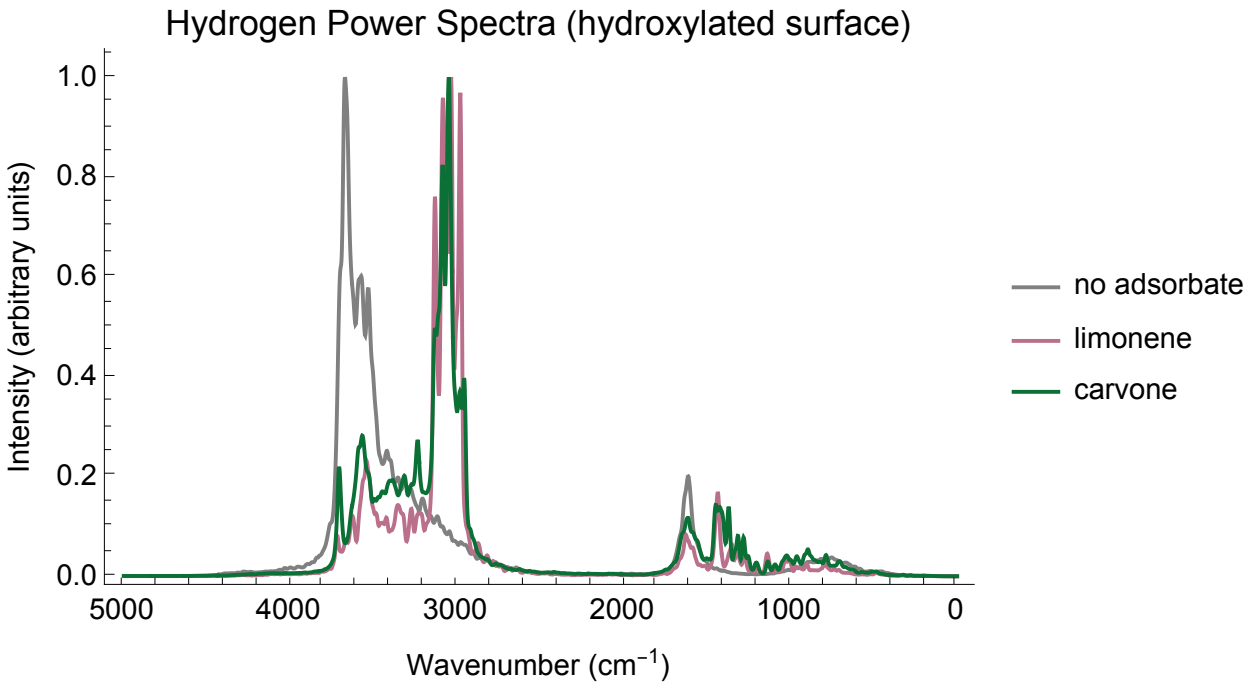

Figure 6.21: Hydrogen power spectra for the hydroxylated TiO_2 surface, the hydroxylated surface with 1 limonene molecule and the hydroxylated surface with 1 carvone molecule. All intensity values have been rescaled to run from 0 to 1.

According to the hydrogen power spectra, we see a decrease in the 3700 cm^{-1} peak with the addition of the adsorbate to the surface, which is in agreement with the Ti-OH loss shown in Figure 6.2. This results in a red shifting of the hydroxyl/water molecules due to the presence of the adsorbate on the surface, which is consistent with our classical MD simulations that show the formation of hydrogen and π-hydrogen bonds. In addition, in the systems with free water molecules, there was a similar interaction pattern as described in the Section 6.3.2., where the adsorbate forms a hydrogen or π-hydrogen bond with a molecule also in a water-water hydrogen bond. Hydrogen bonding statistics for these surfaces are described in Table 6.5.

Surface	Average Number of π-hydrogen bonds		Average Number of hydrogen bonds
	Limonene	Carvone	Carvone
Non-hydroxylated with 4 water molecules	0.18	0	0.98
Hydroxylated	0.35	0.0002	1.96

Table 6.6: Hydrogen bonding statistics for AIMD simulations. The non-hydroxylated surface with 0 water molecules cannot form any hydrogen bonds. Hydrogen bonding criteria was determined in the O-O or O-$C_{sp}{}^2$ distance was less than 3.5 Å and the OH...O angle of OH...$C_{sp}{}^2$ angle was greater than 120°.

Table 6.5 shows consistency with our classical MD simulations where limonene can form more π-hydrogen bonds to the surface and surrounding waters compared to carvone, and that carvone can form many hydrogen bonds via the oxygen atom to the surface and surrounding waters. In our AIMD simulations, we see there is a higher average number of hydrogen bonds for carvone to the surface compared to the classical MD simulations; however, this difference is consistent with our previous studies of carvone on SiO_2.

For the non-hydroxylated TiO_2 surface with 0 water molecules, we see agreement between the trajectories of our classical MD simulations, where the limonene molecule is positioned between two rows of bridging oxygen atoms, and the cavone carbonyl oxygen atom is positioned very close to a surface Ti atom, in this case within 2.5 Å of the surface Ti atom, during the course of the 30 ps simulation. Using AIMD allows us to better probe the carvone carbonyl oxygen – Ti interaction, as Figure 6.22 shows the red shift of the carvone carbonyl stretching frequency on the surface.

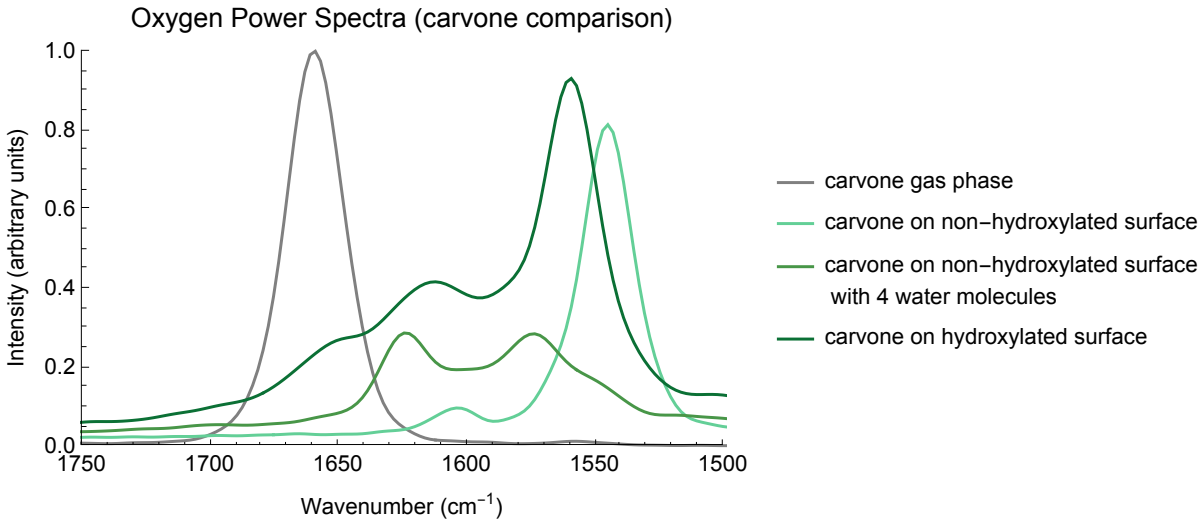

Figure 6.22: Oxygen power spectra of the carvone carbonyl stretching region. We see red shifting when the carvone molecule is on the surface, and greater red shifting without water/hydroxyl groups. All intensity values have been rescaled to run from 0 to 1 and the spectra for carvone on the TiO_2 surfaces has been scaled by 5x for clarity.

For the systems with hydrogen atoms, this red shift arises from the carbonyl oxygen forming hydrogen bonds with surrounding hydrogen atoms, at around ∼1575 cm^{-1}. We see a greater red shift for the non-hydroxylated 0 H_2O surface, at around ∼1525 cm^{-1}, which is consistent with our experimental results that show a peak at 1648 cm-$^{-1}$ at <1 % RH and 1660 cm^{-1} with 67 % RH.

However, since there are no hydrogen atoms in the non-hydroxylated 0 H_2O surface, yet we still see a red shift, we can attribute this shift to the interaction between the carvone oxygen atom and surface Ti atom. This is highlighted in Figure 6.23, which shows the difference in two key distances during the course of the 30 ps simulation. The first distance is between the carvone oxygen atom and Ti atom (the black dashed line in Figure 6.22b) and between the Ti atom and the oxygen atom directly below it (the white dashed line in Figure 6.22b). When this difference is negative it corresponds to the carvone carbonyl oxygen atom being closer to the Ti atom then the crystal oxygen atom. This occurs 20% of the time during the course of the simulation. The result indicates the potential reactivity between oxygenated

species and the bare TiO_2 surface and will be addressed in our future work.

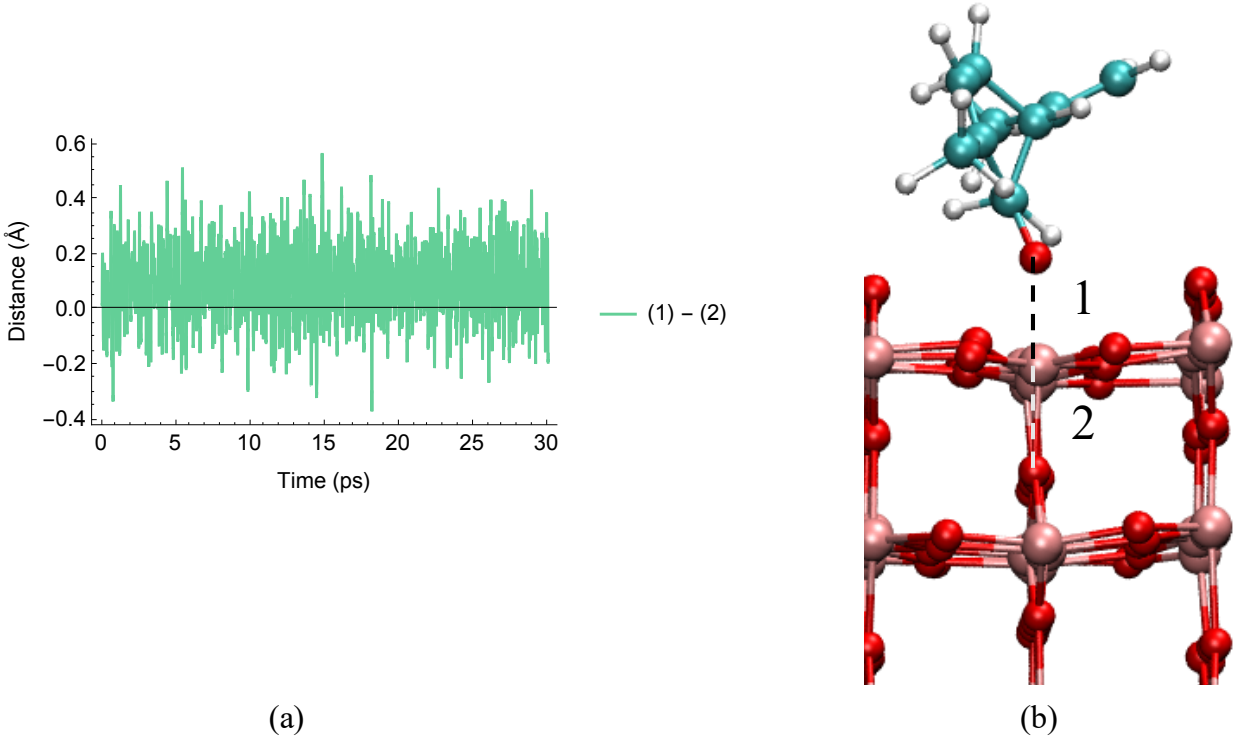

Figure 6.23: Difference between distance (1) and distance (2), in Å , during the course of the 30 ps AIMD simulation.

6.3.4 Kinetic Model Parameters

The surface accommodation coefficient of each molecule on each TiO_2 surface is shown in Table 6.7. This corresponds to the percentage of trajectories that resulted in the adsorbate adsorbed to the surface.

Surface	Adsorbate	Surface Accommodation
non-hydroxylated	limonene	1
0 ML	carvone	0.98
non-hydroxylated	limonene	0.98
0.5 ML	carvone	1
non-hydroxylated	limonene	0.98
1 ML	carvone	1
hydroxylated	limonene	1
0 ML	carvone	1
hydroxylated	limonene	1
0.5 ML	carvone	1
hydroxylated	limonene	0.98
1 ML	carvone	1

Table 6.7: Surface accomadation coefficient for limonene and carvone on various TiO_2 surfaces.

Kinetic model parameters were first attempted using the finite difference method and then were calculated by taking 15 AIMD simulation steps during the course of the simulation and calculating the interaction energy as defined as:

$$(E_{adsorbate} + E_{surface}) - E_{total} \tag{6.2}$$

The average of these 15 snapshots are shown in Table 6.8, and a box and whisker chart showing the spread of the data in Figure 6.24.

Adsorbate	Surface	Mean (kJ/mol)	Standard Deviation (kJ/mol)
Limonene	non-hydroxylated 0 waters	117.8	12.1
	non-hydroxylated 4 waters	103.8	3.5
	hydroxylated	71.0	11.3
Carvone	non-hydroxylated 0 waters	164.7	6.3
	non-hydroxylated 4 waters	168.3	14.8
	hydroxylated	148.8	35.9

Table 6.8: Mean and standard deviation for 15 interaction energies calculated from AIMD simulations for limonene and carvone on TiO_2 surfaces.

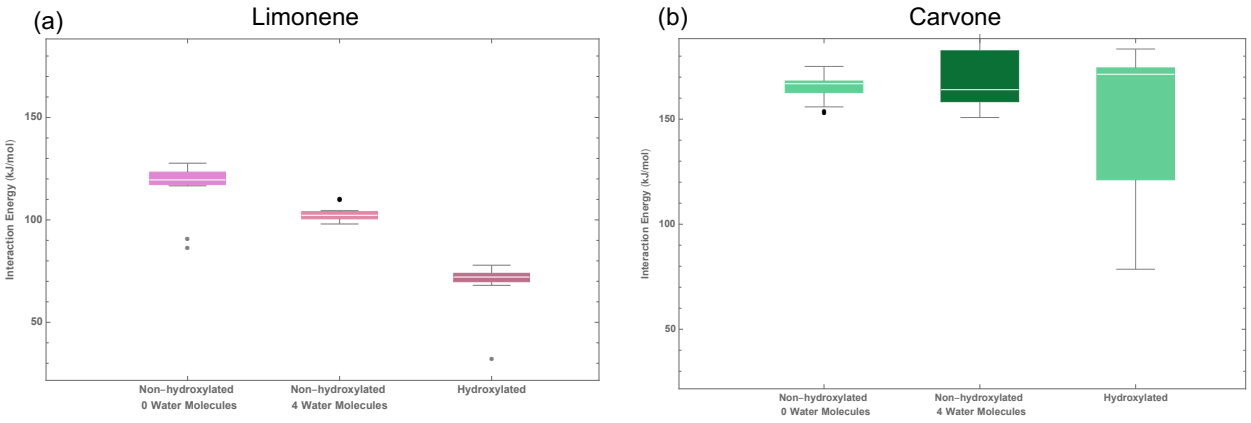

Figure 6.24: Box plot of 15 interaction energies calculated from AIMD simulations for (a) limonene (b) carvone

As seen in this box chart there is a large spread of interaction energies for carvone on the hydroxylated surface, this is due to the fact that during the AIMD simulation, there are portions of the AIMD simulation where the carvone oxygen is not forming a hydrogen bond

with the hydroxylated surface.

To determine the enthalpy of desorption for systems with % RH > 0, the finite-difference temperature derivative of the potential of mean force (PMF) or free energy (ΔG) as a function of the distance from the surface, r, was calculated.

To do this, the following equation was employed based on work by Wang et al. [109]:

$$-T\Delta S(r) = T\frac{\Delta G(r, T + \Delta T) - \Delta G(r, T - \Delta T)}{2\Delta T} \tag{6.3}$$

T and ΔT are 300 and 20 K. Therefore, three separate PMF calculations at 280, 300, and 320 K have been performed for each system. The three PMFs are shown as an example in Figure 6.25, for one water molecule on the hydroxylated surface with 0 ML water.

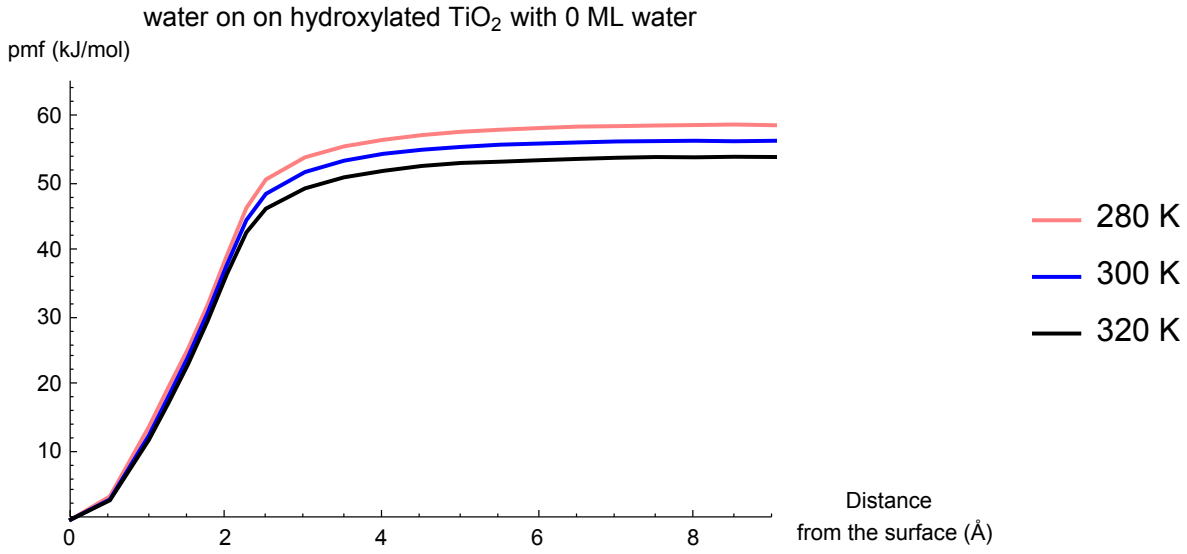

Figure 6.25: Potential of mean force (PMF) for the desorption of one water molecule from the hydroxylated TiO_2 surface with 0 ML water calculated from the classical molecular dynamics simulations. The free energy profiles are placed vertically, such that their minima are at the zero of free energy.

The enthalpy of desorption may be calculated from the equation:

$$\Delta H(r) = \Delta G(r) + T\Delta S(r) \tag{6.4}$$

Figure 6.26 hows the potential of mean force (PMF) or ΔG, the enthalpic contribution, ΔH, used as the desorption enthalpy in the kinetic model, and the entropic contribution -T ΔS for one water molecule on the hydroxylated surface with 0 ML water. Figure 6.27 and 6.28 show the results for limonene and carvone. This method resulted in a ΔH in agreement with experimental results, as discussed in the methods section, but we suggest due to the complexity of the real world TiO_2 surface, failed to adequately describe the desorption of limonene and carvone for the kinetic model.

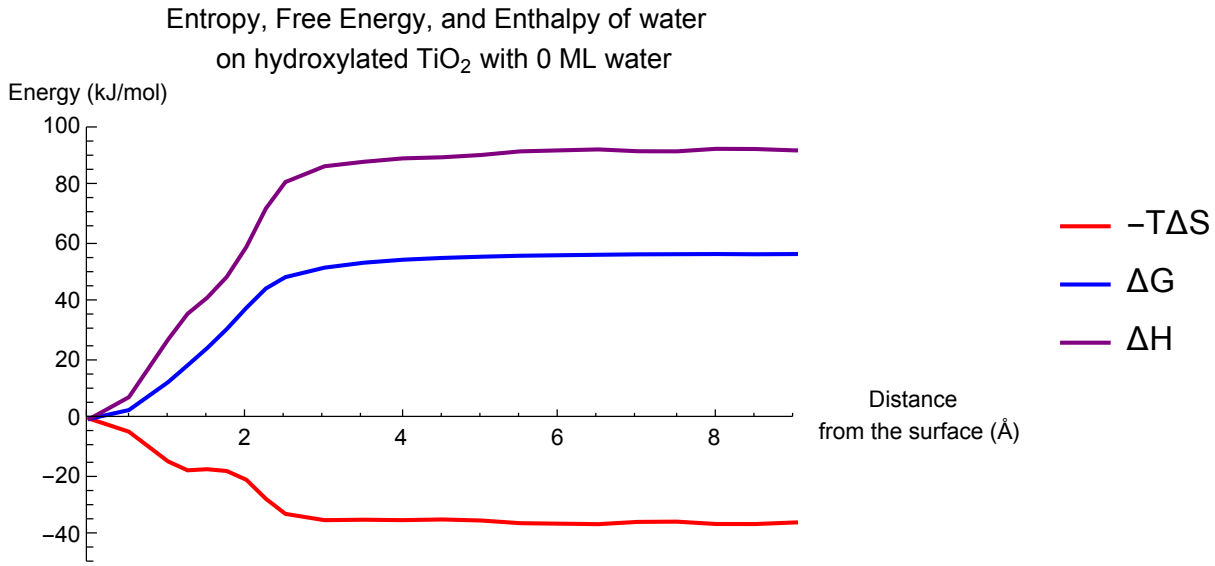

Figure 6.26: Potential of mean force (PMF) or ΔG, the enthalpic contribution, ΔH, used as the desorption enthalpy in the kinetic model, and the entropic contribution -TΔS for one water molecule on the hydroxylated TiO_2 surface with 0 ML water.

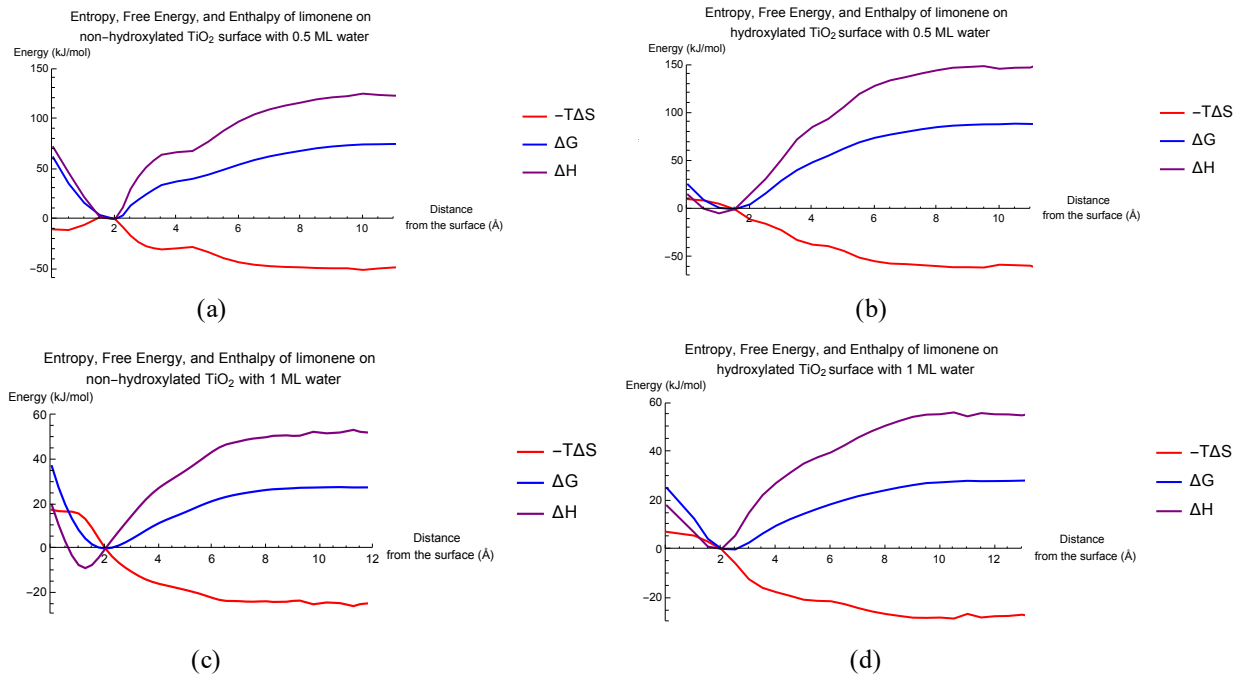

Figure 6.27: Potential of mean force (PMF) or ΔG, the enthalpic contribution, ΔH, used as the desorption enthalpy in the kinetic model, and the entropic contribution -TΔS for limonene on the non-hydroxylated surface with 0.5 ML water (b) the hydroxylated surface with 0.5 ML water, (c) the non-hydroxylated surface with 1 ML water (d) the hydroxylated surface with 1 ML water.

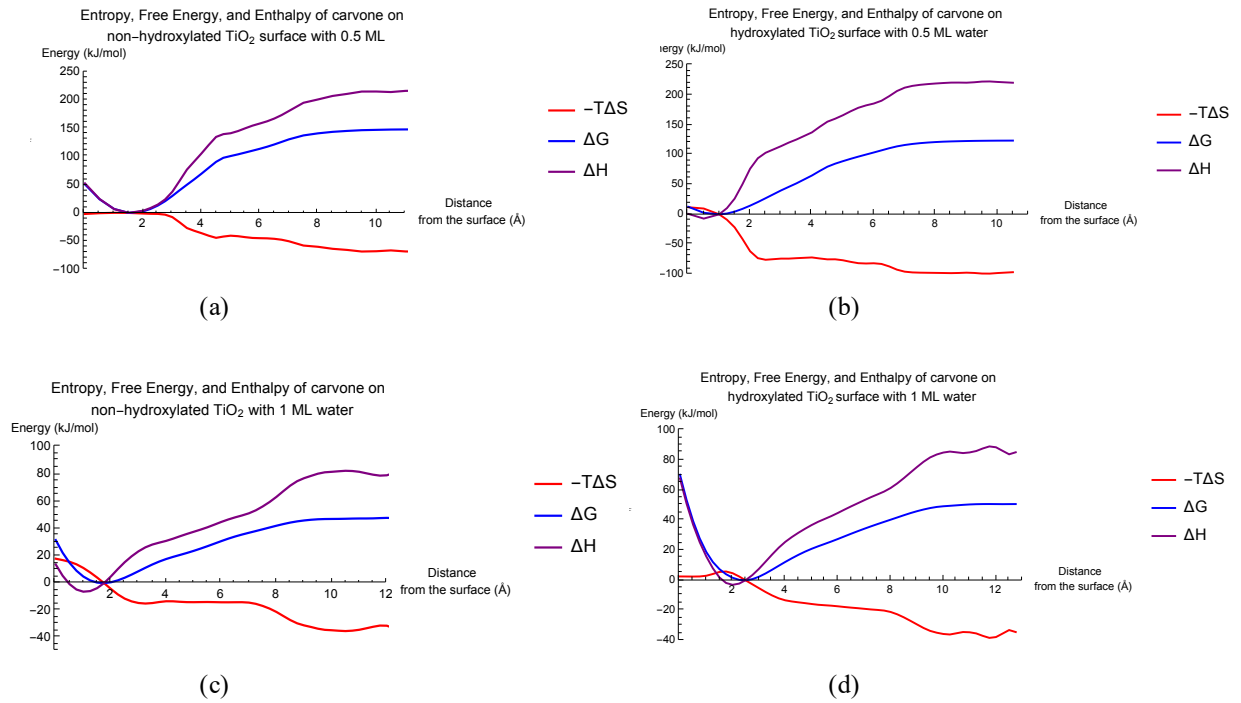

Figure 6.28: Potential of mean force (PMF) or ΔG, the enthalpic contribution, ΔH, used as the desorption enthalpy in the kinetic model, and the entropic contribution -TΔS for carvone on the non-hydroxylated surface with 0.5 ML water (b) the hydroxylated surface with 0.5 ML water, (c) the non-hydroxylated surface with 1 ML water (d) the hydroxylated surface with 1 ML water.

6.4 Conclusions

To conclude, the FT-IR absorbance spectra show that limonene forms TiO_2-OH...π-hydrogen bonds with the hydroxylated TiO_2 surface and surrounding water molecules; and carvone forms O-H hydrogen bonds and π-hydrogen bonds with the hydroxylated TiO_2 surface and surrounding water molecules, as well as forms an interaction between the carvone carbonyl oxygen and surface Ti atoms. As % RH increases, the desorption of these molecules decreases and limonene has a much more dramatic decrease compared to that of carvone. Two idealized surfaces, a non-hydroxylated and fully hydroxylated TiO_2 surface, employed both with classical MD and AIMD simulations were used to describe the experimental design.

Chapter 7

Adsorption of 6-MHO on Two Indoor Relevant Surface Materials: SiO_2 and TiO_2

7.1 Background

In this dissertation, we have only considered one class of indoor pollutants, those that can be emitted from cleaning processes or related to these products via chemical reactions. However, it is vital to extend our study to other indoor pollutants coming from other sources in the indoor environment. One very important source of indoor pollutants are emissions from humans. [1, 3, 112] Human occupants have been shown to emit of volatile compounds from both the skin and human breath as well as chemical reactions involving the human body. [6, 113, 114]

For example, the reaction of ozone with human skin can lead to an increase of concentration of volatile and semi-volatile compounds including mono-carbonyls and di-carbonyls, both

in the gas phase and in skin oils. [9, 115] In addition, secondary carbonyl emissions have also been detected from carpet fibers, showcasing the rather complicated sources of indoor pollutants. [116] Since carbonyls are respiratory and skin irritants, it is pertinent to study the interactions between these molecules and the different compartments within indoor environments to better understand how they may be removed from indoor air whether, for example, through ventilation, surface partitioning or through chemical reactions. [117, 118]

One prevalent carbonyl is 6-methyl-5-hepten-2-one (6-MHO), a product of skin oil ozonolysis and gas phase reactions of ozone and geranyl acetone. [119, 120] 6-MHO has a derived human reference value for sensory irritation of 0.3 ppm and 0.5 ppm for airflow irritation. [121] It has been measured in office air at 0.8 ppb and in more than 50% of 107 commercial flights measured in a field study. [122, 123] In addition, in a simulated office with two subjects and an initial ozone concentration of 33 ppb, 6-MHO has been measured at a concentration of 2.3 ppb. [9] 6-MHO has also been measured to form even after inhabitants have left the indoor environment five days earlier. [124]

Although 6-MHO is prevalent in the indoor environment, one aspect of its indoor chemistry that requires further investigation are its interactions with surfaces. Partitioning of volatile organic compounds to indoor surfaces is important to study due to the high surface area to volume ratios in the indoor environment. While an earlier study suggested surface reservoirs may not be a substantial source of 6-MHO, [124] as discussed in Chapter 1, indoor surfaces are host to complex multiphase and heterogenous processes including surface oxidation, acid-base chemistry, and the adsorption and desorption of molecules. In addition, organic films form readily on indoor surfaces. [125]

Previous AFM-PTIR studies have revealed that glass slides places in a kitchen result in organic films containing a carbonyl stretching frequency associated with an aldehyde compound. [126] Additionally, a study of latex paint surfaces, which contain 38% by volume TiO_2 [93] has shown via portable surface reactor experiments that ketones have significant

partitioning to paint films. [127]

Our results have important implications for the adsorption and partitioning of products of skin oil ozonolysis on indoor surfaces and potentially indoor film formation, as well as possible reactivity between 6-MHO and TiO_2 surfaces. Furthermore, to the best of our knowledge, this is the first time the surface chemistry of 6-MHO has been investigated.

7.2 Computational Methods

Force field-based MD simulations and AIMD simulations were used to investigate the adsorption of 6-MHO on SiO_2 and TiO_2 surfaces. The TiO_2 surfaces have been constructed in the same way as Chapter 6 and the SiO_2 surfaces have been constructed as the same way in Chapter 5.

For the AIMD simulations, it is important to note that the basis sets and functionals used for SiO_2 and TiO_2 simulations are different, thus only comparisons between simulations of the same basis set and functionals have been made.

In order to further study the role of the 6-MHO dihedral angle on surface stability, a relaxed scan of the dihedral angle, detailed in Section 7.3.4., in the gas phase was performed via electronic structure calculations with the Gaussian 16 package. [66] The scan was performed using the M06-2x/6-31g(d) level of theory. [67]

7.2.1 Surface Analysis Techniques

The 6-MHO molecule has a key similarity to the carvone molecule, the presence of a ketone functional group along with $C_{sp}{}^2$ carbon centers. Hydrogen bonding interactions were analyzed in the same way as in Chapters 5 and 6. Regarding the ketone functional group,

as discussed in Chapter 5, oxygen silicon associations have been measured for 6-MHO on the SiO_2 surface, and as discussed in Chapter 6, oxygen surface Ti interactions have been measured for 6-MHO on the non-hydroxylated TiO_2 surface.

To calculate hydrogen bonding probabilities, hydrogen bonds were defined to be present if the distance between donor and acceptor was less 3.5 Å and if the angle between acceptor, donor hydrogen, and donor oxygen was within 120 to 180° for both types of hydrogen bonds. To determine the presence of a 6-MHO oxygen silicon association on the SiO_2 surface, all distances between the 6-MHO oxygen atom and the surface were measured every 1 ps for the last 45 ns of the unbiased MD simulation. The minimum distance between the 6-MHO oxygen and the surroundings was determined per frame and the proportion of these distances that were to a 3-coordinated Si atom was used to determine the probability of an oxygen silicon association.

7.3 Results

This is our first attempt at studying the adsorption of one molecule on two different surfaces. First, the results of the experimental IR measurements will be described in Section 7.3.1, and the classical MD results will be described in Section 7.3.2, the AIMD results will be described in Section 7.3.3, and the electronic structure calculation results are discussed in Section 7.3.4.

7.3.1 Experimental Results

First, we will start with the experimental results for 6-MHO adsorbed on the SiO_2 surface. Figure 7.1(a) shows an IR spectrum of gas-phase 6-MHO at a pressure of 550 mTorr at 296 K. The IR spectra and vibrational modes of 6-MHO are assigned as followed, 2976, 2929,

2872 cm^{-1} for the aliphatic C-H stretching motion; a broad band at 1736 cm^{-1} is observed for the C=O and C=C stretching vibrations; 1445, 1363 cm^{-1} for CH_3 and CH_2 bending vibrations motion, respectively. Figure 7.1(a) shows 6-MHO in the gas phase and Figure 7.1(b) shows 6-MHO on SiO_2 surfaces at shows the IR absorbance spectra of 6-MHO on the SiO_2 surface at 2, 5, 10, 21, 42, 76, 119 and 161 mTorr equilibrium pressure under dry conditions, and Figure 7.1(c) shows a zoomed in for the C=O stretching region. Notice, unlike carvone in Chapter 5, there is no shoulder in the C=O stretching region.

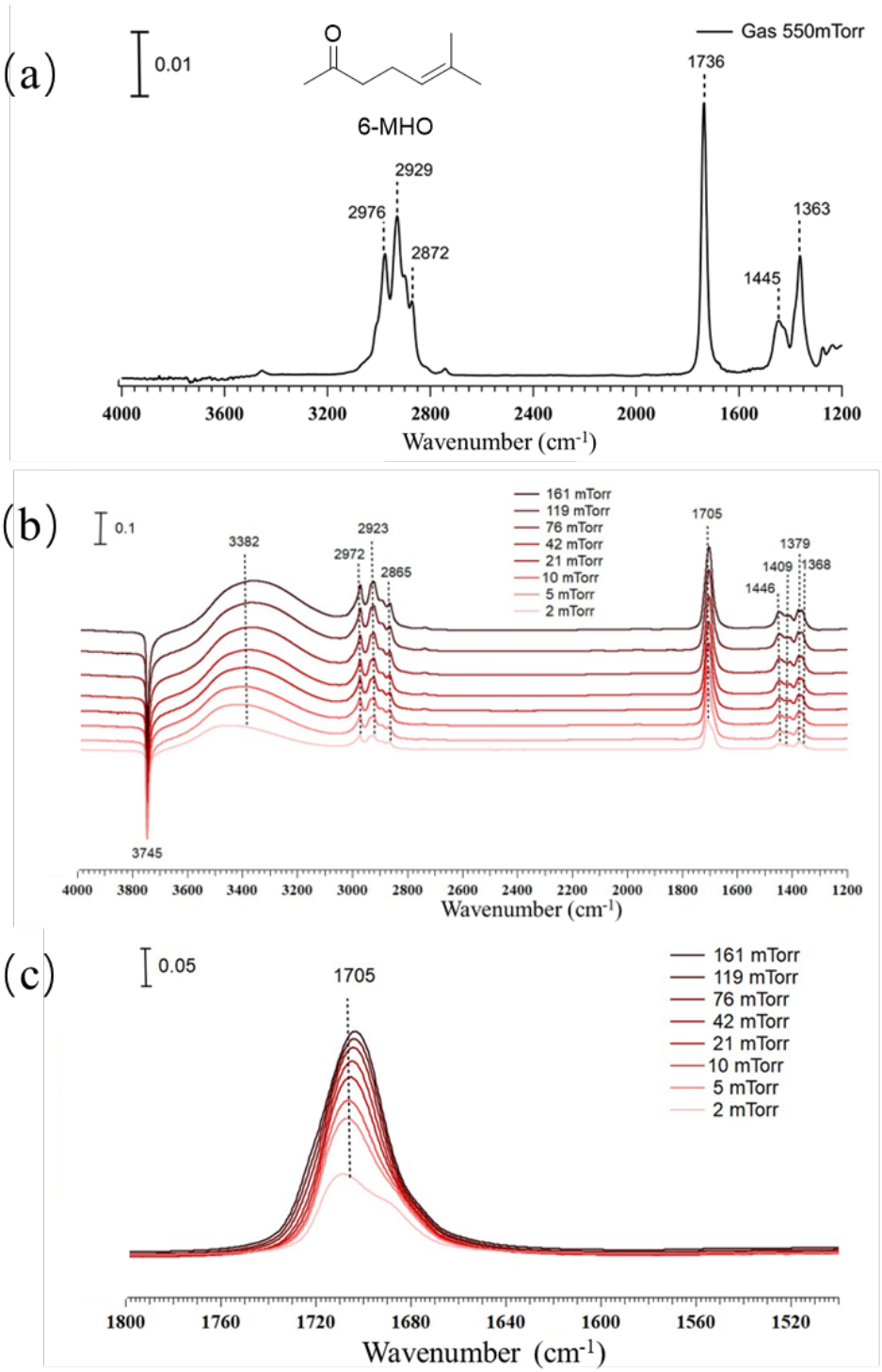

Figure 7.1: FT-IR gas-phase spectra of 550 mTorr 6-MHO at 296 K in the spectral ranges extending from ca. 1200 to 4000 cm^{-1}. (scale bar = 0.01 absorbance units) (b) FT-IR absorbance spectra of 6-MHO on the SiO_2 surface at an equilibrium pressure of 2, 5, 10, 21, 42, 76, 119, and 161 mTorr under dry conditions, respectively. (scale bar = 0.1 absorbance units) (c) The surface adsorption spectral range extending from ca. 1500 to 1800 cm^{-1} as function of pressures from (b). (scale bar = 0.05 absorbance units)

The assigned modes for Figure 7.1(b) are as follows: the negative peak at 3745 cm^{-1} is attribute to the loss of isolated Si-OH groups due to the hydrogen-bonding interactions with 6-MHO, as observed in the shifted broad peak centered at 3384 cm^{-1}. [18] The adsorption bands at 2972 cm^{-1}, 2923 cm^{-1} and 2865 cm^{-1} are for the C-H sp^3 stretching motion from alkene; a big broad band at 1705 cm^{-1} is observed for the C=O and C=C stretching vibrations; and the region from 1446, 1409 and 1379, 1368 cm^{-1} are for CH_3 and CH_2 bending vibrations motion, respectively. The C=O and C=C groups are involved in the interactions with the hydroxylated SiO_2 surface, producing a shift toward lower wavenumber of 21 cm^{-1} in the corresponding stretching band when compared to the gas-phase spectra.

Figure 7.1(c) shows the IR absorbance spectra of 6-MHO on SiO_2 surface as function of pressure in the spectra ranging from ca. 1500 to 1800 cm^{-1} as shown in the Figure 1(b), there is no significant peak shift during the growth of 6-MHO adsorbed on SiO_2 surface as discussed in Chapter 5, indicating a lack of oxygen silicon associations from the experimental results. There is no increase of adsorbed 6-MHO after 21 mTorr due to the lack of free Si-OH functional groups on the SiO_2 surface. As the 6-MHO pressure changes from 21 mTorr to 161 mTorr, there is about 24% increase in 6-MHO on the SiO_2 surface as determined by the integrated peak area of 6-MHO at 1705 cm^{-1}. Once the monolayer coverage of 6-MHO on the SiO_2 surface is reached, the ratio according to equation 7.1, which is the same as discussed in Chapter 6, is 0.17.

$$\frac{\Delta increase\ amount\ of\ adsorbate}{\Delta increase\ pressure} \tag{7.1}$$

Compared to carvone, at one monolayer coverage, there is a 30 % of amount carvone increased on the SiO_2 surface, and when the carvone pressure changes from 4 mTorr to 52 mTorr the ratio in equation 7.1 is 0.63, which is 3.7 times of that of 6-MHO.

Figure 7.2 shows the adsorption-desorption kinetics of 6-MHO onto the hydroxylated SiO_2

surface at an equilibrium pressure of 5, 12, 24, and 48 mTorr under dry conditions. The surface coverages were determined by integrating the absorption bands from 1640 to 1760 cm^{-1} for the adsorbed 6-MHO.

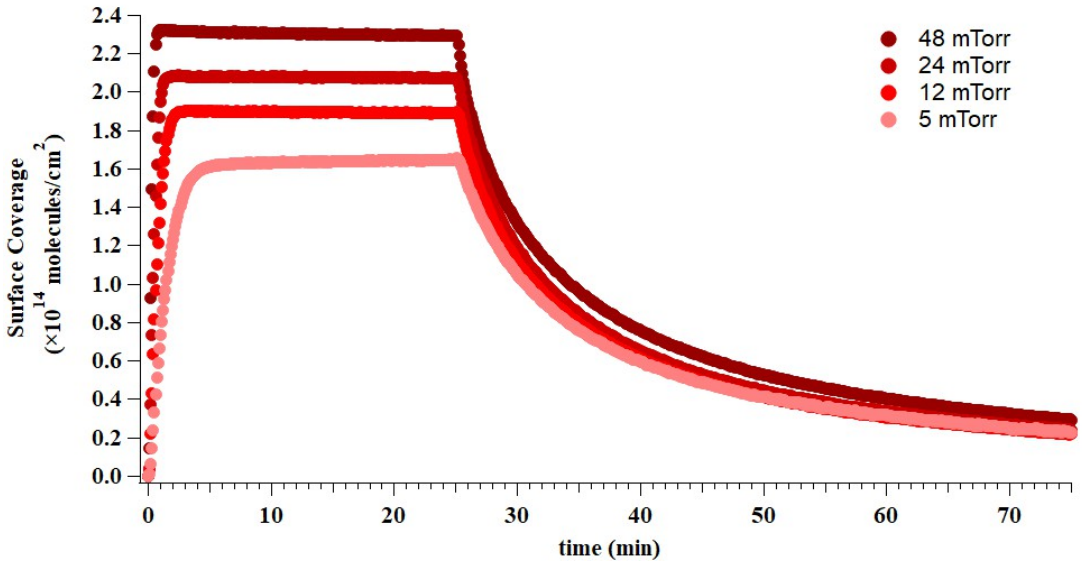

Figure 7.2: Temporal evolution of 6-MHO adsorption on the hydroxylated SiO_2 surface at an equilibrium pressure of 5, 12, 24, and 48 mTorr under dry conditions

A similar analysis to what is described in Chapter 3 has been done and and the kinetics for α-terpineol, carvone, dihydromyrcenol, linalool, 6-MHO, and limonene are all shown in Figure 7.3. In the classical MD results section, these trends will be discussed.

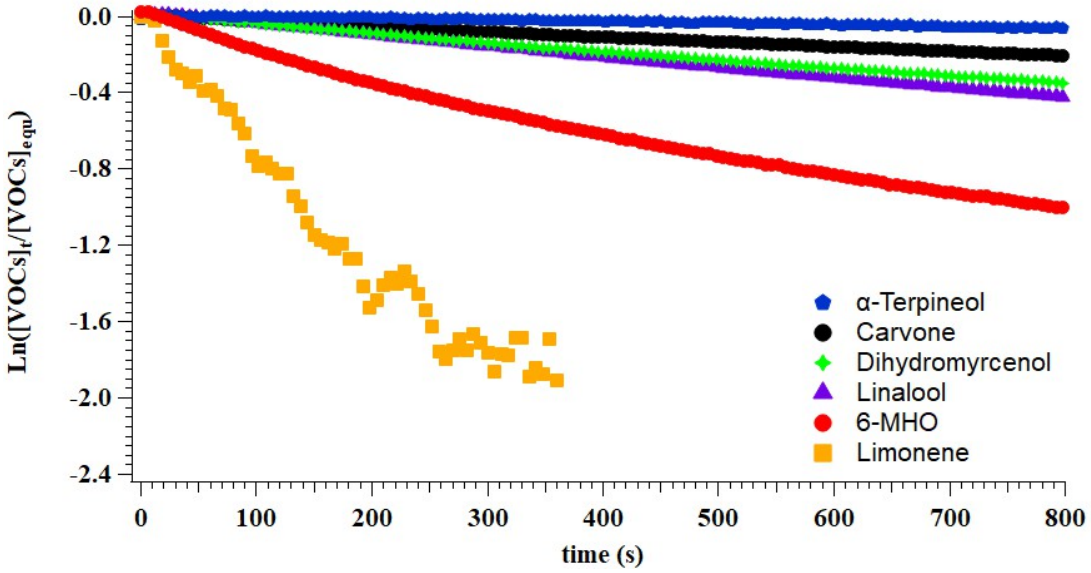

Figure 7.3: The apparent first order desorption kinetics $ln\frac{[VOC]_t}{[VOC]_{equ}}$ vs t(s)) for α-terpineol (blue solid pentagons), carvone (black solid circles), dihydromyrcenol (green solid diamonds), linalool (purple solid triangles), 6-MHO (red solid circles) and limonene (yellow solid squares) at 4 mTorr from the hydroxylated SiO_2 surface under dry conditions. The order of desorption kinetics are: $k_{des}^{\alpha-terpineol} < k_{des}^{carvone} < k_{des}^{dihydromyrcenol} < k_{des}^{linalool} < k_{des}^{6-MHO} < k_{des}^{limonene}$

Now, I will detail the experimental results for 6-MHO adsorbed on the TiO_2 surface. Figure 7.4 shows FT-IR absorbance spectra of 6-MHO on the TiO_2 surface at an equilibrium pressure of 3 mTorr at 297 $\pm$ 1 K under dry conditions, using the TiO_2 surface prior to adsorption as the background and with gas-phase contributions subtracted from the spectra.

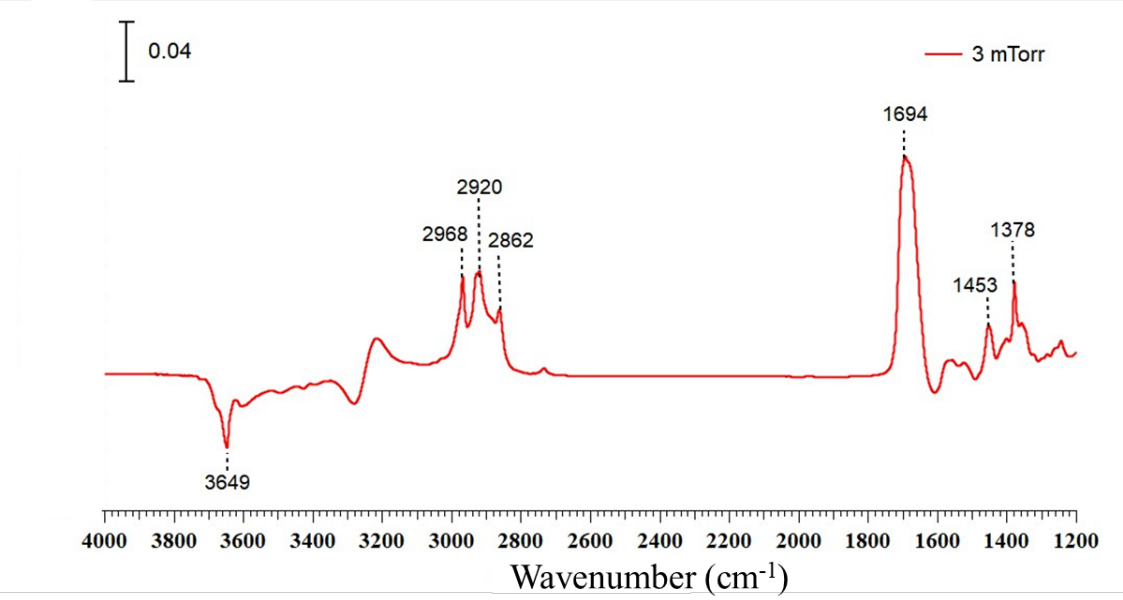

Figure 7.4: Absorbance FT-IR spectra of 6-MHO adsorbed on TiO_2 surface under dry conditions at an equilibrium pressure of 3 mTorr in the spectral range extending from ca. 1200 to 4000 cm^{-1}. (scale bar = 0.05 absorbance units)

Spectral changes are seen after the initial adsorption suggesting 6-MHO can undergo additional surface chemistry on the TiO_2 surface. The observed IR absorption band frequencies are in general agreement with gas-phase 6-MHO vibrational frequencies with the exception of the spectral range extending from ca. 1600 to 1800 cm^{-1}. The modes are assigned as follows: the negative peak at 3649 cm^{-1} is attribute to the loss of Ti-OH groups due to the hydrogen-bonding interactions with 6-MHO; 2968 cm^{-1}, 2920 cm^{-1} and 2862 cm^{-1} are for the C-H sp^3 stretching motion from the vinyl CH_3 groups; a big broad band centered at 1694 cm^{-1} with a red shift of 42 cm^{-1} when compared to the gas-phase spectra in Figure 7.1(a) due to the possible hydrogen binding interactions formed between 6-MHO carbonyl O atom and surface Ti-OH groups, is observed for the coupling of C=O and C=C stretching vibrations; and the region from 1446, 1409 and 1379, 1368 cm^{-1} are for CH_3 and CH_2 bending vibrations motion, respectively.

7.3.2 Classical Molecular Dynamics Results

To study the interactions of 6-MHO on indoor surfaces using classical molecular dynamics, we first performed a 50 ns unbiased simulation of 6-MHO on each surface. The SiO_2 surface is hydroxylated with a silanol surface density of 4.7 OH nm^{-2}, which resulted in surface 3-coordinated Si atoms. As discussed in our earlier work, [128] this allows for the prevalence of oxygen silicon associations between the carbonyl oxygen atom and 3-coordinated Si atoms. We determined oxygen silicon associations are prevalent in 58% of the last 45 ns of the unbiased MD simulations. The is a much lower portion of the simulation compared to our study of carvone, and this difference is due to the more flexible structure of 6-MHO that allows for the 6-MHO oxygen atom to more easily engage in hydrogen bonding. As discussed in the methods section and our previous work, there are two TiO_2 surfaces, one fully hydroxylated surface and one non-hydroxylated surface. Molecular snapshots in Figure 7.5 show 6-MHO on both TiO_2 surfaces and in the two predominant orientations on the SiO_2 surface.

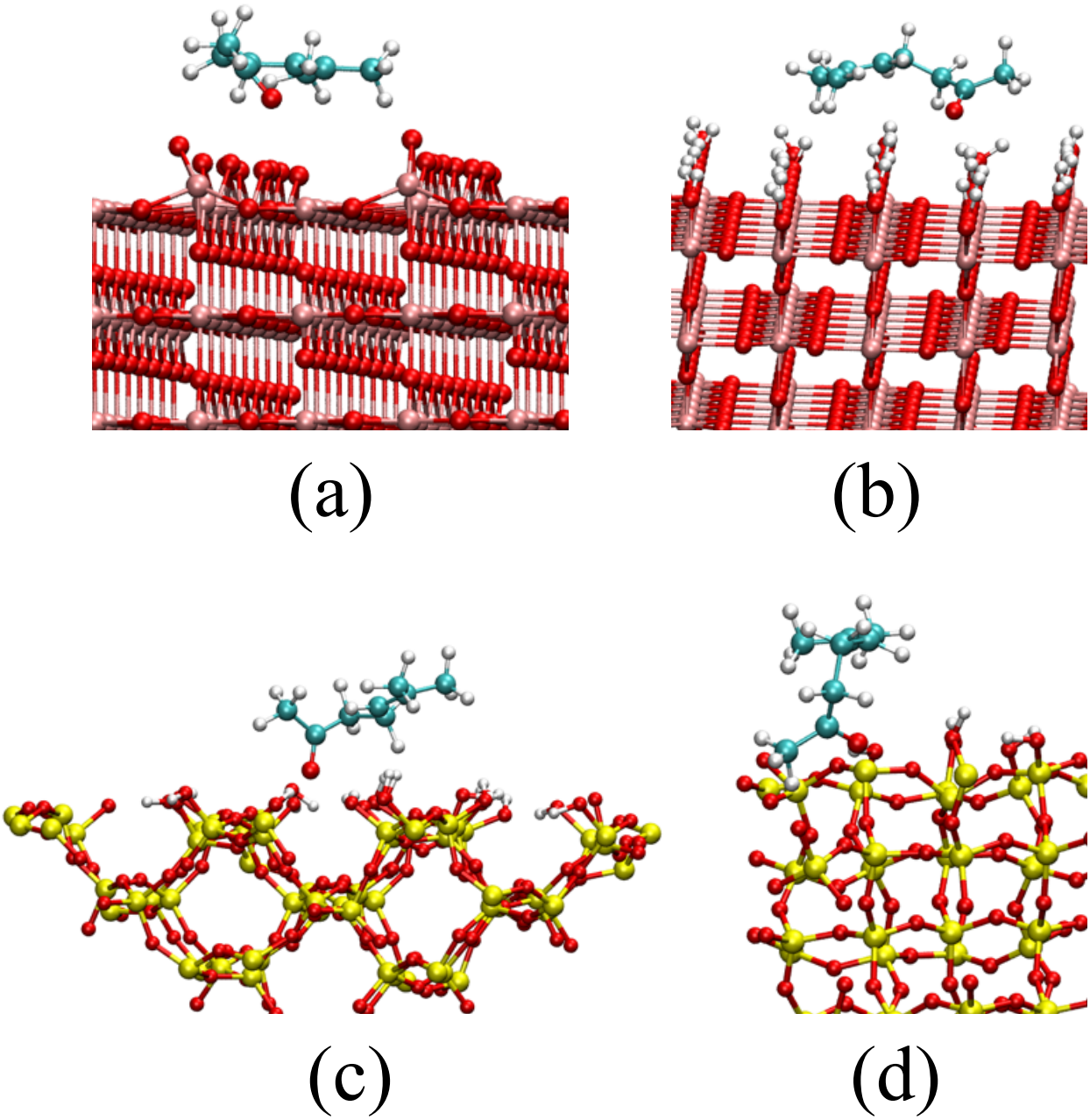

Figure 7.5: Molecular snapshots of 6-MHO on the SiO_2 and TiO_2 surfaces from force field-based MD simulations. (a) 6-MHO on the non-hydroxylated TiO_2 surface. (b) 6-MHO on the hydroxylated TiO_2 surface. (c) 6-MHO on the SiO_2 surface where the 6-MHO oxygen atom is engaged in a hydrogen bond with the surface OH groups. (d) 6-MHO on the TiO_2 surface where the 6-MHO oxygen atom is engaged in an oxygen silicon association. O atoms are colored red, Ti atoms pink, Si atoms yellow, H atoms white, and C atoms, cyan.

During the course of all the unbiased simulations, we determined the 6-MHO oxygen was

engaged in surface interactions. However, the conformation of the 6-MHO molecule varied depending on surface and interaction type. To characterize the conformational preferences, we measured the dihedral angle, ϕ, (shown in Figure 7.6a and Figure 7.6b) as shown in Figure 7.6c.

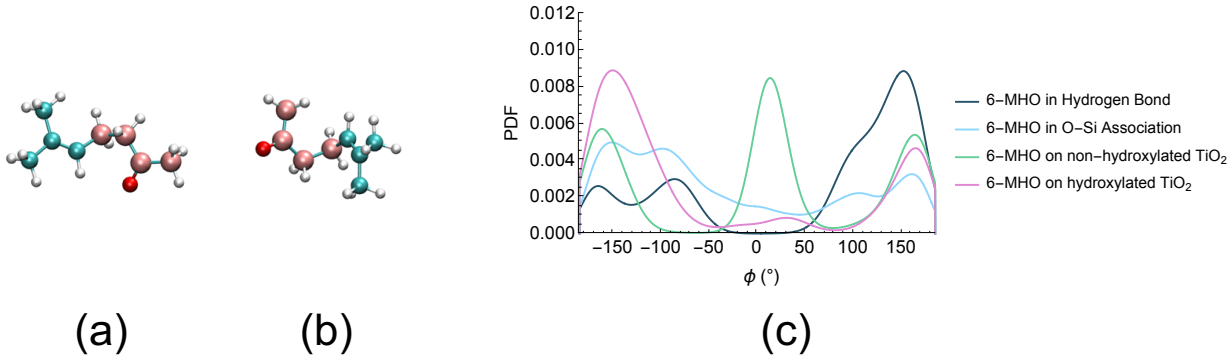

Figure 7.6: (a) 6-MHO with a dihedral angle of 151°, with the atoms used to measure the dihedral angle colored pink. This is a common dihedral angle measured for all surfaces and surface interaction types. (b) 6-MHO with a dihedral angle of 21°, which is frequently observed for 6-MHO on the non-hydroxylated TiO_2 surface and less often observed for 6-MHO on the hydroxylated TiO_2 surface and the SiO_2 surface with 6-MHO is in an oxygen silicon association. (c) Distribution of the 6-MHO dihedral angle on SiO_2 when the 6-MHO oxygen is engaged in a hydrogen bond, for SiO_2 when the 6-MHO oxygen is engaged in an oxygen silicon association, for the non-hydroxylated TiO_2 surface, and for the hydroxylated TiO_2 surface

Figure 7.4c shows an interesting trend, that for all surfaces, 6-MHO will often assume an extended conformation on the surface. However, given the broad distributions, this dihedral angle is a soft degree of freedom. This is in agreement with our previous study of two other linear molecules adsorbed on the SiO_2 surface, dihydromyrcenol and linalool. For our configurations that show hydrogen bonding between the 6-MHO oxygen atom and surface, we find the extended conformations of 6-MHO are highly favored. Extended conformations of 6-MHO enable more of the molecule to be positioned on the surface instead of pointing away from the surfaces, resulting in the formation of more stabilizing π-hydrogen bonds.

Interestingly, when 6-MHO interaction on the surface without a hydrogen bond between the 6-MHO oxygen atom and surface, 6-MHO sometimes forms a more bend structure. An

analysis of the dihedral angle ϕ in the gas phase shows that $\phi \sim 20°$ degrees is energetically unfavorable by 0.0092 kJ/mol compared to 150° based on our dihedral angle scan (discussed in Section 7.3.4). This small difference indicates a slight lack in stability of the surface interactions when 6-MHO is in these orientations.

From our unbiased simulations, we calculated the average number of hydrogen bonds and π-hydrogen bonds with 6-MHO on the surface. In Table 1, we show the average number of hydrogen bonds during the course of the trajectory and delineate between the entire trajectory of 6-MHO on the SiO_2 surface and the portions of the trajectory when 6-MHO is in a hydrogen bond with the SiO_2 surface. Note that there are no hydrogen atoms on the non-hydroxylated TiO_2 surface, so there are no hydrogen bonding statistics for that simulation.

Surface	Average number of hydrogen bonds	Average number of π-hydrogen bonds
SiO_2 (full simulation)	0.60	0.08
SiO_2 (when in a hydrogen bond)	1.46	0.07
TiO_2 (hydroxylated surface)	1.62	0.30

Table 7.1: Hydrogen bonding statistics for 6-MHO for the full simulation on the SiO_2 surface, for the portions of the simulation where the 6-MHO oxygen atom was in a hydrogen bond, and for the hydroxylated TiO_2 surface. π-hydrogen bonding criteria was determined if the $C_{sp}{}^2$-O distance was less than 3.5 Å and the OH- $C_{sp}{}^2$ angle was > 120 ° and hydrogen bonding criteria was determined if the O-O distance was less than 3.5 Å and the OH-O angle was > 120 °.

Table 1 shows that 6-MHO can form many hydrogen bonds on the SiO_2 and TiO_2 surface. We see that when the 6-MHO oxygen is in a hydrogen bond with the SiO_2 surface, there is a substantially higher average number of π-hydrogen bonds. In addition, both the hydrogen and π-hydrogen bonding numbers are greater when compared to those of the carvone molecule. We attribute this increase to the extended conformations of 6-MHO. For the SiO_2

surface, when the 6-MHO oxygen is in a hydrogen bond and consequentially is extended, there is a much greater probability of π-hydrogen bond formation. Although 58% of the trajectory shows 6-MHO is in an oxygen silicon association, we attribute this as an overpopulation of the trajectory due to the high partial charge of the Si atoms, and this is consistent with our studies of carvone. In addition, we suggest that the lower average number of π-hydrogen bonds for 6-MHO on the TiO_2 surface compared to the SiO_2 surface is due to the more rigid structure of the hydroxylated TiO_2 surface.

We have also calculated the free energy profiles (also referred to as potentials of mean force of PMF) for the desorption of 6-MHO from the SiO_2 and TiO_2 surface, as shown in Figure 7.7. The free-energy profiles are placed vertically such that their minima are at the zero of free energy.

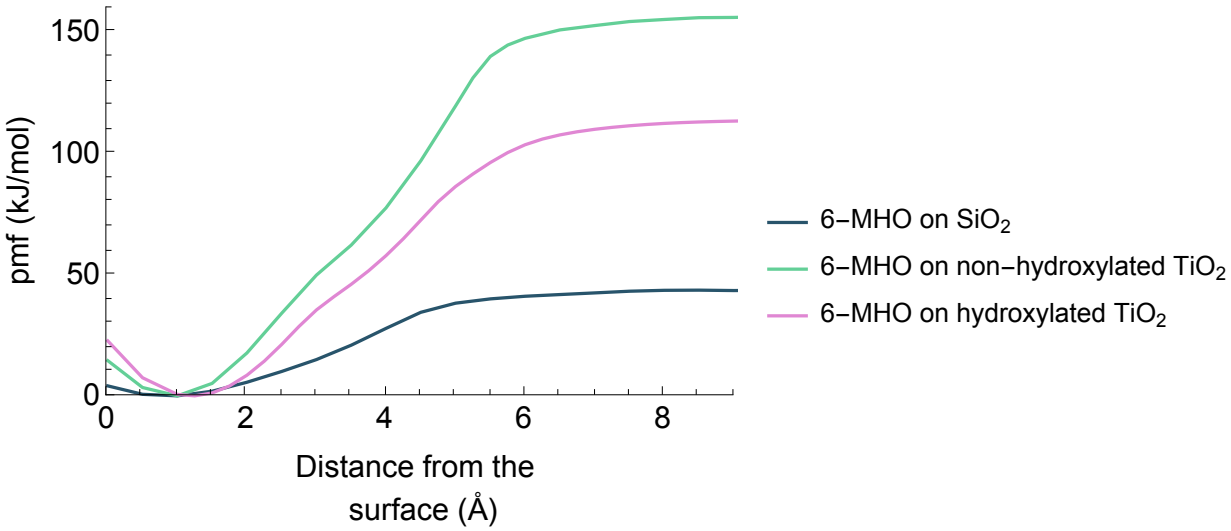

Figure 7.7: Potential of mean force (PMF) for the desorption of 6-MHO on the SiO_2 and TiO_2 surfaces calculated using classical MD simulations and umbrella sampling.

Figure 7.7 shows the free energy of desorption is much greater for the TiO_2 surface compared to SiO_2, and the free energy of desorption is greatest for the non-hydroxylated surface. We attribute this to the role of the electrostatic interaction from surface Ti atoms, with a partial charge of $+1.8365e$. These results are consistent with our earlier studies of limonene and

carvone on SiO_2 and TiO_2 surfaces. For the SiO_2 surface, the minima is much wider compared to TiO_2. This is due to relatively greater roughness of the amorphous SiO_2 surface compared to the rigid TiO_2 surface.

As discussed in Figure 7.3, the order of desorption kinetics for indoor relevant organic molecules on SiO_2 surfaces is $k_{des}^{\alpha-terpineol} < k_{des}^{carvone} < k_{des}^{dihydromyrcenol} < k_{des}^{linalool} < k_{des}^{6-MHO} < k_{des}^{limonene}$. We will now use our molecular dynamics simulations and experimental results to understand this trend in desorption kinetics.

Our MD simulations and experimental results together shed light on this trend in desorption kinetics. There are many important characteristics of surface adsorbates that affect desorption kinetics, and here we will investigate the role of surface interactions and molecular shape. Limonene, which lacks oxygen atoms and can only form π-hydrogen bonds with the surface shows the fastest desorption kinetics, suggesting that molecules that can form oxygen-based hydrogen bonds will consequently have longer desorption lifetimes. In addition, some molecules may on average form more hydrogen bonds. For example, dihydromyrcenol has a slightly slower desorption lifetime compared to linalool. In addition, during the course of an AIMD simulation trajectory, it was determined that dihydromyrcenol can form an average of 0.5 more hydrogen bonds to surface OH groups compared to linalool.

Molecular shape also affects desorption lifetimes. As discussed in Diaz et al, there is a fundamental difference in the adsorption on SiO_2 for linear versus ring containing molecules. [86] In their comparison of four different organic probes, citronellal, the only linear molecule, was shown to have the lowest amount adsorbed per unit surface area. It was suggested that the adsorption of the linear molecule results in a flat adsorption that blocks smaller pores that in which ring containing molecules may become trapped. This may explain why carvone and α-terpineol have lower desorption lifetimes compared to the linear dihydromyrcenol and linalool molecules. In addition, carvone may undergo a possible tautomerization as reported in the literature, resulting in a longer desorption lifetime. Our experimental evidence suggests

that 6-MHO does get trapped in pores and our dihedral angle distributions indicate that 6-MHO exists in a variety of surface geometries during the course of our MD simulations (even when only considering when the molecule is engaged in an oxygen-based hydrogen bond). Therefore, we that suggest pores can be blocked by extended 6-MHO molecules and occupied by bent 6-MHO molecules, leading to the shorter desorption lifetime when compared to carvone. In addition, the 6-MHO C=C bonds former π-hydrogen bonds compared to linalool and dihydromyrcenol, leading to the shorter desorption lifetime when compared to the above molecules. In addition, due to oxygen-based hydrogen bonds, the desorption lifetime of 6-MHO is longer than that of limonene.

7.3.3 *ab initio* Molecular Dynamics Results

In order to further investigate the interactions between 6-MHO and SiO_2 and TiO_2 surface, as well as to provide computational power spectra to compare to our experimental results, AIMD simulations of 6-MHO and SiO_2 and TiO_2 surfaces were performed.

As described in Chapters 5, two SiO_2 surfaces were considered, one with full surface hydroxylation, and one with a partially dehydroxylated surface with 2 dehydroxylated Si atoms, allowing for oxygen silicon associations to occur on the surface. The power spectra for the hydrogen atoms are shown in Figure 7.8, and the power spectra for the oxygen atoms n the carbonyl stretching region is shown in Figure 7.9. Note that the positions and not exact intensities are comparable to experimental data. However, it is reasonable to compare the trends in AIMD power spectra to trends in the experimental FT-IR spectra.

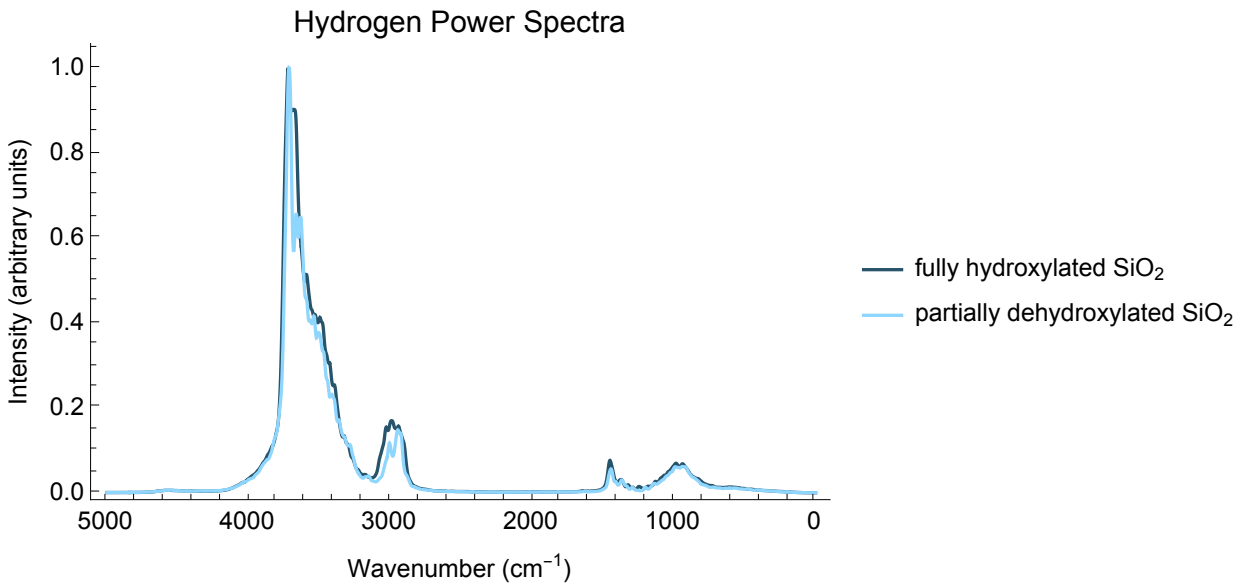

Figure 7.8: Power spectra for all hydrogen atoms for 6-MHO adsorbed on the fully hydroxylated SiO_2 surface and partially dehydroxylated SiO_2 surface. All intensity values have been rescaled to run from 0 to 1.

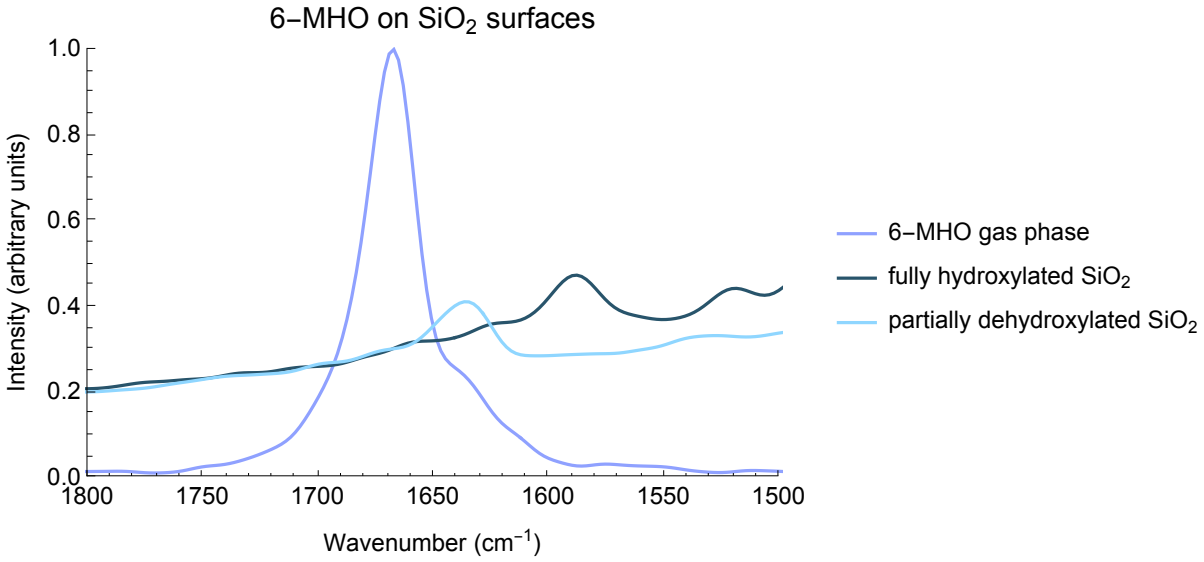

Figure 7.9: Power spectra for all oxygen atoms in the region of the 6-MHO C=O stretch for 6-MHO in the gas phase, on a fully hydroxylated SiO_2 surface, and on a partially dehydroxylated SiO_2 surface. There is a slight red shift in the 1670 cm^{-1} wavenumber peak for 6-MHO on either surface. Consistent with our study of carvone, the red shift is greater for the fully hydroxylated SiO_2 surface compared to the partially dehydroxylated SiO_2 surface. All intensity values have been rescaled to run from 0 to 1 and the spectra for 6-MHO on the fully hydroxylated and partially dehydroxylated surfaces has been scaled by 5x for clarity.

The hydrogen power spectra show red shifting for the surface OH groups for both SiO_2 surfaces because, during the course of the 16 ps AIMD simulation of the partially dehydroxylated surface, only 7% of the time, the 6-MHO oxygen is in an oxygen silicon association. We find this lower fraction of the trajectory is consistent with the lack of shoulder at 1705 cm^{-1} in the experimental results and our previous discussion of the stability of 6-MHO in the linear geometry. This is a departure from our study of carvone that showed a more pronounced shoulder in the experimental IR spectra of the C=O stretch region at high mTorr. However, consistent with our study of carvone, the red shift is greater for the fully hydroxylated SiO_2 surface when the 6-MHO molecule can only for hydrogen bond, affirming that, for both molecules, hydrogen bonding is the dominant form of surface interaction.

Three TiO_2 surfaces have been considered to model the TiO_2 surface, as described in Chapter 6: a non-hydroxylated TiO_2 surface with 0 water molecules, second, a non-hydroxylated TiO_2 surface with 4 water molecules, and third, a fully hydroxylated surface. Power spectra for the hydrogen atoms of each system are depicted in Figure 7.10, for the oxygen atoms in Figure 7.11, and for the oxygen atoms in the carbonyl stretching region in Figure 7.12. Note that the non-hydroxylated TiO_2 surface with 0 water molecules has no surface hydrogen atoms, so no hydrogen power spectra was calculated.

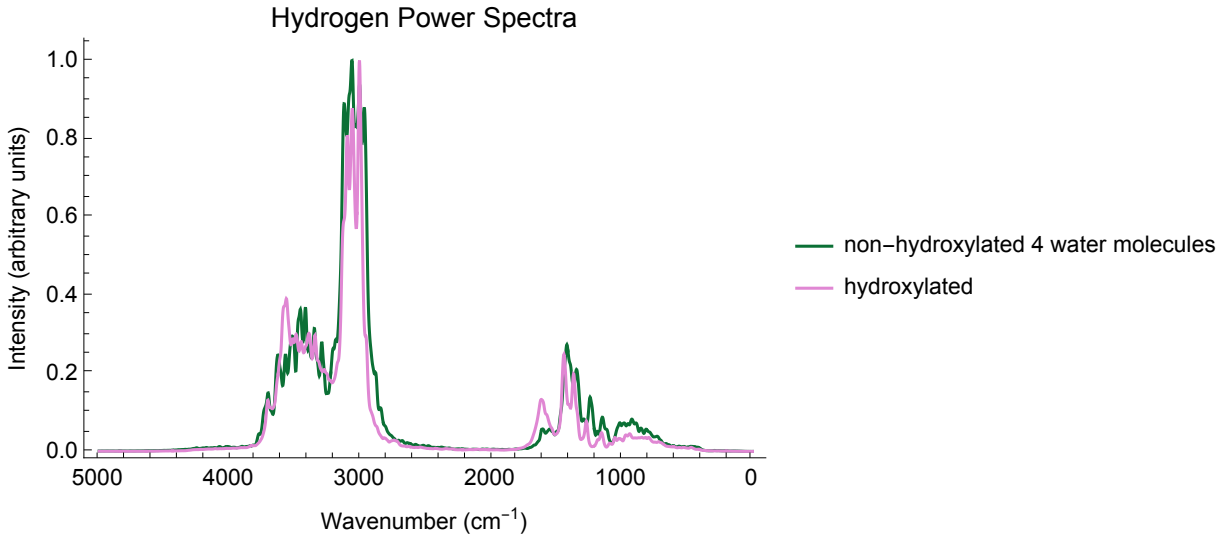

Figure 7.10: Power spectra for all hydrogen atoms for 6-MHO adsorbed on the non-hydroxylated TiO_2 surface with 4 water molecules and for 6-MHO adsorbed on the hydroxylated TiO_2 surface. All intensity values have been rescaled to run from 0 to 1.

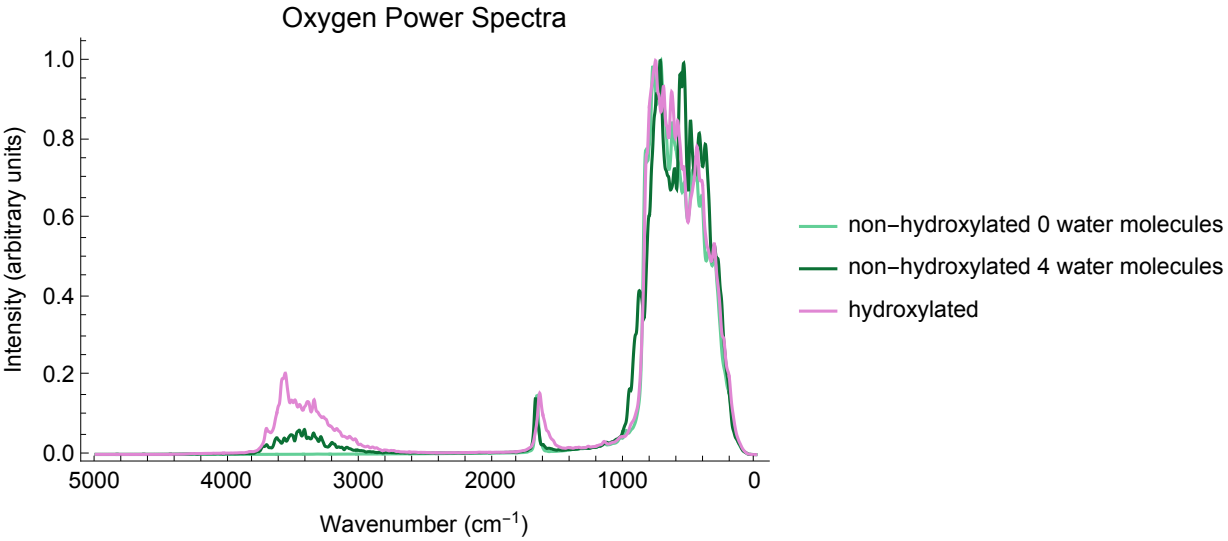

Figure 7.11: Power spectra for all oxygen atoms for 6-MHO adsorbed on the non-hydroxylated TiO_2 surface with 0 water molecules, for 6-MHO adsorbed on the non-hydroxylated TiO_2 surface with 4 water molecules, and for 6-MHO adsorbed on the hydroxylated TiO_2 surface. All intensity values have been rescaled to run from 0 to 1.

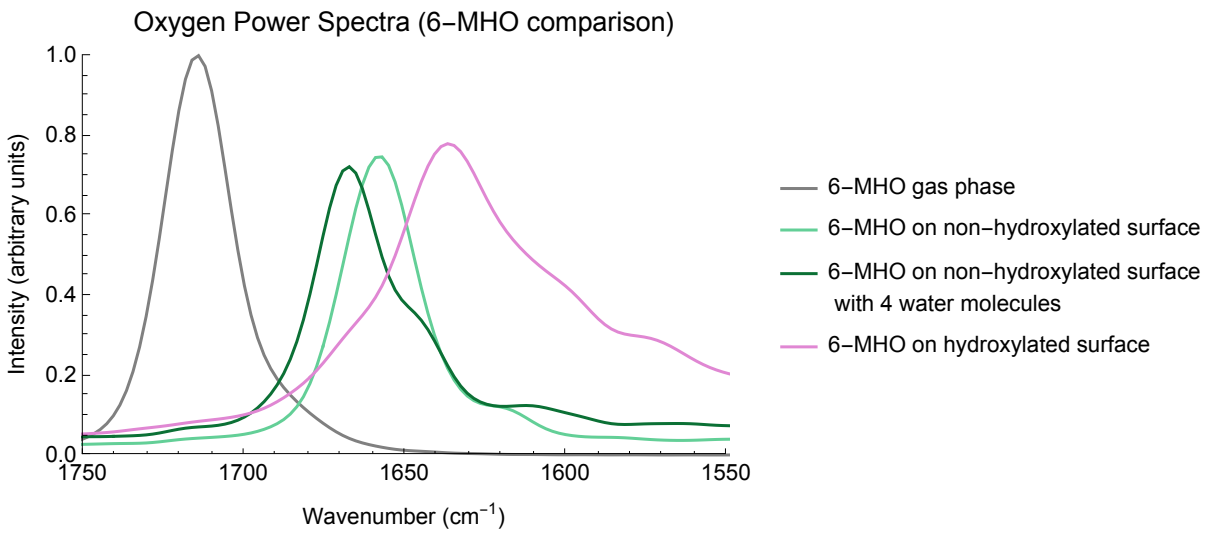

Figure 7.12: Power spectra for all oxygen atoms in the region of the 6-MHO C=O stretch for 6-MHO in the gas phase, on a non-hydroxylated TiO_2 surface with 0 water molecules, on a non-hydroxylated TiO_2 surface with 4 water molecules, and on a hydroxylated TiO_2 surface. Note, compared to Figure 7.10, there are slight differences in the 6-MHO gas phase spectra due to the difference in AIMD functional used. There is a slight red shift in the 1710 cm^{-1} for 6-MHO in the gas phase compared to TiO_2 on any TiO_2 surface. All intensity values have been scaled by 5x for clarity.

The hydrogen power spectra show a red shift consistent with our experimental results, which arises from the surface OH groups and water molecules engaging in hydrogen bonding with the 6-MHO oxygen atom and π-hydrogen bonding with the 6-MHO $C_{sp}{}^2$ atoms. In the oxygen power spectra, we observed that all AIMD simulations show a red shift, and for 6-MHO on the fully hydroxylated surface, this red shift is greater when compared to that of 6-MHO on SiO_2, consistent with our experimental observations. This suggests 6-MHO has a stronger interaction with the TiO_2 surface, which is consistent with our classical MD results.

Similar to our study of carvone, there is a red shift of the 6-MHO carbonyl stretch when in the presence of a non-hydroxylated surface with no water molecules. We find that during the course of that simulation the average 6-MHO oxygen to surface Ti atom distance is 2.13 $\pm$ 0.09 Å and 10% of the time the distance between the surface Ti atom to the 6-MHO oxygen

atom is shorter than that of the surface Ti atom to the oxygen below it in the TiO_2 crystal. This kind of close interaction is no seen in our study of 6-MHO on the SiO_2 surface, and due to our previous studies, we suggest this 6-MHO oxygen - Ti interaction may be the starting point for further surface interactions and surface chemistry.

7.3.4 Electronic Structure Calculation results

The gas phase scan of the dihedral angle shown in Figure 7.13 is shown here. The scan indicates at dihdedral angles of -150° and 150°, the molecule is more stable.

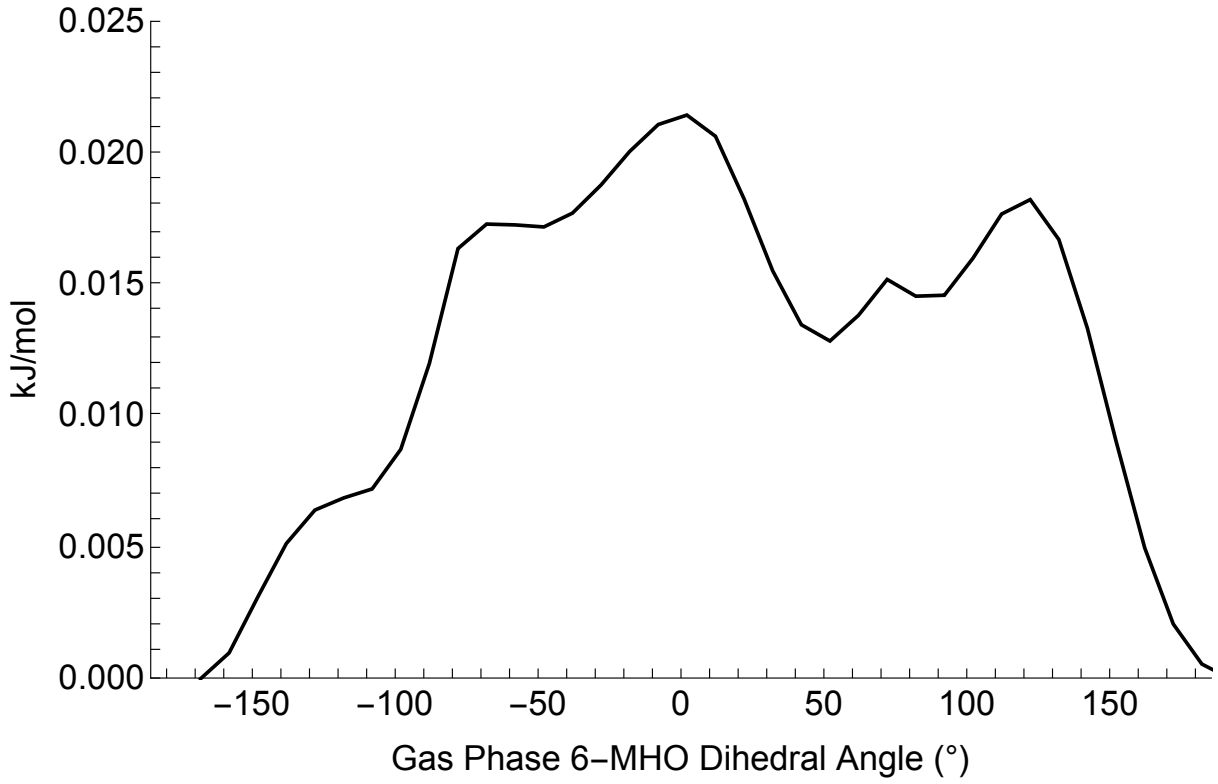

Figure 7.13: Gas phase scan of 6-MHO dihedral angle.

7.4 Conclusions

This study investigated the adsorption of an organic compound uniquely found in indoor environments, 6-MHO, on two indoor relevant surfaces, SiO_2 and TiO_2, utilizing both experimental and computational approaches. The FT-IR absorption spectra and MD simulations show that 6-MHO is adsorbed to the hydroxylated SiO_2 surface via dispersion forces, hydrogen bonds formed between the 6-MHO oxygen atom and surface OH groups, and π-hydrogen bonds formed between the 6-MHO $C_{sp}{}^2$ carbon atoms and surface OH groups, resulting in a red shift in both the experimental IR spectra and the power spectra as computed by our AIMD simulations. The interactions formed between 6-MHO and the hydroxylated SiO_2 surface are relatively strong, and the desorption kinetics of 6-MHO from the SiO_2 surface are about 3.7 time slower than that of limonene, but 6 times faster than that of carvone. Our classical force field-based MD simulations indicate that the free energy of desorption for 6-MHO on a TiO_2 surface is much greater than that of 6-MHO on a hydroxylated SiO_2 surface. In addition, we revealed that 6-MHO can adsorb to a TiO_2 surface via dispersion forces, hydrogen bonds formed between the 6-MHO oxygen atom and surface OH groups, π-hydrogen bonds formed between the 6-MHO $C_{sp}{}^2$ carbon atoms and surface OH groups, and a potential interaction between the 6-MHO oxygen atom and surface Ti atoms.

These results highlight the ability of 6-MHO, a linear ketone, which has been detected widely in indoor environments, to adsorb on to indoor relevant surfaces. It is suggested from this study that surface partitioning is therefore an additional pathway for the products of skin oil ozonolysis in the indoor environment and provides insights into our understanding of the role of human occupants on indoor chemistry and indoor air quality.

Chapter 8

Conclusion

8.1 Using Computational Chemistry Study the Indoor Environment

Computational chemistry is not widely used to study the indoor environment. However, these studies show how computational chemistry can be used to elucidate indoor air process and parameterize kinetic models. These studies also show the powerful ability of computational chemistry to strengthen conclusions made by experimental measurements. There has been great agreement across content studied, from surfaces, adsorbates, to even the role of % RH.

A computational chemistry approach has helped explain issues pertaining to indoor molecules on a hydroxylated SiO_2 surface, which is a proxy for a glass surface. We have discussed how limonene is retained on a SiO_2 surface even at high % RH through stabilizing π-hydrogen bonds and dispersion forces. We have discussed how certain limonene isomers are able to retain on SiO_2 surfaces longer than other isomers, and the interesting role that the location of C=C bonds plays in these differences. We have also discussed the heterogeneous interactions

of oxygen containing molecules, including separate studies of molecules with OH groups and molecules with ketone groups. In this work, we have discussed the role of the shape of the adsorbate and the location of $C_{sp}{}^2$ and oxygen atoms.

A computational chemistry approach has also helped explain issues pertaining to indoor molecules on a TiO_2 surface. Although there is some uncertainty of the nature of the real world 110 rutile TiO_2 surface and a single model surface has not been constructed, by utilizing two extrema of the real world TiO_2 surface, we have achieved agreement with experimental measurements. Our studies of TiO_2 surfaces have indicated the unique role of water on the TiO_2 surface, the potential interaction between oxygen containing molecules and surface Ti atoms, as well as the formation of hydrogen and π-hydrogen bonds between adsorbates and TiO_2 surfaces. Our work has also formed a connection to a kinetic process model for adsorption of limonene on the TiO_2 surface.

Overall, there are many more interesting ways continue to study the indoor environment, and I pose some questions below:

- What is the role of thin films on the adsorption of indoor pollutants on SiO_2 surfaces?
- How do indoor relevant organic molecules interact with other prevalent indoor surfaces such as a carpet, drywall, or wooden surface?
- How do brominated flame retardants from plastics and computer electronics interact with indoor surfaces?

It is my hope that computational chemistry will continue to be a useful and efficient way to study these questions and many others. This work has showcased the potential of computational chemistry to study the indoor environment.

Bibliography

[1] W. W. Nazaroff and A. H. Goldstein. Indoor chemistry: research opportunities and challenges. *Indoor Air*, 25(4):357–361, 8 2015. ISSN 09056947. doi: 10.1111/ina.12219. URL http://doi.wiley.com/10.1111/ina.12219.

[2] Max G. Adam, Phuong T.M. Tran, and Rajasekhar Balasubramanian. Air quality changes in cities during the COVID-19 lockdown: A critical review. *Atmospheric Research*, 264:105823, 12 2021. ISSN 0169-8095. doi: 10.1016/J.ATMOSRES.2021.105823.

[3] Jonathan P.D. Abbatt and Chen Wang. The atmospheric chemistry of indoor environments. *Environmental Science: Processes and Impacts*, 22 (1):25–48, 1 2020. ISSN 20507895. doi: 10.1039/c9em00386j. URL https://pubs.rsc.org/en/content/articlehtml/2020/em/c9em00386jhttps://pubs.rsc.org/en/content/articlelanding/2020/em/c9em00386j.

[4] Peder Wolkoff and Gunnar D. Nielsen. Organic compounds in indoor air-their relevance for perceived indoor air quality? *Atmospheric Environment*, 35(26):4407–4417, 9 2001. ISSN 13522310. doi: 10.1016/S1352-2310(01)00244-8.

[5] Sasho Gligorovski and Jonathan P.D. Abbatt. An indoor chemical cocktail: The chemistry that determines human exposure to indoor pollutants is incompletely understood. *Science*, 359(6376):632–633, 2 2018. ISSN 10959203. doi: 10.1126/science.aar6837.

[6] Caleb Arata, Nadja Heine, Nijing Wang, Pawel K. Misztal, Pawel Wargocki, Gabriel Bekö, Jonathan Williams, William W. Nazaroff, Kevin R. Wilson, and Allen H. Goldstein. Heterogeneous Ozonolysis of Squalene: Gas-Phase Products Depend on Water Vapor Concentration. *Environmental science & technology*, 53(24):14441–14448, 12 2019. ISSN 15205851. doi: 10.1021/ACS.EST.9B05957/SUPPL{_}FILE/ES9B05957{_}SI{_}001.PDF. URL https://pubs.acs.org/doi/abs/10.1021/acs.est.9b05957.

[7] Ayesha Asif, Muhammad Zeeshan, and Muhammad Jahanzaib. Indoor temperature, relative humidity and CO2 levels assessment in academic buildings with different heating, ventilation and air-conditioning systems. *Building and Environment*, 133:83–90, 4 2018. ISSN 03601323. doi: 10.1016/j.buildenv.2018.01.042.

[8] A. M. Johnson, M. S. Waring, and P. F. DeCarlo. Real-time transformation of outdoor aerosol components upon transport indoors measured with aerosol mass spectrometry. *Indoor Air*, 27(1):230–240, 1 2017. ISSN 1600-0668. doi: 10.1111/INA.12299. URL https://onlinelibrary.wiley.com/doi/full/10.1111/ina.12299https://onlinelibrary.wiley.com/doi/abs/10.1111/ina.12299https://onlinelibrary.wiley.com/doi/10.1111/ina.12299.

[9] Armin Wisthaler and Charles J. Weschler. Reactions of ozone with human skin lipids: Sources of carbonyls, dicarbonyls, and hydroxycarbonyls in indoor air. *Proceedings of the National Academy of Sciences of the United States of America*, 107(15):6568–6575, 4 2010. ISSN 00278424. doi: 10.1073/PNAS.0904498106. URL www.pnas.org/cgi/doi/10.1073/pnas.0904498106.

[10] S. Liu, R. Li, R. J. Wild, C. Warneke, J. A. de Gouw, S. S. Brown, S. L. Miller, J. C. Luongo, J. L. Jimenez, and P. J. Ziemann. Contribution of human-related sources to indoor volatile organic compounds in a university classroom. *Indoor Air*, 26(6):925–938, 12 2016. ISSN 1600-0668. doi: 10.1111/INA.12272. URL https://onlinelibrary.wiley.com/doi/full/10.1111/ina.12272https://onlinelibrary.wiley.com/doi/abs/10.1111/ina.12272https://onlinelibrary.wiley.com/doi/10.1111/ina.12272.

[11] Xiaochen Tang, Pawel K. Misztal, William W. Nazaroff, and Allen H. Goldstein. Volatile organic compound emissions from humans indoors. *Environmental Science and Technology*, 50(23):12686–12694, 12 2016. ISSN 15205851. doi: 10.1021/ACS.EST.6B04415/ASSET/IMAGES/LARGE/ES-2016-04415H{_}0004.JPEG. URL https://pubs.acs.org/doi/full/10.1021/acs.est.6b04415.

[12] J. P.S. Wong, N. Carslaw, R. Zhao, S. Zhou, and J. P.D. Abbatt. Observations and impacts of bleach washing on indoor chlorine chemistry. *Indoor Air*, 27(6):1082–1090, 11 2017. ISSN 1600-0668. doi: 10.1111/INA.12402. URL https://onlinelibrary.wiley.com/doi/full/10.1111/ina.12402https://onlinelibrary.wiley.com/doi/abs/10.1111/ina.12402https://onlinelibrary.wiley.com/doi/10.1111/ina.12402.

[13] Anita M. Avery, Michael S. Waring, and Peter F. DeCarlo. Human occupant contribution to secondary aerosol mass in the indoor environment. *Environmental Science: Processes & Impacts*, 21(8):1301–1312, 8 2019. ISSN 2050-7895. doi: 10.1039/C9EM00097F. URL https://pubs.rsc.org/en/content/articlehtml/2019/em/c9em00097fhttps://pubs.rsc.org/en/content/articlelanding/2019/em/c9em00097f.

[14] G. C. Morrison, N. Carslaw, and M. S. Waring. A modeling enterprise for chemistry of indoor environments (CIE). *Indoor Air*, 27(6):1033–1038, 11 2017. ISSN 1600-0668. doi: 10.1111/INA.12407. URL https://onlinelibrary.wiley.com/doi/full/10.1111/ina.12407https://onlinelibrary.wiley.com/doi/abs/10.1111/ina.12407https://onlinelibrary.wiley.com/doi/10.1111/ina.12407.

[15] Brett C. Singer, Alfred T. Hodgson, Toshifumi Hotchi, Katherine Y. Ming, Richard G. Sextro, Emily E. Wood, and Nancy J. Brown. Sorption of organic gases in residential rooms. *Atmospheric Environment*, 41(15):3251–3265, 5 2007. ISSN 13522310. doi: 10.1016/j.atmosenv.2006.07.056.

[16] Glenn C. Morrison. Interfacial chemistry in indoor environments. *Environmental Science and Technology*, 42(10):3495–3499, 5 2008. ISSN 0013936X. doi: 10.1021/es087114b.

[17] Charles J. Weschler, Alfred T. Hodgson, and John D. Wooley. Indoor Chemistry: Ozone, Volatile Organic Compounds, and Carpets. *Environmental Science and Technology*, 26(12):2371–2377, 12 1992. ISSN 15205851. doi: 10.1021/es00036a006.

[18] Yuan Fang, Dominika Lesnicki, Kristin J. Wall, Marie Pierre Gaigeot, Marialore Sulpizi, Veronica Vaida, and Vicki H. Grassian. Heterogeneous Interactions between Gas-Phase Pyruvic Acid and Hydroxylated Silica Surfaces: A Combined Experimental and Theoretical Study. *Journal of Physical Chemistry A*, 123(5):983–991, 2 2019. ISSN 15205215. doi: 10.1021/acs.jpca.8b10224. URL `https://pubs.acs.org/sharingguidelines`.

[19] Donald A. McQuarrie. *Statistical Mechanics*. 2000. URL `https://archive.org/details/StatisticalMechanics_201709`.

[20] Fang Yu Lin and Alexander D. MacKerell. Force Fields for Small Molecules. In *Methods in Molecular Biology*, volume 2022, pages 21–54. Humana Press Inc., 2019. doi: 10.1007/978-1-4939-9608-7{_}2.

[21] Christopher G. Mayne, Jan Saam, Klaus Schulten, Emad Tajkhorshid, and James C. Gumbart. Rapid parameterization of small molecules using the force field toolkit. *Journal of Computational Chemistry*, 34(32):2757–2770, 12 2013. ISSN 01928651. doi: 10.1002/jcc.23422. URL `http://doi.wiley.com/10.1002/jcc.23422`.

[22] L. T. Zhuravlev. The surface chemistry of amorphous silica. Zhuravlev model. *Colloids and Surfaces A: Physicochemical and Engineering Aspects*, 173(1-3):1–38, 11 2000. ISSN 09277757. doi: 10.1016/S0927-7757(00)00556-2.

[23] Erik G. Brandt and Alexander P. Lyubartsev. Systematic Optimization of a Force Field for Classical Simulations of TiO2-Water Interfaces. *Journal of Physical Chemistry C*, 119(32):18110–18125, 7 2015. ISSN 19327455. doi: 10.1021/acs.jpcc.5b02669.

[24] G. M. Torrie and J. P. Valleau. Nonphysical sampling distributions in Monte Carlo free-energy estimation: Umbrella sampling. *Journal of Computational Physics*, 23(2): 187–199, 2 1977. ISSN 10902716. doi: 10.1016/0021-9991(77)90121-8.

[25] Johannes Kästner. Umbrella sampling. *Wiley Interdisciplinary Reviews: Computational Molecular Science*, 1(6):932–942, 2011. ISSN 17590884. doi: 10.1002/wcms.66.

[26] Alan Grossfield. "WHAM: the weighted histogram method", version 2.0.9.1. URL `http://membrane.urmc.rochester.edu/?page_id=126`.

[27] P. Hohenberg and W. Kohn. Inhomogeneous electron gas. *Physical Review*, 136(3B): B864, 11 1964. ISSN 0031899X. doi: 10.1103/PHYSREV.136.B864/FIGURE/1/THUMB. URL https://journals.aps.org/pr/abstract/10.1103/PhysRev.136.B864.

[28] W. Kohn and L. J. Sham. Self-consistent equations including exchange and correlation effects. *Physical Review*, 140(4A):A1133, 11 1965. ISSN 0031899X. doi: 10.1103/PHYSREV.140.A1133/FIGURE/1/THUMB. URL https://journals.aps.org/pr/abstract/10.1103/PhysRev.140.A1133.

[29] Reiner M. Dreizler and Eberhard K. U. Gross. The Kohn-Sham Scheme. *Density Functional Theory*, pages 43–74, 1990. doi: 10.1007/978-3-642-86105-5{_}4.

[30] Thomas D. Kühne, Marcella Iannuzzi, Mauro Del Ben, Vladimir V. Rybkin, Patrick Seewald, Frederick Stein, Teodoro Laino, Rustam Z. Khaliullin, Ole Schütt, Florian Schiffmann, Dorothea Golze, Jan Wilhelm, Sergey Chulkov, Mohammad Hossein Bani-Hashemian, Valéry Weber, Urban Borštnik, Mathieu Taillefumier, Alice Shoshana Jakobovits, Alfio Lazzaro, Hans Pabst, Tiziano Müller, Robert Schade, Manuel Guidon, Samuel Andermatt, Nico Holmberg, Gregory K. Schenter, Anna Hehn, Augustin Bussy, Fabian Belleflamme, Gloria Tabacchi, Andreas Glöß, Michael Lass, Iain Bethune, Christopher J. Mundy, Christian Plessl, Matt Watkins, Joost VandeVondele, Matthias Krack, and Jürg Hutter. CP2K: An electronic structure and molecular dynamics software package -Quickstep: Efficient and accurate electronic structure calculations. *Journal of Chemical Physics*, 152(19):194103, 5 2020. ISSN 10897690. doi: 10.1063/5.0007045. URL https://doi.org/10.1063/5.0007045.

[31] Martin Brehm and Barbara Kirchner. TRAVIS - A Free Analyzer and Visualizer for Monte Carlo and Molecular Dynamics Trajectories. *Journal of Chemical Information and Modeling*, 51(8):2007–2023, 8 2011. ISSN 1549-9596. doi: 10.1021/ci200217w. URL https://pubs.acs.org/doi/10.1021/ci200217w.

[32] Martin Thomas, Martin Brehm, Reinhold Fligg, Peter Vöhringer, and Barbara Kirchner. Computing vibrational spectra from ab initio molecular dynamics. *Physical Chemistry Chemical Physics*, 15(18):6608–6622, 5 2013. ISSN 14639076. doi: 10.1039/c3cp44302g.

[33] R. El Diasty, P. Fazio, and I. Budaiwi. The dynamic modelling of air humidity behaviour in a multi-zone space. *Building and Environment*, 28(1):33–51, 1 1993. ISSN 03601323. doi: 10.1016/0360-1323(93)90004-M.

[34] Joshua Abelard, Amanda R. Wilmsmeyer, Angela C. Edwards, Wesley O. Gordon, Erin M. Durke, Christopher J. Karwacki, Diego Troya, and John R. Morris. Adsorption of Substituted Benzene Derivatives on Silica: Effects of Electron Withdrawing and Donating Groups. *Journal of Physical Chemistry C*, 120(24):13024–13031, 2016. ISSN 19327455. doi: 10.1021/acs.jpcc.6b02028.

[35] Mathew E. McKenzie, Sushmit Goyal, Sung Hoon Lee, Hyun Hang Park, Elizabeth Savoy, Aravind R. Rammohan, John C. Mauro, Hyunbin Kim, Kyoungmin Min, and

Eunseog Cho. Adhesion of organic molecules on silica surfaces: A density functional theory study. *Journal of Physical Chemistry C*, 121(1):392–401, 2017. ISSN 19327455. doi: 10.1021/acs.jpcc.6b10394.

[36] Andrea B. Voges, Grace Y. Stokes, Julianne M. Gibbs-Davis, Robert B. Lettan, Paul A. Bertin, Rachel C. Pike, Son Binh T. Nguyen, Karl A. Scheidt, and Franz M. Geiger. Insights into heterogeneous atmospheric oxidation chemistry: Development of a tailor-made synthetic model for studying tropospheric surface chemistry. *Journal of Physical Chemistry C*, 111(4):1567–1578, 2007. ISSN 19327447. doi: 10.1021/jp065277l.

[37] Erik Uhde and Nicole Schulz. Impact of room fragrance products on indoor air quality. *Atmospheric Environment*, 106:492–502, 4 2015. ISSN 18732844. doi: 10.1016/j.atmosenv.2014.11.020.

[38] S. C. Rastogi, S. Heydorn, J. D. Johansen, and D. A. Basketter. Fragrance chemicals in domestic and occupational products. *Contact Dermatitis*, 45(4):221, 10 2001. ISSN 0105-1873. doi: 10.1034/j.1600-0536.2001.450406.x. URL `http://www.deepdyve.com/lp/wiley/fragrance-chemicals-in-domestic-and-occupational-products-KKUASSYmlfhttps://www.deepdyve.com/lp/wiley/fragrance-chemicals-in-domestic-and-occupational-produc`

[39] Thomas Wainman, Junfeng Zhang, Charles J. Weschler, and Paul J. Lioy. Ozone and limonene in indoor air: A source of submicron particle exposure. *Environmental Health Perspectives*, 108(12):1139–1145, 2000. ISSN 00916765. doi: 10.1289/ehp.001081139.

[40] William W. Nazaroff and Charles J. Weschler. Cleaning products and air fresheners: Exposure to primary and secondary air pollutants. *Atmospheric Environment*, 38(18): 2841–2865, 6 2004. ISSN 13522310. doi: 10.1016/j.atmosenv.2004.02.040.

[41] William L. Jorgensen, Jayaraman Chandrasekhar, Jeffry D. Madura, Roger W. Impey, and Michael L. Klein. Comparison of simple potential functions for simulating liquid water. *The Journal of Chemical Physics*, 79(2):926–935, 7 1983. ISSN 00219606. doi: 10.1063/1.445869. URL `http://aip.scitation.org/doi/10.1063/1.445869`.

[42] Steve Plimpton. Fast Parallel Algorithms for Short-Range Molecular Dynamics. Technical report, 1995. URL `http://www.cs.sandia.gov/sjplimp/main.html`.

[43] Loup Verlet. Computer "experiments" on classical fluids. I. Thermodynamical properties of Lennard-Jones molecules. *Physical Review*, 159(1):98–103, 7 1967. ISSN 0031899X. doi: 10.1103/PhysRev.159.98. URL `https://journals.aps.org/pr/abstract/10.1103/PhysRev.159.98`.

[44] Rolf E. Isele-Holder, Wayne Mitchell, and Ahmed E. Ismail. Development and application of a particle-particle particle-mesh Ewald method for dispersion interactions. *Journal of Chemical Physics*, 137(17), 11 2012. ISSN 00219606. doi: 10.1063/1.4764089.

[45] Shuichi Nosé. A unified formulation of the constant temperature molecular dynamics methods. *The Journal of Chemical Physics*, 81(1):511–519, 7 1984. ISSN 00219606. doi: 10.1063/1.447334. URL `http://aip.scitation.org/doi/10.1063/1.447334`.

[46] Jean Paul Ryckaert, Giovanni Ciccotti, and Herman J.C. Berendsen. Numerical integration of the cartesian equations of motion of a system with constraints: molecular dynamics of n-alkanes. *Journal of Computational Physics*, 23(3):327–341, 3 1977. ISSN 10902716. doi: 10.1016/0021-9991(77)90098-5.

[47] Chengteh Lee, Weitao Yang, and Robert G. Parr. Development of the Colle-Salvetti correlation-energy formula into a functional of the electron density. *Physical Review B*, 37(2):785–789, 1 1988. ISSN 01631829. doi: 10.1103/PhysRevB.37.785. URL `https://journals.aps.org/prb/abstract/10.1103/PhysRevB.37.785`.

[48] A. D. Becke. Density-functional exchange-energy approximation with correct asymptotic behavior. *Physical Review A*, 38(6):3098–3100, 9 1988. ISSN 10502947. doi: 10.1103/PhysRevA.38.3098.

[49] Joost VandeVondele and Jürg Hutter. Gaussian basis sets for accurate calculations on molecular systems in gas and condensed phases. *Journal of Chemical Physics*, 127 (11):114105, 9 2007. ISSN 00219606. doi: 10.1063/1.2770708. URL `http://aip.scitation.org/doi/10.1063/1.2770708`.

[50] Stefan Grimme, Jens Antony, Stephan Ehrlich, and Helge Krieg. A consistent and accurate ab initio parametrization of density functional dispersion correction (DFT-D) for the 94 elements H-Pu. *Journal of Chemical Physics*, 132(15):154104, 4 2010. ISSN 00219606. doi: 10.1063/1.3382344.

[51] Joost VandeVondele and Jürg Hutter. An efficient orbital transformation method for electronic structure calculations. *Journal of Chemical Physics*, 118(10):4365–4369, 3 2003. ISSN 00219606. doi: 10.1063/1.1543154. URL `http://aip.scitation.org/doi/10.1063/1.1543154`.

[52] A. L. Goodman, E. T. Bernard, and V. H. Grassian. Spectroscopic study of nitric acid and water adsorption on oxide particles: Enhanced nitric acid uptake kinetics in the presence of adsorbed water. *Journal of Physical Chemistry A*, 105(26):6443–6457, 7 2001. ISSN 10895639. doi: 10.1021/jp003722l.

[53] Yuan Fang, Pascale S.J. Lakey, Saleh Riahi, Andrew T. McDonald, Mona Shrestha, Douglas J. Tobias, Manabu Shiraiwa, and Vicki H. Grassian. A molecular picture of surface interactions of organic compounds on prevalent indoor surfaces: Limonene adsorption on SiO2. *Chemical Science*, 10(10):2906–2914, 3 2019. ISSN 20416539. doi: 10.1039/c8sc05560b.

[54] Ya Juan Feng, Teng Huang, Chao Wang, Yi Rong Liu, Shuai Jiang, Shou Kui Miao, Jiao Chen, and Wei Huang. π-Hydrogen Bonding of Aromatics on the Surface of Aerosols: Insights from Ab Initio and Molecular Dynamics Simulation. *Journal of Physical Chemistry B*, 120(27):6667–6673, 7 2016. ISSN 15205207. doi: 10.1021/acs.jpcb.6b01180. URL `https://pubs.acs.org/sharingguidelines`.

[55] S. K. Brown, M. R. Sim, M. J. Abramson, and C. N. Gray. Concentrations of Volatile Organic Compounds in Indoor Air – A Review. *Indoor Air*, 4(2):

123–134, 6 1994. ISSN 16000668. doi: 10.1111/j.1600-0668.1994.t01-2-00007.x. URL https://onlinelibrary.wiley.com/doi/full/10.1111/j.1600-0668.1994.t01-2-00007.xhttps://onlinelibrary.wiley.com/doi/abs/10.1111/j.1600-0668.1994.t01-2-00007.xhttps://onlinelibrary.wiley.com/doi/10.1111/j.1600-0668.1994.t01-2-00007.x.

[56] Alfred T Hodgson and Hal Levin. Volatile organic compounds in indoor air: A review of concentrations measured in North American since 1990. *Atmospheric Environment*, 4 2003. URL https://escholarship.org/uc/item/0hj3n87n.

[57] Sylwia Król, Jacek Namieśnik, and Bozena Zabiegała. α-Pinene, 3-carene and d-limonene in indoor air of Polish apartments: The impact on air quality and human exposure. *Science of the Total Environment*, 468-469:985–995, 1 2014. ISSN 18791026. doi: 10.1016/j.scitotenv.2013.08.099.

[58] Junming Ho, Brian T. Psciuk, Hilary M. Chase, Benjamin Rudshteyn, Mary Alice Upshur, Li Fu, Regan J. Thomson, Hong Fei Wang, Franz M. Geiger, and Victor S. Batista. Sum Frequency Generation Spectroscopy and Molecular Dynamics Simulations Reveal a Rotationally Fluid Adsorption State of α-Pinene on Silica. *Journal of Physical Chemistry C*, 120(23):12578–12589, 6 2016. ISSN 19327455. doi: 10.1021/acs.jpcc.6b03158.

[59] Hilary M. Chase, Junming Ho, Mary Alice Upshur, Regan J. Thomson, Victor S. Batista, and Franz M. Geiger. Unanticipated Stickiness of α-Pinene. *Journal of Physical Chemistry A*, 121(17):3239–3246, 5 2017. ISSN 15205215. doi: 10.1021/acs.jpca.6b12653.

[60] Elianna S. Frank, Hanyu Fan, Mona Shrestha, Saleh Riahi, Douglas J. Tobias, and Vicki H. Grassian. Impact of adsorbed water on the interaction of limonene with hydroxylated SiO2: Implications of π-hydrogen bonding for surfaces in humid environments. *Journal of Physical Chemistry A*, 124(50):10592–10599, 2020. ISSN 15205215. doi: 10.1021/acs.jpca.0c08600. URL https://pubs.acs.org/doi/abs/10.1021/acs.jpca.0c08600.

[61] A. Colombo, M. De Bortoli, E. Pecchio, H. Schauenburg, H. Schlitt, and H. Vissers. Chamber testing of organic emission from building and furnishing materials. *Science of The Total Environment*, 91(C):237–249, 2 1990. ISSN 0048-9697. doi: 10.1016/0048-9697(90)90301-A.

[62] Huey Jen Su, Chung Jen Chao, Ho Yuan Chang, and Pei Chih Wu. The effects of evaporating essential oils on indoor air quality. *Atmospheric Environment*, 41(6):1230–1236, 2 2007. ISSN 1352-2310. doi: 10.1016/J.ATMOSENV.2006.09.044.

[63] Tunga Salthammer. Emissions of Volatile Organic Compounds from Products and Materials in Indoor Environments. *Handbook of Environmental Chemistry*, 4:37–71, 2004. doi: 10.1007/B94830. URL https://link.springer.com/chapter/10.1007/b94830.

[64] K. V Vejrup and P Wolkoff. VOC emissions from some floor-cleaning agents. In *Healthy Buildings*, Budapest, Hungary, 1994.

[65] Liubin Huang, Elianna S. Frank, Saleh Riahi, Douglas J. Tobias, and Vicki H. Grassian. Adsorption of constitutional isomers of cyclic monoterpenes on hydroxylated silica surfaces. *The Journal of Chemical Physics*, 154(12):124703, 3 2021. ISSN 0021-9606. doi: 10.1063/5.0042467. URL https://aip.scitation.org/doi/10.1063/5.0042467.

[66] M. J. T. Frisch, G. W. Trucks, H. B. Schlegel, M. A. Scuseria, J. R. Robb, G. Cheeseman, V. Scalmani, G. A. Barone, H. Petersson, and et al. Nakatsuji. Gaussian 16, 2016.

[67] Yan Zhao and Donald G. Truhlar. The M06 suite of density functionals for main group thermochemistry, thermochemical kinetics, noncovalent interactions, excited states, and transition elements: two new functionals and systematic testing of four M06-class functionals and 12 other functionals. *Theoretical Chemistry Accounts 2007 120:1*, 120(1):215–241, 7 2007. ISSN 1432-2234. doi: 10.1007/S00214-007-0310-X. URL https://link.springer.com/article/10.1007/s00214-007-0310-x.

[68] S. F. Boys and F. Bernardi. The calculation of small molecular interactions by the differences of separate total energies. Some procedures with reduced errors. *Molecular Physics*, 19(4):553–566, 1970. ISSN 13623028. doi: 10.1080/00268977000101561. URL https://www.tandfonline.com/doi/abs/10.1080/00268977000101561.

[69] Charith E. Nanayakkara, James K. Dillon, and Vicki H. Grassian. Surface adsorption and photochemistry of gas-phase formic acid on TiO2 nanoparticles: The role of adsorbed water in surface coordination, adsorption kinetics, and rate of photoproduct formation. *Journal of Physical Chemistry C*, 118(44):25487–25495, 11 2014. ISSN 19327455. doi: 10.1021/JP507551Y/SUPPL{_}FILE/JP507551Y{_}SI{_}001.PDF. URL https://pubs.acs.org/doi/abs/10.1021/jp507551y.

[70] Crystal D. Forester, Jason E. Ham, and J. R. Wells. Gas-phase chemistry of dihydromyrcenol with ozone and OH radical: Rate constants and products. *International Journal of Chemical Kinetics*, 38(7):451–463, 7 2006. ISSN 1097-4601. doi: 10.1002/KIN.20174. URL https://onlinelibrary.wiley.com/doi/full/10.1002/kin.20174https://onlinelibrary.wiley.com/doi/abs/10.1002/kin.20174https://onlinelibrary.wiley.com/doi/10.1002/kin.20174.

[71] Xi Chen and Philip K. Hopke. A chamber study of secondary organic aerosol formation by linalool ozonolysis. *Atmospheric Environment*, 43(25):3935–3940, 8 2009. ISSN 1352-2310. doi: 10.1016/J.ATMOSENV.2009.04.033.

[72] Y. Yang and M. S. Waring. Secondary organic aerosol formation initiated by α-terpineol ozonolysis in indoor air. *Indoor Air*, 26(6):939–952, 12 2016. ISSN 1600-0668. doi: 10.1111/INA.12271. URL https://onlinelibrary.wiley.com/doi/full/10.1111/ina.12271https://onlinelibrary.wiley.com/doi/abs/10.1111/ina.12271https://onlinelibrary.wiley.com/doi/10.1111/ina.12271.

[73] J. R. Wells. Gas-Phase Chemistry of α-Terpineol with Ozone and OH Radical: Rate Constants and Products. *Environmental Science and Technology*, 39(18):6937–6943, 9 2005. ISSN 0013936X. doi: 10.1021/ES0481676. URL https://pubs.acs.org/doi/abs/10.1021/es0481676.

[74] Roger Atkinson, Christopher N. Plum, William P.L. Carter, Arthur M. Winer, and James N. Pitts. Rate constants for the gas-phase reactions of nitrate radicals with a series of organics in air at 298 ± 1 K. *Journal of Physical Chemistry*, 88(6):1210–1215, 1984. ISSN 00223654. doi: 10.1021/J150650A039/ASSET/J150650A039.FP.PNG{_}V03. URL https://pubs.acs.org/doi/abs/10.1021/j150650a039.

[75] Charles J. Weschler and Helen C. Shields. Production of the Hydroxyl Radical in Indoor Air. *Environmental Science and Technology*, 30(11):3250–3258, 1996. ISSN 0013936X. doi: 10.1021/ES960032F. URL https://pubs.acs.org/doi/abs/10.1021/es960032f.

[76] N. Yamamoto, D. G. Shendell, A. M. Winer, and J. Zhang. Residential air exchange rates in three major US metropolitan areas: results from the Relationship Among Indoor, Outdoor, and Personal Air Study 1999–2001. *Indoor Air*, 20(1):85–90, 2 2010. ISSN 1600-0668. doi: 10.1111/J.1600-0668.2009.00622.X. URL https://onlinelibrary.wiley.com/doi/full/10.1111/j.1600-0668.2009.00622.xhttps://onlinelibrary.wiley.com/doi/abs/10.1111/j.1600-0668.2009.00622.xhttps://onlinelibrary.wiley.com/doi/10.1111/j.1600-0668.2009.00622.x.

[77] Manolis N. Romanías, Habib Ourrad, Frédéric Thévenet, and Véronique Riffault. Investigating the Heterogeneous Interaction of VOCs with Natural Atmospheric Particles: Adsorption of Limonene and Toluene on Saharan Mineral Dusts. *Journal of Physical Chemistry A*, 120(8):1197–1212, 3 2016. ISSN 15205215. doi: 10.1021/ACS.JPCA.5B10323/SUPPL{_}FILE/JP5B10323{_}SI{_}001.PDF. URL https://pubs.acs.org/doi/abs/10.1021/acs.jpca.5b10323.

[78] Jorly Joseph and Eluvathingal D. Jemmis. Red-, blue-, or no-shift in hydrogen bonds: A unified explanation. *Journal of the American Chemical Society*, 129(15):4620–4632, 4 2007. ISSN 00027863. doi: 10.1021/ja067545z.

[79] Ann-Therése -T Karlberg, Kerstin Magnusson, and Ulrika Nilsson. Air oxidation of d-limonene (the citrus solvent) creates potent allergens. *Contact Dermatitis*, 26(5):332–340, 5 1992. ISSN 1600-0536. doi: 10.1111/J.1600-0536.1992.TB00129.X. URL https://onlinelibrary.wiley.com/doi/full/10.1111/j.1600-0536.1992.tb00129.xhttps://onlinelibrary.wiley.com/doi/abs/10.1111/j.1600-0536.1992.tb00129.xhttps://onlinelibrary.wiley.com/doi/10.1111/j.1600-0536.1992.tb00129.x.

[80] K. Arata, S. Akutagawa, and K. Tanabe. Isomerization of d-limonene oxide over solid acids and bases. *Journal of Catalysis*, 41(1):173–179, 1 1976. ISSN 0021-9517. doi: 10.1016/0021-9517(76)90213-X.

[81] A.-T Karlberg, L P Shao, U Nilsson, E Gafvert, and J L G Nilsson. Hydroperoxides in oxidized d-limonene identified as potent contact allergens. Technical report, 1994.

[82] Per Axel Clausen, Cornelius Ken Wilkins, Peder Wolkoff, and Gunnar Damgård Nielsen. Chemical and biological evaluation of a reaction mixture of R-(+)-limonene/ozone: Formation of strong airway irritants. *Environment International*, 26(7-8):511–522, 2001. ISSN 18736750. doi: 10.1016/S0160-4120(01)00035-6. URL www.elsevier.com/locate/envint.

[83] Nathan L Anderson, Ravi Pramod Vedula, Peter A Schultz, R M Van Ginhoven, and Alejandro Strachan. First-Principles Investigation of Low Energy E 0 Center Precursors in Amorphous Silica. 106(20):206402, 2011. doi: 10.1103/PhysRevLett.106.206402.

[84] Curt M. Breneman and Kenneth B. Wiberg. Determining atom-centered monopoles from molecular electrostatic potentials. The need for high sampling density in formamide conformational analysis. *Journal of Computational Chemistry*, 11 (3):361–373, 4 1990. ISSN 1096-987X. doi: 10.1002/JCC.540110311. URL https://onlinelibrary.wiley.com/doi/full/10.1002/jcc.540110311https://onlinelibrary.wiley.com/doi/abs/10.1002/jcc.540110311https://onlinelibrary.wiley.com/doi/10.1002/jcc.540110311.

[85] Eric F. Pettersen, Thomas D. Goddard, Conrad C. Huang, Gregory S. Couch, Daniel M. Greenblatt, Elaine C. Meng, and Thomas E. Ferrin. UCSF Chimera—A visualization system for exploratory research and analysis. *Journal of Computational Chemistry*, 25(13):1605–1612, 10 2004. ISSN 1096-987X. doi: 10.1002/JCC.20084. URL https://onlinelibrary.wiley.com/doi/full/10.1002/jcc.20084https://onlinelibrary.wiley.com/doi/abs/10.1002/jcc.20084https://onlinelibrary.wiley.com/doi/10.1002/jcc.20084.

[86] L. Diaz, C. M. Liauw, M. Edge, N. S. Allen, A. McMahon, and N. Rhodes. Investigation of factors affecting the adsorption of functional molecules onto gel silicas. 1. Flow microcalorimetry and infrared spectroscopy. *Journal of colloid and interface science*, 287(2):379–387, 7 2005. ISSN 0021-9797. doi: 10.1016/J.JCIS.2004.09.039. URL https://pubmed.ncbi.nlm.nih.gov/15925601/.

[87] Liubin Huang, Elianna S. Frank, Mona Shrestha, Saleh Riahi, Douglas J. Tobias, and Vicki H. Grassian. Heterogeneous Interactions of Prevalent Indoor Oxygenated Organic Compounds on Hydroxylated SiO ¡sub¿2¡/sub¿ Surfaces. *Environmental Science & Technology*, 55(10):6623–6630, 5 2021. ISSN 0013-936X. doi: 10.1021/acs.est.1c00067. URL https://pubs.acs.org/doi/10.1021/acs.est.1c00067.

[88] Chenghua Sun, Li Min Liu, Annabella Selloni, Gao Qing Lu, and Sean C. Smith. Titania-water interactions: A review of theoretical studies. *Journal of Materials Chemistry*, 20(46):10319–10334, 12 2010. ISSN 09599428. doi: 10.1039/c0jm01491e. URL https://pubs.rsc.org/en/content/articlehtml/2010/jm/c0jm01491ehttps://pubs.rsc.org/en/content/articlelanding/2010/jm/c0jm01491e.

[89] Changjun Zhang and Philip J.D. Lindan. A density functional theory study of the coadsorption of water and oxygen on TiO2(110). *Journal of Chemical Physics*, 121(8), 2004. ISSN 00219606. doi: 10.1063/1.1775784.

[90] Philip J.D. Lindan, N. M. Harrison, and M. J. Gillan. Mixed Dissociative and Molecular Adsorption of Water on the Rutile (110) Surface. *Physical Review Letters*, 80(4):762, 1 1998. ISSN 10797114. doi: 10.1103/PhysRevLett.80.762. URL `https://journals.aps.org/prl/abstract/10.1103/PhysRevLett.80.762`.

[91] Leonard A. Harris and Andrew A. Quong. Molecular Chemisorption as the Theoretically Preferred Pathway for Water Adsorption on Ideal Rutile TiO2. *Physical Review Letters*, 93(8), 2004. ISSN 0031-9007.

[92] Joan Margineda and Niall J. English. Dynamical and structural properties of adsorbed water molecules at the TiO2 rutile-(110) surface: interfacial hydrogen bonding probed by ab-initio molecular dynamics. *Molecular Physics*, 118(9-10), 6 2020. ISSN 13623028. doi: 10.1080/00268976.2020.1725166. URL `https://www.tandfonline.com/action/journalInformation?journalCode=tmph20`.

[93] Eric W S Hagan, Maria N Charalambides, Christina T Young, · Thomas, J S Learner, and Stephen Hackney. Tensile properties of latex paint films with TiO 2 pigment. *Mech Time-Depend Mater*, 13:149–161, 2009. doi: 10.1007/s11043-009-9076-y.

[94] Anantha Iyengar Gopalan, Jun Cheol Lee, Gopalan Saianand, Kwang Pill Lee, Prashant Sonar, Rajarathnam Dharmarajan, Yao Long Hou, Ki Yong Ann, Venkatramanan Kannan, and Wha Jung Kim. Recent progress in the abatement of hazardous pollutants using photocatalytic TiO2-based building materials. *Nanomaterials*, 10(9): 1–50, 9 2020. ISSN 20794991. doi: 10.3390/NANO10091854.

[95] L Frazer. Titanium dioxide: environmental white knight? *Environmental Health Perspectives*, 109(4), 4 2001. ISSN 0091-6765. doi: 10.1289/EHP.109-A174.

[96] F. Thevenet, L. Olivier, F. Batault, L. Sivachandiran, and N. Locoge. Acetaldehyde adsorption on TiO2: Influence of NO2 preliminary adsorption. *Chemical Engineering Journal*, 281:126–133, 12 2015. ISSN 13858947. doi: 10.1016/J.CEJ.2015.06.084.

[97] Hyun Ook, Seo • Dae, Han Kim, Kwang-Dae Kim, Eun Ji Park, Chae Won, Sim • Young, and Dok Kim. Adsorption and desorption of toluene on nanoporous TiO 2 /SiO 2 prepared by atomic layer deposition (ALD): influence of TiO 2 thin film thickness and humidity. doi: 10.1007/s10450-013-9550-3.

[98] F. Thevenet, M. Verriele, P. Harb, S. Thlaijeh, R. Brun, M. Nicolas, and S. Angulo-Milhem. The indoor fate of terpenes: Quantification of the limonene uptake by materials. *Building and Environment*, page 107433, 11 2020. ISSN 03601323. doi: 10.1016/j.buildenv.2020.107433.

[99] Alireza Haghighat Mamaghani, Fariborz Haghighat, and Chang Seo Lee. Effect of titanium dioxide properties and support material on photocatalytic oxidation of indoor

air pollutants. *Building and Environment*, 189:107518, 2 2021. ISSN 0360-1323. doi: 10.1016/J.BUILDENV.2020.107518.

[100] Mahiko Nagao and Yasuharu Suda. Adsorption of Benzene, Toluene, and Chlorobenzene on Titanium Dioxide. *Langmuir*, 5(1):42–47, 1 1989. ISSN 15205827. doi: 10.1021/LA00085A009.

[101] Michael R. Alves, Yuan Fang, Kristin J. Wall, Veronica Vaida, and Vicki H. Grassian. Chemistry and Photochemistry of Pyruvic Acid Adsorbed on Oxide Surfaces. *Journal of Physical Chemistry A*, 123(35):7661–7671, 9 2019. ISSN 15205215. doi: 10.1021/ACS.JPCA.9B06563/SUPPL{_}FILE/JP9B06563{_}SI{_}001.PDF. URL https://pubs.acs.org/doi/abs/10.1021/acs.jpca.9b06563.

[102] Timothy N. Obee and Robert T. Brown. TiO2 Photocatalysis for Indoor Air Applications: Effects of Humidity and Trace Contaminant Levels on the Oxidation Rates of Formaldehyde, Toluene, and 1,3-Butadiene. *Environmental Science and Technology*, 29(5):1223–1231, 1995. ISSN 15205851. doi: 10.1021/ES00005A013/ASSET/ES00005A013.FP.PNG{_}V03. URL https://pubs.acs.org/doi/abs/10.1021/es00005a013.

[103] Rosana M. Alberici and Wilson F. Jardim. Photocatalytic destruction of VOCs in the gas-phase using titanium dioxide. *Applied Catalysis B: Environmental*, 14(1-2):55–68, 12 1997. ISSN 0926-3373. doi: 10.1016/S0926-3373(97)00012-X.

[104] Lexuan Zhong, Chang Seo Lee, and Fariborz Haghighat. Adsorption performance of titanium dioxide (TiO2) coated air filters for volatile organic compounds. *Journal of Hazardous Materials*, 243:340–349, 12 2012. ISSN 0304-3894. doi: 10.1016/J.JHAZMAT.2012.10.042.

[105] Gayan Volp and Vicki H. Grassian. Role(s) of adsorbed water in the surface chemistry of environmental interfaces. *Chemical Communications*, 49 (30):3071–3094, 3 2013. ISSN 1364-548X. doi: 10.1039/C3CC38872G. URL https://pubs.rsc.org/en/content/articlehtml/2013/cc/c3cc38872ghttps://pubs.rsc.org/en/content/articlelanding/2013/cc/c3cc38872g.

[106] Daniel Vildozo, Raquel Portela, Corinne Ferronato, and Jean Marc Chovelon. Photocatalytic oxidation of 2-propanol/toluene binary mixtures at indoor air concentration levels. *Applied Catalysis B: Environmental*, 107(3-4):347–354, 9 2011. ISSN 0926-3373. doi: 10.1016/J.APCATB.2011.07.035.

[107] Materials Project. https://materialsproject.org/materials/mp-2657/. URL https://materialsproject.org/materials/mp-2657/.

[108] Erik G. Brandt and Alexander P. Lyubartsev. Molecular Dynamics Simulations of Adsorption of Amino Acid Side Chain Analogues and a Titanium Binding Peptide on the TiO2 (100) Surface. *Journal of Physical Chemistry C*, 119(32):18126–18139, 7 2015. ISSN 19327455. doi: 10.1021/acs.jpcc.5b02670.

[109] Xiang Wang, Xiao Yang, Huijun Chen, Xiaoning Yang, and Zhijun Xu. Entropy-Enthalpy Compensation in Peptide Adsorption on Solid Surfaces: Dependence on Surface Hydration. *Langmuir*, 36(36):10822–10829, 2020. ISSN 15205827. doi: 10.1021/acs.langmuir.0c01845.

[110] John P. Perdew, Kieron Burke, and Matthias Ernzerhof. Generalized gradient approximation made simple. *Physical Review Letters*, 77(18):3865–3868, 1996. ISSN 10797114. doi: 10.1103/PHYSREVLETT.77.3865.

[111] P. Pulay. Improved SCF convergence acceleration. *Journal of Computational Chemistry*, 3(4):556–560, 12 1982. ISSN 1096-987X. doi: 10.1002/JCC.540030413. URL https://onlinelibrary.wiley.com/doi/full/10.1002/jcc.540030413https://onlinelibrary.wiley.com/doi/abs/10.1002/jcc.540030413https://onlinelibrary.wiley.com/doi/10.1002/jcc.540030413.

[112] Engineering National Academies of Sciences and Medicine. Why Indoor Chemistry Matters. 5 2022. doi: 10.17226/26228. URL https://www.nap.edu/catalog/26228.

[113] Laurent Dormont, Jean Marie Bessière, and Anna Cohuet. Human Skin Volatiles: A Review. *Journal of Chemical Ecology*, 39(5):569–578, 5 2013. ISSN 00980331. doi: 10.1007/S10886-013-0286-Z/TABLES/2. URL https://link.springer.com/article/10.1007/s10886-013-0286-z.

[114] Magdalena Kruza and Nicola Carslaw. How do breath and skin emissions impact indoor air chemistry? *Indoor Air*, 29(3):369–379, 5 2019. ISSN 16000668. doi: 10.1111/INA.12539.

[115] Shouming Zhou, Matthew W. Forbes, and Jonathan P.D. Abbatt. Kinetics and Products from Heterogeneous Oxidation of Squalene with Ozone. *Environmental Science and Technology*, 50(21):11688–11697, 11 2016. ISSN 15205851. doi: 10.1021/ACS.EST.6B03270/SUPPL{_}FILE/ES6B03270{_}SI{_}001.PDF. URL https://pubs.acs.org/doi/abs/10.1021/acs.est.6b03270.

[116] Glenn C. Morrison and William W. Nazaroff. Ozone interactions with carpet: Secondary emissions of aldehydes. *Environmental Science and Technology*, 36(10):2185–2192, 5 2002. ISSN 0013936X. doi: 10.1021/ES0113089/ASSET/IMAGES/MEDIUM/ES0113089E00005.GIF. URL https://pubs.acs.org/doi/full/10.1021/es0113089.

[117] Stacey E. Anderson, J. R. Wells, Adam Fedorowicz, Leon F. Butterworth, B. J. Meade, and Albert E. Munson. Evaluation of the Contact and Respiratory Sensitization Potential of Volatile Organic Compounds Generated by Simulated Indoor Air Chemistry. *Toxicological Sciences*, 97(2):355–363, 6 2007. ISSN 1096-6080. doi: 10.1093/TOXSCI/KFM043. URL https://academic.oup.com/toxsci/article/97/2/355/1648946.

[118] Stacey E. Anderson, Jennifer Franko, Laurel G. Jackson, J. R. Wells, Jason E. Ham, and B. J. Meade. Irritancy and Allergic Responses Induced by Exposure to the Indoor Air Chemical 4-Oxopentanal. *Toxicological Sciences*, 127(2):371–381, 6 2012.

ISSN 1096-6080. doi: 10.1093/TOXSCI/KFS102. URL https://academic.oup.com/toxsci/article/127/2/371/1705661.

[119] P. Fruekilde, J. Hjorth, N. R. Jensen, D. Kotzias, and B. Larsen. Ozonolysis at vegetation surfaces: a source of acetone, 4-oxopentanal, 6-methyl-5-hepten-2-one, and geranyl acetone in the troposphere. *Atmospheric Environment*, 32(11):1893–1902, 6 1998. ISSN 1352-2310. doi: 10.1016/S1352-2310(97)00485-8.

[120] Crystal D. Forester and J. Raymond Wells. Yields of carbonyl products from gas-phase reactions of fragrance compounds with OH radical and ozone. *Environmental Science and Technology*, 43(10):3561–3568, 5 2009. ISSN 0013936X. doi: 10.1021/ES803465V/SUPPL{_}FILE/ES803465V{_}SI{_}001.PDF. URL https://pubs.acs.org/doi/full/10.1021/es803465v.

[121] Peder Wolkoff, Søren T. Larsen, Maria Hammer, Vivi Kofoed-Sørensen, Per A. Clausen, and Gunnar D. Nielsen. Human reference values for acute airway effects of five common ozone-initiated terpene reaction products in indoor air. *Toxicology Letters*, 216(1):54–64, 1 2013. ISSN 03784274. doi: 10.1016/J.TOXLET.2012.11.008.

[122] Heidi J. Salonen, Anna Liisa Pasanen, Sanna K. Lappalainen, Henri M. Riuttala, Tapani M. Tuomi, Pertti O. Pasanen, Beatrice C. Bäck, and Kari E. Reijula. Airborne Concentrations of Volatile Organic Compounds, Formaldehyde and Ammonia in Finnish Office Buildings with Suspected Indoor Air Problems. *http://dx.doi.org/10.1080/15459620802707835*, 6(3):200–209, 2009. ISSN 15459632. doi: 10.1080/15459620802707835. URL https://www.tandfonline.com/doi/abs/10.1080/15459620802707835.

[123] Jun Guan, Kai Gao, Chao Wang, Xudong Yang, Chao Hsin Lin, Caiyun Lu, and Peng Gao. Measurements of volatile organic compounds in aircraft cabins. Part I: Methodology and detected VOC species in 107 commercial flights. *Building and Environment*, 72:154–161, 2 2014. ISSN 0360-1323. doi: 10.1016/J.BUILDENV.2013.11.002.

[124] Yingjun Liu, Pawel K. Misztal, Caleb Arata, Charles J. Weschler, William W. Nazaroff, and Allen H. Goldstein. Observing ozone chemistry in an occupied residence. *Proceedings of the National Academy of Sciences of the United States of America*, 118(6), 2 2021. ISSN 10916490. doi: 10.1073/PNAS.2018140118/SUPPL{_}FILE/PNAS.2018140118.SD01.XLSX. URL https://www.pnas.org.

[125] Craig M. Butt, Miriam L. Diamond, Jennifer Truong, Michael G. Ikonomou, and Arnout F.H. Ter Schure. Spatial Distribution of Polybrominated Diphenyl Ethers in Southern Ontario As Measured in Indoor and Outdoor Window Organic Films. *Environmental Science and Technology*, 38(3):724–731, 2 2004. ISSN 0013936X. doi: 10.1021/ES034670R/SUPPL{_}FILE/ES034670R{_}S.PDF. URL https://pubs.acs.org/doi/abs/10.1021/es034670r.

[126] Victor W. Or, Michael R. Alves, Michael Wade, Sarah Schwab, Richard L. Corsi, and Vicki H. Grassian. Crystal Clear? Microspectroscopic Imaging and Physicochemical Characterization of Indoor Depositions on Window Glass. *Environmental Science*

and Technology Letters, 5(8):514–519, 8 2018. ISSN 23288930. doi: 10.1021/ACS.ESTLETT.8B00355/SUPPL{_}FILE/EZ8B00355{_}SI{_}001.PDF. URL https://pubs.acs.org/doi/abs/10.1021/acs.estlett.8b00355.

[127] Lucas B. Algrim, Demetrios Pagonis, Joost A. de Gouw, Jose L. Jimenez, and Paul J. Ziemann. Measurements and modeling of absorptive partitioning of volatile organic compounds to painted surfaces. *Indoor Air*, 30(4):745–756, 7 2020. ISSN 1600-0668. doi: 10.1111/INA.12654. URL https://onlinelibrary.wiley.com/doi/full/10.1111/ina.12654https://onlinelibrary.wiley.com/doi/abs/10.1111/ina.12654https://onlinelibrary.wiley.com/doi/10.1111/ina.12654.

[128] Hanyu Fan, Elianna S. Frank, Pascale S. J. Lakey, Manabu Shiraiwa, Douglas J. Tobias, and Vicki H. Grassian. Heterogeneous Interactions between Carvone and Hydroxylated SiO2. *The Journal of Physical Chemistry C*, 126(14):6267–6279, 4 2022. ISSN 1932-7447. doi: 10.1021/ACS.JPCC.2C00815. URL https://pubs.acs.org/doi/abs/10.1021/acs.jpcc.2c00815.